Single- and Two-Phase Flow Modeling for Coupled Neutronics / Thermal-Hydraulics Transient Analysis of Advanced Sodium-Cooled Fast Reactors

THÈSE Nº 5172 (2011)

PRÉSENTÉE LE 24 OCTOBRE 2011 À LA FACULTÉ SCIENCES DE BASE LABORATOIRE DE PHYSIQUE DES RÉACTEURS ET DE COMPORTEMENT DES SYSTÈMES PROGRAMME DOCTORAL EN ENERGIE

ÉCOLE POLYTECHNIQUE FÉDÉRALE DE LAUSANNE

POUR L'OBTENTION DU GRADE DE DOCTEUR ÈS SCIENCES

PAR

Aurélia CHENU

acceptée sur proposition du jury:

Prof. M. Q. Tran, président du jury Prof. R. Chawla, directeur de thèse Prof. K. Ivanov, rapporteur Dr K. Mikityuk, rapporteur Dr A. Zaetta, rapporteur



Abstract

Nuclear power is nowadays in the front rank as regards helping to meet the growing worldwide energy demand while avoiding an excessive increase in greenhouse gas emissions. However, the operating nuclear power plants are mainly thermal-neutron reactors and, as such, can not be maintained on the basis of the currently identified uranium resources beyond one century at the present consumption rate. Sustainability of nuclear power thus involves closure of the fuel cycle through breeding. With a uranium-based fuel, breeding can only be achieved using a fast-neutron reactor. Sodium-cooled fast reactor (SFR) technology benefits from 400 reactor-years of accumulated experience and is thus a prime candidate for the implementation of so-called Generation-IV nuclear energy systems. In this context, the safety demonstration of SFRs remains a major R&D related issue.

The current doctoral research aims at the development of a computational tool for the in-depth understanding of SFR core behavior during accidental transients, particularly those including boiling of the coolant. An accurate modeling of the core physics during such transients requires the coupling between 3D neutron kinetics and thermal-hydraulics in the core, to account for the strong interactions between the two-phase coolant flow and power variations caused by the sodium void effect. Models for the representation of sodium two-phase flow are not present in most of the thermal-hydraulics codes used currently, and these have specifically been focused upon. The particular contributions of the present research are: (1) implementation of sodium two-phase flow models into the thermal-hydraulics code TRACE, which forms part of the FAST code system at PSI and, as such, can easily be coupled to the spatial neutron kinetics code PARCS; (2) validation of the TRACE sodium single- and two-phase flow modeling using out-of-pile sodium boiling experiments; (3) validation of the coupled TRACE/PARCS code system on the basis of experimental reactor data; and (4) application of the developed new tool for the core behavior analysis of an advanced SFR during a transient with boiling onset.

The extension of the TRACE code, previously limited to the simulation of singlephase sodium flow, has been carried out through the implementation of equationsof-state and closure relations specific to sodium. A review has first been performed of the models available in the open literature for the representation of the interfacial and wall-to-fluid transfer mechanisms. The different correlations have then been implemented as options in the extended TRACE code. From the validation study carried out, it has been possible to recommend a set of models which provide satisfactory results, while considering annular flow as the dominant regime up to dryout and a smooth breakdown of the liquid film after dryout onset.

The validation of the extended TRACE code has been achieved through the successful simulation of out-of-pile experiments. A review of available sodium boiling test data has first been carried out, and complementary tests have then been selected to assess the quality of the different physical models. These tests, performed in the 1980s, include the study of the pressure drop and cooling limits under quasi steady-state conditions, as well as the simulation of a loss-of-flow transient. Sensitivity analyses, using the specifically implemented correlations, have enabled one to identify the most pertinent physical parameters and to define, for each, the most appropriate model. Usage of the set of models thus selected has demonstrated the capacity of the extended TRACE code to predict, with satisfactory accuracy, the main thermal-hydraulics characteristics such as the single- and two-phase pressure drop and heat transfer, as also the characteristic quantities describing the sodium two-phase flow, e.g. boiling inception, void fraction evolution and expansion of the boiling region, pressure evolution, as well as coolant and clad temperatures.

The natural convection test conducted in 2009 in the Phenix reactor has been used to validate TRACE single-phase sodium flow modeling. This represents the first international benchmark exercise conducted on the basis of actual SFR experimental data. Data from the Phenix test have additionally been used as basis for the validation of the FAST code system as a whole. Analyses based on a point-kinetics TRACE model and on coupled TRACE/PARCS 3D-kinetics modeling have enabled an in-depth understanding of the transient behavior of a sodium-cooled fast reactor core, as well as the identification of potential improvements in the FAST code system. The experimental power evolution could be satisfactorily reproduced within the measurement uncertainties with both models, and the detailed analysis of the core neutronics has enabled one to define the most important reactivity feedbacks taking place during the considered transient.

In the final part of the thesis, the developed tool has been applied to the simulation of a hypothetical, unprotected loss-of-flow event for one of the European SFR (ESFR) core concepts. This study has demonstrated the new calculational tool's capability to adequately simulate the core response through the modeling of single- and two-phase sodium flow, coupled to 3D neutron kinetics. Thereby, the space-dependent reactivity feedbacks, such as the void and Doppler effects, have been shown to be modeled accurately. The resulting analysis has shown the ability of the TRACE/PARCS modeling to predict the expansion of the boiling region and calculate the resulting feedbacks, as well as to predict the interactions between parallel boiling channels. This first-of-a-kind study has provided detailed results for the thermal-hydraulics and neutronics parameters during the pre-severe phase of the simulated accident, thus allowing a comprehensive understanding of the core behavior during such transients.

In brief, the present research has led to the development of a key calculational tool for SFR safety analysis. A first application of the new tool has demonstrated its potential for usage in SFR design optimization aimed at enhanced safety.

Keywords: Sodium-cooled Fast Reactor (SFR), Generation-IV nuclear power plants, ESFR, safety demonstration, transient analysis, thermal-hydraulics, sodium two-phase flow, 3D neutron kinetics, FAST code system, TRACE, PARCS, sodium boiling experiments, Phenix tests.

Résumé

L'énergie nucléaire est actuellement au premier rang pour répondre à la demande mondiale croissante d'énergie tout en évitant une émission excessive de gaz à effet de serre. Cependant, les centrales nucléaires en opération sont principalement des réacteurs à neutrons thermiques, qui ne peuvent être maintenues au-delà d'un siècle au taux de consommation actuel en considérant les ressources identifiées en uranium. Assurer une production d'énergie nucléaire pérenne implique donc la fermeture du cycle du combustible à travers la régénération. Avec un combustible à base d'uranium, seuls les réacteurs à neutrons rapides (RNR) offrent une telle possibilité. La filière à caloporteur sodium (RNR-Na) bénéficie à ce jour d'une expérience accumulée de 400 réacteur-ans, ce qui la place parmi les premiers candidats pour le déploiement de systèmes d'énergie nucléaire dits de Génération IV. Dans ce contexte, la démonstration de sûreté des RNR-Na représente un enjeu de R&D majeur.

La présente recherche doctorale vise à développer un outil de calcul approprié pour la compréhension approfondie du comportement du cœur des RNR-Na lors de transitoires accidentels, en particulier ceux impliquant l'ébullition du caloporteur. Une modélisation précise de la physique du cœur dans ce type de régime nécessite le couplage entre la cinétique neutronique 3D et la thermo-hydraulique du cœur, afin de rendre compte des fortes interactions entre l'écoulement diphasique du caloporteur et les variations de puissance induites par l'effet de vide sodium. La représentation d'un écoulement sodium diphasique faisant défaut dans la plupart des codes de thermo-hydraulique actuellement utilisés, celle-ci a fait l'objet de développements spécifiques. Les contributions particulières de la présente recherche sont (1) l'implémentation d'un modèle d'écoulement sodium diphasique dans le code de thermohydraulique TRACE, qui fait partie intégrante du système de codes FAST à PSI et peut, en tant que tel, être facilement couplé au code de cinétique neutronique spatiale PARCS; (2) la validation de la modélisation d'un écoulement sodium simple et double phase avec TRACE en utilisant des données d'expériences hors pile sur l'ébullition du sodium; (3) la validation du système de codes couplés TRACE/PARCS à partir de données expérimentales en réacteur; et (4) l'application du nouvel outil développé pour l'analyse du comportement du cœur d'un RNR-Na avancé pendant un transitoire avec début d'ébullition.

L'extension du code TRACE, auparavant limité à la simulation d'un écoulement sodium liquide, a été réalisée à travers l'implémentation d'équations d'état et de relations de fermeture spécifiques au sodium. Tout d'abord, une révision des modèles disponibles dans la littérature pour la représentation des mécanismes de transfert à l'interface ainsi qu'entre la paroi et le fluide a été réalisée. Les différentes corrélations ont alors été implémentées comme options dans le code TRACE étendu. L'étude de validation a permis de recommander un ensemble de modèles dont les résultats sont satisfaisants en considérant un écoulement annulaire comme régime dominant jusqu'à l'assèchement, et une rupture régulière du film liquide après initiation de l'assèchement.

La validation de la version étendue de TRACE a été réalisée à travers la simulation d'expériences hors-pile. Après une révision des données de tests relatifs à l'ébullition du sodium disponibles dans la littérature, des expériences complémentaires ont été sélectionnées afin d'évaluer la qualité des différents modèles physiques. Ces tests, réalisés dans les années 80, incluent l'étude de la chute de pression et des limites de refroidissement dans des conditions quasiment stables, ainsi que la simulation d'un transitoire de perte de débit. Des analyses de sensibilité utilisant les corrélations spécifiquement implémentées ont permis d'identifier les paramètres physiques les plus pertinents, et pour chacun, le modèle le plus approprié. L'utilisation de l'ensemble des corrélations ainsi sélectionnées a démontré la capacité du code TRACE étendu à prédire de manière satisfaisante les principales propriétés thermo-hydrauliques telles que la perte de charge et le transfert de chaleur en simple et double phase ainsi que les grandeurs caractéristiques d'un écoulement sodium diphasique, e.g. le début de l'ébullition, l'évolution de la fraction de vide et l'expansion de la zone d'ébullition, l'évolution de la pression ainsi que des températures du caloporteur et de la gaine.

Le test de convection naturelle conduit en 2009 dans le réacteur Phénix a été utilisé pour valider la modélisation dans TRACE d'un écoulement de sodium simple phase. Ceci constitue le premier benchmark international réalisé à partir de résultats expérimentaux d'un RNR-Na. Les données du test Phénix ont en outre été utilisées pour la validation du système de codes FAST dans son intégralité. Les analyses s'appuyant sur un modèle de cinétique point dans TRACE et sur le modèle couplé TRACE/PARCS de cinétique spatiale ont permis une compréhension approfondie du comportement d'un cœur de RNR refroidi au sodium en régime transitoire, ainsi que l'identification de potentielles améliorations du système de codes FAST. L'évolution de la puissance expérimentale a pu être reproduite avec succès dans l'ordre des incertitudes de mesure avec les deux modèles, et l'analyse détaillée de la neutronique du cœur a permis de définir les contre-réactions les plus importantes ayant lieu au cours du transitoire considéré.

Dans la partie finale de la thèse, l'outil développé a été utilisé pour la simulation d'une hypothétique perte de débit non protégée dans un des concepts de cœur européen du RNR-Na, l'ESFR. Cette étude a démontré la capacité du nouvel outil de calcul à simuler de manière appropriée la réponse du cœur à travers la modélisation couplée de l'écoulement sodium diphasique et de la cinétique neutronique 3D. Ainsi, il a été vérifié que les contre-réactions de réactivité telles que l'effet de vide et l'effet Doppler ont été correctement représentées. L'analyse des résultats a montré la capacité de la modélisation TRACE/PARCS à prédire l'expansion de la zone d'ébullition et à calculer les contre-réactions résultantes, ainsi qu'à simuler les interactions entre des assemblages parallèles bouillants. Cette étude, la première en son genre, a fourni des résultats détaillés concernant les paramètres thermo-hydrauliques et neutroniques pendant la phase pre-sévère d'une simulation d'accident, permettant ainsi une compréhension détaillée du comportement du cœur pendant de tels transitoires.

En résumé, la présente recherche a conduit au développement d'un outil de calcul clé pour l'analyse de la sûreté des RNR-Na. Une première application du nouvel outil a démontré son potentiel pour une utilisation dans le cadre d'optimisation de concepts de cœur de RNR-Na visant à une amélioration de la sûreté.

Mots clés : Réacteur à neutrons rapides refroidi au sodium (RNR-Na), centrales nucléaires de Génération IV, ESFR, démonstration de sûreté, analyse de transitoires, thermo-hydraulique, écoulement sodium diphasique, cinétique neutronique 3D, système de codes FAST, TRACE, PARCS, expériences d'ébullition du sodium, tests Phénix.

Contents

\mathbf{A}	bstra	let	i
Re	ésum	ié	iii
Co	onter	ıts	\mathbf{v}
1	Intr	oduction	1
	1.1	The status of nuclear energy today	1
		1.1.1 Present nuclear technology, potential and limitations	1
		1.1.2 Conditions for breeding	2
	1.2	Fast neutron-spectrum reactors	3
		1.2.1 Past and present (sodium) fast reactors	3
		1.2.2 Sodium as a fast reactor coolant	4
	1.3	Generation-IV systems	6
	1.4	Goals and scope of the present study	7
	1.5	Structure of the thesis	9
2	The	esis background	11
	2.1	Development of SFR technology	11
		2.1.1 Comparison of fast reactor coolants	11
		2.1.2 Influence of the coolant on SFR design	13
	2.2	Status of sodium-cooled fast reactor projects worldwide	14
		2.2.1 France: the Phenix reactor and other concepts	14
		2.2.2 In Europe: the ESFR project	17
		2.2.3 Japan: Joyo, Monju reactors and the FaCT project	18
		2.2.4 India: FBTR, PFBR	19
		2.2.5 China and the CEFR	19
		2.2.6 The republic of Korea and the KALIMER concept	19
		2.2.7 The Russian federation and the BN reactors	19
		2.2.8 Projects in the USA	20
	2.3	Calculational tools	20
		2.3.1 Historical review of dedicated sodium thermal-hydraulics calculational tools	
		2.3.2 State-of-the-art sodium codes	23
		2.3.3 The FAST code system	25
3	\mathbf{Sim}	ulation of sodium single- and two-phase flow with the TRACE code	35
	3.1	Two-phase flow models	36
	3.2	Sodium boiling features	38
	3.3	TRACE two-fluid non-homogeneous non-equilibrium model	40
	3.4	Closure relations as implemented in TRACE	41

		$3.4.1 \\ 3.4.2$	Interfacial area	
		3.4.2 3.4.3	Interfacial heat transfer	
		3.4.4	Wall heat transfer	
		3.4.5	Wall drag	
	3.5		sions	
4	Vali	idation	of TRACE sodium flow modeling using experimental data	61
	4.1	Study	of the pressure drop in steady-state boiling	. 62
		4.1.1	Description of the Ispra experiments	. 62
		4.1.2	Assessment of TRACE models for the prediction of pressure drop	. 63
		4.1.3	Conclusions from this study	. 76
	4.2		sis of dryout in pin bundles	. 77
		4.2.1	Description of the experiments and phenomenology of dryout in sodium flow	. 78
		4.2.2	Interpretation of the experimental results	
		4.2.2 4.2.3	Analysis of the experiments with TRACE and sensitivity study	
	4.3		tion of sodium boiling under loss-of-flow conditions	
	т.0	4.3.1	The KNS test facility and 37-pin bundle test section	
		4.3.2	Description of the reference test L22	
		4.3.3	One-dimensional calculations	
		4.3.4	Two-dimensional calculations	
		4.3.5	Conclusions from this study	
	4.4	Conclu	sions	. 99
5	Vali	idation	of TRACE and PARCS using Phenix reactor test data	101
5	\mathbf{Vali} 5.1		of TRACE and PARCS using Phenix reactor test data ption of the Phenix reactor	
5				. 102
5		Descrij	ption of the Phenix reactor	. 102 . 102
5		Descrij 5.1.1 5.1.2	ption of the Phenix reactorPhenix reactor circuits	. 102 . 102 . 102
5	5.1	Descrip 5.1.1 5.1.2 Descrip	ption of the Phenix reactor	. 102 . 102 . 102 . 105 . 107
5	5.1 5.2	Descrip 5.1.1 5.1.2 Descrip	ption of the Phenix reactor	. 102 . 102 . 102 . 105 . 107
5	5.1 5.2	Descrip 5.1.1 5.1.2 Descrip TRAC 5.3.1 5.3.2	ption of the Phenix reactor	 . 102 . 102 . 102 . 105 . 107 . 107 . 108
5	5.1 5.2	Descrij 5.1.1 5.1.2 Descrij TRAC 5.3.1 5.3.2 5.3.3	ption of the Phenix reactor	. 102 . 102 . 102 . 105 . 107 . 107 . 108 . 109
5	5.1 5.2	Descrip 5.1.1 5.1.2 Descrip TRAC 5.3.1 5.3.2 5.3.3 5.3.4	ption of the Phenix reactor	. 102 . 102 . 102 . 105 . 107 . 107 . 107 . 108 . 109 . 113
5	5.1 5.2	Descrij 5.1.1 5.1.2 Descrij TRAC 5.3.1 5.3.2 5.3.3 5.3.4 5.3.5	ption of the Phenix reactorPhenix reactor circuitsPhenix corePhenix coreption of the natural convection testption of the natural convection testE point kinetics analysis of the Phenix core responseTRACE model of the Phenix coreOptimization of the kinetics parametersImplemented reactivity feedbacksComparison of the TRACE results with the experimental dataSensitivity analysis with respect to the different reactivity feedbacks	. 102 . 102 . 102 . 105 . 107 . 107 . 107 . 108 . 109 . 113 . 113
5	5.1 5.2 5.3	Descrij 5.1.1 5.1.2 Descrij TRAC 5.3.1 5.3.2 5.3.3 5.3.4 5.3.5 5.3.6	ption of the Phenix reactorPhenix reactor circuitsPhenix corePhenix coreption of the natural convection testE point kinetics analysis of the Phenix core responseTRACE model of the Phenix coreOptimization of the kinetics parametersImplemented reactivity feedbacksComparison of the TRACE results with the experimental dataSensitivity analysis with respect to the different reactivity feedbacksConclusions from the point kinetics analysis	. 102 . 102 . 102 . 105 . 107 . 107 . 108 . 109 . 113 . 113 . 116
5	5.1 5.2	Descrip 5.1.1 5.1.2 Descrip TRAC 5.3.1 5.3.2 5.3.3 5.3.4 5.3.5 5.3.6 Couple	ption of the Phenix reactorPhenix reactor circuitsPhenix coreption of the natural convection testption of the natural convection testption of the natural convection testPhenix corePoint kinetics analysis of the Phenix core responseTRACE model of the Phenix coreOptimization of the kinetics parametersImplemented reactivity feedbacksComparison of the TRACE results with the experimental dataSensitivity analysis with respect to the different reactivity feedbacksconclusions from the point kinetics analysised TRACE/PARCS 3D-kinetics analysis of the Phenix NC test	 . 102 . 102 . 102 . 105 . 107 . 107 . 108 . 109 . 113 . 113 . 116 . 117
5	5.1 5.2 5.3	Descrip 5.1.1 5.1.2 Descrip TRAC 5.3.1 5.3.2 5.3.3 5.3.4 5.3.5 5.3.6 Couple 5.4.1	ption of the Phenix reactorPhenix reactor circuitsPhenix coreption of the natural convection testption of the natural convection testE point kinetics analysis of the Phenix core responseTRACE model of the Phenix coreOptimization of the kinetics parametersImplemented reactivity feedbacksComparison of the TRACE results with the experimental dataSensitivity analysis with respect to the different reactivity feedbacksconclusions from the point kinetics analysis of the Phenix NC testDevelopment of the TRACE/PARCS model	. 102 . 102 . 102 . 105 . 107 . 107 . 107 . 108 . 109 . 113 . 113 . 116 . 117 . 118
5	5.1 5.2 5.3	Descrip 5.1.1 5.1.2 Descrip TRAC 5.3.1 5.3.2 5.3.3 5.3.4 5.3.5 5.3.6 Couple 5.4.1 5.4.2	ption of the Phenix reactorPhenix reactor circuitsPhenix coreption of the natural convection testption of the natural convection testE point kinetics analysis of the Phenix core responseTRACE model of the Phenix coreOptimization of the kinetics parametersImplemented reactivity feedbacksComparison of the TRACE results with the experimental dataSensitivity analysis with respect to the different reactivity feedbacksconclusions from the point kinetics analysisconclusions from the point kinetics analysis of the Phenix NC testDevelopment of the TRACE/PARCS modelValidation of the coupled TRACE/PARCS model	. 102 . 102 . 102 . 105 . 107 . 107 . 108 . 109 . 113 . 113 . 113 . 116 . 117 . 118 . 120
5	5.15.25.35.4	Descrip 5.1.1 5.1.2 Descrip TRAC 5.3.1 5.3.2 5.3.3 5.3.4 5.3.5 5.3.6 Couple 5.4.1 5.4.2 5.4.3	ption of the Phenix reactorPhenix reactor circuitsPhenix coreption of the natural convection testption of the natural convection testE point kinetics analysis of the Phenix core responseTRACE model of the Phenix coreOptimization of the kinetics parametersImplemented reactivity feedbacksComparison of the TRACE results with the experimental dataSensitivity analysis with respect to the different reactivity feedbacksconclusions from the point kinetics analysisconclusions from the point kinetics analysis of the Phenix NC testDevelopment of the TRACE/PARCS modelValidation of the coupled TRACE/PARCS modelTransient calculation	 . 102 . 102 . 102 . 105 . 107 . 107 . 108 . 109 . 113 . 113 . 116 . 117 . 118 . 120 . 124
	 5.1 5.2 5.3 5.4 5.5 	Descrij 5.1.1 5.1.2 Descrij TRAC 5.3.1 5.3.2 5.3.3 5.3.4 5.3.5 5.3.6 Couple 5.4.1 5.4.2 5.4.3 Conclu	ption of the Phenix reactor	 . 102 . 102 . 102 . 105 . 107 . 107 . 108 . 109 . 113 . 113 . 116 . 117 . 118 . 120 . 124 . 128
5	 5.1 5.2 5.3 5.4 5.5 Cot 	Descrij 5.1.1 5.1.2 Descrij TRAC 5.3.1 5.3.2 5.3.3 5.3.4 5.3.5 5.3.6 Couple 5.4.1 5.4.2 5.4.3 Conclu upled T	ption of the Phenix reactor Phenix reactor circuits Phenix core Phenix core ption of the natural convection test Phenix core ption of the natural convection test Phenix core E point kinetics analysis of the Phenix core response Phenix core TRACE model of the Phenix core Phenix core Optimization of the kinetics parameters Phenix core Implemented reactivity feedbacks Phenix core Comparison of the TRACE results with the experimental data Phenix core Conclusions from the point kinetics analysis Phenix NC test Conclusions from the point kinetics analysis of the Phenix NC test Phenix Ceres model Validation of the coupled TRACE/PARCS model Phenix NC test Transient calculation Phenix core Prace/PARCS transient analysis of the ESFR	. 102 . 102 . 102 . 105 . 107 . 107 . 107 . 108 . 109 . 113 . 113 . 113 . 116 . 117 . 118 . 120 . 124 . 128 131
	 5.1 5.2 5.3 5.4 5.5 	Descrij 5.1.1 5.1.2 Descrij TRAC 5.3.1 5.3.2 5.3.3 5.3.4 5.3.5 5.3.6 Couple 5.4.1 5.4.2 5.4.3 Conclu upled T The ES	ption of the Phenix reactor Phenix reactor circuits Phenix core Phenix core ption of the natural convection test Phenix core E point kinetics analysis of the Phenix core response Phenix core TRACE model of the Phenix core Phenix core Optimization of the kinetics parameters Phenix core Implemented reactivity feedbacks Phenix core Comparison of the TRACE results with the experimental data Phenix core Sensitivity analysis with respect to the different reactivity feedbacks Phenix NC test Conclusions from the point kinetics analysis of the Phenix NC test Phenix NC test Development of the TRACE/PARCS model Phenix NC test Transient calculation Phenix Soft the ESFR SFR project and core concepts Soft the ESFR	. 102 . 102 . 102 . 105 . 107 . 107 . 108 . 109 . 113 . 113 . 113 . 113 . 116 . 117 . 120 . 124 . 128 131 . 131
	 5.1 5.2 5.3 5.4 5.5 Cot 	Descrij 5.1.1 5.1.2 Descrij TRAC 5.3.1 5.3.2 5.3.3 5.3.4 5.3.5 5.3.6 Couple 5.4.1 5.4.2 5.4.3 Conclu pled T The Ef 6.1.1	ption of the Phenix reactor	. 102 . 102 . 102 . 105 . 107 . 107 . 108 . 109 . 113 . 113 . 116 . 117 . 118 . 120 . 124 . 128 131 . 131 . 131
	 5.1 5.2 5.3 5.4 5.5 Cot 6.1 	Descrij 5.1.1 5.1.2 Descrij TRAC 5.3.1 5.3.2 5.3.3 5.3.4 5.3.5 5.3.6 Couple 5.4.1 5.4.2 5.4.3 Conclu ipled T The ES 6.1.1 6.1.2	ption of the Phenix reactor Phenix reactor circuits Phenix core Phenix core ption of the natural convection test Phenix core ption of the natural convection test Phenix core E point kinetics analysis of the Phenix core response Phenix core TRACE model of the Phenix core Phenix core Optimization of the kinetics parameters Phenix core Implemented reactivity feedbacks Phenix core Comparison of the TRACE results with the experimental data Phenix core Conclusions from the point kinetics analysis Phenix NC test Conclusions from the point kinetics analysis of the Phenix NC test Phenix core Validation of the coupled TRACE/PARCS model Phenix core Validation of the coupled TRACE/PARCS model Phenix core Pransient calculation Phenix core SFR project and core concepts Phenix core The project Phenix core Considered ESFR core Considered ESFR core	. 102 . 102 . 102 . 105 . 107 . 107 . 108 . 109 . 113 . 113 . 113 . 116 . 117 . 118 . 120 . 124 . 128 131 . 131 . 131 . 132
	 5.1 5.2 5.3 5.4 5.5 Cot 	Descrij 5.1.1 5.1.2 Descrij TRAC 5.3.1 5.3.2 5.3.3 5.3.4 5.3.5 5.3.6 Couple 5.4.1 5.4.2 5.4.3 Conclu ipled T The ES 6.1.1 6.1.2 Develo	ption of the Phenix reactor	. 102 . 102 . 102 . 105 . 107 . 107 . 107 . 108 . 109 . 113 . 113 . 113 . 113 . 114 . 120 . 124 . 128 131 . 131 . 132 . 134
	 5.1 5.2 5.3 5.4 5.5 Cot 6.1 	Descrij 5.1.1 5.1.2 Descrij TRAC 5.3.1 5.3.2 5.3.3 5.3.4 5.3.5 5.3.6 Couple 5.4.1 5.4.2 5.4.3 Conclu ipled T The ES 6.1.1 6.1.2	ption of the Phenix reactor Phenix reactor circuits Phenix core Phenix core ption of the natural convection test Phenix core ption of the natural convection test Phenix core E point kinetics analysis of the Phenix core response Phenix core TRACE model of the Phenix core Phenix core Optimization of the kinetics parameters Phenix core Implemented reactivity feedbacks Phenix core Comparison of the TRACE results with the experimental data Phenix core Conclusions from the point kinetics analysis Phenix NC test Conclusions from the point kinetics analysis of the Phenix NC test Phenix core Validation of the coupled TRACE/PARCS model Phenix core Validation of the coupled TRACE/PARCS model Phenix core Pransient calculation Phenix core SFR project and core concepts Phenix core The project Phenix core Considered ESFR core Considered ESFR core	. 102 . 102 . 102 . 105 . 107 . 107 . 108 . 109 . 113 . 113 . 113 . 116 . 117 . 118 . 120 . 124 . 124 . 128 131 . 131 . 131 . 132 . 134 . 134

	$\begin{array}{c} 6.3 \\ 6.4 \end{array}$	Verification of the TRACE/PARCS modelAnalysis of the ESFR core response to a ULOF6.4.1Description of the accident scenario	. 137
		6.4.2 Results of the TRACE/PARCS analysis and their discussion	. 138
		6.4.3 Detailed analysis of a two-phase flow instability	. 144
	6.5	Conclusions	. 148
7	Con	clusions and recommendations for future work	151
	7.1	Chapter-wise thesis summary	
	7.2	Main achievements	
	7.3	Recommendations for future work	
	7.4	Concluding remarks	. 159
\mathbf{A}	ppen	dices	161
A	Equ	ations-of-state	163
в	Rev	view of sodium boiling experiments available for code benchmarking	169
	B.1	Pool boiling experiments	
	B.2	The SIENA experiments	
		B.2.1 The annular test section and associated tests	
		B.2.2 The 7-pin bundle test section and associated tests	
		B.2.3 The 19-pin bundle test section and associated tests	
		B.2.4 The 37-pin bundle test section and associated tests	
	B.3	The KNS experiments	
		B.3.1 The tubular test section and associated tests	
		B.3.2 The 7-pin bundle test section and associated tests	
	D (B.3.3 The 37-pin bundle test section and associated tests	
	B.4	Other experiments	. 198
\mathbf{C}		ACE analysis of the latter part of the Phenix Natural Convection test	199
	C.1	F /	
		C.1.1 The core	
		C.1.2 Hot and cold pools	
		C.1.3 IHX and secondary circuit	
	C.2		
	O.2	C.2.1 Cold conditions: 400° C	
		C.2.2 Nominal power: 350 MWth	
		C.2.3 Reduced power: 120 MWth	
	C_{3}	Results of the NC test	
	C.4		
Bi	ibliog	graphy	213
		abbreviations and symbols	225
		wledgments	233
$\mathbf{C}_{\mathbf{I}}$	urric	ulum Vitæ	235

Chapter

Introduction

THIS OPENING CHAPTER briefly gives the status of nuclear energy today, with an emphasis of the long-term potential of breeder reactors (Section 1.1). In particular, a historical review is presented of fast neutron-spectrum reactors (Section 1.2), which in most cases have used sodium as coolant. Section 1.3 provides an overview of the international initiative for advanced, Generation-IV systems. The scope of the present doctoral research, that focuses on Sodium-cooled Fast Reactors (SFRs), is described in Section 1.4. The structure of the thesis is given in Section 1.5.

1.1 The status of nuclear energy today

1.1.1 Present nuclear technology, potential and limitations

After the demonstration of electricity generation using nuclear (fission) energy in the 1950s, the first commercial nuclear power plants entered operation in the early 1960s. Nuclear capacity grew rapidly during the 1970s and 1980s, as countries sought to reduce their dependence on fossil fuels. Following the Three Mile Island and Chernobyl accidents, the growth stagnated in the 1990s due to increased concerns about safety.

Today, nuclear power provides around 14% of the global electricity, and it has a strong potential to help meet the increasing energy demand while avoiding an excessive increase in greenhouse gas emissions. The 374 GW are produced by 442 power reactors distributed over 30 countries (see Fig. 1.1). The large majority (85%) of existing nuclear power plants (NPPs) are light water reactors (LWRs), considered as Generation II, where water is used both to moderate neutrons and to remove the heat generated from the nuclear fuel. The two broad categories of LWRs are pressurized water reactors¹ (PWRs), where the primary coolant remains in the liquid phase and steam is generated in a secondary loop, and boiling water reactors² (BWRs), where steam is generated in the primary loop and directly used to drive a turbine-generator. These nuclear power plants rely upon UO₂ enriched to 3-5wt% of 235 U, the only fissile nucleus present in nature, or, in some cases, a mixture of UO₂ and PuO₂ (MOX) fuel.

As fission in 235 U is induced much easier with thermal (slow) neutrons, the water in LWRs – serving as moderator – slows the produced fast neutrons down to thermal energies. Ordinary (light) water, however, absorbs too many neutrons to be used with unenriched fuel. Other systems, called Pressurized Heavy Water Reactors (PHWRs), use natural uranium fuel (99.27% 238 U, 0.72% 235 U) in combination with heavy water as neutron moderator. The remaining

 $^{^1\}mathrm{Primary}$ pressure around 15.5 MPa and temperature $\sim 315^\circ\mathrm{C}$

 $^{^{2}\}mathrm{Pressure}$ around 7.5 MPa and boiling at $285^{\circ}\mathrm{C}$

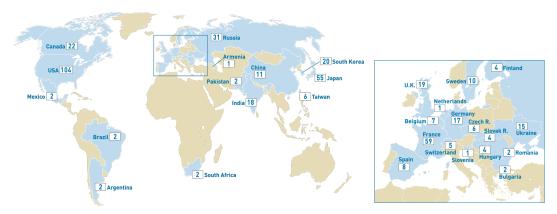


Figure 1.1. Nuclear power plants in the world [Nuk10]

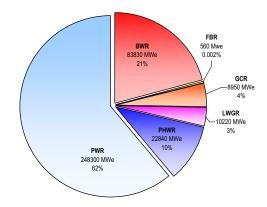


Figure 1.2. Reactor types in use worldwide (as of 2010 [IAE10])

NPPs use different coolants, e.g. gas (gas-cooled graphite-moderated reactors) or sodium (Fast Breeder Reactors (FBRs)). Figure 1.2 shows the number and type of power reactors in use worldwide.

The global natural-uranium requirements of NPPs, are presently about 68,000 tonnes. The ratio of the currently known conventional uranium resources (about 6.3 million tonnes) to the present consumption rate thus represents only about 100 years' supply [NEA10] and, as such, is comparable to that for other mineral energy resources. Obviously, this cannot ensure a sustainable contribution to the world's energy needs. Considering that spent nuclear fuel typically contains about 96% of uranium (mostly ²³⁸U with less than 1% ²³⁵U) and 1% plutonium, it can be recycled in a closed fuel cycle to generate new nuclear fuel, provided advanced reactors and closed fuel cycles are deployed for breeding, i.e. to convert fertile ²³⁸U into fissile plutonium at a greater rate than the consumption of the fissile material itself. This would enable one to obtain much more energy from each tonne of uranium, thus extending the duration of existing conventional uranium resources to more than 3000 years' supply [NEA08].

1.1.2 Conditions for breeding

As mentioned, 235 U, which occurs to the extent of as little as 0.72% in natural uranium, is the only fissile nuclide which nature has provided. The rest of natural uranium (99.28%) is mainly the fertile isotope 238 U which, like the second naturally occurring fertile nuclide, 232 Th (100% of natural thorium), can be converted in a nuclear reactor to 'artificial' fissile material. The corresponding fissile nuclides are the isotopes 239 Pu and 233 U, respectively, as per the following

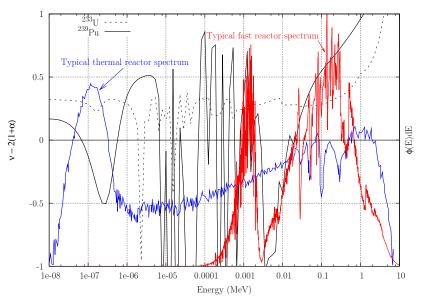


Figure 1.3. Number of neutrons available for breeding, per fissile nucleus fissioned, $N = \nu(E) - 2(1 + \alpha(E))$, and typical neutron spectra

reactions:

$$^{238}\text{U} + n \rightarrow ^{239}\text{U} \xrightarrow{\beta^-} ^{239}\text{Np} \xrightarrow{\beta^-} ^{239}\text{Pu}$$
 (1.1)

$$^{232}\text{Th} + n \rightarrow ^{233}\text{Th} \xrightarrow{\beta^-}_{22.3 \text{ min}} ^{233}\text{Pa} \xrightarrow{\beta^-}_{27 \text{ days}} ^{233}\text{U}$$
 (1.2)

There are certain important neutronics conditions, which need to be met, for one to be able to breed fissile material, i.e. to generate more than is consumed. This is because the neutron balance becomes much tighter, with one neutron required (per fissile nucleus destroyed) to sustain the nuclear chain reaction and at least one other for being captured in a fertile nucleus. More specifically, if $\alpha = \frac{\sigma_c}{\sigma_f}$ is the ratio of the capture cross-section σ_c to the fission cross-section σ_f of the fissile nucleus, $1 + \alpha$ neutrons need to be absorbed in fissile material for one fissile nucleus to be fissioned, i.e. for sustaining the nuclear chain reaction. In order to generate as much fissile material as has been destroyed (zero breeding), $1 + \alpha$ neutrons have to be captured in fertile nuclei. Considering that the number of neutrons released per fissile nucleus fissioned is ν , the number of neutrons available after generating as much fissile material as has been consumed is $N = \nu - 2(1 + \alpha)$. This clearly needs to be greater than 0 for finite breeding to occur. It can be seen from Fig. 1.3 that the breeding condition is only satisfied with a fast neutron spectrum in the case of uranium based fuel, while both fast and thermal spectra can be used in the case of thorium based fuel. Also, ²³⁹Pu appears to be the most effective fissile nuclide from the breeding viewpoint.

1.2 Fast neutron-spectrum reactors

1.2.1 Past and present (sodium) fast reactors

Fast reactors are not a new technology, and since the beginning of nuclear energy in the 1950s, fast reactor R&D programs have been carried out worldwide, leading to the construction and

1. INTRODUCTION

operation of experimental and prototype fast reactors. These are presented in Table 1.1, along with their main design characteristics and operating time. It is interesting to notice that all the reactors use liquid metal as coolant, and mainly sodium. This is due to the relatively high power density associated with fast reactor cores, which requires the use of an efficient coolant for effective heat removal. The development of (liquid metal) fast reactors over the last 50 years has enabled one to achieve more than 300 reactor-years of operating experience.

The world's first fast neutron reactor, Clementine, was built at Los Alamos in 1946 by the USA, and electricity from a fast reactor was first generated by the EBR-I in Idaho, USA, in 1951. The subsequent basic R&D and construction in the US aimed at increasing power (EBR-II, FERMI and FFTF). Other countries built their own demonstration reactors, such as the USSR (BR-10 and BOR-60), the UK (DFR) and France (Rapsodie), shortly followed by Germany (KNK-II) and Japan (JOYO). The growing interest in fast reactors brought the IAEA to establish a permanent International Working Group on Fast Reactors (IWG-FR), providing an international exchange framework for the six members, i.e. USA, USSR, UK, France, Germany and Japan. The experience gained from experimental reactors (mainly providing irradiation facilities for R&D) led to the construction of commercial size reactors, such as Phenix and Superphenix in France, BN-350 and BN-600 in the USSR, PFR in the UK, SNR-300 in Germany and Monju in Japan.

While the interest in this technology began to increase in developing countries, the development of fast reactors slowed down in the West. The SNR-300 in Germany was completed but not taken into operation for political reasons, and the KNK-II was permanently shut down in 1991. By 1994 in the USA, the CRBR project had been canceled and the FFTF shut down. The EBR-II was planned to serve as basis for the Integral Fast Reactor (IFR, originally Advanced Liquid Metal Reactor), but the project was canceled because of political pressure and the EBR-II shut down in 1998. In the UK, PFR was shut down and, in France, Superphenix was shut down because of political pressure. During the past 15 years, the industrial countries previously intensively involved in fast reactors have almost stopped their activities entirely. In effect – even though the demonstration of fast breeder reactor capabilities had been achieved – the technology suffered from anti-nuclear movements, as also the lack of real economic needs. However, the scientific community acknowledges that fast reactors are essential for contributing to sustainable economic development worldwide. This has been recently confirmed by the development of fast reactors in Asia (Japan, India, China), as well as by the renewal of interest in fast reactors in the developed countries within the framework of the INPRO and Generation-IV programs.

1.2.2 Sodium as a fast reactor coolant

From the very beginning of the nuclear era, scientists have considered almost everything available as possible for primary coolant for a reactor core, e.g. water, liquid metals, gas, fluid fuel, organic compounds, etc. As mentioned, due to the relatively high power density in a fast reactor core, liquid metals have been strongly considered in this specific case, because of their high thermal conductivity and useful temperature range at low pressure. In particular, sodium received so much special attention that a supplement in the Liquid-Metal Handbook was dedicated to sodium and sodium-potassium alloys [Com55]. Use of lead and/or liquidbismuth eutectic (LBE) requires a high pumping power, and the only lead-cooled reactors ever built are those developed by the USSR (Table 1.1). Even today, lead/LBE corrosion remains a considerable scientific challenge. Finally, no gas-cooled *fast* reactor has ever been constructed. In effect, an extensive testing of different coolants has historically led to sodium being chosen as the primary coolant in nearly all fast reactors.

Plant	Country	Coolant	Primary circuit	Nominal full power	First critical-	Final shut
			conf.	(MWth)	ity	down
Experimental F						
Clementine	USA	mercury		0.025	1946	1952
EBR-I	USA	sodium	pool	0.2	1951	1963
BR-10	USSR	sodium	loop	8	1958	2003
DFR	UK	NaK	loop	60	1959	1977
BOR-60	USSR	sodium	loop	55	1968	in op.
EBR-II	USA	sodium	pool	62.5	1963	1998
Fermi	USA	sodium	loop	200	1963	1975
Rapsodie	France	sodium	loop	40	1967	1983
KNK-II	Germany	sodium	loop	58	1972	1991
PEC	Italy	sodium	loop	120	constr. i	n 1974,
					cancele	d later
Joyo	Japan	sodium	loop	140	1977	in op.
FFTF	ŪŜA	sodium	loop	400	1980	1996
FBTR	India	sodium	loop	40	1985	in op.
CEFR	China	sodium	pool	65	2010	in op.
Prototype Fast	Reactors					
BN-350	Kazakhstan	sodium	loop	750	1972	1999
Phenix	France	sodium	pool	563	1973	2009
PFR	UK	sodium	pool	650	1974	1994
BN-600	USSR	sodium	pool	1470	1980	in op.
SNR-300	Germany	sodium	loop	762	compl. i	-
5111-500	Germany	sourum	loop	102	canceled	,
MONJU	Japan	sodium	loop	714	1994	in op.
PFBR	India	sodium	pool	1250	in co	-
CRBRP	USA	sodium	loop	975	canc	
IFR	USA	sodium	pool	840	canceled	
KALIMER-150	Rep. of Korea	sodium	-	392.9		
	USSR	Pb-Bi	pool	$\frac{592.9}{265}$	proj	500
SVBR-75/100			pool			oot
BREST-300	USSR	lead	pool	700	proj	
ASTRID	France	sodium			proj	ect
Commercial Siz		_				
Superphenix 1	France	sodium	pool	2990	1985	1998
Superphenix 2	France	sodium	pool	3600	canc	
SNR 2	Germany	sodium	pool	34200	integrat	
CDFR	UK	sodium	pool	38000	EF	
EFR	Europe	sodium	pool	3600	canc	eled
DFBR	Japan	sodium	loop	1600	proj	ect
JSFR-1500	Japan	sodium	loop	3530	proj	ect
KALIMER-600	Rep. of Korea	sodium	pool	600 MWe	proj	ect
KALIMER-1200	Rep. of Korea	sodium	pool	$1200\ {\rm MWe}$	proj	ect
BN-800	USSR	sodium	pool	2100	constr.	
BN-1800	USSR	sodium	pool	4000	project f	or 2020
BREST-1200	\mathbf{USSR}	lead	pool	2800	proj	

Table 1.1. Fast reactors in the world (adapted from IAEA FR database [IAE06])

1.3 Generation-IV systems

As discussed previously, nuclear energy has a long-term potential to help meet future global energy needs, provided breeder reactors are deployed to enable efficient use of fuel resources. However, for this to happen in an effective and economically acceptable manner, the development of advanced nuclear technology is required. Various scientific breakthroughs (especially in material science) are needed to achieve the commercial deployment of advanced systems, which have significantly different characteristics as compared to existing nuclear technologies (mainly Generation-II reactors). Improved current-day technology reactors (Generation III and III+) are expected to dominate the nuclear energy scene till well beyond 2030, when most actual systems will have reached the end of their operating licenses and advanced systems (Generation IV) will start getting deployed (see Fig. 1.4). To prepare this deployment, R&D programs are being carried out in several countries, mostly in the context of international frameworks. In particular, the Generation-IV International Forum (GIF), launched in 2001 and comprising 12 leading countries plus EURATOM, focuses on collaborative R&D programs for selected innovative nuclear systems. The major goals defined in the GIF roadmap are [GIF02]:

- *sustainability*, through effective fuel utilization, minimization of waste (especially long-term elements), and clean air objectives
- *economics*, that should be competitive with alternative energies and represent a comparative level of financial risk
- *safety and reliability*, based on advanced risk assessment methods and incorporating passive and inherent safety systems
- *proliferation resistance*, preventing the misuse of nuclear materials and facilities, and *physical protection* against acts of terrorism.

Accordingly, among more than a hundred different nuclear energy systems initially proposed to the GIF, six innovative concepts have been selected for in-depth R&D studies, namely the Sodium-cooled Fast Reactor (SFR), Gas-cooled Fast Reactor (GFR), Lead-cooled Fast Reactor (LFR), Molten Salt Reactor (MSR), Supercritical-Water-Cooled Reactor (SCWR) and Very-High-Temperature Reactor (VHTR). The selected systems are presented in Fig. 1.5, along with their main design characteristics and benefits. Though technically very different, each reactor type offers a number of advantages, while facing specific R&D challenges. Among the Gen-IV systems, three reactor types use a fast-neutron spectrum.

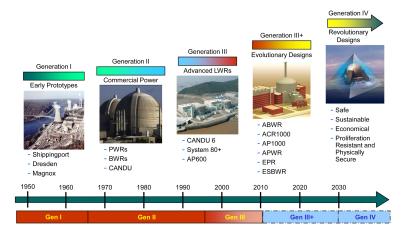


Figure 1.4. The evolution of nuclear energy systems in terms of generations [GIF02]

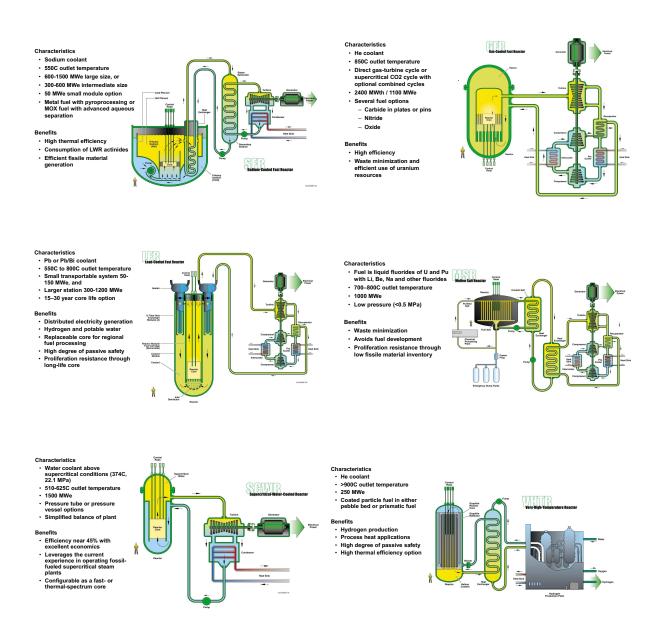


Figure 1.5. Generation-IV reactor concepts (adapted from [GIF02])

1.4 Goals and scope of the present study

As seen from Subsection 1.2.2, sodium has, to date, been the most widespread choice as fast reactor coolant. Since the coolant has a strong impact on the design, one can consider that – among the different Gen-IV fast reactor concepts – it is SFR technology which benefits from over 400 reactor-years of operation. As such, the SFR is the most mature, and hence, the most promising candidate for implementation of advanced fast reactor technology in the medium-term future. However, fulfilling the GIF goals represents a number of significant scientific challenges, the most important one being the demonstration of SFR safety. Since the recent, most unfortunate events at Fukushima, it is abundantly clear that any future nuclear system must exhibit a degree of safety that practically rules out the possibility of a significant release of radioactivity outside the plant.

1. INTRODUCTION

The safety characteristics of the SFR strongly depend upon the thermal-hydraulics response of the reactor core to external perturbations, specifically because of the strong interaction in transient conditions between the core reactivity and two-phase thermal-hydraulics. Thus, while the fuel Doppler effect and core thermal expansion are the two major instant negative contributions to changes in the core reactivity, the sodium void reactivity effect could be positive. The value and even sign of this effect is strongly spatially dependent, due to the competition of several physical processes (spectrum hardening, increased leakage, reduction of sodium capture and change in resonance self-shielding).

On the one hand, the sodium void reactivity effect is dependent on sodium two-phase flow phenomena, e.g. the onset of boiling, vapor generation rate, change of pressure drop, etc. On the other hand, the change in power caused by this reactivity effect has a strong impact on the two-phase flow development. These features of sodium-cooled systems emphasize the importance of an adequately detailed coupling being considered between thermal-hydraulics, neutronics and thermal-mechanics in transient analysis. In particular, the coolant void effect – the integral value for which can, as mentioned, be positive – needs to be simulated accurately, since its magnitude (and even sign) is spatially dependent.

It is in the above context that the present doctoral research has been conducted, the principal aim being to make available a new computational tool for the accurate simulation of coupled neutronics/thermal-hydraulics phenomena in an SFR core. This has been done in the framework of PSI's FAST project, which is primarily dedicated to the development and application of the FAST code system, employing a number of individual codes in coupled mode to enable the transient analysis of different advanced fast reactor concepts [Mik05]. With the overall goal of the thesis being to achieve an in-depth understanding of the transient behavior of SFRs, developments specific to sodium single- and two-phase flow modeling have had to be focused upon. Essentially, the present research has involved four phases:

1. Adaptation of the TRACE code for sodium two-phase flow

Since the thermal-hydraulics code used in the FAST code system, TRACE v5.0, is originally limited to the simulation of sodium in single liquid phase, the first step has been to implement models for sodium two-phase flow analysis. The models available in TRACE for steam-water two-phase flow simulation have been used as basis, and the current extension of the code is largely based on changes made in the logics of the existing two-fluid, non-homogeneous, non-equilibrium models. Additional equations-of-state (EOSs) have been implemented to describe the liquid and vapor phases of sodium. Also, after an extensive literature review, a number of new physical models for representation of the closure relations specific to sodium have been implemented.

2. Validation of the sodium single- and two-phase flow models

The developed two-phase flow models have been benchmarked through code-to-code comparisons and the simulation of suitable experiments. SIMMER, a reference state-of-the-art code for analysis of liquid-metal fast reactor (LMFR) severe accidents, has been used for comparison of the physical effects. After an extensive review of experimental data available in the open literature, a number of experiments have been selected to validate the developed models, under both steady-state and transient conditions with special consideration of 1D, 2D effects. Thereby, emphasis has been placed on specific characteristics of sodium boiling. The extended TRACE code has also been used to simulate a recently conducted, pre-shutdown test in the French Phenix reactor, involving the establishment of natural convection in a power reactor. The comparison with experimental data in this case has enabled a valuable validation of the single-phase models and provided supplementary insights into important transient phenomena. 3. Validation of the coupled TRACE/PARCS calculational scheme Experimental data from the Phenix natural convection test prior to the SCRAM have been used to validate the coupling of the extended TRACE code to core neutronics within the FAST code system. To start with, a standalone, point-kinetics TRACE model has first been developed to gain understanding of the important reactivity feedbacks taking place during the considered transient. Then, TRACE has been coupled to the spatial (3D) neutron kinetics code PARCS, which forms part of the FAST code system. The comparison with the Phenix test data of results obtained from the coupled TRACE/PARCS modeling of the reactor has enabled validation of the FAST code system as a whole and provided the basis for further improvements.

4. Coupled neutronics/thermal-hydraulics analysis of an advanced SFR

The new computational tool, as integrated into the FAST code system, has been used to provide an in-depth understanding of the coupled transient behavior of an advanced SFR. This has involved the development of a TRACE/PARCS model of the core of a Gen-IV SFR concept, viz. the European Sodium-cooled Fast Reactor (ESFR). The simulation of a hypothetical ESFR transient where boiling is anticipated, i.e. an unprotected loss-of-flow (ULOF) event, has demonstrated the new tool's capability to predict the expansion of the boiling region and the subsequent changes in reactor power. The results provide a basis for safety improvements of advanced SFR cores through design optimization.

1.5 Structure of the thesis

The present doctoral research is organized in seven chapters.

Following this introductory chapter, the second chapter provides an overview of sodiumcooled fast reactor technology worldwide and of the state-of-the-art concerning calculational tools for sodium systems. Also described in this chapter is the code system used as basis for the present study, viz. the FAST code system, containing TRACE for the thermal-hydraulics modeling and PARCS for treatment of the spatial neutron kinetics.

Chapter 3 details the extension of the TRACE code, previously limited to liquid sodium coolant, to the modeling of sodium two-phase flow. The two-fluid, 6-equation model available for steam-water flow in TRACE and used as basis is presented, along with a review of closure relations suitable for sodium flow modeling introduced as different options into the extended code.

The quality of the models, as implemented in TRACE, are assessed in Chapter 4. The different steps are presented for the validation of the sodium two-phase flow modeling using out-of-pile experimental data. These correspond to the analysis of experiments dedicated to the study of (i) pressure drop and (ii) dryout under quasi steady-state boiling conditions, and (iii) sodium boiling during loss-of-flow transients. The selected experiments are used to validate the extended code under different conditions, and to assess the influence of the interfacial and wall-to-fluid transfer mechanisms. The various analyses have served to demonstrate the ability of the code to satisfactorily predict the main boiling phenomena – such as boiling onset and the evolution of void fraction, pressure, and coolant and clad temperatures.

As mentioned earlier, validation of the coupled TRACE/PARCS calculational scheme has been performed on the basis of the unprotected part of the Phenix natural convection test. This is presented in Chapter 5. Following description of the point kinetics analysis with TRACE, the coupled TRACE/PARCS model of the Phenix core is developed. Its application to the above mentioned transient allows one, for the first time, to compare results from the FAST code system with experimental data from a sodium-cooled fast reactor. Certain limitations of the TRACE/PARCS modeling, i.e. of the FAST code system as a whole, are identified, the comparison of core-integral parameters, such as evolution of the power and average coolant temperatures, being given to assess the accuracy of the results.

Finally, the new calculational tool is applied to the analysis of the ESFR (as example of an advance SFR) under hypothetical accident conditions, including coolant boiling. The results are presented in Chapter 6. The analysis of the core behavior during an unprotected loss-of-flow event demonstrates the ability of the FAST code system, with the extended TRACE code, to predict the boiling onset and to describe the following development of the boiling phenomena. The overall core behavior is presented, along with an analysis of the instabilities which develop in the boiling sub-assemblies. The results illustrate the new tool's potential for SFR design optimization for achieving enhanced safety.

The main findings of the thesis are summarized in Chapter 7, along with recommendations for future work and concluding remarks.

CHAPTER 2

Thesis background

THIS CHAPTER provides the thesis background, first in a general manner through the description of SFR technology, and then focusing on the calculational tools used in the thesis for simulation of sodium-cooled systems.

Section 2.1 presents the advantages, as well as drawbacks, of sodium in comparison to other fast reactor coolants, and also how it impacts the reactor design. A brief description of selected worldwide projects and R&D programs related to sodium-cooled fast reactors is given in Section 2.2, with an emphasis placed on the French Phenix reactor. Section 2.3 gives a historical review of thermal-hydraulics codes developed in the past. In particular, the main characteristics of the current state-of-the-art 'sodium' codes are given. Finally, a detailed description of the FAST code system, as used in this thesis, is presented. It essentially consists of the following individual codes coupled together:

- ERANOS, for static core neutronics;
- PARCS, for 3D reactor kinetics;
- TRACE, for thermal-hydraulics;
- FRED, for thermal-mechanical fuel analysis.

2.1 Development of SFR technology

2.1.1 Comparison of fast reactor coolants

In a breeder reactor, neutron economy is of prime importance for breeding of fissile material. As such, neutron moderation in the core needs to be minimized, and the coolant volume fraction is reduced compared to thermal systems. This leads to a high concentration of fuel, and hence to a high power density, in the core. The resulting stringent requirements for a fast reactor coolant are: (1) minimal neutron moderation, (2) ability to deal with a very high power density (four time that in an LWR) and (3) minimal neutron absorption [Wal81]. The first requirement eliminates water and any organic fluid due to the presence of hydrogen. Among the remaining candidates (gases and liquid metals), liquid metals are more appropriate since they provide an excellent heat-removal capacity and exhibit relatively high boiling temperature (at low vapor pressure), which enables operation at low pressure.

From thermal considerations, a high thermal conductivity and heat exchange coefficient are desirable for the coolant. From the viewpoint of hydraulics, the pumping power needed to pump the coolant through the core should be minimized. In addition to the thermal-hydraulics

2. Thesis background

properties, nuclear properties such as moderating power, absorption cross-section, activation and radiation stability should be considered. Though liquid metals are particularly resistant to radiation damage because of their simple structure, they can be activated. Sodium, for example, exhibits a high degree of short half-life activation, which results in 1.37 and 2.74 MeV gamma emission:

23
Na + $n \rightarrow ^{24}$ Na $\xrightarrow{\beta^-}_{15h} ^{24}$ Mg. (2.1)

Though lead has little induced gamma activity, activation of impurities needs to be considered. In the case of LBE, the activation of bismuth which decays into polonium represents a significant biological hazard due to the long half-time of this toxic alpha-emitter:

²⁰⁹Bi +
$$n \to {}^{210}$$
Bi $\xrightarrow{\beta^-}{5d} {}^{210}$ Po $\xrightarrow{\alpha}{138d} {}^{206}$ Po. (2.2)

Helium is transparent to neutrons and, as inert gas, is insensible to radiation. Its biggest advantage compared with the liquid metals is that the void reactivity effect is negligible.

Table 2.1 summarizes the important physical properties of a number of possible fast reactor coolant materials. Among the liquid metals, lithium has the most favorable pumping power but also has a strong moderating power and high power absorption (via ⁶Li), and is thus unfavorable in a fast-neutron spectrum. Lead requires a high pumping power. Besides, the solubility and erosion of structural materials in lead and LBE is of particular concern. (The current approach is to maintain a protective oxide layer on the cladding and minimize the coolant flow velocity to limit erosion.) Moreover, the activation leading to Po-generation requires a special radioprotection solution. Helium is still considered in GFR R&D programs, the main problem being the removal of decay heat under depressurized conditions, e.g. a loss-of-coolant accident (LOCA). All in all, with various evaluation criteria considered collectively, sodium appears to be the most favorable fast reactor coolant.

Nevertheless, sodium has two drawbacks: it is opaque (compared, for example, to helium) and hence appropriate maintenance techniques need to be developed, and it produces a chemical reaction when in contact with air or water. In contact with air, sodium exhibits a burning reaction characterized by a zone of small flames at the interface, formation of Na_2O on the surface and vigorous emission of oxide fumes. This reaction is slow (4 times slower than in the case of gasoline), and the energy released is relatively low (15 times lower than for gasoline). In operating, sodium-cooled reactors, most sodium leaks have been small and resulted from design or fabrication deficiencies. Such leaks can be detected through appropriate gas sampling techniques. Sodium also reacts with water in two stages. The first, high rate reaction releases gaseous hydrogen:

$$Na + H_2O \rightarrow NaOH + 1/2H_2 + 140 \text{ kJ/mole}$$

$$(2.3)$$

The second stage involves the resulting by-products and the excess sodium:

$$2Na + NaOH \rightarrow Na_2O + NaH$$
 (2.4)

$$Na + 1/2 H_2 \rightarrow NaH.$$
 (2.5)

Detection of the hydrogen can be used to detect the leaks. An appropriate design of the plant (through the use of an intermediate loop) and of the steam generators (SGs, with double walls) can enable one to minimize the risk of potential primary sodium/water interactions.

		Na	Pb	LBE	Li	He
Atomic weight	-	23	207	208	7	4
Melting temperature	$^{\circ}\mathrm{C}$	98	327	125	181	n/a
Boiling temperature	$^{\circ}\mathrm{C}$	892	1737	1670	1342	-267
Density ρ	$ m kg/m^3$	880	10500	10300	534	0.178
Specific heat c_p	$J/kg \cdot K$	1300	160	146	3582	5200
Thermal conductivity k	$W/m \cdot K$	76	16	11	84.7	0.238
Dynamic viscosity ν	$Pa \cdot s$	0.0037	0.02 - 0.025	0.017	0.000374	0.00031

Table 2.1. Thermophysical properties for fast reactor coolants

2.1.2 Influence of the coolant on SFR design

The choice of the coolant determines the main design options for a nuclear reactor. Compared to the case of a PWR, the choice of sodium for a fast reactor leads to broad design differences such as the absence of high pressure in the primary circuit (near-to atmospheric pressure instead of 15.5 MPa) and a higher operating temperature (550°C, compared to 315°C at core outlet), resulting in a higher temperature of the produced steam and thus increasing the energy conversion efficiency. As mentioned earlier, in order to optimize the breeding of fissile material in a fast reactor, the volume fraction of fuel should be maximized and that of the coolant minimized. This results in the use of a triangular arrangement for the fuel lattice (which intrinsically allows a higher fuel volume fraction than a square lattice), sub-assembly wrappers being employed to force the coolant to flow within the tight sub-assemblies.

Because of the neutron activation of the primary sodium coolant and the risk of its chemical interaction with water, the SFR requires an intermediate system between the primary circuit and the steam generator. This enables one to isolate the radioactivity of the reactor coolant from the power conversion unit, thus reducing the containment requirements on the latter. Two different plant layouts, presented in Fig. 2.1, can be used for an LMFBR: the pool type, where either the intermediate heat exchanger (IHX) and primary pumps are placed inside the reactor tank or the loop type, in which these components are located in an adjacent loop connected with pipes to the reactor vessel. In the first layout, the probability of leakage from the primary system pipes is reduced. The sodium mass (three times higher than in the loop type) provides higher heat capacity, dampening the rise of temperature and thermal effects in others parts of the system in transient conditions. The loop type offers a simpler maintenance since components can be separated. In the loop layout, natural circulation can be enhanced through the higher vertical elevation of the IHX relative to the core. Besides, less neutron shielding is needed to prevent activation of the intermediate loop coolant.

2. Thesis background

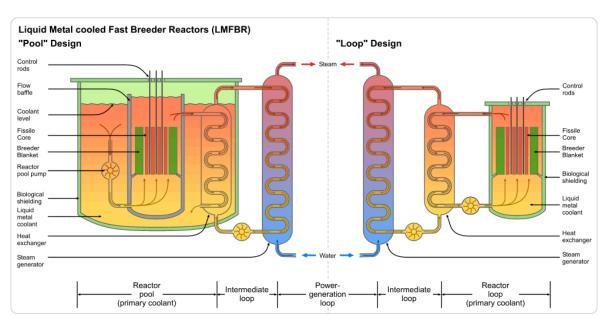


Figure 2.1. Pool vs. loop designs of Liquid Metal Fast Breeder Reactors [Wik07]

2.2 Status of sodium-cooled fast reactor projects worldwide

2.2.1 France: the Phenix reactor and other concepts

Phenix (560 MWth) [Sau09] is a prototype fast reactor that was operated from 1973 to 2009 by the French Commissariat à l'énergie atomique (CEA) and Electricité de France (EDF) at Marcoule, France. 'Phenix' refers to the mythical bird, phoenix, which, after a life of hundreds of years, burnt fiercely, was reduced to ash and then was reborn from its own ashes. By analogy, the Phenix reactor was given its name since it was capable of producing energy from by-products of the burn-up of its own core. During its 35-years operation, Phenix fulfilled every expectation. The first demonstration was the viability of using sodium as coolant for a 300-MWe-type reactor, the only other power plant producing electricity in the same power range in France at that time being an LWR. The second major result was the effective demonstration of breeding, with about 16% more fissile material being produced than being consumed. The core was actually completely recycled 3 times. This experience has confirmed the possibility of using uranium in its entirety through breeding. As prototype reactor, Phenix has provided the international scene with major results of relevance for future fast reactor designs.

As mentioned earlier, the end-of-life tests performed in 2009 have been used in the context of the present research, for the benchmarking of TRACE point-kinetics and TRACE/PARCS 3D-kinetics models (Chapter 5). Therefore, a detailed description of the Phenix reactor is given in the corresponding chapter. This subsection presents the general context of the reactor's development, its main characteristics, as also – through a brief description of the final tests – part of the valuable experience gained from its operation.

Phenix: The context

At the end of the 1950s in France, the CEA developed natural-uranium/gas/graphite (UNGG) reactors to produce electricity and plutonium for military purposes. In 1970, EDF had to choose the main reactor type for the industrial implementation of nuclear energy, and selected

the PWR, for which reliability had already been demonstrated in the USA. A first 300 MWe unit was then already in operation in France.

At the same time, fast reactors remained very promising, because of their breeding capabilities, and during the late 1950s, an R&D program for the development of fast reactors was funded. France, which mastered the reprocessing of spent fuel from UNGG, had enough plutonium available to start a cycle, and $(U-Pu)O_2$ mixed oxide was chosen as fuel. Considering the performance required, sodium was chosen as coolant. In 1958, a first design for an experimental breeder reactor using a fast neutron spectrum and sodium coolant was drawn up, and the experimental reactor Rapsodie was built between 1962 and 1966. Its basic characteristics were quite representative of an industrial reactor, a number of design choices having been fixed for applicability to future larger reactors: hexagonal sub-assemblies, suspended vessel, IHX, etc.

Prior to the operation of Rapsodie, and following on American (EBR-II) and British (DFR) success, a preliminary study for a 1000 MWe prototype reactor was carried out in 1964. The power was then scaled down to 250 MWe, in order to allow the use of a standard-design turbogenerator that had proven its reliability in EDF's conventional coal and oil power plants. Following the success of the Rapsodie reactor, the same fuel and coolant were chosen for the prototype. All the elements were integrated into a large primary vessel, as in EBR-II in the USA. This enabled to better deal with thermal transients (because of the large quantities of sodium), as also with leakages of the primary sodium. The IHX allowed isolation of the steam generator from the primary radioactive coolant. In this way, a leak in an SG, and the resulting sodiumwater reaction, would only involve the non-nuclear part of the facility, thus being classified as a chemical accident.

Construction of the Phenix reactor was accomplished between 1968 and 1972. First criticality was obtained, after a series of start-up tests, in 1973. The reactor was definitively shut down in 2009, after 35 years of successful operation and solid demonstration of the viability of sodium-cooled fast breeder reactors. Table 2.2 summarizes the main characteristics of the Phenix reactor.

Phenix: Final tests prior to shut-down

In July 2009, the Phenix reactor was disconnected from the grid and prepared for final tests. The idea was to create special operating conditions so as to learn more from the prototype reactor and thus contribute to the further development of the SFR. Two main objectives have been set: first, to acquire data for the qualification of neutronics, thermal-hydraulics and fuel behavior simulation tools and, second, to provide an understanding of the negative reactivity trip transients that occurred in 1989 and 1990.

Thermal-hydraulics tests

One test consisted in creating an azimuthal asymmetry in the reactor vessel through the cooling deficit generated by the trip of a secondary pump. Another test aimed at studying the establishment of natural circulation in the core, by tripping the primary pumps and then one of the two secondary loops in operation. The test was initiated with dryout of the SG, the pump and reactor trips being initiated afterwards. Sodium then circulated naturally in the primary circuits and in one of the secondary circuits. The decay power was evacuated by the air, also circulating naturally in the SG units, and by thermal losses from the loop. This particular test has been studied presently, for the validation of the single-phase flow simulation with TRACE. The response of the core before SCRAM, following dryout of the SG, has been simulated with both a TRACE point-kinetics model and coupled TRACE/PARCS transient calculations. This test will thus be discussed in detail later, in Chapter 5.

Thermal power	$563 \mathrm{MWth}$
Electrical output	$250 \mathrm{~MWe}$
Neutron flux at core centre	$7 \times 10^{15} \text{ n/cm}^2 \cdot \text{s}$
Fraction of delayed neutrons	360 pcm^*
Active volume of the core	1.4 m^3
Maximum temperature at pellet centre	$2300^{\circ}\mathrm{C}$
Average power density	$1200 \ \mathrm{MW} \cdot \mathrm{m}^{-3}$
Maximum linear power rating	$450 \mathrm{W/cm}$
Maximum temperature of cladding	$700^{\circ}\mathrm{C}$
Sodium core inlet temperature	400°C
Sodium core outlet temperature	$560^{\circ}\mathrm{C}$
Primary sodium flow rate in the core	$2800 \mathrm{~kg/s}$
Sodium temperature at IHX inlets	$350^{\circ}\mathrm{C}$
Sodium temperature at IHX outlets	$550^{\circ}\mathrm{C}$
Secondary sodium flow in each circuit	740 kg/s
Water temperature at SG inlets	$246^{\circ}\mathrm{C}$
Water temperature at SG outlets	$512^{\circ}\mathrm{C}$
Steam pressure at superheater outlet	165 bar
Steam pressure at reheater outlet	34 bar
Water flow rate in each SG	$210 \mathrm{~kg/s}$

 Table 2.2.
 Phenix, nominal characteristics
 [Sau09]

 $1 \text{ pcm} = 10^{-5}$

Neutronics tests

Final tests aimed at measuring the weight in reactivity of the various types of sub-assembly (SA), for different burn-ups, as well as the control rod (CR) worth, using a variety of methods. Also, the impact of control rod movements on the radial distribution of power in the core was investigated. This test, referred to as the control rod shift (CRS) test, is briefly presented in Chapter 5. Selected experimental data have been used for the validation of the Phenix coupled TRACE/PARCS model.

Then, a special device (helium tank operated by a CR mechanism) was built to measure the sodium void effect at different axial positions in the core. This aims at the qualification of methods for calculating the effect of void on the reactivity, which could result from boiling or from a gas bubble.

Fuel behavior

An accidental situation involving a fast increase of power in SAs has been simulated in pins with different geometries and burn-ups. The power ramp (from 300 MWth to 371 MWth in 6 min) triggered partial melting of the fuel in these pins. The tests on different geometries (e.g. pellets with and without a central hole) are expected to allow fuel improvements for future reactors. The use of different burn-ups allows one to study the impact of the fuel structure modification on fuel behavior during an accident.

From Phenix to Superphenix

The energy scene in the early 1970s was marked by the first petroleum shock and the sharp rise in oil prices. With the aim of greater energetic independence, France decided to accelerate its development of nuclear power. Following the success of the experimental reactor Rapsodie (40 MWth) and the prototype reactor Phenix (560 MWth), plans were laid for Superphenix (3000 MWth), the first large industrial fast breeder reactor worldwide. The basic reactor design was effectively extrapolated from that of the Phenix reactor, even though its large size required a different specific design for many of its components.

Construction began in 1976 in Creys-Malville, France. From the very beginning, the international anti-nuclear movement expressed its strong opposition to the project, and a number of demonstrations delayed the construction. Criticality was first achieved in 1985. The reactor then faced a number of technical incidents – sodium leak in the main storage drum vessel (8month shutdown), contamination of the primary sodium due to air infiltration into the argon cover gas (7-month work), etc. – as well as hostile demonstrations from the public. It was definitively shut down, for political reasons, in 1997, 20 years before the end of the plant's designed lifetime. Its total operation time sums up to 53 months, during which it produced 8×10^9 kWh. Though decommissioned early, Superphenix demonstrated that large-scale fast reactors are easy to operate from the neutronics point of view, the large thermal inertia being a real advantage in limiting reactivity feedback effects. The return-of-experience has been considerable – with respect to design, technology, operation and safety, and large components. The acquired knowledge has been integrated into the European Fast Reactor (EFR) project, a 1500 MWe reactor concept in continuation of Superphenix.

EFR project

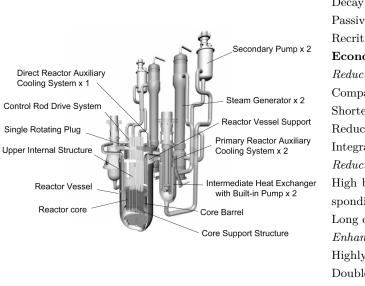
With France in the leading role, the EFR project was launched in 1988. The EFR design synthesizes the extensive experience of France, Germany and the UK with large pool-type oxide-fueled reactors. The principal goal was to improve economics and safety features in order to provide higher competitivity with respect to PWRs. Though the construction of a reactor based on the EFR design may never come to light, the project represents an important step forward on the road to the commercial utilization of fast reactors.

ASTRID project

In France, an R&D program – led jointly by CEA, EDF and AREVA – was initiated in 2007 with the objective to develop and implement, by 2020, promising innovations for a new generation of SFRs into a new prototype [Rou09]. As such, this new demonstrator, the ASTRID (Advanced Sodium Technology Research for Industrial Demonstration) prototype, is expected to serve as the precursor of a first-of-its-kind commercial reactor, which can meet the stringent GIF criteria with respect to safety, economy and proliferation resistance. ASTRID should also help further develop SFR-MOX fuel reprocessing, and, as such, will serve to provide a global demonstration of Generation-IV SFR concepts.

2.2.2 In Europe: the ESFR project

Currently, research on fast reactors is being strengthened in Europe under the umbrella of the GIF. In particular, a collaborative project – involving 25 participants from 10 different countries – was launched in 2009 for the development of a Gen-IV European Sodium-cooled Fast Reactor (ESFR) [Fio11]. This was done within the frame of EURATOM's 7th Framework program for nuclear research and training. The main objectives of the project are improvements



Safety

Decay heat removal only by natural circulation Passive shutdown syst. using Curie-point magnets Recriticality-free core via special subassembly **Economic Competitiveness** Reduction of Construction Costs Compacted reactor vessel Shortening of piping (adoption of high-Cr steel) Reduction of loop number (2-loop system) Integrated IHX with primary pump Reduction of Fuel Cycle Costs High burn-up core with blanket fuels using corresponding ODS cladding material Long operation-cycle core (>18 months)Enhancement of Reliability and Availability Highly reliable SG, i.e., double-wall-tube Double-boundary system for sodium Special inspection and repair technology

Figure 2.2. Main features of the Japanese sodium-cooled FBR (JSFR) [Ich07]

in safety level, environmental impact, resource utilization and waste minimization (through the management of minor actinides). The schedule of this 4-year project targets an industrial deployment of ESFR technology around 2040, a demonstrator being foreseen by 2020-2025.

In the present research, the oxide-fuel ESFR core concept has been used for the application of the developed calculational tool to the coupled transient analysis of an advanced SFR. Therefore, the project and corresponding concept will be described in greater detail later, viz. in Chapter 6.

2.2.3 Japan: Joyo, Monju reactors and the FaCT project

In Japan, the significance of fast breeder reactor technology development, from the viewpoints of global energy resources and environment issues, has been recognized for decades. The experimental fast reactor Joyo (140 MWth) has shown excellent performance during its almost 30 years operation, beginning 1977. In 1994, a 280 MWe loop-type MOX fueled prototype reactor, Monju, achieved initial criticality. Its goal is to confirm the technological database for qualification of design and safety tools, and to accumulate operating experience for SFRs. It was recently restarted after a 14-year shutdown due to a sodium leak in the non-radioactive secondary heat-transport system that occurred in December 1995.

The conclusion of the 'Feasibility Study on Commercialized FBR Cycle Systems', initiated in 1999, was that the most viable option for commercialization of an FBR is the $(U-Pu)O_2$ mixed oxide fueled, sodium-cooled fast breeder reactor [Ich07]. Figure 2.2 shows the main features of the Japanese SFR design.

In 2006, JAEA launched the Fast Reactor Cycle Technology development (FaCT) project, in collaboration with the Japanese electrical utilities and several ministries (MEXT and METI). This R&D program should provide a conceptual design for demonstration and commercial FBR fuel cycle facilities by 2015. A demonstration FBR should be launched around 2025, and a commercial system deployed by 2050. Joyo and Monju will thus play important roles for the establishment of sodium handling technology, as well as experience with the fast reactor irradiation of different materials.

2.2.4 India: FBTR, PFBR

On the basis of its indigenous natural resources (limited in uranium, but having about 32% of the world's thorium resources), India set up a three-stage nuclear energy development program as early as in the 1950s. This is based on closed fuel cycles, starting with heavy water reactors using natural uranium, through fast reactors first using plutonium-based fuel and then thorium-based fuel, to thorium-based advanced breeders, for a sustainable future energy scenario.

India has been operating the Fast Breeder Test Reactor (FBTR) since 1985. This is a 40 MWth loop-type design based on the French reactor Rapsodie. Currently, the Prototype Fast Breeder Reactor (PFBR), a 500 MWe pool-type MOX fueled reactor, is uder construction. The primary objective of the PFBR is the technological and economical demonstration of FBRs for deployment on an industrial scale. After its commissioning, India is planning to build four 500 MWe FBRs with improved economics and safety (including passive features for shutdown and decay heat removal). MOX fuel has been chosen for these reactors. However, metallic fuel is being considered for the future, since this would allow a higher breeding ratio and a faster expansion of nuclear power once the fuel fabrication technology is mature enough.

2.2.5 China and the CEFR

Basic research on fast reactor technology in China started in the mid-1960s and continued for 20 years with little manpower and few resources. In 1986, the development of FBRs was promoted by the National High-Tech Program. The resulting conceptual design of the China Experimental Fast Reactor (CEFR), a 65 MWth pool-type SFR, was completed in 1993. Criticality of this small reactor has been reached in 2010. This program, though marginal in comparison with the PWR projects foreseen to provide part of the vast energy needs in that country, shows the interest of China in fast reactor technology. The CEFR will be used as a tool for qualification of computer codes, for studying safety characteristics and safe operation, and for applied research for the following fast reactor prototype and demonstrator. The latter represent the next two stages in the Chinese FBR development program, viz. the construction of a 600 MWe prototype fast reactor (CPFR), for which design work started in 2005, and a 1000-1500 MWe demonstration reactor (CDFR).

2.2.6 The republic of Korea and the KALIMER concept

Nuclear power is a key resource in Korea, which imports about 97% of its energy resources. Development of fast reactor technology started in 1992, with a long-term R&D plan for SFRs. The conceptual design of KALIMER-600, an advanced SFR concept proposed by the Korea Atomic Energy Research Institute (KAERI), was completed in 2007. It is a pool-type reactor, loaded with a single Pu-content metal fuel, without blanket assemblies, the core power flattening being achieved through different cladding thicknesses in the different core regions. The advanced concept is currently under development. After testing the passive decay heat removal circuit, an integral testing loop will be constructed. A demonstration reactor is planned to be constructed and operated by 2028.

2.2.7 The Russian federation and the BN reactors

The Russians have significant experience with SFRs, and there are currently two fast reactors operating in Russia, viz. the experimental reactor BOR-60 and the BN-600, commercial Unit 3 of the Beloyarsk nuclear power plant. The BOR-60 reactor, in operation since 1968, has been primarily used for material tests, isotope production and fast reactor equipment tests. For the demonstration of a commercial-size reactor, based on the BOR-60 achievements, the prototype

BN-350 reactor was built in Kazakhstan. BN-350 was used for electricity production and water desalination, as well as for experiments supporting fast reactor development. No dismantling program has been yet established, though the unit was shutdown in 1999. Design improvements were made in the secondary system and the fuel burn-up was doubled in the BN-600 reactor, which has now been in operation since 1980. It is a loop-type reactor fueled with enriched UO_2 (~ 20% of ²³⁵U), the largest fast reactor operated worldwide, with excellent safety performance and operating reliability.

The construction of the next generation fast reactor (BN-800) is well under way and commissioning is foreseen for 2012. The BN-800 has improved features including fuel flexibility (U+Pu nitride, MOX or metal fuel) and a breeding ratio of up to 1.3. In 2009, two BN-800 reactors were sold to China, with construction due to start in 2011. BN-800 represents a scaling step toward the development of a large-scale reactor for commercial application (BN-1800) over the next 15 years and possible construction after 2020. In addition, R&D work is being carried out for the conceptual development of a small, modular and transportable two-circuit SFR with a gas turbine.

Apart from the SFR program, Russia is also working on the development of heavy liquid metal reactors. In particular, R&D is being conducted for the lead cooled BREST-OD-300 reactor, as also for the basic design of a lead-bismuth cooled reactor (SVBR-75/100 facility).

2.2.8 Projects in the USA

In 1983, the U.S. Department of Energy (DOE) began the Advanced Liquid Metal Reactor (ALMR) program, which aimed at increasing the efficiency of uranium use by breeding plutonium. This program was funded until 1994, giving birth to the PRISM reactor (150 MWe) concept, an advanced sodium-cooled fast neutron reactor with passive shutdown, decay heat removal and cavity cooling, followed by a 1400 MWe conceptual design.

While these projects were abandoned, a number of new initiatives, such as the GIF and the Global Nuclear Energy Partnership (GNEP) programs, have been launched. Today, the main DOE objective seems to be to facilitate the deployment of advanced light water reactors (ALWRs), while its GNEP program seeks to develop advanced technology for recycling spent fuel. Fast reactors are seen as tools for closed recycling and burning of transuranium nuclides, the aim being to improve utilization of the US geological repository. The overall strategy focuses on waste management and non-proliferation benefits.

2.3 Calculational tools

2.3.1 Historical review of dedicated sodium thermal-hydraulics calculational tools

Sodium thermal-hydraulics phenomena have been investigated since the 1960s in laboratories involved in LMFBRs development throughout the world. The involved scientists spontaneously set up a working group (Liquid Metal Boiling Working Group; (LMBWG)) at the first Fast Breeder Safety conference in 1966. This initiative was supported by CENG Grenoble (France), UKAEA Risley (UK), KfK Karlsruhe (Germany), CNEN Casaccia (Italy), CEN Petten (The Netherlands), SCK/CEN Mol (Belgium), JRC Ispra (Italy), ANL Argonne (USA) and JAERI (Japan). The LMBWG, holding meetings every 2 years, gathered nearly all experts involved in the design development of LMFBRs, and was especially dedicated to safety problems. As such, it had a most valuable influence on both basic and safety research.

Considerable progress in the field of macroscopic effects has led to good general knowledge of sodium single- and two-phase forced convective flow, natural convection and boiling behavior.

The 26-year activity of the LMBWG was reported upon in 1994 by Kottowski [Kot94], who summarized the state-of-the-art thermal-hydraulics at a time when political decisions had begun to slow down LMFBR development. This subsection attempts to briefly review the calculational tools developed from the beginning of LMFBR R&D, with a strong emphasis on reactor safety and sodium boiling representation. The main characteristics of the developed codes have been compiled in Table 2.3. It is seen that the focus has been on spatial representation through multi-dimensional solutions, time-dependent solution methods and boiling representation.

The methods developed for rod bundle representation may be divided into three categories, viz.: fine mesh, sub-channel and porous medium. The fine-mesh approach requires a considerable number of nodes to represent a complete rod bundle. It is mainly being used to study local phenomena, or to provide averaged quantities for use with sub-channel and porous medium codes. In the sub-channel approach, the hydraulic equations are solved for every sub-channel, each being represented radially by a single node. Interactions with the structure are generally determined by correlated friction factors. This representation provides results for each sub-channel, allowing direct physical interpretation. However, the mesh is determined by the bundle geometry. This results in a large number of nodes in large bundles, raising difficulties to represent adjacent open flow regions or bundles with different geometry. In the porous medium approach, the bundle cross-section is homogenized over a single mesh and the hydrodynamic equations are averaged over the appropriate fluid volume fraction in the resulting node. After averaging, the mesh is completely flexible, which overcomes the problems due to the mesh rigidity in the sub-channel approach. On the other hand, the physical details are given on a larger-scale due to the averaging process, resulting in a less detailed representation compared with sub-channel analysis.

To summarize, the fine-mesh approach is appropriate for representing detailed behavior within the sub-channel, the sub-channel representation gives the individual sub-channel behavior, and the porous-medium approach allows the analysis of larger scale phenomena over the entire bundle.

Concerning the representation of boiling, three major approaches have been used in thermalhydraulics codes, viz. bubble modeling, homogeneous flow, and two-fluid modeling. It should be mentioned that, for fast reactor applications, the prime interest is the representation of sodium boiling at relatively low pressures. In these conditions, the vapor density is three orders of magnitude lower than the liquid density. Boiling thus results in large effects on the flow, which are liable to produce numerical difficulties in the solution methods.

In bubble modeling, boiling is represented via pure vapor bubbles in the channel center, with a liquid film remaining on the channel wall. This allows a realistic physical representation of the bubbles in slug and annular flow regimes. However, it is difficult to generalize to more than a single channel, and difficulties remain in the correct modeling of the film thickness and bubble size, which is very sensitive to the superheat required for bubble formation. In the homogeneous flow approach, the two-phase flow is represented as a single fluid, the properties of which are determined from correlated constituent relationships. Two types of models have been commonly used, viz. slip and drift flux models. In the first one, the slip (defined as the ratio between the vapor and liquid velocities) is calculated from empirical correlations. Drift flux modeling is similar but correlates the vapor velocity relative to the liquid. This gives satisfactory results in forced convection but is limited when the velocity fields are no longer parallel, such as in the case of low flows with significant buoyancy effects. Improved modeling is obtained with the 2-fluid representation, where the mass, momentum and energy conservation of each phase are considered separately. The resulting equations are considerably more difficult to solve than the single-fluid equations, and appropriate correlations are needed for closure of the sets of

Code	Developer	Bundle representation	Dimensionality	Two-phase models	Present status
General codes:					
CAFCA [Oli84]	EDF	porous medium	3D	Slip	currently used
COMMIX2 [Bot84]	ANL	porous medium	3D	2-fluid UVET*	superseded by BACCHUS
SIMMER [Boh90]	Los Alamos	porous medium	2D	2-fluid UVUT*	currently maint. by JAEA
THERMIT [No87]	MIT	porous medium	3D	2-fluid UVET+UVUT	obsolete
Specialized geometry for bundles:	or bundles:				
BACCHUS [Bas84, Bot87]	CEA/KfK	porous medium	3D	slip, 2-fluid UVUT	currently used
MULTICANA [Pap84]	CEA	porous medium	2D	homogeneous	obsolete
Subchannel:					
SABENA [Nin90]	JAERI	triangular rod arrays	3D	2-fluid UVUT	currently used
SABRE [Mac84]	UKAEA	triangular rod arrays	3D	slip, 2-fluid UVUT	obsolete
THEBES [Cam82]	CEA	triangular rod arrays	3D	slip (with delay)	obsolete
Single-channel bubble:					
BLOW [Dev86]	KfK	porous medium	1D	bubble from superheat	obsolete
SAS [Cah00]	ANL	porous medium	1D	bubble from superheat	currently used
Monte Carlo STATEN [Wev84]	UKAEA	I	3D		obsolete

equations. However, this allows one to achieve a more accurate physical representation of the system. It is this approach which has been applied in the present research.

The codes presented in Table 2.3 have been validated individually against experiments, and benchmark validations have been performed in the framework of the LMBWG. In 1982, benchmark exercises were carried out for single-channel boiling under quasi steady-state conditions [Kot84], as also for single-phase temperatures behind corner and central blockages. In 1984, benchmark comparisons were made for a 37-pin bundle flow rundown transient [Hub82b, Bot90]. Appendix B presents a review of out-of-pile experimental data available for validation of sodium boiling calculational tools.

It should be borne in mind that most of the codes mentioned in this subsection are not being used anymore for SFR analysis.

2.3.2 State-of-the-art sodium codes

Currently, the most important experimental and theoretical findings related to sodium twophase flow have been integrated into state-of-the-art sodium codes, among which SAS4A/ SASSYS-1 and SIMMER-III/IV appear as reference tools. Accordingly, we present here a short description of these codes, emphasizing their relative advantages and limitations.

SAS4A/SASSYS-1

The SAS4A and SASSYS-1 computer codes [Cah00] are being developed at ANL for the transient analysis of LMFBRs. The activity was initiated in the frame of the Integral Fast Reactor (IFR) program.

The SAS4A computer code is being developed to perform the deterministic analysis of severe, core disruptive accidents in LMFBRs. Detailed, mechanistic models of steady-state and transient thermal, hydraulic, neutronics, and mechanical phenomena are employed to describe the response of the reactor core and its coolant, fuel elements and structural materials to accident conditions caused by loss of coolant flow, loss of heat removal or reactivity insertion. The initiating phase of the accident is modeled, including coolant heating and boiling, fuel cladding failure, and fuel melting and relocation. SAS4A analysis is terminated upon loss of subassembly hexcan integrity. The objective of SAS4A analysis is to quantify severe accident consequences as measured by the generation of energy sufficient to challenge reactor vessel integrity, leading possibly to public health and safety risk. Originally developed for the analysis of sodium-cooled reactors with oxide fuel clad by stainless steel, the models in SAS4A were subsequently extended to metallic fuel with advanced alloys cladding and to heavy liquid metal (Pb and Pb-Bi) coolants.

The SASSYS-1 system code is designed to perform the deterministic analysis of design basis and beyond-design basis accidents, as also of passive safety response mechanisms in anticipated transients without SCRAM (ATWSs), in LMFBR plants. The SASSYS-1 code contains the same models as SAS4A for fuel element heat transfer and single/two-phase coolant hydraulics. In addition, it has the capability to provide a detailed thermal-hydraulics simulation of the primary and secondary coolant loops, the reactor control and protection systems, and the balanceof-plant response to accidents caused by loss of coolant flow, loss of heat removal or reactivity insertion. The consequences of single and double-fault accidents are modeled, including fuel and coolant heating, fuel and cladding mechanical behavior, core reactivity feedbacks, coolant loops performance including natural circulation, and decay heat removal. SASSYS-1 analysis is terminated upon demonstration of reactor and plant shutdown to permanently coolable conditions, or upon violation of design basis margins. The objective of SASSYS-1 analysis is to quantify accident consequences as measured by the transient behavior of system performance parameters, such as fuel and cladding temperatures, reactivity, and cladding strain.

In spatial terms, each SAS4A/SASSYS-1 channel models a fuel pin and its associated coolant. A channel represents one or more fuel pins in a single or multiple pin model of a subassembly. In a single pin model, a channel represents all of the pins in a subassembly, and possibly all the pins in a group of subassemblies. In a multiple pin model, many channels are employed to represent a subassembly. In either case, many parallel channels are usually employed for a whole-core representation. Heat transfer in each pin is modeled with a two-dimensional (R-Z) heat conduction equation. Single and two-phase coolant thermal-hydraulics is simulated with a unique, one-dimensional (axial), multiple-bubble liquid metal boiling model. The transient fuel and cladding mechanical behavior model, integrated with fission product production, release, and transport models, provides prediction of fuel element dimensional changes, margins to cladding failure, and cladding failure time and location. In SAS4A, fuel and cladding melting and subsequent relocation are described with multiple-component fluid dynamics models, with material motions driven by gravity and pressures from coolant vaporization, fission gas release, and fuel and cladding vaporization. Thermal-hydraulics models of the reactor and intermediate coolant loops analyze heat removal via both forced and natural circulation, along with the transient performance of loop components including pumps, heat exchangers, valves, and plena. Reactivity feedbacks from fuel heating (axial expansion and Doppler), coolant heating and boiling, and fuel and cladding relocation are tracked. Reactivity effects from reactor structural temperature changes yielding radial core expansion are modeled. Numerical solution methods used in the code modules range from semi-implicit to explicit. The coupling of modules in time is semi-explicit within a multiple-level time step framework.

SAS4A/SASSYS-1 have been coupled to nodal spatial kinetics computer codes – VARIANT-K (static multigroup neutron diffusion and transport solutions) and DIF3D-K (time-dependent multigroup neutron diffusion solutions) – for accurate analysis of coupled spatial neutron kinetics and thermal-hydraulics effects [Cah00].

SIMMER-III/IV

SIMMER is an advanced safety analysis computer code for core disruptive accidents (CDAs). CDAs have been a major concern for the safety of SFRs, because of the energetics potential resulting from a recriticality event. A reactor safety analysis code relevant to this area, SIMMER-II, was developed as the first practical tool of its kind [Boh90], and has been used in many experimental and reactor analyses. The code has played a pioneering role, especially in the advancement of mechanistic simulations of CDAs, but at the same time extensive worldwide code applications have revealed many limitations due to the code framework, as well as the need for model improvement. To overcome these limitations and so provide a more reliable tool for the analysis of CDAs, the development of a totally new code, SIMMER-III, was undertaken in the 1980s by the JAEA, in collaboration with the Forschungszentrum Karlsruhe (FZK) of Germany and the CEA (which, at the time, also included the French Institut de Radioprotection et de Sûreté Nucléaire, IRSN) [Tob02].

The actual versions of the SIMMER code allow an evaluation of the transition phase of a CDA, through the simulation of the entire core and the modeling of key thermodynamic and neutronics phenomena occurring during the accident progression. SIMMER-III is a two-dimensional multi-velocity-field, multiphase, multi-component, Eulerian fluid-dynamics code, coupled with a fuel-pin model and a space- and energy-dependent neutron kinetics model [Tob02, Yam03]. The philosophy behind the SIMMER-III development has been to generate a versatile and flexible tool, applicable for the safety analysis of various reactor types with different neutron spectra and coolants, including accelerator-driven systems for waste transmutation. The development

of the code has reached a milestone, in that all the models originally intended have now been made available. Since one of the major limitations of SIMMER-III has been its dimensionality, a new, three-dimensional version is currently being developed, viz. SIMMER-IV [Yam08]. This is a direct extension of SIMMER-III to three dimensions, with full retention of the SIMMER-III framework as regards physical models. The main backbone for analysis, however, is still SIMMER-III.

The code essentially consists of three elements: the fluid-dynamics model, the structure (fuel-pin) model and the neutronics model. The fluid-dynamics part, which constitutes about two-thirds of the code, is interfaced with the structure model through heat and mass transfer at structure surfaces. The neutronics part provides nuclear heat sources based on the time dependent neutron flux distribution consistent with the mass and energy distributions. The code models the five basic SFR core materials (in solid, liquid, and vapor states), viz. fuel, steel, sodium, control rods and fission gas. The mass and energy distributions are modeled in terms of structure, liquid and vapor fields. The structure-field components, which consist of fuel pins and cladding walls, are immobile. For the mobile components, the original SIMMER-III/IV code had three velocity-fields (two for liquids and one for vapor), which have been extended to eight fields to improve the code precision. The spatial differencing method is based on Eulerian staggered mesh with a higher-order differencing scheme to mitigate numerical diffusion. An improved analytic equation-of-state model provides good accuracy, especially at high temperature and pressure. Multiple flow-regime treatment is available over the entire void fraction range. An interfacial area convection model improves the flexibility of the code by tracing the transport and history of interfaces and thereby better represents physical phenomena.

2.3.3 The FAST code system

The FAST (Fast-spectrum Advanced Systems for power production and resource managemenT) code system is currently being developed at PSI for static and transient analysis of the main Gen-IV fast-neutron spectrum reactor concepts: sodium, gas and lead-cooled fast reactors. The main goal is to allow an analysis of advanced fast-spectrum systems including different coolants and fuel types. This unique computational tool allows, through safety-related analysis, to provide the basic feasibility of advanced fast reactors, in particular those proposed by the GIF. The reactor modeling includes an integral representation of the core neutronics, thermal-hydraulics and fuel behavior, and the reactor primary and secondary systems. The code system has been assembled from well established existing codes, extended to the simulation of fast reactor features when necessary, namely: ERANOS, for static neutronics, PARCS, for reactor kinetics, TRACE, for system thermal-hydraulics, and FRED, for thermal mechanics. The flow chart of the FAST code system, presented in Fig. 2.3, shows the main codes used, together with the information exchanged through the coupling.

The basic nuclear data (macroscopic cross-section and their derivatives with respect to fuel temperature, coolant density, and core dimensions) are provided by the ERANOS code system, which is a reference tool for fast reactor static analysis. The spatial neutron kinetics code PARCS, after adaptation for fast-spectrum system calculations, is being used in the FAST code system for neutron kinetics. PARCS solves the steady-state and time-dependent, multi-group neutron diffusion and transport equations to provide the reactor power. PARCS is coupled directly with TRACE, the thermal-hydraulics code that provides the temperature and coolant density field information to PARCS during the transient calculation, in order to recalculate the cross-sections of the corresponding materials. TRACE solves the balance of mass, momentum and energy for the liquid and vapor phases, while considering the interactions of these phases with the structures to provide static and transient simulation of the reactor system. The thermal-mechanical behavior of structural elements is calculated by FRED. The FRED code

2. Thesis background

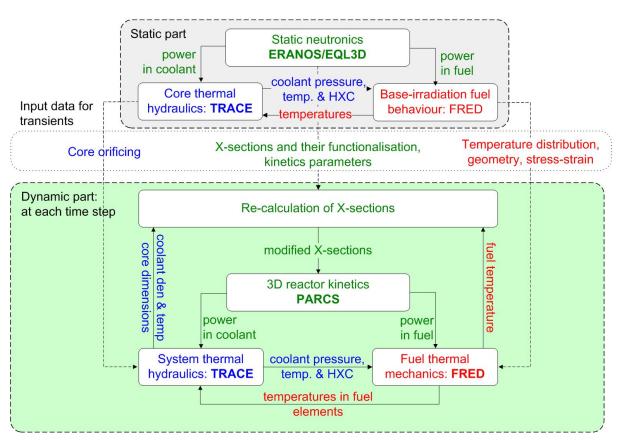


Figure 2.3. FAST code system flow chart

uses the fields of temperature and pressure in the surrounding fluid calculated by TRACE, as well as the power distribution provided by PARCS. The calculated heat fluxes on the fuel rod surfaces are send back to TRACE, and the fuel and clad temperatures are send back to PARCS, to re-calculate the resulting reactivity changes.

A more detailed description of the different individual codes is provided below.

ERANOS: static neutronics

The ERANOS code [Rim02], European Reactor ANalysis Optimized calculation System, has been developed and validated with the aim of providing a suitable basis for reliable neutronics calculations of current and advanced fast reactor cores. The deterministic neutronics code system consists of data libraries, codes and calculation procedures that have been developed over the past 15 years to answer the needs of both industrial and R&D organizations. ERANOS 2 allows reference and design core calculations for LMFBRs (with extended capabilities for advanced reactor fuel sub-assemblies and core features), accelerator driven systems (ADSs) and GFRs. In this thesis, ERANOS 2.1 has been used to compute the macroscopic cross-sections and derivatives needed to create PARCS inputs and perform transient analysis of an advanced SFR core using TRACE/PARCS.

ERANOS is written with the ALOS software, which includes advanced programming features for Fortran 77. A modular structure was adopted for easier evolution and incorporation of new functionalities. The core neutronics parameters (such as the effective multiplication factor $k_{\rm eff}$ and the fine flux ϕ at each point modeled in the system) are computed in two steps: first, a cell/lattice calculation is performed with ECCO, followed by the full-core calculation, performed using either the variational nodal method with TGV/VARIANT for a 3D core geometry or the finite-difference solution with BISTRO S_n model for a 2D core geometry.

Consideration can be made of other features, such as actual reactor operating conditions, energy release, damage rate, fuel burn-up and effects requiring perturbation analysis. The corresponding ERANOS procedures and modules, however, are not being described here.

Nuclear data libraries

The ECCO/ERANOS 2.0 code package contains two neutron cross-section libraries: JEC-COLIB2 and ERALIB1. The former is based on JEF-2.2 evaluated nuclear data files, while the latter is an adjusted data library. ERANOS 2.1 has been extended with additional neutron libraries derived from JEFF-3.1, JENDL3.3 and ENDFB6.8 evaluated nuclear data files. Each library includes:

- a 1968-group (1/120-width in lethargy) library for the 37 main (resonant) nuclides,
- a 33-group library for fast-neutron spectrum applications,
- a 175-group library for shielding calculations,
- a 172-group library for thermal-spectrum applications.

Other nuclear data (fission yields and energies, decay constants, gamma production and interaction libraries, etc.) are provided in separate files.

Cell/lattice calculations with the ECCO module

The ECCO cell/lattice code [Rim97, Rim02] is used to compute the self-shielded macroscopic cross-sections and scattering matrices for each core region (e.g. fissile SA, fertile SA, reflector, and control assembly (CA)). It combines the slowing-down treatment in many (1968) groups with the subgroup method within each fine group. The subgroup method is particularly suitable for highly heterogeneous lattices. It takes into account the resonance structure of heavy nuclides by means of probability tables, assuming that the neutron source is uniform in lethargy within a given fine group. These calculations are very accurate, as the fine group plus subgroup scheme has been set up to accurately represent the reaction thresholds and the resonances in any situation, narrow or wide.

The self-shielding formula for the effective cross-section σ_x , (x being the total, capture, fission, elastic or inelastic reaction), for each energy group g, is the following:

$$\tilde{\sigma}_{xi}^g = \frac{\sum_j S_j^g \sum_{k \in g} \alpha_k \, \sigma_{x_k} \, p_{ij}(\Sigma_{t_k})}{\sum_j S_j^g \sum_{k \in g} \alpha_k \, p_{ij}(\Sigma_{t_k})}$$
(2.6)

where S_j^g is the neutron source in energy group g and spatial region j, α_k is the probability in the group g to find the partial cross-section $\sigma_{x_k}^g$, to which corresponds the total cross-section $\sigma_{t_k}^g$, and $p_{ij}(\Sigma_{t_k})$ is the reduced collision probability for subgroup k within group g.

Many types of geometries are available within the ECCO code, among which is a 2D hexagonal lattice description of cylindrical pins within a hexagonal wrapper that is used for SFR core description. After computation, the self-shielded cross-sections and matrices are condensed and smeared to provide effective data according to a broader group scheme, defined by the user. The condensed data are subsequently used in full-core ERANOS calculations, for example using the S_n transport module BISTRO or the nodal variation transport module TGV/VARIANT.

Flux solvers: BISTRO and VARIANT

As mentioned, once the cross-sections and scattering matrices for all cells have been calculated, either 2D BISTRO or 3D VARIANT can be used to compute the neutron flux in the whole core and to solve the k_{eff} (eigenvalue) problem.

Three main classes of flux solvers are available, viz. finite difference diffusion and transport calculations, as well as the variational nodal method. In each case, external sources, up-scattering and adjoint calculations can be addressed. Anisotropic scattering is available for transport calculations.

In 2D geometries, BISTRO [Pal87] can be used to compute the neutron flux in the whole core and to solve the eigenvalue problem. BISTRO is a finite difference code with a particularly efficient algorithm. Both S_n transport and diffusion are available, the latter being also used to accelerate the convergence scheme in the transport mode. The standard S_n method is used to discretize the Boltzmann equation in 2D geometries (X-Y or R-Z). There are different algorithms available (step, diamond and 'theta-weighted'), and a negative flux fix-up capability exists.

For the calculation of the sensitivities required in cross-section adjustment studies, perturbation theory calculations are performed within ERANOS using either the transport theory module (for the critical masses and reactivity coefficients) or the diffusion theory module (for parameters described with a fundamental-mode distribution).

The variational nodal method developed for the VARIANT code [Pal93, Car92] has been implemented in the TGV/VARIANT module. This method is based on the second-order form of the even-parity transport equation. A solution is searched for in the form of expansions for the even and odd parity fluxes in pre-computed angular and spatial basis functions with unknown coefficients. These basis functions are orthogonal polynomials for the spatial variables and spherical harmonics for the angular variables. Both Cartesian and hexagonal geometries are available. Also, the user can specify the order of the spatial expansions to be used for the source and flux within a node, and for the flux at the boundary of nodes, as well as the angular expansion (diffusion, simplified transport or transport) within or at the boundary of a node. The simplified transport option (by neglecting the high-order cross-terms in the angular developments) allows one to reduce the computational time required and is recommended for the reference route.

In addition to the TGV/VARIANT module, a kinetics driver named KIN3D [Rin97] was developed and integrated into ERANOS.

ERANOS reference calculation route

In summary, ERANOS allows one to compute characteristic neutronics core features. Recommendations for a typical core calculation have led to a reference route which includes the following steps [Rim02] (also see schematic view in Fig. 2.4):

- use of the ECCO cell code with a fully explicit description of the subassembly, including the wrapper tube and the array of pins, and with a fine (1968) group calculation including a sub-group treatment for the self-shielding calculation; results are given in 33 groups for the equivalent homogenised cell,
- use of the reactivity equivalence method for the preparation of the cross-sections for control rods,
- use of the nodal variational code TGV/VARIANT for the determination of the critical

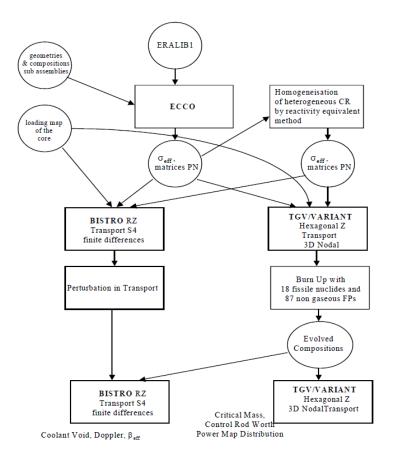


Figure 2.4. Reference core calculation scheme in ERANOS [Rim02]

mass, the control-rod reactivity worth, the power distribution, and also for the burn-up reactivity swing,

- use of decay chains made of 18 heavy nuclides and 87 fission products for fuel burn-up calculations,
- use of the S_n transport module BISTRO in R-Z geometry for the determination of certain parameters which are not very sensitive to the geometrical representation of the core (including k_{eff} , the sodium-void reactivity worth and the Doppler coefficient),
- use of perturbation modules associated with the BISTRO code for the characterisation of kinetics parameters.

The ERANOSTOPARCS subroutine

To extend usage of the cross-sections and scattering matrices produced by ERANOS, a special interface code, ERANOSTOPARCS, has been developed at PSI in the framework of the FAST project. This allows to convert, for each core region, the cross-sections produced with the cell code ECCO as well as dedicated kinetics parameters, into a format suitable for use in PARCS. In particular, the output provides the macroscopic cross-sections and their derivatives with respect to the fuel temperature, coolant density, as also axial and radial core expansion.

PARCS: 3D neutron kinetics

PARCS (Purdue Advanced Reactor Core Simulator) [Dow06] is a 3D reactor core simulator which solves the steady-state and time-dependent, multi-group neutron diffusion and SP3 transport equations in square and hexagonal geometries. PARCS is directly coupled to the thermal-hydraulics code TRACE which provides it with the temperature and coolant density field information during the transient calculation. After re-calculation of the macroscopic cross-sections and computation of the core neutron kinetics, PARCS feeds back the resulting power distribution to TRACE that can iterate the time-step.

Spatial kinetics calculations involve the solution of the eigenvalue problem and the timedependent neutron transport equation. The eigenvalue calculation is necessary to initiate the steady state. PARCS uses the Wielandt eigenvalue shift method. The obtained $k_{\rm eff}$ is then used to adjust the ν values in the subsequent transient calculation and make the initial state critical.

The balance equations require to be discretized in both time and space prior to the resolution. The temporal differencing is based on the exponential transformation and the theta method. For spatial discretization, the efficient nonlinear nodal method is employed in which the coarse mesh finite difference (CMFD) problems and the local two-node problems are repetitively solved during the course of the nonlinear iteration. The temporal and spatial differencing of the spatial kinetics equation results in a fixed-source type of problem at every time step. The solution of a transient fixed-source problem (TFSP) consists of simultaneously solving the CMFD and two-node problems.

In PARCS, the cross-section parameterization uses macroscopic cross-sections for a reference state and their derivatives with respect to state variables, to account for the reactivity feedbacks, assuming a linear dependency of the different effects. Since the code was originally developed for light water reactor applications, the cross-section parameterization was modified at PSI to enable fast-neutron spectrum system analysis [Mik05]. More specifically, the modifications include a different functional dependence of the Doppler reactivity on the fuel temperature, the absence of boron regulation, and the changes of reactivity due to control rod position, core dimension and effective fuel density change (through changes in neutron leakage). Equation 2.7 represents the current procedure for recalculating a macroscopic cross-section during transients:

$$\Sigma(T_f, \rho_c, R, H, Z) = \Sigma_0 + \left[\frac{\partial \Sigma}{\partial \ln T_f}\right]_{T_{f_0}} (\ln T_f - \ln T_{f_0}) + \left[\frac{\partial \Sigma}{\partial \rho_c}\right]_{\rho_{c_0}} (\rho_c - \rho_{c_0})$$

$$+ \left[\frac{\partial \Sigma}{\partial R}\right]_{R_0} (R - R_0) + \left[\frac{\partial \Sigma}{\partial H}\right]_{H_0} (H - H_0) + \left[\frac{\partial \Sigma}{\partial Z}\right]_{Z_0} (Z - Z_0)$$
(2.7)

where Σ is the macroscopic cross-section, T_f the fuel temperature, ρ_c the coolant density, R the average core radius, H the average core height, and Z the control rod position. The subscript 0 refers to the values at the reference state (usually chosen at room temperature). Also, the dependence considered is linear in each case, except for the Doppler effect where a logarithmic dependency on the fuel temperature is assumed.

In the FAST project, the self-shielded macroscopic cross-sections and their derivatives with respect to state variables are produced using the cell code ECCO and transferred into PARCS-compatible format with the in-house routine ERANOSTOPARCS. The complementary kinetics parameters, i.e. the fission spectra, delayed neutron fraction β_i , and the decay constant λ_i of the *i*th group, are also provided from an ERANOS calculation.

Recently, a σ_0 method, based on the microscopic cross-section, has been implemented into PARCS at PSI [Pel11]. This allows a more accurate computation of the macroscopic cross-

sections in the case of transients with strong interactions between the reactivity feedbacks, which cannot be properly described using the derivatives.

TRACE: thermal-hydraulics

TRACE is a thermal-hydraulics code developed by the U.S. Nuclear Regulatory Commission (NRC). Formerly called TRAC-M, TRAC/RELAP Advanced Computation Engine is the latest in a series of advanced, best-estimate reactor system codes. It combines the capabilities of the NRC's four main systems codes (TRAC-P, TRAC-B, RELAP5 and RAMONA) into a single modernized computational tool. TRACE has been originally designed to perform best-estimate analyses of loss-of-coolant accidents (LOCAs), operational transients, and other accident scenarios in PWRs and BWRs. Also, its versatility allows one to model a wide variety of thermal-hydraulics experiments in reduced-scale facilities. Models used include multidimensional two-phase flow, non-equilibrium thermodynamics, generalized heat transfer, reflood, level tracking, and reactor kinetics. The programming language is standard Fortran 90.

The partial differential equations that describe two-phase flow and heat transfer are solved using finite-volume numerical methods. The heat transfer equations are evaluated using a semiimplicit time-differencing technique. The fluid-dynamic equations in the spatial 1D, 2D and 3D components use a multistep procedure (SETS numerics). The finite-difference equations for hydrodynamic phenomena form a system of coupled, nonlinear equations that are solved by the Newton-Raphson iteration method. The resulting linearized equations are solved by direct matrix inversion.

The modeling of a reactor system is based on a component approach. Each physical piece of equipment in a flow loop can be represented as some type of component, and each component can be further nodalized into some number of physical volumes (cells) over which the fluid, conduction, and kinetics equations are averaged. The number of reactor components in a problem and the manner in which they are coupled, are arbitrary. The only limit on the problem size is the amount of computer memory. The hydraulic components available in TRACE for the reactor description include, among others, PIPEs (1D), VESSELs (3D), PLENUMS (0D), PUMPs, VALVEs and TEEs. The fuel elements and heated walls in the reactor system can be modeled with HTSTRs (heat structures), that compute 2D conduction and surface-convection heat transfer in X-Y or R-Z geometries. The energy delivered to the fluid via the HTSTRs is specified in the POWER components. The power generation in the reactor core can be specified in different ways: either constant or via a time-dependent table, calculated from the point-reactor kinetics with reactivity feedbacks, or calculated from 3D kinetics (when TRACE is used in coupled mode with PARCS that provides the reactor power and power distribution at each time-step). The boundary conditions in the hydraulic components are applied from the FILL and BREAK components, used to apply the desired coolant-flow and pressure boundary conditions, respectively.

The code's computer execution time is highly problem dependent and is a function of the total number of mesh cells, the maximum allowable time-step size, and the rate of change of the neutronics and thermal-hydraulics phenomena being evaluated. The stability-enhancing two-step SETS numerics in hydraulic components allows the material Courant limit to be exceeded. This allows very large time steps to be used in slow transients. This, in turn, can lead to significant speedups in simulations (one or two orders of magnitude) of slow-developing accidents and operational transients. Automatic steady-state and restart capabilities are also provided to split the problem into different parts (steady-state, transient) and to save computational time.

Some important TRACE characteristics are outlined below.

2. Thesis background

Coolant properties

The TRACE database includes physical properties for several coolants that can be used as the main working fluid in TRACE, viz. light water (gas-liquid), heavy water (gas-liquid), sodium (liquid), lead-bismuth (liquid), air (gas), CO₂ (gas) and helium (gas). Furthermore, a number of non-condensable gases are available: air, hydrogen, helium, argon, nitrogen, xenon and krypton. It is possible to use a gas mixture from any combination of the available gases.

Variable-dimensional fluid dynamics

Though the flow within the loop components is usually treated one-dimensionally using PIPE components, the VESSEL component allows more accurate computation of complex multidimensional flow patterns through a 3D (r, θ, z) flow calculation. The combination of 1D and 3D components allows a better modeling of complex flow networks caused by asymmetric perturbations.

Non-homogeneous, non-equilibrium modeling

TRACE uses a full two-fluid, six-equation hydrodynamics model to describe the steam-water flow in the hydraulic components, resolving for each phase the conservation of mass, momentum and energy partial differential equations. This approach allows important phenomena, such as a counter-current flow, to be treated explicitly. A seventh field equation (mass balance) describes a non-condensable gas field, and an eighth field equation tracks dissolved solutes in the liquid field. In the present research, the models available for steam-water flow simulation have been used as basis for simulation of sodium two-phase flow.

Flow-regime-dependent constitutive equation package

Closure of the sets of equations requires a number of constitutive equations to describe the transfer mechanisms between the phases, and between the phases and the wall. Because these interactions are dependent on the flow topology, a flow-regime dependent constitutive-equation package is being used in the code. To accurately simulate sodium boiling, closure relations specific to sodium have been incorporated, where necessary (see Chapter 3).

Heat-conduction in structural materials

TRACE incorporates detailed heat-transfer analysis of the vessel and the loop components. It includes a 2D R-Z treatment of fuel-rod heat conduction and other system structures. The heat transferred to the fluid is calculated from flow-regime-dependent heat transfer coefficients (HTCs) obtained from a generalized boiling surface based on local conditions. Models specific to sodium have been incorporated in the frame of the present research.

Component and functional modularity

As mentioned, TRACE is completely modular in terms of components. The available components allow the user, through input data, to model virtually a wide range of thermal-hydraulics phenomena in experimental and reactor-design configurations. This provides a great versatility as regards the range of possible applications.

The TRACE code is also modular by function, i.e. the major aspects of the calculations are performed in separate modules. For example, the basic 1D hydrodynamics solution algorithm, the wall-temperature-field solution algorithm, HTC selection, closure relation selection and other functions are performed in separate sets of routines that are accessed by all component modules. This modularity allows the code to be extended easily and upgraded readily, as improved correlations and test information become available. Most of the modifications for extension of TRACE to sodium boiling have been performed in the ClosureModelsM and RefloodM modules.

FRED: fuel thermal-mechanics

FRED has been integrated into the FAST code system to account for the thermal-mechanical behavior of the fuel. FRED is a thermal-mechanical code for steady-state and transient conditions [Mik11]. It was originally developed to investigate LWR fuel rod behavior. It has been integrated into the FAST code system to compute fuel base irradiation, transient related changes in the fuel and cladding temperatures, and the heat fluxes in the fuel rods. Furthermore, FRED can be used to evaluate stress-strain conditions, as well as the failure probability for structural materials such as fuel rods, heat exchanger tubes, reactor vessel, etc.

For implementation into the FAST code system, FRED has in fact been integrated into TRACE. It has its own time integration scheme and has the option to divide the TRACE time-step into sub-steps if convergence is not obtained.

CHAPTER **•**

Simulation of sodium single- and two-phase flow with the TRACE code

THIS CHAPTER deals with the selection of appropriate models for the simulation of single- and two-phase sodium flow. Effectively, this has implied the extension of the non-homogeneous, non-equilibrium two-fluid models, which are available in TRACE for steam-water, to sodium two-phase flow simulation.

It appears that the two-fluid, 6-equation model – available in TRACE for steam-water flow – allows a general description of the flow without restrictions on the temperature or velocity conditions. Moreover, the TRACE code, as integrated into the FAST code system, has been coupled with static neutronics (via ERANOS), spatial neutron kinetics (via PARCS) and fuel rod behavior (via FRED), this flexible platform having being extensively verified for a range of fast reactor applications [Mik10]. Thus, the extension of TRACE, originally limited to the simulation of single-phase sodium, to two-phase sodium flow, will enable one to enlarge the range of SFR transient analyses possible with the FAST code system. In specific terms, transients in which boiling is anticipated will be included, allowing one to perform the coupled analysis of pre-severe accident events for SFRs.

Section 3.1 first presents a number of generic two-phase flow models, along with their respective advantages and limitations. Then, in Section 3.2, the special features of sodium boiling are described. The aim thereby is to provide the basis for identifying the most suitable models available in TRACE for application to two-phase sodium flow simulation.

Following identification of a suitable formulation for sodium two-phase flow modeling, the corresponding efforts made to extend TRACE are described in Sections 3.3 and 3.4. As mentioned, the current extension of the code is largely based on the existing models developed for steam-water two-phase flow, changes being made in the logics to enable sodium two-phase flow modeling, along with modifications of the closure relations when necessary. The original fluid-field equations and closure relations are first presented in Section 3.3. The focus is set on the latter since the accuracy of a two-fluid model strongly depends on these correlations, mostly empirical. A review then follows, in Section 3.4, of the available models for description of the interfacial and wall-to-fluid transfer mechanisms in sodium flow. It is these correlations which have been implemented as options in the TRACE code for the simulation of sodium two-phase flow. The qualification of the extended code and the sensitivity of the calculated results to the various implemented models are addressed later, in Chapter 4.

3.1 Two-phase flow models

The formulation of appropriate models for two-phase flow in nuclear, chemical and mechanical industries has been of interest since the mid-1960s. The fundamental difficulty of two-phase flow description arises from the multiplicity of internal configurations that must be taken into consideration. According to the flow regime, a local sensor may see one phase continuously (e.g. in the case of annular flow) or the two phases intermittently (e.g. in bubbly flow). On the other hand, the viewer of the cross-section of a two-phase flow channel can only observe the space-averaged behavior of the mixture of the two phases. It is this global behavior that is of practical interest. However, the interactions between the two phases, or between the phases and the structures, depend to a great extent on the local behavior. An appropriate model should be able to predict the needed averaged behavior corresponding to whatever local behavior may exist. This is easily fulfilled in single-phase flow, since the observer of a point within the single-phase volume sees one continuous medium. However, in the case of a two-phase flow, the presence of inter-phase surfaces leads to jump conditions between the two phases. The two phases may be considered as a single fluid only if the properties of the two phases are properly averaged and the jump conditions are properly accounted for. These jump conditions describe the mass, momentum and energy exchange between the two phases.

There is a wide variety of existing two-phase flow models, in which the description of the flow ranges from a pseudo single-phase fluid (mixture) to a multi-fluid flow (e.g. liquid film, vapor and droplets). Generally, as the two-phase flow model becomes more complex, more constitutive equations are required to represent the interaction between the phases. The simplest of the mixture models is the homogeneous equilibrium model (HEM). This assumes zero relative velocity and thermodynamic equilibrium between the two phases. The HEM assumptions are clearly limiting but, in this case, the mass, momentum, and energy balance equations of the mixture are sufficient to describe the flow. This model can be extended to include relative velocity (i.e. slip) or thermal non-equilibrium between the phases, by supplying external, usually empirical, constitutive relations to specify the interactions between the two phases. These methods allow for more accurate velocity and enthalpy predictions.

A more general description of two-phase flow can be obtained from a two-fluid model (also called six-equation model), solving the three conservation equations for both the vapor and the liquid phases. This requires more constitutive relations, the most important ones being those describing the transfer of mass (Γ), transfer of momentum (F_i), and transfer of energy (Q_i) across the liquid-vapor interface. The advantage of this model is that it allows a general description of the two phases without restrictions on the temperature or velocity conditions. The two-fluid model can also be extended to multi-fluid models, in which vapor bubbles, a continuous vapor, a continuous liquid, and liquid droplets are described by separate sets of conservative equations. These more complex models have not been as widely used as the two-fluid model.

Table 3.1 lists a wide variety of possible models to describe two-phase flow. The choice among the alternative models depends on the nature of the problem to be solved.

 Table 3.1. Two-phase flow models (adapted from [Tod90])

		Conservation equations	n equatio	suc	Impose	Imposed restrictions				Constitutive laws	ive laws		
)		impho ii		200 duin								
								5	Wall		Interphase		
Two-phase flow model	Mass	Energy	Mom.	Total	Phase enthalpy or tempera- tures	Phase velocities	Total	Mom. F_w	Energy \mathbf{Q}_w	$Mass$ Γ	$\underset{\mathbf{Q}_{i}}{\mathrm{Energy}}$	Mom. F_i	Total
3-equation models	-		1	e	T_v and T_l specified	Specified	က	1		0	0	0	5
Homogeneous equilibrium	1	-	1	က	T_v and T_l equilibrium	Equal	က	1	1	0	0	0	7
Equilibrium drift flux	1		1	က	$\operatorname{T}_v^{\circ}$ and $\operatorname{T}_l^{\circ}$ equilibrium	Specified drift flux	က	1	1	0	0	0	7
4-equation models													
Y Y	2	1	1	4	$T_v \text{ or } T_l$ equilibrium	Slip relation	7	1	1	1	0	0	က
В	1	2	1	4	$T_v \text{ or } T_l$	Slip	7	1	2	*⊣	1	0	ъ
G	1	-	7	4	equinibul T_v and T_l equilibrium	None	13	7	1	*	0	1	ю
5-equation models													
Υ	7	2	1	ю	None	Slip relation	1	1	2	1	1	0	Ŋ
В	7	1	2	Ŋ	$T_v \text{ or } T_l$	None	1	7		1	0		Ŋ
C	1	2	7	Ŋ	$T_v \text{ or } T_l$ equilibrium	None	1	7	2		1	1	1
Two-fluid	2	2	7	9	None	None	0	7	2	1	1	1	4
Three-fluid : cont. liquid, vapor and liquid drops	က	က	ŝ	6	None	None	0	co	က	7	7	0	12
${}^{*}\Gamma$ is needed whenever \mathbf{Q}_{i} or \mathbf{F}_{i} is needed	$\mathfrak{Q}_i ext{ or } \mathrm{F}_i$	is needed	_ ,										

3.2 Sodium boiling features

Before selecting a model for the appropriate simulation of sodium two-phase flow, the generic features of sodium boiling and a representative sequence of events are described. A qualitative picture of the different boiling flow patterns in a vertical channel is shown in Fig. 3.1.

In fast reactor applications, sodium boiling will occur at relatively low pressures whenever the coolant flow through a heated channel is too low to remove the heat in the liquid phase. Liquid metals show a different boiling behavior as compared to organic or inorganic liquids, essentially due to differences in the physical properties. For illustration, a comparison of water and sodium is given in Table 3.2. Shown are the material characteristics which determine the liquid behavior (i) at boiling inception and (ii) during stationary boiling. Surface tension, latent heat of evaporation, and to a lesser extent, specific heat determine nucleation, and consequently superheating, whereas density, liquid/vapor density ratio and heat conductivity mainly influence the flow patterns during stationary boiling. Under reactor conditions (i.e. at low pressure), the surface tension of sodium is one order of magnitude higher, the latent heat of evaporation is greater by a factor of 2 and the specific heat is about 1/4 that of water. These characteristics show that sodium tends to superheat at boiling inception. Also, the vapor density is three orders of magnitude less than the liquid density, which indicates that two-phase flow with a high vapor volume will develop preferably. Consequently, boiling has a large effect on the flow, which is not homogeneous, especially as far as its space and time-dependent pattern is concerned. A vapor quantity as small as $\sim 5\%$ can result in a void fraction of as much as 90%. The above mentioned features strongly influence the characteristics of both steady-state and transient boiling patterns. There is experimental evidence that, in restricted geometry (e.g. a fuel bundle), the sodium boiling flow regime is characterized by single vapor bubbles which are separated by very thin liquid plugs.

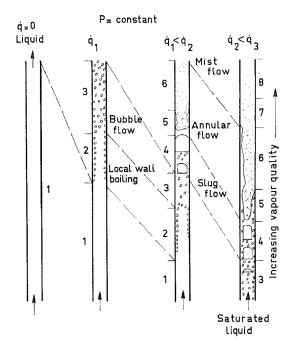


Figure 3.1. Example of flow patterns in vertical flow with boiling for increasing heat flux [Kot84] – 1=liquid, 2=subcooled boiling, 3=bubbly flow, 4=slug flow, 5+6=film boiling, 7=mist flow, 8=vapor flow

		$\rm H_2O$	H_2O	Na
	Pressure (bar)	2	80	2
	Boiling point ($^{\circ}C$)	119.62	294.97	965
i	Surface tension (N/m)	0.054	0.016	0.106
	Heat of evaporation (J/kg)	$2.2 imes 10^6$	$1.449 imes 10^6$	$3.7 imes 10^6$
	Specific heat $(J/kg \cdot C)$	4245	5673	1310
	Thermal conductivity (W/m·°C)	0.685	0.554	43.7
ii	Liquid density (kg/m^3)	945	725.37	720
11	Vapor density (kg/m^3)	1.11	41.5	0.436
	Liquid/vapor density ratio $(-)$	850	17.5	1650

Table 3.2. Characteristic physical properties determining boiling behavior for water and sodium – physical properties dominating (i) start of boiling, (ii) stationary boiling

The first bubble which nucleates will contain vapor at a higher pressure than the static pressure in the surrounding liquid, because of superheat [Pep70]. This pressure increase will deactivate any other potential nucleation sites in the neighborhood of the first bubble. The expanding vapor bubble ejects the liquid coolant from the channel, and only a thin liquid layer remains on the channel walls. As soon as the bubble reaches cooler zones of the channel, temperature and pressure of the vapor bubble will decrease. This leads to a deceleration and then to reversal of the flow of the ejected liquid. The static pressure will also be reduced at the same time. If the temperature of the liquid is sufficiently high, this pressure reduction will induce another bubble to nucleate. The second bubble behaves similarly to the first bubble with respect to liquid ejection and reentry. The first bubble will be totally expelled from the hot part of the channel and will condense completely.

This sequence of events will repeat until the heated part of the coolant channel is completely filled with one single bubble. Upon the reentry of liquid and pressure reduction, the surface area for vapor condensation is reduced until vaporization again overrides condensation. This process leads to a sequence of expulsion and reentry. Whether or not the reentrant liquid is able to completely compress the bubble depends upon the details of the particular case. At typical heat fluxes, experimental evidence indicates that the reentrant liquid is reversed and ejected before it even enters the heated part of the channel. In the heated part of the channel which is not rewetted by the reentrant liquid, the liquid layer on the wall continues to evaporate until the wall is completely dry. Up to this point, the vaporization of the liquid layer provides adequate cooling to prevent an excessive temperature of the heater. After dryout, the cooling capacity is lost and structure temperatures will increase rapidly.

In summary, mostly due to the high superheat and high thermal conductivity, sodium (like, in general, other liquid metals) boils with the formation of a few large bubbles contrary to the case of relatively homogeneous two-phase mixtures, e.g. water. In liquid metal boiling, at around atmospheric pressure, slug and annular flow regimes tend to prevail, while bubbly flow is more characteristic under high pressure in light water reactors. Nevertheless, the boiling phenomena for water and sodium will be similar in uniform temperature fields provided they have the same superheat [Pep70, Pla73].

3.3 TRACE two-fluid non-homogeneous non-equilibrium model

Considering the sodium boiling features presented above, the homogeneous model, which assumes no slip between the phases, is clearly not adequate for sodium modeling since the high density-ratio (1:1500) induces high slip between liquid and vapor. Among the possible twophase flow models, the two-fluid, six-equation model should provide, in theory, the maximum in capability and physical consistency. Accordingly, the two-fluid, 6-equation model used in TRACE for steam-water flow representation has been considered to be an appropriate basis for the current developments for sodium two-phase flow simulation. The approach taken has been, first, to add all necessary equations-of-state (EOSs) for liquid sodium and vapor to the code, and, second, to use as much as possible the internal logics of the TRACE models developed for steam-water flow while replacing, where necessary, the water-specific correlations by those for liquid metal. The implemented EOSs have been tested against open-source data and against the SIMMER-III code [Tob02]. This study is presented in Appendix A. The implemented models are presented in the following section.

As mentioned, TRACE uses a non-homogeneous, non-equilibrium model for steam-water two-phase flow representation. Each phase is considered separately in terms of two sets of conservation equations governing the balance of mass, momentum and energy for each phase. The basic volume- and time-averaged, two-phase, two-fluid model consists of the following six partial differential equations [Spo00]¹:

• Mass conservation equations

$$\frac{\partial [(1-\alpha)\rho_l]}{\partial t} + \nabla [(1-\alpha)\rho_l \vec{v_l}] = -\Gamma$$
(3.1)

$$\frac{\partial(\alpha\rho_g)}{\partial t} + \nabla .(\alpha\rho_g \vec{v_g}) = \Gamma$$
(3.2)

• Momentum conservation equations

$$\frac{\partial \vec{v_l}}{\partial t} + \vec{v_l} \cdot \nabla \vec{v_l} = -\frac{1}{\rho_l} \nabla P + \frac{c_i}{(1-\alpha)\rho_l} (\vec{v_g} - \vec{v_l}) |\vec{v_g} - \vec{v_l}| - \frac{c_{wl}}{(1-\alpha)\rho_l} \vec{v_l} |\vec{v_l}| + \vec{g} - \frac{\Gamma^-}{(1-\alpha)\rho_l} (\vec{v_g} - \vec{v_l})$$
(3.3)

$$\frac{\partial \vec{v_g}}{\partial t} + \vec{v_g} \cdot \nabla \vec{v_g} = -\frac{1}{\rho_g} \nabla P + \frac{c_i}{\alpha \rho_g} (\vec{v_g} - \vec{v_l}) |\vec{v_g} - \vec{v_l}| - \frac{c_{wg}}{\alpha \rho_g} \vec{v_g} |\vec{v_g}| + \vec{g} - \frac{\Gamma^+}{\alpha \rho_g} (\vec{v_g} - \vec{v_l})$$

$$(3.4)$$

¹In the nomenclature used here, the term *gas* implies a general mixture of sodium vapor and non-condensable gas, and the term *liquid* implies pure liquid sodium. The subscript g refers to the gas mixture, the subscript v applies to sodium vapor and the subscript l to liquid sodium.

• Energy conservation equations

$$\frac{\partial(\alpha\rho_g e_g)}{\partial t} + \nabla (\alpha\rho_g e_g \vec{v_g}) = -P \frac{\partial\alpha}{\partial t} - P \nabla (\alpha \vec{v_g}) + q_{wg} + q_{dg} + q_{ig} + q_{gl} + \Gamma h'_v \qquad (3.5)$$
$$\frac{\partial [(1-\alpha)\rho_l e_l + \alpha\rho_g e_g]}{\partial t} + \nabla [(1-\alpha)\rho_l e_l \vec{v_l} + \alpha\rho_g e_g \vec{v_l}]$$

$$\frac{(1-\alpha)\rho_l e_l + \alpha \rho_g e_g g_j}{\partial t} + \nabla \cdot \left[(1-\alpha)\rho_l e_l \vec{v_l} + \alpha \rho_g e_g \vec{v_g} \right]$$
$$= -P\nabla \cdot \left[(1-\alpha)\vec{v_l} + \alpha \vec{v_g} \right] + q_{wl} + q_{wg} + q_{dl} + q_{dg}$$
(3.6)

Closure is obtained for these equations using normal thermodynamic relations (see Appendix A) and specifications for the interfacial drag coefficients (c_i) , the interfacial heat transfer $(q_{ig} \text{ and } q_{il})$, the phase-change rate (Γ) , the wall-shear coefficients $(c_{wg} \text{ and } c_{wl})$, and the wall heat flux $(q_{wl} \text{ and } q_{wg})$.

The phase-change rate required by the equation set is evaluated from a simple thermalenergy-jump relation:

$$\Gamma = \frac{-(q_{ig} + q_{il})}{h'_v - h'_l} \tag{3.7}$$

where

$$q_{ig} = \frac{P_v}{P} h_{ig} A_i \frac{T_{sv} - T_g}{vol}$$
(3.8)

and

$$q_{il} = h_{il}A_i \frac{T_{sv} - T_l}{vol} \tag{3.9}$$

Here A_i is the interfacial area, h_{ig} and h_{il} are interfacial HTCs, and T_{sv} is the saturation temperature corresponding to the partial steam pressure. The closure relationships used to define A_i , h_{ig} and h_{il} are presented in the following section. The term $\Gamma^{+(-)}$ is equal to Γ for positive (negative) Γ and zero for negative (positive) Γ . The quantities h'_v and h'_l are the appropriate enthalpies of the vapor and liquid, respectively, i.e. the bulk fluid enthalpy for the phase moving to the interface and the saturation enthalpy for the product of the phase change.

The wall heat-transfer terms are calculated using Newton's law of cooling extended to a thermal non-equilibrium situation:

$$q_{wg} = h_{wg} A_w \frac{T_w - T_g}{B_{cell}}$$

$$(3.10)$$

and

$$q_{wl} = h_{wl} A_w \frac{T_w - T_l}{B_{cell}} \tag{3.11}$$

where A_w is the actual heated surface area and B_{cell} the cell volume.

The following section presents the physical models currently implemented in TRACE for representation of the interfacial and fluid-to-wall transfer mechanisms in sodium two-phase flow.

3.4 Closure relations as implemented in TRACE

Closure of the 6-equation set is obtained using flow-regime dependent correlations, representing the various transfer mechanisms between phases, as well as between phases and the wall. Since the accuracy of the two-fluid model strongly depends on its constitutive equations, these relations have been studied in detail for sodium two-phase flow analysis. A general brief overview of the original TRACE models is presented below, together with a summary of specific liquidmetal correlations that have currently been implemented in the code where necessary. The sensitivity of the calculated results on the closure relations has been studied for a set of selected experiments and is presented in Chapter 4.

As mentioned, the TRACE closure relations can be divided into the following categories: interfacial mass, momentum and energy exchanges, as well as wall friction and wall heat flow for each phase. Moreover, interfacial area is necessary to evaluate the transfer mechanisms between phases. All these closure relations are dependent on the local fluid conditions, as identified in TRACE with the use of a flow-regime map. The flow-regime map implemented in TRACE consists of the following regimes: bubbly flow ($\alpha \leq 0.3$), bubbly-slug flow ($0.3 < \alpha \leq 0.5$), churn-flow ($0.5 < \alpha \leq 0.75$), and annular-mist-flow ($\alpha > 0.75$), where α is the void fraction. Considering the special features of sodium boiling described in Section 3.2 and the experimental observations of sodium two-phase flow behavior, it has been assumed that annular flow is the dominant flow regime up to dryout. Different models will thus be considered for the pre-dryout and the post-dryout regimes.

3.4.1 Interfacial area

The interfacial area needs to be specified for closure of the set of field equations, and specifically to define the heat-transfer rate and momentum exchange between phases. Because this area is highly dependent on the flow regime, TRACE, as indicated above, uses different correlations for each regime. In bubbly and bubbly-slug flow, calculation of the interfacial area is based on the work of Ishii and Mishima [Ish80], and is a function of the average void fraction. For annular-mist flow, it is based on a superposition of film and droplet fields [Spo00]. In between, the interfacial area for the churn-flow regime is calculated as a weighted average of the bubblyslug and annular-mist interfacial areas. Details of the calculation are presented in the TRACE theory manual [Spo00].

Among the correlations available in the open literature for liquid-metal flow, the three correlations presented below have been implemented in TRACE. Two of these are based upon geometrical considerations of liquid-metal specific flow patterns in a triangular array of cylindrical pins. The first one, proposed by No and Kazimi [No87], assumes that annular flow is dominant, i.e. liquid films are supposed to remain on the wall while vapor appears in the form of large bubbles in a bulk flow. The interfacial area density in this model is given by:

$$A_i = \frac{4\pi\alpha}{D\left[2\sqrt{3}\left(\frac{P}{D}\right)^2 - \pi\right]} \min\left(\frac{1-\alpha}{1-0.957}, 1\right)$$
(3.12)

The second correlation was recommended by Schor [Sch84] and describes the interfacial area concentration A_i as:

$$A_{i} = \begin{cases} \frac{4}{D} \sqrt{\frac{\pi \alpha}{3\left[2\sqrt{3}\left(\frac{P}{D}\right)^{2} - \pi\right]}} & \text{for } \alpha < 0.6\\ \frac{4\sqrt{\pi}}{3D\left[2\sqrt{3}\left(\frac{P}{D}\right)^{2} - \pi\right]} \sqrt{(1 - \alpha)2\sqrt{3}\left(\frac{P}{D}\right)^{2} + \pi\alpha} \times \min\left(\sqrt{\frac{1 - \alpha}{1 - 0.957}}, 1\right) & \text{for } \alpha \ge 0.6 \end{cases}$$
(3.13)

where P/D is the pitch-to-diameter ratio and α the void fraction. The discontinuity at $\alpha = 0.6$ (see Fig. 3.2) represents the transition from bubbly to annular flow. There is no discontinuity at all for $P/D \approx 1.25$.

Both correlations use $\alpha = 0.957$ as dryout criterion. This consideration is derived from experiments dealing with the steady-state flow of sodium in a heated tube [Aut79], where it was shown that vapor does not contact the wall until the void fraction exceeds 0.957.

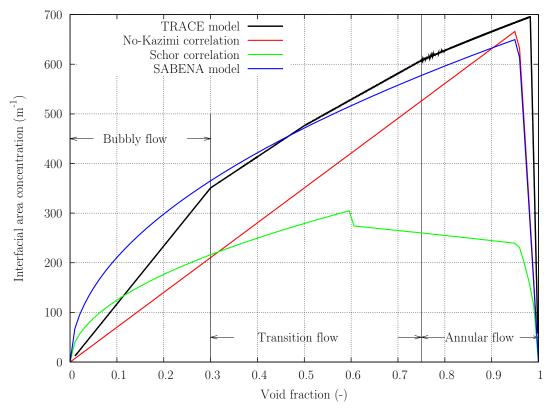


Figure 3.2. Comparison of the different models for the interfacial area concentration (indicated flow regimes correspond to the original TRACE regimes)

The last correlation listed here has been used in SABENA, a subassembly code developed for sodium boiling representation [Nin90]. The first versions of the code used different representations according to the flow regime [Nin88]. The latest model [Nin90] corresponds to the use of a single correlation based on the assumption that the annular flow regime dominates in sodium two-phase flow. Then, the interfacial area per unit volume is described as:

$$A_i = 4 \frac{\sqrt{\alpha}}{D_h} \tag{3.14}$$

The above correlations have been implemented as options in the extended TRACE code. Comparisons with the original TRACE model are presented in Fig. 3.2 (for $D_h = 6$ mm and P/D = 1.33). The sensitivity of the results to the different interfacial area models, together with the other constitutive relations, has been studied on a set of selected experiments and is presented in Chapter 4.

3.4.2 Interfacial momentum exchange

The interfacial shear force is included in TRACE, in both liquid and vapor momentum equations (Eqs. 3.3 and 3.4). In the original version, the interfacial shear coefficient c_i is calculated using a flow-regime dependent model [Spo00]. In the annular-flow regime, the film interfacial friction

factor f_i is based on the Wallis correlation given by:

$$f_i = 0.005 \left[1 + 75(1 - \alpha) \right] \tag{3.15}$$

In rod bundle geometry, it can be described as the sum of the shear coefficients as calculated in bubbly flow (corrected by a profile factor) and in annular-mist flow. Certain sodium-specific correlations are available in the open literature and have been considered for sodium two-phase flow analysis.

No and Kazimi [No87] recommend the following correlation for a pin bundle configuration, assuming that annular flow is dominant:

$$c_i = A_i \frac{\rho_g}{2} f_i \text{ with } f_i = 0.005 \left[1 + 234.3(1 - \sqrt{\alpha})^{1.15} \right]$$
 (3.16)

where A_i is the interfacial area density defined by Eq. 3.12, and f_i is the interfacial friction factor.

Another empirical correlation has been proposed by Autruffe [Aut79], on the basis of experimental data [Kai78] from the Kernforschungszentrum Karlsruhe (KfK), and is recommended by Schor [Sch84]. This correlation is also independent of the flow regime:

$$c_i = \frac{4.31}{2D_h} \rho_g \left[(1 - \alpha) \left(1 + 75(1 - \alpha) \right) \right]^{0.95}$$
(3.17)

In the SABENA code, the Wallis model is used to describe the interfacial friction coefficient in the annular flow regime, considered as dominant regime [Nin90]:

$$c_i = A_i \frac{\rho_g}{2} f_i \text{ with } f_i = 0.005 \left[1 + 150(1 - \sqrt{\alpha}) \right]$$
 (3.18)

These correlations, represented in Fig. 3.3 (for $D_h = 6$ mm) together with the original TRACE annular-flow model, have currently been implemented in TRACE as options for simulation of sodium two-phase flow.

3.4.3 Interfacial heat transfer

For the fluid energy closure in TRACE, the heat-transfer rates per unit volume from the interface (assumed always to be at saturation) to the vapor q_{ig} and to the liquid q_{il} have been given in Eqs. 3.8 and 3.9, respectively. The interfacial heat-transfer coefficients (HTCs) h_{ig} and h_{il} are evaluated by Nusselt numbers:

$$h_{ig} = Nu \frac{k_g}{D}$$

$$h_{il} = Nu \frac{k_l}{D}$$
(3.19)

where D is an appropriate length characterizing either the bubble or droplet diameter, according to the flow regime. In TRACE, flow regime dependent Nusselt numbers are used for interfacial heat transfer:

$$Nu = 2 + 0.6\sqrt{Re}Pr^{0.3333} \tag{3.20}$$

(with Re calculated using the bubble diameter and velocity) for bubbly-slug flow, and

$$Nu = 0.023 Re^{0.8} Pr^{0.4} \tag{3.21}$$

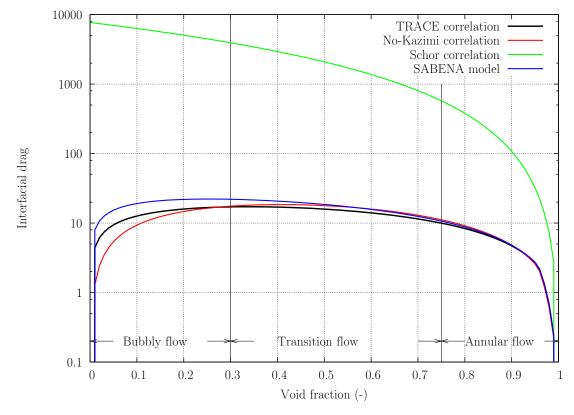


Figure 3.3. Comparison of the different models for the interfacial momentum transfer (indicated flow regimes correspond to the original TRACE regimes)

(with *Re* calculated for vapor flow) for annular-mist flow. A detailed analysis of the original TRACE model is given in the TRACE theory manual [Spo00].

No and Kazimi developed a model based on the vapor kinetic theory described by turbulent flow theory, modified to account for conductive heat losses from eddies. The interfacial HTCs are calculated from:

$$\begin{cases} h_{il}^{a} = \frac{k_{l}}{\alpha(1-\alpha)} A_{i} + 27.73 c_{p,l} G_{l} Pr_{l} \\ h_{il}^{b} = \sqrt{\frac{M}{2\pi R}} \frac{(\rho_{g} H_{fg})^{2}}{P\sqrt{T_{s}}} \\ h_{il} = \min(h_{il}^{a}; h_{il}^{b}) \end{cases}$$
(3.22)

where $c_{p,l}$, k_l , G_l , and Pr_l are the specific heat capacity at constant pressure, the liquid conductivity, the mass flux, and the Prandtl number for the liquid phase, respectively. P, T_s , H_{fg} , M, and R are the pressure, the saturation temperature, the latent heat, the molar mass and the gas constant, respectively.

Schor proposed to calculate the interfacial HTCs from the Nusselt number and recommended, on the basis of experimental considerations, the use of a constant value for both gas and liquid phases [Sch84]:

$$Nu = 10 \tag{3.23}$$

In the SABENA code, the coefficient of interface heat transfer from vapor to liquid is based

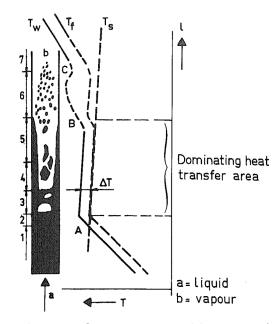


Figure 3.4. Correlation between flow patterns and heat transfer during boiling [Kot84] (1=liquid, 2=subcooled and bulk boiling, 3=bubble boiling, 4&5=film boiling, 6=misty flow, 7=vapor flow)

on the interfacial resistance model [Nin86]:

$$h_{il} = \frac{2\sigma}{2-\sigma} \sqrt{\frac{M}{2\pi R}} \frac{h_{fg}^2 M P_s(T_l)}{R T_s^{2.5}}$$
(3.24)

where σ is a coefficient accounting for evaporation and condensation in non-equilibrium systems. The literature shows a wide variation in the value of σ for sodium, ranging from $\sigma = 1.0$ to 0.001 for different pressures. Wilcox and Rohsenow [Wil69], however, attributed this variation to the presence of non-condensable gases, and tests conducted without any gases present at the interface led to $\sigma = 1.0$ for all pressures. In SABENA, the vapor phase temperature is also kept close to the saturation temperature, with a large value for $A_i \times h_{iv}$ (as much as $10^8 \text{ W/m}^3 \cdot \text{K}$) in order to prohibit high superheat of the vapor in a two-phase situation.

All the above models for interfacial heat-transfer have been implemented in the code as alternatives to the original TRACE correlations.

3.4.4 Wall heat transfer

Final closure of the fluid energy equations requires specification of the wall-to-liquid and wallto-gas heat-transfer rates per unit volume, q_{wg} and q_{wl} , as defined by Eqs. 3.10 and 3.11. This, in turn, requires the calculation of the wall-to-liquid and wall-to-gas heat-transfer coefficients h_{wl} and h_{wg} . The HTCs are clearly functions of the heat-transfer regime. This is illustrated in Fig. 3.4 which shows that, in the two-phase flow regime, three main heat-transfer processes can be distinguished: (a) subcooled-bubble boiling corresponding to zone 2, (b) saturated-bubble and film boiling corresponding to zones 3-5, and (c) misty flow, in which the two-phase flow temperature is determined by the droplet vapor pressure.

For practical use, the transition between zones 5 and 6 is of particular interest because, at this point, the liquid film breaks up, with a consequent sharp decrease of cooling and increase of the wall temperature. Process (c) is of minor importance. While the transition from zone 1

to 2 is important for water – due to an improved cooling – zone 2 is abolished in the case of liquid-metal boiling. Therefore, in liquid-metal two-phase flow, the heat-transfer mechanisms are simplified [Kot84].

For steam-water flow, TRACE considers the following individual heat-transfer models: forced convection to single-phase liquid, nucleate boiling, transition boiling, film boiling, convection to single-phase vapor, convection to a two-phase mixture, condensation and natural convection to single-phase liquid. Heat transfer models specific to sodium flow which have currently been implemented are for convection to single-phase liquid, boiling regime, transition boiling and convection to single-phase vapor.

Single-phase liquid regime

The heat transfer coefficients are obtained from the Nusselt number Nu, such that the wall-toliquid HTC is calculated from:

$$h_{wl} = Nu \, \frac{k_l}{D_h} \tag{3.25}$$

The form of the Nu number, generally empirically determined, depends on the flow regime and on the coolant. For metallic liquids, the molecular thermal conductivity is so high (Pr < 0.4), that the relative effect of turbulence at high values of Re is not as significant as in the case of non-metallic flows. It is experimentally established that the behavior of Nu for liquid metals follows the relation:

$$Nu = A + B P e^C aga{3.26}$$

where Pe = Re Pr is the Peclet number, which characterizes the ratio of heat transferred by convection to that transferred by conduction. A, B and C are constants that depend on the geometry and the boundary conditions. The constant A reflects the fact that significant heat transfer in the liquid metal still occurs even as Re goes to zero.

Earlier work performed by Mikityuk provided a review of the correlations to calculate the heat transfer to liquid metal in tube bundles with both square and triangular lattice geometry [Mik09]. The different models were implemented as options in TRACE. The correlation currently used for heat transfer to liquid in natural convection, laminar and turbulent flow is that proposed by Mikityuk:

$$Nu = 0.047 \left(1 - e^{-3.8(P/D-1)} \right) \left(Pe^{0.77} + 250 \right)$$
(3.27)

where P/D is the pitch-to-diameter ratio and Pe the Peclet number. This correlation has been established for $1.1 \le P/D \le 1.95$ and $30 \le Pe \le 5000$.

Boiling regime

There are few correlations for flow boiling heat transfer for liquid metals. A first attempt was made by Chen following the same approach as his method for non-liquid metal [No82], which assumes the total wall heat flux to be equal to the summation of nucleate-boiling and convective mechanisms. For liquid metals as well, he postulated that two mechanisms contribute to total wall heat transfer for the boiling of saturated fluids with flow: the ordinary macroconvective mechanism of heat transfer which normally operates with flowing fluids, and the micro-convective mechanism associated with bubble nucleation and growth [Che66].

No and Kazimi [No82] theoretically derived the wall heat-transfer coefficient for sodium boiling and condensation in forced convective flow using the momentum-heat transfer analogy and the logarithmic law for velocity distribution in the liquid film. Only one constant in the logarithmic formula is empirically determined. The correlation is given in detail in [No82]. Noyes and Lurie [Noy66] provided experimental sodium boiling results which showed that the effect of boiling on the wall heat transfer flux is not important. Unlike the familiar boiling curve of water which shows nucleate boiling over a wide range of heat flux, convection heat transfer dominates almost up to the critical heat flux for sodium, because of its high thermal conductivity and resulting high convective heat transfer coefficient.

Zeigarnick and Litvinov [Zei80] provided data for sodium boiling in a tube that enabled one, among other things, to better understand the mechanisms determining the heat transfer. It was found that the phase change in sodium occurs by evaporation from the vapor-liquid interface without bubble generation at the wall. This confirmed that the macro-convective contribution to the wall heat transfer in forced two-phase convection in sodium is highly dominant over the micro-convective contribution due to nucleate boiling.

Based on the above stated observations, and on the particularity of sodium boiling features described in Section 3.2, the forced-convection correlation (Eq. 3.27) is used currently up to dryout onset.

Critical Heat Flux (CHF)

The critical heat flux model defines the cooling limit and provides the transition point or boundary between the nucleate and transition boiling heat-transfer regimes. Different dryout criteria used in the past for sodium flow simulation are briefly discussed below.

On the basis of a correlation established for potassium flow in tubes and measurements for sodium two-phase flow, Kottowski and Savatteri established a new critical heat flux correlation for tubes and rod bundles, based on inlet flow conditions [Kot91]:

$$q_{CHF} = \frac{a \, G^b \left(1 - 2x_{in}\right) H_{fg}}{\left(\frac{L}{D_h}\right)^{0.8}} \tag{3.28}$$

where L is the length of the heated test section, $x_{in} = \frac{c_p (T_s - T_l)}{H_{fg}}$ is the inlet vapor quality and the terms a and b account for the test-section geometry.

It was shown that this form of correlation for dryout in sodium represents the correct dependencies of dryout on most experimental parameters. However, a more detailed inspection has revealed that there are discrepancies significant in terms of fast reactor safety analysis, since the correlation does not provide a conservative estimation of dryout conditions [Wal86]. An alternative approach based on local conditions was investigated by Wall. In his work, he highlighted the clear dependency of the dryout heat flux on the local void fraction and proposed [Wal86]:

$$q_{CHF} = K(1-\alpha)\frac{A}{P_w}$$
(3.29)

where K is a constant, the value of which depends on the channel geometry (tube, grid- or wire-spaced bundle) and P_w is the wetted perimeter.

In the same way, No and Kazimi used a simple dryout criterion based on Autruffe's experiments on steady-state sodium two-phase flow in a heated tube [No87]. The analysis indicated that vapor did not come into contact with the wall until the void fraction exceeded 0.957. This value was then used in the THERMIT-6S code for the dryout criterion: the authors assumed that, below $\alpha = 0.957$, the entire surface of the rod is covered with liquid, and that the liquid contact fraction decreases linearly from 1 to 0 when the void fraction is increased from 0.957 to 1.

In the BACCHUS-3D/TP code, developed for LMFBR two-phase thermal-hydraulics analysis, the liquid phase is assumed to be in contact with the cladding up to a void fraction α_{crit} which corresponds to dryout [Bot87]. However, in a later study, the dryout criterion is based on the thermodynamic quality $-x = \left(\frac{h_m - h_{ls}}{h_{gs} - h_{ls}}\right)$ – and dryout is simulated for $x_{crit} > 0.3$ [Bot90].

Following the recommendations used for sodium flow, a parametrized correlation, taking into account both the void fraction and the vapor quality, has currently been implemented in TRACE. The fraction of liquid in contact with the wall, Cf_{wl} is described as:

$$\begin{cases} Cf_{wl} = 1.0 & \text{for } 0 \le \alpha \le \alpha_{crit} \text{ and } x < x_{crit} \\ Cf_{wl} = \left(\frac{\alpha_{SPV} - \alpha}{1 - \alpha_{crit}}\right)^{a_0} \left(\frac{1 - x}{1 - x_{crit}}\right)^{b_0} & \text{for } \alpha > \alpha_{crit} \text{ and } x > x_{crit} \end{cases}$$
(3.30)

where α_{SPV} is the void fraction above which the flow is in the single-phase vapor regime $(\alpha_{SPV} = 0.9999 \text{ in TRACE})$, and the coefficients a_0 and b_0 can be set by the user. The set $(a_0 = 0.5, b_0 = 1.5, \alpha_{crit} = 0.957, x_{crit} = 0.3)$ is currently used, following the assessment of the correlation in pin-bundle experiments (presented in Section 4.2). These parameters having been obtained on the basis of a rather restricted set of experimental data, more validation work is clearly needed before recommending any final correlation.

Transition regime

During the transition regime, the liquid film in contact with the wall smoothly disappears. The total wall heat flux for transition boiling is defined as the sum of the wall-to-liquid and wall-to-gas phasic heat-flux terms:

$$q'' = Cf_{wl} h_{wl} (T_w - T_l) + (1 - Cf_{wl}) h_{wg} (T_w - T_g)$$
(3.31)

The heat-transfer coefficient for the liquid film h_{wl} is calculated from Eqs. 3.25 and 3.27, that for the vapor phase h_{wg} from Eq. 3.33.

Single-phase vapor regime

Under single-phase vapor conditions in the post-dryout regime, the wall-to-liquid heat-transfer coefficient is equal to zero:

$$h_{wl} = 0.0$$
 (3.32)

For the wall-to-gas heat-transfer coefficient, the Dittus-Boelter correlation is currently used:

$$h_{wg} = 0.023 \, Re_q^{0.8} \, Pr_q^{0.4} \tag{3.33}$$

3.4.5 Wall drag

At the fluid/wall interface, closure of the liquid- and gas-field momentum equations requires two additional parameters: the wall drag coefficient for the liquid phase c_{wl} and the wall drag coefficient for the gas c_{wg} (see Eqs. 3.3 and 3.4). For 1D components, these two drag coefficients are defined as:

$$c_{wl} = \frac{(1-\alpha)\rho_l f_l}{2D_h} \tag{3.34}$$

$$c_{wg} = \frac{\alpha \rho_g f_g}{2D_h} \tag{3.35}$$

where f_l and f_g are in the form of the Darcy friction factors [Moo44] for the liquid and gas phases, respectively.

In the case of an abrupt change in flow direction and/or geometry (such as, for example, across grid spacers), an additional loss of pressure should be accounted for. The form loss for the phase j is given by:

$$\Delta P_{Form} = K_j \frac{\rho_j v_j^2}{2} \tag{3.36}$$

In the following, correlations available in the open literature and implemented in TRACE are first reviewed for computation of the liquid-to-wall friction factor f_l in tubes, and in wire-spaced and grid-spaced bundles. Two-phase models are detailed subsequently, for both pre- and post-dryout regimes. The assessment of the various correlations is presented in Chapter 4.

Single-phase wall drag model

Tubular section

In circular pipes with single-phase flow, the friction factor between the wall and the j^{th} phase of the fluid f_j can be obtained from the Blasius formula in the turbulent flow regime (Re>3000), in combination with the Hagen-Poiseuille equation in the laminar flow regime (Re<2000), with a linear interpolation for $2000 \leq Re \leq 3000$:

$$\begin{cases} f = \frac{0.316}{Re^{0.25}} = \frac{0.316}{\left(\frac{\rho_l v_l D_h}{\mu_l}\right)^{0.25}} & \text{for } Re > 3000\\ f = \frac{64}{Re} & \text{for } Re < 2000 \end{cases}$$
(3.37)

The original TRACE model uses the Churchill correlation, which is a fit to the Moody diagram for laminar, transition and turbulent flow and is defined as:

$$f = 8 \left[\left(\frac{8}{Re}\right)^{12} + \frac{1}{(a+b)^{3/2}} \right]^{1/12}$$
(3.38)

where Re is the liquid Reynolds number, and a and b are defined according to:

$$\begin{cases} a = \left[2.475 \ln \left(\frac{1}{\left(\frac{7}{Re}\right)^{0.9} + \frac{0.27\epsilon}{D_h}} \right) \right]^{16} \\ b = \left(\frac{37530}{Re} \right)^{16} \end{cases}$$
(3.39)

for $Re \geq 100$, and where ϵ is the wall roughness.

Wire-wrapped bundle

The pressure loss due to the wire-wrapper is calculated in the same way as the wall-to-liquid friction pressure drop in circular section but with an appropriate friction factor to account for the spacers. For the present study, the following models have been selected:

1. Rehme model (1973)

On the basis of results measured with 80 different arrangements of wire-wrapped rod bundles, Rehme proposed the following model for calculation of the friction factor [Reh73]:

$$F = \sqrt{P_t/D_{rod}} + \left[7.6\frac{D_{rod} + D_{wire}}{H} \left(\frac{P_t}{H}\right)^2\right]^{2.16}$$
$$f = \left(\frac{64}{Re}F^{0.5} + \frac{0.0816}{Re^{0.133}}F^{0.9335}\right)\frac{P_{bundle}}{P_{bundle} + P_{wall}}$$
(3.40)

where the bundle perimeter is calculated in function of the number of rods n_{rod} : $P_{bundle} =$ $n_{rod} \pi (D_{rod} + D_{wire})$. This correlation is valid over a broad range of geometrical parameters: $P_t/D_{rod} = 1.125$ to 1.417, $H/D_{wire} = 6$ to 45 and $n_{rod} = 7$ to 61.

2. Engel model (1979)

Engel et al. [Eng79] measured the pressure drop in four 61-pin bundles, two of which were cooled by sodium and two by water. The friction factor has been correlated in a simple form, but the correlated constants were later corrected by the authors. The reported revised form is [Tod84]:

where the subscripts L, T and Tt refer to laminar, turbulent and transition flow, respectively.

3. Modified Engel model (2008)

After reviewing and analyzing the friction factor in wire-spaced bundles, Bubelis and Schikorr [Bub08] recommended the Engel model with modified correlated constants and proposed:

4600

The friction factor for a wire-wrapped fuel bundle in the Baxi-DD model is based on the Novendstern correlation [Nov72] for turbulent flow and is calculated according to the following correlations [Fen81]:

$$f_{L} = \left(\frac{K}{Re}\right) \left(\frac{T_{w}}{T_{B}}\right) \text{ with } K = \frac{80}{\sqrt{H}} \left(\frac{P_{t}}{D_{rod}}\right)^{1.5} (\text{H in cm}) \qquad Re < 400$$

$$f_{T} = \frac{0.316 M}{Re^{0.25}} \text{ with } M = \left[\frac{1.034}{\left(\frac{P_{t}}{D_{rod}}\right)^{0.124}} + \frac{29.7 \left(\frac{P_{t}}{D_{rod}}\right)^{6.9}}{\left(\frac{H}{D_{rod}} + D_{wire}\right)^{2.239}} Re^{0.086}\right]^{0.885} \qquad Re > 5000$$

$$f_{T} = \int_{0}^{\infty} \sqrt{1 + \frac{1}{2}} \left(\frac{1}{1 + \frac{1}{2}} + \frac{Re - 400}{Re - 400}\right)^{1.5} (\text{H in cm}) \qquad 100 \text{ f} R_{T} = \frac{1}{2} \int_{0}^{\infty} \sqrt{1 + \frac{1}{2}} \left(\frac{1}{1 + \frac{1}{2}} + \frac{Re - 400}{Re - 400}\right)^{1.5} (\text{H in cm}) \qquad 100 \text{ f} R_{T} = \frac{1}{2} \int_{0}^{\infty} \sqrt{1 + \frac{1}{2}} \left(\frac{1}{1 + \frac{1}{2}} + \frac{Re - 400}{Re - 400}\right)^{1.5} (\text{H in cm}) \qquad 100 \text{ f} R_{T} = \frac{1}{2} \int_{0}^{\infty} \sqrt{1 + \frac{1}{2}} \left(\frac{1}{1 + \frac{1}{2}} + \frac{Re - 400}{Re - 400}\right)^{1.5} (\text{H in cm}) \qquad 100 \text{ f} R_{T} = \frac{1}{2} \int_{0}^{\infty} \sqrt{1 + \frac{1}{2}} \left(\frac{1}{1 + \frac{1}{2}} + \frac{1}{2} + \frac{1}{2} \int_{0}^{\infty} \sqrt{1 + \frac{1}{2}} \left(\frac{1}{1 + \frac{1}{2}} + \frac{1}{2} + \frac{1}$$

$$f_{Tt} = f_T \sqrt{\psi} + f_L \sqrt{1 - \psi} \text{ with } \psi = \frac{Re^{-400}}{4600}$$

$$400 < Re < 5000$$
(3.43)

5. No-Kazimi model (1987)

In their study on sodium thermal-hydraulics, No and Kazimi [No87] recommended a combination of the laminar correlation of Markley and Engel [Mar76] and a simplified version of Novendstern's turbulent correlation [Nov72]. Thus, they proposed:

$$f_L = \frac{32}{\sqrt{H}} \left(\frac{D}{P}\right)^{1.5} \frac{1}{Re}, \qquad \qquad Re < 400$$

$$f_T = \frac{0.316 M}{Re^{0.25}}$$
 (M defined as in Eq. 3.43 – Novendstern's model), $Re > 2600$
 $f_T = f_{T2}\sqrt{4b} + f_{T2}\sqrt{1-4b}$ with $4b = \frac{Re - 400}{Re - 400}$ $400 < Re < 2600$

$$f_{Tt} = f_T \sqrt{\psi} + f_L \sqrt{1 - \psi}, \text{ with } \psi = \frac{1}{2200} \qquad 400 < Re < 2600 \qquad (3.44)$$

6. Sobolev model (2006)

The friction factor for the wire-wrapped fuel bundle in the Sobolev model [Sob06] is calculated as:

$$f = \left(1 + 600 \left(\frac{D_{rod}}{H}\right)^2 \left(\frac{P_t}{D_{rod}} - 1\right)\right)$$
$$\times \left(\frac{0.210}{Re^{0.25}} \left(1 + \left(\frac{P_t}{D_{rod}} - 1\right)^{0.32}\right)\right)$$
(3.45)

As illustrative example, the single-phase friction factor calculated from the different models are compared in Fig. 3.5. The analysis of these models is given in Subsection 4.1.2 on the basis of sodium experiments in a 12-pin wire-wrapped bundle.

Grid-spaced bundle

Because of variation and complexity of geometry, it is extremely difficult to establish a pressure loss coefficient correlation of general validity for grid spacers. However, predictions of reasonable accuracy can be achieved for computing the local pressure losses across grid spacers using a spacer loss coefficient K:

$$\Delta P = K \, \frac{\rho_l v_l^2}{2} \tag{3.46}$$

where v_l is the bulk liquid velocity. Empirical models for K as described below may be used.

Rehme [Reh73] assumed that the relative plugging $\epsilon = \frac{A_v}{A_s}$, where A_v is the projected grid cross section and A_s is the undisturbed flow section, constitutes the main factor influencing the pressure and proposed:

$$K = \epsilon^2 C_v \tag{3.47}$$

where C_v is the modified loss coefficient. The following empirical models, found in the literature, have been considered for implementation in TRACE:

1. Vog [Vog71, Eif80] (1971).

Vog developed a correlation based on sodium flow experiments in triangular bundles:

$$K = \epsilon^2 C_v = \epsilon^2 \left(9.9 + \frac{2.2}{10^{-4} Re}\right)$$
(3.48)

2. Savatteri [Sav86] (1986).

Savatteri developed a correlation based on sodium flow experiments in a 12-pin grid-spaced triangular bundle; the experiments are described in Section 4.1.

$$K = \epsilon^2 C_v = \epsilon^2 \left(9 + \frac{3.8}{(10^{-4}Re)^{0.25}} + \frac{0.82}{(10^{-4}Re)^2}\right)$$
(3.49)

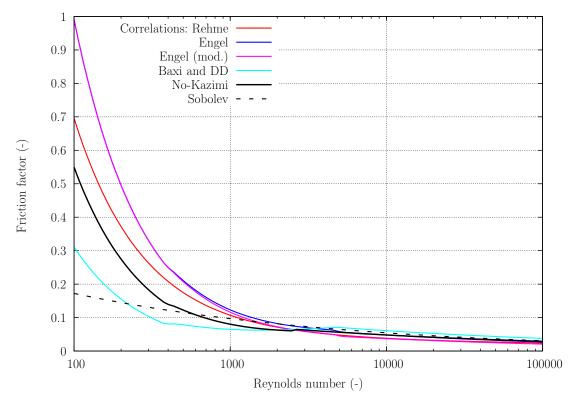


Figure 3.5. Comparison of models for computation of the single-phase pressure drop in wire-wrapped bundles

3. Cigarini and Dalle-Donne (CDD) [Cig88] (1988). Cigarini and Dalle-Donne proposed the following correlation on the basis of Rehme's experimental data for water in a 12-pin triangular bundle with rounded leading-edge spacer grids:

$$K = \epsilon^2 C_v = \min\left(\epsilon^2 \left(3.5 + \frac{73.14}{Re^{0.264}} + \frac{2.79 \times 10^{10}}{Re^{2.79}}\right), 2\right)$$
(3.50)

4. Cevolani [Cev95] (1995).

Cevolani proposed the following correlation for water in triangular bundles:

$$K = \epsilon^2 C_v = \min\left(\epsilon^2 \exp(7.69 - 0.9421 \ln(Re) + 0.0379 \ln^2(Re)), 2\right)$$
(3.51)

5. Epiney [Epi10] (2010).

Based on a review of experimental data for air flow, Epiney proposed a correlation for sharp-edged spacers with a lower dependency on the relative plugging, also called grid solidity [Epi10]:

$$K = \epsilon^{0.2} C_v = \epsilon^{0.2} \left(1.104 + \frac{791.8}{Re^{0.748}} + \frac{3.348 \times 10^9}{Re^{5.652}} \right)$$
(3.52)

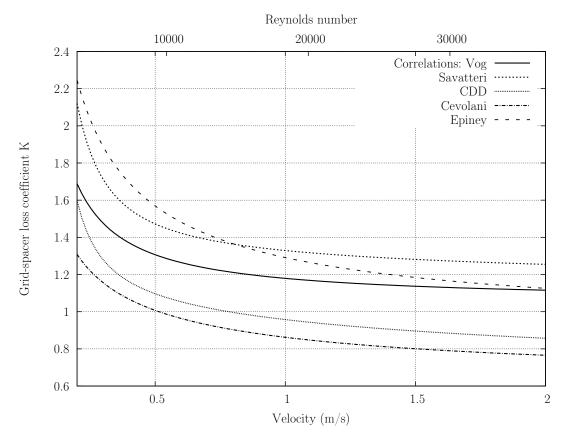


Figure 3.6. Comparison of the spacer loss coefficient K calculated using different models $(\epsilon = 0.326)$

In order to compare these correlations, the grid loss coefficient K calculated with the different models is presented in Fig. 3.6 (for $\epsilon = 0.326$). It appears that the Vog, Savatteri and Epiney models yield larger coefficients than the CDD and Cevolani models. It should be mentioned that the latter were specifically developed for grids with round leading edges, whereas the other models correspond to grids with sharp edges. The higher drag coefficient values found for sharp edges can largely be explained by the different grid characteristics. Indeed, the pressure drop of grid spacers can be decomposed into the contributions of (i) a reduction of the effective flow area at the grid entrance and the corresponding form resistance, dependent on the sharpness of the grid edges, (ii) an increase of the friction pressure loss inside the grid due to an increased wetted surface, and (iii) a form resistance caused by the sudden change in flow area at the outlet of the grid. Eifler found that the differences between the correlations was of the order of the contribution of the first term [Eif80].

The above mentioned correlations have been implemented in TRACE as options to simulate the local pressure drop in grid spacers. An analysis of a sodium test is presented in Section 4.1, where it is found that the Epiney model is of particular interest since it is much less sensitive to the relative plugging than the other models.

Two-phase wall drag model: Pre-dryout regime

Two-phase friction pressure drop

Up to dryout onset, it is assumed that only the liquid phase is in contact with the wall. There-

fore, the vapor friction coefficient is set to zero:

$$f_q = 0.0$$
 (3.53)

In two-phase flow, it has been experimentally observed that, for a given mass flow, the pressure drop can be much greater than for the corresponding single-phase flow. In order to correlate two-phase frictional losses, one classical approach is to consider the pressure drop which would exist if the phase is assumed to flow alone and to use a multiplier (ϕ_l^2) to account for the two-phase effects. Thus, referring to the liquid phase, the two-phase friction factor can be expressed as:

$$f_{l,2\phi} = \phi_l^2 f_{l,1\phi} \tag{3.54}$$

where $f_{l,1\phi}$ corresponds to the liquid single-phase friction factor flowing alone in the same duct with mass flow rate corresponding to the mixture flow rate.

This subsection presents a selection of correlations implemented in TRACE for computation of the two-phase friction multiplier factor ϕ_l^2 used to calculate the liquid-to-wall friction factor f_l in two-phase sodium flow.

1. Lockhart-Martinelli [Loc49] (1949).

Lockhart and Martinelli defined the parameter X_{LM} such that:

$$X_{LM} = \left(\frac{1-x}{x}\right)^{0.9} \left(\frac{\rho_g}{\rho_l}\right)^{0.5} \left(\frac{\mu_l}{\mu_g}\right)^{0.1}$$
(3.55)

The authors suggested, on the basis of measurements for air-water horizontal flow in pipes at near to atmospheric pressure, that ϕ_l can be correlated uniquely as a function of X_{LM} and is found, for turbulent flow, to be given by:

$$\phi_l^2 = 1 + \frac{20}{X_{LM}} + \frac{1}{X_{LM}^2} \tag{3.56}$$

2. Lottes-Flinn [Lot56] (1956).

Lottes and Flinn expressed the friction multiplier as a function of the vapor volume fraction, independent of pressure and flow rate. They proposed that, for small values of quality, the frictional effect is primarily due to drag of the liquid phase along the wall and can be written as:

$$\phi_l^2 = \left(\frac{1}{1-\alpha}\right)^2 \tag{3.57}$$

This model results directly from the triangular relationship which relates the liquid film flow rate with the film thickness and wall shear stress. It has been used by Ninokata in the SABENA code for prediction of the sodium two-phase pressure drop [Nin89].

For the sake of discussion and for comparison with the other models presented in Fig. 3.7, this correlation can be expressed as a function of the X_{LM} parameter using the correlation of Nguyen for the void fraction [Ngu85]:

$$\alpha = (1 + X_{LM}^{0.8})^{-0.378} \tag{3.58}$$

3. Kottowski [Kot84] (1984).

Kottowski derived a correlation on the basis of the round-tube, quasi steady-state sodium boiling experiments presented in Section 4.1 [Kot84]. The least-squares fit correlation derived from the measurement data is given by:

$$\log \phi = 0.1046 (\log X_{LM})^2 - 0.5098 \log X_{LM} + 0.6252$$
(3.59)

for $0.07 < X_{LM} < 30$.

4. Kaiser [Kai88] (1988).

The Kaiser correlation was obtained from quasi steady-state sodium boiling experiments carried out in an electrically heated 7-pin test section:

$$\ln \phi = 1.48 - 1.05 \ln \sqrt{X_{LM}} + 0.09 \left(\ln \sqrt{X_{LM}} \right)^2$$
(3.60)

5. Other correlations

On the basis of the air-water horizontal flow data from Lockhart and Martinelli, several authors plotted ϕ_l^2 against $(1 - \alpha)$ and found $\phi_l^2 = (1 - \alpha)^{-n}$. Lottes and Flinn [Lot56] adopted n = 2 (Eq. 3.57), whereas later analyses such as those of Katsuhara [Kat58] and Richardson [Ric58] suggested n = 1.75.

Then, on the basis of measurements in a sodium loop with an induction heated round test section of 9 mm inner diameter and 200 mm heated length, Kaiser derived the following correlation for the two-phase friction pressure drop multiplier [Kai74]:

$$\phi_l = 8.2 X_{LM}^{-0.55} \tag{3.61}$$

Finally, we should also mention the correlation proposed by Chen and Kalish on the basis of measurements with potassium [Che70]:

$$\ln\left(\frac{1}{\phi}\right) = -1.59 + 0.518\ln(X_{LM}) - 0.0867(\ln X_{LM})^2 \tag{3.62}$$

In order to compare the different models, results obtained using the above listed correlations are presented as a function of X_{LM} in Fig. 3.7, together with a selection of experimental sodium boiling data.

It appears that there are large discrepancies among the different models. This is related to the difficulties in providing an accurate model for the prediction of the friction pressure drop. Indeed, the different contributions to the two-phase flow pressure drop (elevation, acceleration, friction, singular) cannot be measured separately, except perhaps for the singular pressure drop. The data used for the empirical determination of the models provide total pressure drops over a given length of the experimental device. Moreover, validation of the correlations requires knowledge of the two-phase flow parameters (α, x) . Since the measurement of these parameters in boiling liquid metal is quite difficult, the friction pressure drop correlations have generally been derived using a supporting boiling model (providing α and x) – with associated numerical approximations. Finally, one should also consider the difficulties related to experimental errors. These are mainly due to [Kot94]:

- pressure measurement errors related to high temperatures, temperature gradients and temperature variations;
- the existence of heat losses due to the high-temperature operation; these can strongly influence the thermal balance considerations made for determining the quality or void fraction.

The first set of data was published by Lurie, and is based on sodium boiling in an annular test-section (6.35 inner and 12.7 mm outer diameter) [Lur64]. After post-processing of the total pressure drop measurements, the data presented correspond to the frictional pressure drop. Over the range of flow rates and pressure covered during the experiments (liquid Reynolds numbers of 6,000 to 34,000 and pressures of 0.1 to 0.7 bar), no additional parametric dependencies could be discerned when the pressure drop ratio was plotted as a function of the parameter X_{LM} , the slight scattering indicated being due to experimental variations and errors (especially in the high X_{LM} , low quality region). Most of the data fall between the Lockhart-Martinelli correlations for laminar and turbulent flow, as presented by the authors [Lur64].

The other sets of data presented here were measured by Kaiser et al. [Kai74, Kai79] in the sodium boiling loop KNS, Karlsruhe, with different test sections: a round tube and a 7-pin bundle. The test sections are shown in Appendix B (Fig. B.15). As only the total pressure drop could be measured, the friction pressure drop was calculated by an iterative procedure [Kai74]. The data based on the round tube experiments show very little scattering but could confirm neither the correlation of Lockhart and Martinelli nor that of Chen and Kalish existing at that time. The best approximation of these data is represented by Eq. 3.61. The quasi-steady state boiling experiments – carried out in the electrically heated 7-pin bundle – yielded more than 60 experimental points representing the two-phase pressure drop. The data obtained cover a wide range of flow conditions. They are presented in Fig. 3.7, together with the boundary lines containing the maximum experimental scattering evaluated by the author [Kai79]. The correlation represented by Eq. 3.60 is based on these experimental results.

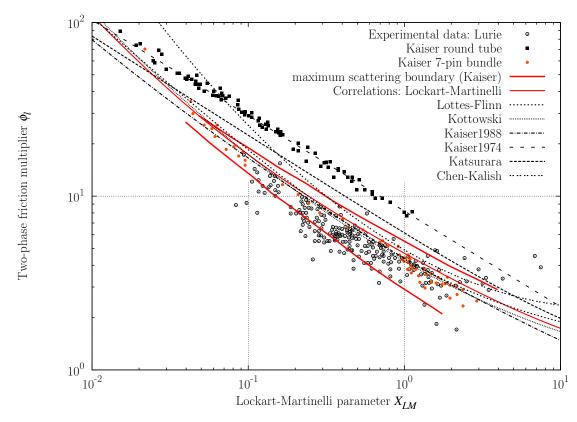


Figure 3.7. Comparison of the two-phase friction multiplier for different models with experimental data

From Fig. 3.7, it appears that the data measured in the round tube by Kaiser are very different from the other sets of experimental data presented here. The measurements performed on the 7-pin bundle by Kaiser fall within the range of the Lurie measurements. In both sets of experiments, there is more scattering for the low quality region. As the measurements from Lurie lie within the boundary of maximum scattering of the Kaiser experimental data for the 7-pin bundle, it has been limits to restrict the study to the correlations which cover this range. In other words, the evaluation of the quality of the correlations presented in Chapter 4 has been performed for a number of selected models, viz. the Lockhart-Matinelli (Eq. 3.56), Lottes-Flinn (Eq. 3.57), Kottowski (Eq. 3.59) and Kaiser (Eq. 3.60) models.

Two-phase local pressure drop

The two-phase pressure loss due to local flow obstructions, such as grid spacers, is treated as the frictional pressure loss. Thus, as in Eq. 3.54, the corresponding single-phase pressure drop is multiplied by an appropriate two-phase multiplier to yield the local two-phase pressure drop:

$$K_{2\phi} = K_{1\phi} \Phi \tag{3.63}$$

where Φ is the two-phase local loss multiplier. Two different models have been considered for implementation in TRACE.

1. Homogeneous model:

Based on extensive experimental data, Lahey and Moody [Lah93] reported that a homogeneous multiplier does a fairly good job of correlating the two-phase pressure drop data for a wide range of grid-type spacers and proposed:

$$\Phi = \left(\frac{x}{\rho_g} + \frac{1-x}{\rho_l}\right)\rho_l \tag{3.64}$$

2. Slip model:

Assuming a slip between the vapor and liquid phases, the two-phase pressure loss multiplier can be obtained from

$$\Phi = \frac{\rho_l}{\alpha \rho_g + (1 - \alpha)\rho_l} \text{ with, by definition, } \alpha = \frac{1}{1 + \left(\frac{1 - x}{x}\right) S \frac{\rho_g}{\rho_l}}$$
(3.65)

It may be noted that the slip model reduces to the homogeneous model if the slip ratio $S = \frac{v_g}{v_l}$ is equal to 1.

Two-phase wall drag model: Post-dryout regime

After dryout onset, the correlation of the liquid-to-wall friction factor for annular flow is assumed to hold true. Accounting for the reduced contact area, the wall drag is estimated as:

$$f_{l,2} = C f_{wl} f_{l,1} \tag{3.66}$$

where Cf_{wl} is the wall contact area of the liquid fraction as defined in Eq. 3.30, $f_{l,2}$ represents the post-dryout wall drag coefficient in the post-dryout regime, and $f_{l,1}$ that in the pre-dryout regime as discussed in the previous subsection.

Similarly, the vapor drag coefficient is calculated from

$$f_{g,2} = (1 - Cf_{wl}) f_{g,1} \tag{3.67}$$

where $f_{g,1}$ is obtained from one of the single-phase correlations described by Eqs. 3.37 and 3.38.

3.5 Conclusions

From the different formulations for two-phase flow modeling, it has been seen that the twofluid model allows the most general representation of the flow, without restriction on either the velocity or temperature field. As such, the basic two-fluid model available in TRACE has appeared suitable for being adapted to the simulation of sodium two-phase flow. The FAST code system would then provide the platform for coupling of the thermal-hydraulics code with 3D neutronics and thus allow the coupled analysis of SFR transients in which boiling is anticipated.

For this purpose, the TRACE code has been extended to sodium two-phase flow, as presented in this chapter. The basis has been to use the models already available and verified for steam-water flow simulation and to implement physical models specific to sodium for the closure relations. From the consideration of sodium boiling features, annular flow has been considered as the dominant flow regime up to dryout. A review of the models available in the open literature for representation of the different transfer mechanisms between the phases, as well as between the phases and the wall, has been presented. The corresponding models have been introduced as options into the extended TRACE code. The assessment of the quality of the different models is addressed in the next chapter, together with the validation of the new computational tool.

Chapter 4

Validation of TRACE single- and two-phase sodium flow modeling using out-of-pile experimental data

THE VALIDATION of the physical models implemented in TRACE, as presented in Chapter 3, has been carried out on the basis of a range of out-of-pile sodium boiling experiments. First, a review has been performed of the experimental data involving sodium two-phase flow available in the open literature. A summary of the most relevant experiments for code benchmarking is given in Appendix B. Three different sets of experiments have been chosen currently in order to validate the extended TRACE code for sodium flow modeling. These are:

1. Pressure drop measurements in quasi steady-state sodium boiling;

2. Dryout measurements in quasi steady-state sodium boiling;

3. Sodium boiling experiments in loss-of-flow conditions.

The first set of experiments, discussed in Section 4.1, was used to check the applicability of the physical models for sodium boiling modeling through the comparison of measured and calculated two-phase flow characteristics in different geometries (tubular test section and pin bundle). A sensitivity study of the calculated results on the different models has been performed in order to select the most appropriate closure relations for an accurate representation of sodium two-phase flow. The modeling of the spacers (wire-wrappers and grid-spacers) has also been investigated for single- and two-phase sodium flow in pin-bundle geometry.

In Section 4.2, test data related to dryout mechanisms in sodium are discussed. These have allowed us to assess the extended TRACE code capability to predict cooling limits and the evolution of the wall temperature after dryout.

Section 4.3 describes experiments simulating an unprotected loss-of-flow via boiling onset up to dryout in similar-to-reactor conditions. These have been selected for further validation of the new tool in transient situations.

Finally, conclusions of the chapter are presented in Section 4.4.

4.1 Study of the pressure drop in steady-state boiling

4.1.1 Description of the Ispra experiments

In the 1980s, Kottowski and Savatteri investigated the fundamentals of liquid metal boiling thermal-hydraulics at the Joint Research Center (JRC), Ispra, Italy. They studied basic phenomena in the liquid-metal boiling domain, including nucleation, flow pattern, two-phase flow boiling characteristics and dryout. The loop facility used for these investigations has been described in detail by Kottowski [Kot84]. The main components are an interchangeable test section with adjustable electrical heating (of 300 kW maximum power), an electromagnetic pump (maximum 3×10^{-2} m³/s, 10 bar pressure head), four 40-kW pre-heaters, a 600-kW air heat exchanger in parallel with ten 35-kW water evaporation heat exchangers, and a sodium steam condenser. The central part of the test section was exchangeable and different geometries have been studied, namely tubular, annular and 12-pin bundles. In the pin bundles, both wire-and grid-spacers have been used in order to investigate the influence of the spacers on the flow. An illustration of the test-section mounting as employed for the tubular test section is shown in Fig. 4.1. Three pressure control valves were part of the test section flow and a by-pass flow. The by-pass and test section flows joined in the condenser.

In the following, a detailed description is given of the different test sections used for the set of experiments currently selected to validate the extended TRACE code.

Tubular test-section

The tubular test section used in the Ispra experiments is presented in Fig. 4.2. This was a thick-walled tube made of Fluginox (DIN 2,4964), with a 6-mm inner diameter and a 29-mm outer diameter. It consisted of a 380 mm unheated inlet zone, a 1000 mm heated part, and a 380 mm unheated section downstream of the test section. With direct current heating of the tube, a heat flux of up to 300 W/cm² was available. The axial non-uniformity of the mean flux was $\pm 2.5\%$ of the measured value. The heat generated in the test-section wall and in the sodium was 92% and 8%, respectively.

Thermocouples and void sensors were mounted along the test section. Static and dynamic pressure measurements were performed at the inlet and outlet, and also at the top end of the unheated section. The resolution limit of the data acquisition system was 0.1 mbar for the pressure.

The 12-pin bundle test-sections

Four different 12-pin bundle test sections were used for the investigation of two-phase flow boiling characteristics and dryout. Since the original aim of the program was to study the influence of spacers on the flow characteristics, the bundles had identical cross-sections but different spacers. Two test sections were grid-spaced and two of identical design were wirespaced. For each spacer type (grid and wire), a short and a long bundle was built. The long bundles consisted of three zones: an unheated inlet zone (540 mm), the heated region (500 mm) and an unheated section downstream (735 mm). The dummy length downstream was used to simulate an unheated breeder zone. In the short test sections, the bundle simulating the upper blanket was not mounted, i.e. the bundles ended after the heated zone and the housing in the unheated downstream part consisted of an open channel.

The bundles were electrically heated with a uniform heat flux, the subchannel walls being designed such as to establish an as-uniform-as-possible radial temperature distribution. Downstream from the start of the test-section heated part, several sensors were positioned to measure

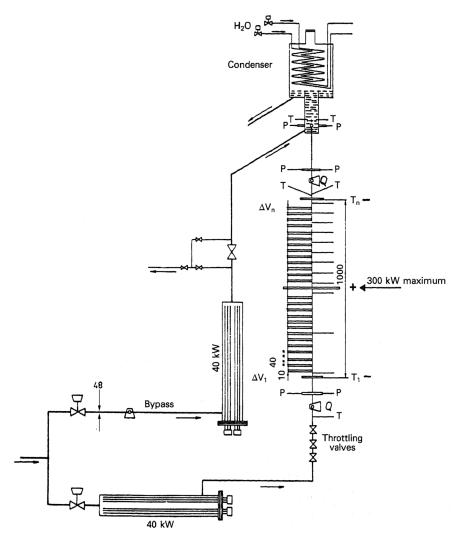


Figure 4.1. Schematic view of the semi-scale test loop at Ispra JRC (dimensions in mm) [Kot91]

local pressure, void, as well as cladding and fluid temperatures. Axial cuts of the bundles and their instrumentation are shown in Fig. 4.3. Figure 4.3b also shows the position of the grids which were 11 mm tall honeycomb spacers with sharp entrance edges. The axial pitch of the wire spacers was 150 mm. The main bundle design characteristics are presented in Table 4.1. The full-bundle hydraulic diameter was calculated taking into account the total wetted perimeter of the bundle flow cross-section. For the wire-spaced bundle, the wire perimeter was also included in the calculation. Figure 4.4 shows radial cross-sections of the 12-pin bundles and rods.

4.1.2 Assessment of TRACE models for the prediction of pressure drop

The pressure drop is an easily measurable parameter characterizing two-phase flow and can thus be used as an indirect check of the applicability of the current models for sodium listed in Section 3.4. For the Ispra steady-state boiling experiments, the most interesting comparison of computed results with the experimental data is in terms of the total pressure drop characteristic

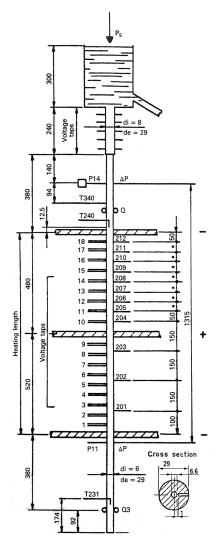


Figure 4.2. Schematic view of the tubular test section at Ispra JRC (dimensions in mm) [Kot84, Kot91]

curve ΔP as a function of the test section inlet velocity (with the specified values of inlet temperature, outlet pressure and added power).

Tubular test section

As an initial step, experimental data from the tubular test section have been used to assess the quality of the models as integrated into the TRACE code.

Interfacial closure relations

First, the models for the interfacial transfer mechanisms have been studied, using fixed models for the wall-to-fluid closure relations, viz. the Churchill correlation and the Kaiser model for the liquid-to-wall friction factor and the two-phase flow multiplier, respectively. Fig. 4.5a shows a comparison of the experimental data with TRACE results using the different sets of models for the interfacial closure relations as represented by Eqs. 3.12 to 3.24. More specifically, it presents the results for the total pressure drop as a function of the single-phase flow velocity at the inlet of the test section, for one of the different sets of test conditions, viz. q = 159 W/cm²,

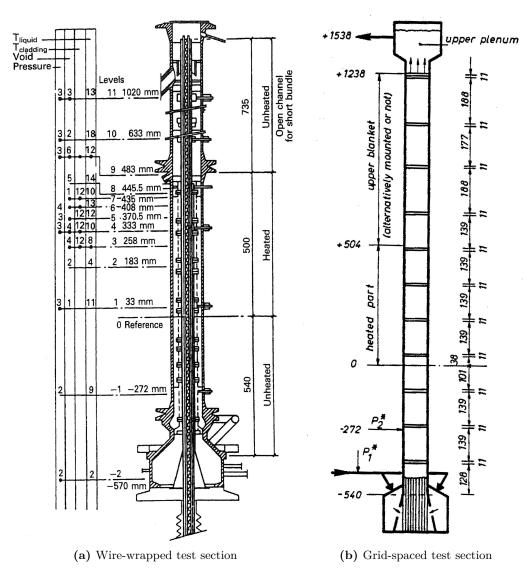


Figure 4.3. Ispra 12-pin bundle test sections [Kot84], [Eif80] (dimensions in mm)

 $T_{in} = 585^{\circ}$ C and $P_s = 1$ bar. The comparison of TRACE predictions with the measurements shows that the correlations recommended by No-Kazimi as well as these used in the SABENA code give similar predictions, which match very well with the experimental data, whereas Schor's model overpredicts the pressure drop in the two-phase flow region.

In order to understand the source of these differences, a complementary sensitivity study on each of the interfacial parameters – viz. A_i , c_i and h_i – has been performed. Using SABENA models for two of these parameters, the pressure drop was computed using the different correlations for the third variable. The results are presented in Figs. 4.5b to 4.5d. It appears that, considering the proposed models, the computed two-phase flow characteristic is very sensitive to the interfacial friction model and much less to the interfacial area or to the interfacial heattransfer models. On the basis of these observations and of a further sensitivity study performed using a different set of experimental data (in the KNS loop, as presented in Section 4.3), the models used in the SABENA code – i.e. A_i from Eq. 3.14, c_i from Eq. 3.18 and h_{il} from Eq. 3.24 – have been considered as the most accurate ones for the prediction of the interfacial transfer mechanisms in sodium two-phase flow. These will thus be used for the analyses presented later.

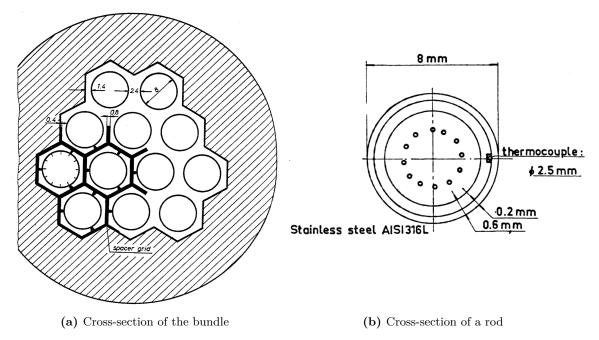


Figure 4.4. Radial cross-sections of the Ispra 12-pin bundles [Eif80] (dimensions in mm)

	Short grid-spaced bundle	Short wire-spaced bundle	Long grid-spaced bundle	Long wire-spaced bundle
Number of pins	12	12	12	12
Pin diameter (mm)	$8 {\pm} 0.05$	$8 {\pm} 0.05$	$8 {\pm} 0.05$	$8 {\pm} 0.05$
Pitch (mm)	10.4	10.4	10.4	10.4
Hydraulic diameter (mm)	4.93	3.8	4.93	3.8
Flow cross-section (mm^2)	550.8	496.5	550.8	496.5
Unheated inlet length (mm)	540 ± 8	540 ± 8	540 ± 8	540 ± 8
Heated length (mm)	500 ± 8	500 ± 8	500 ± 8	500 ± 8
Unheated breeder simulation (mm)	_	_	735 ± 8	735 ± 8
Maximum power per heated length (W/cm)	750	750	750	750
Maximum power per heating surface (W/cm^2)	300	300	300	300

 Table 4.1. Design features of the Ispra 12-pin test bundles

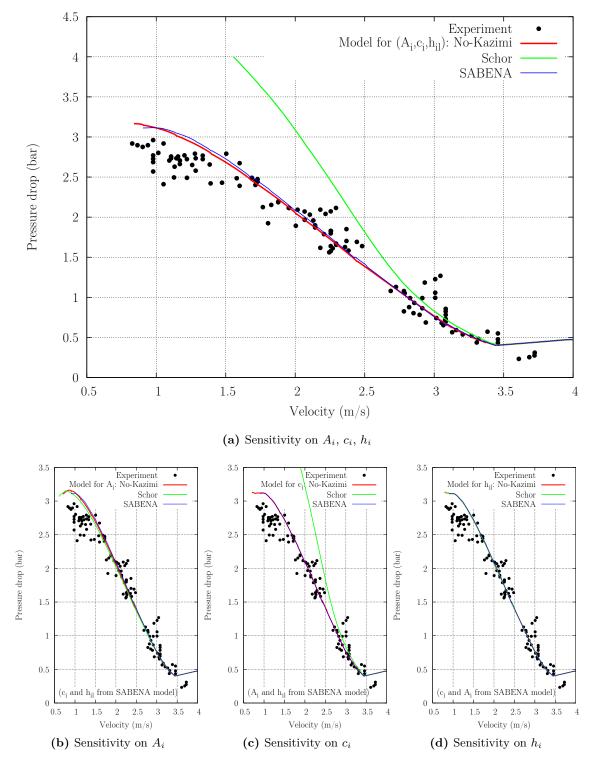


Figure 4.5. Two-phase flow pressure drop measured in the Ispra tubular section (q = 159 W/cm², $T_{in} = 585^{\circ}$ C), in comparison with results obtained using the different interfacial models

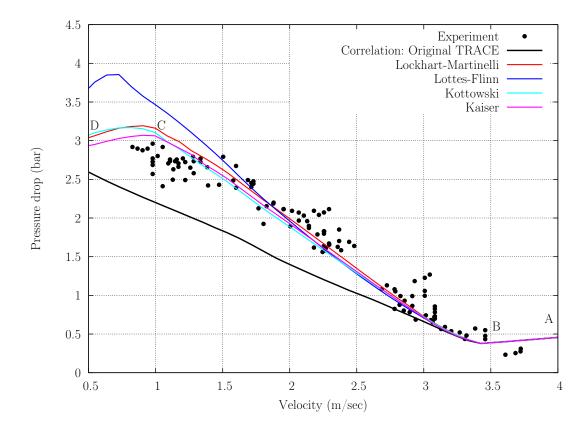


Figure 4.6. Two-phase flow pressure drop measured in the Ispra tubular section (q = 159 W/cm², $T_{in} = 585^{\circ}$ C), in comparison with results obtained using the different ϕ_l^2 models

Wall-to-fluid closure relations

Then, the wall-to-fluid closure relations have been studied in detail, with a particular emphasis on the liquid-to-wall friction factor correlations (Eqs. 3.37 to 3.67). The wall-to-fluid heat transfer models have been studied on the basis of the experiments performed in the pin bundle for investigation of the dryout and are presented in Section 4.2.

The experimental data from the tubular test section have been used to assess the quality of the two-phase friction multiplier ϕ_l^2 correlations (Eqs. 3.56 to 3.60), as integrated into the TRACE code. Figure 4.6 shows the experimental results for the test conditions: $q = 159 \text{ W/cm}^2$, $T_{in} = 585^{\circ}\text{C}$ and $P_s = 1$ bar. Comparison is made with TRACE predictions for pressure drop between the inlet and the outlet of the test section, using the different models for the two-phase multiplier, the Blasius correlation having been employed for the liquid-to-wall friction factor f_l (Eq. 3.37). It has been found that, for round tubes, the Blasius and Churchill correlations (Eq. 3.37 - 3.38) give very similar results in the boiling regime, so that the influence of the two-phase friction multiplier can in fact be studied independently from the single-phase friction factor itself.

At a high enough flow velocity (beyond point A in Fig. 4.6), the channel has liquid singlephase flow throughout its length. The single-phase region A-B is mainly characterized by a pressure drop that decreases as v^{2-n} , where n is the exponent of the velocity in the governing expression for the friction factor (n = 0.25, assuming a Blasius model as in Eq. 3.37). At

 Table 4.2. Comparison of the quality of the predictions for the different two-phase friction multiplier correlations (absolute values in mbar)

Correlation	LM	LF	Kot	Kaiser
$\overline{\varepsilon}$	-66	-93	1	-9
σ	157	258	151	159
r	170	274	151	159

point B, boiling is initiated in the channel, and the vapor generation is sufficient to reverse the trend of decreasing ΔP with decreasing v. Effectively, the two-phase flow leads to a decrease in the liquid flow cross-section, thus increasing the friction pressure drop which overcomes the decrease in the gravity pressure drop due to decrease of the mixture density. This increase in total pressure gradient is characteristic of the boiling regime. Decreasing the flow velocity generates more vapor in the channel, and point C marks the transition between two-phase flow and pure-vapor flow. Below that point, referred to as dryout, the friction pressure drop reduces and the pressure drop also decreases as v^{2-n} .

It can be seen from Fig. 4.6 that the original TRACE model, developed for water-steam flow, significantly under-predicts the pressure gradient. This can be explained by an over-estimation of the void fraction, resulting in a higher liquid velocity than the currently implemented models, which enable one to better reproduce the experimental data. It also appears that, for high vapor volume (low velocity, v < 1.5 m/s), the Lottes-Flinn model gives too high wall friction, which results in a higher total pressure drop as compared to the Lockhart-Martinelli, Kottowski and Kaiser predictions. One of the reasons for this behavior could be that the Lottes-Flinn model directly results from the triangular relationship, which may not be applicable to extremely high void fractions without droplet entrainment [Nin89].

In order to determine the quality of the predictions, the absolute error ε for each data point has been calculated as:

$$\varepsilon_i = \Delta P_i^m - \Delta P_i^c \tag{4.1}$$

where ΔP_i^m is the measured pressure drop and ΔP_i^c is the pressure drop calculated with TRACE using a given correlation for ϕ_l^2 . The mean absolute error $\overline{\varepsilon}$, the standard deviation of the absolute error σ and the root-mean-square error r, defined according to the following equations, were used to quantify the overall quality of the different correlations:

$$\overline{\varepsilon} = \sum_{i=1}^{N} \varepsilon_i / N \tag{4.2}$$

$$\sigma = \sqrt{\frac{\sum_{i=1}^{N} (\varepsilon_i - \overline{\varepsilon})^2}{N - 1}}$$
(4.3)

$$r = \sqrt{\frac{\sum_{i=1}^{N} \varepsilon_i^2}{N}} \tag{4.4}$$

where N is the number of test points (N = 140 here). The results are presented in Table 4.2 for the four considered correlations: Lockhart-Martinelli (LM), Lottes-Flinn (LF), Kottowski (Kot) and Kaiser model. Figure 4.7 presents the pressure drop calculated with the different models, versus the measured value, together with the dispersion of the calculated data.

It appears that the Kottowski correlation gives the lowest absolute error (1 mbar) and also

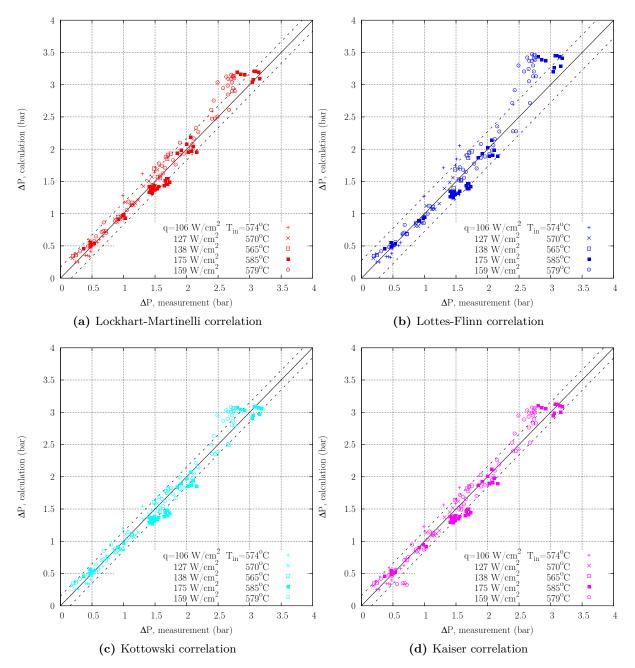


Figure 4.7. Predictions of the total pressure drop with the different correlations vs. the experimental data (tubular section)

the lowest dispersion (0.15 bar). This was predictable, considering that this correlation was derived from the same experimental data as has currently been used for qualification of the different models. The second best set of results is obtained with the Kaiser correlation, which presents a low absolute error (-9 mbar) and about the same dispersion as the Kottowski model. Although it was derived from 7-pin bundle sodium boiling experiments, this model is seen to predict the round-tube pressure loss very well. The third correlation giving good results is the well-known correlation of Lockhart-Martinelli which can, according to this study, also be used to calculate the pressure drop in sodium boiling. The model proposed by Lottes-Flinn shows an overestimation of the pressure drop for high pressure gradients (corresponding to the high vapor quality), what shows the limitations of the model's approximations. For low pressure drops (< 2.5 bar), however, the predictions are in good agreement with the measurements.

Wire-wrapped bundle

For a wire-wrapped bundle, the calculation of the pressure drop across the bundle length must account for the wire-wrappers. In order to evaluate the quality of the corresponding correlations for both the single-phase friction factor and the two-phase friction multiplier, presented through Eqs. 3.40 - 3.45 and Eqs. 3.56 - 3.60, respectively, experimental results of sodium boiling in the Ispra wire-wrapped test section have been used.

Single-phase flow

Experimental measurements of the pressure drop over a module length – corresponding to one axial pitch of the wire-wrapper (150 mm) – are available. This pressure drop is composed of the pressure drop of the undisturbed module plus that of the spacer. Figure 4.8 shows the test data of the pressure drop over one axial pitch of the wire-wrapper as function of the velocity at the bundle inlet, compared with the TRACE predictions for the different models presented in Subsection 3.4.5.

It can be seen that the modified Engel model is very similar to the Rehme predictions. The Sobolev model gives similar results to the original Engel model. The comparison with the experimental data shows that the most appropriate model for prediction of the pressure drop is the Baxi-DD model, with results for the Sobolev and original Engel models being quite satisfactory as well. Although these three correlations appear to be more appropriate than the others for predicting the single-phase pressure drop, it is difficult to make recommendations on the basis of the restricted number of experimental results considered here. A complete review of the single-phase friction factor in wire-wrapped bundles can be found in [Bub08]. The various, currently studied correlations have all been used for the two-phase flow study presented in the following paragraph.

Two-phase flow

The pressure drop characteristics measured under quasi steady-state boiling conditions in the wire-spaced bundle have been used to assess the appropriate models for the friction factor and the two-phase flow multiplier, $f_{l,1\phi}$ and ϕ_l^2 , respectively. First, the sensitivity to the single-phase friction factor $f_{l,1\phi}$ has been studied. Figure 4.9a shows the pressure drop characteristics at 144 kW ($q = 95.5 \text{ W/cm}^2$, $T_{in} = 550^{\circ}\text{C}$) in the long wire-wrapped bundle, together with TRACE predictions using the different single-phase correlations (here, the two-phase friction multiplier from Kaiser (Eq. 3.60) has been used throughout). The results present the pressure difference between level -2 and level 11 of the test section (see Fig. 4.3a), corresponding to a total length of 1590 mm. It can be seen that there are relatively large differences in the calculated results already at the single-phase stage (up to 50 mbar difference between Baxi-DD and Rehme models). After boiling onset, a small reduction of the velocity leads to strong pressure drop increase.

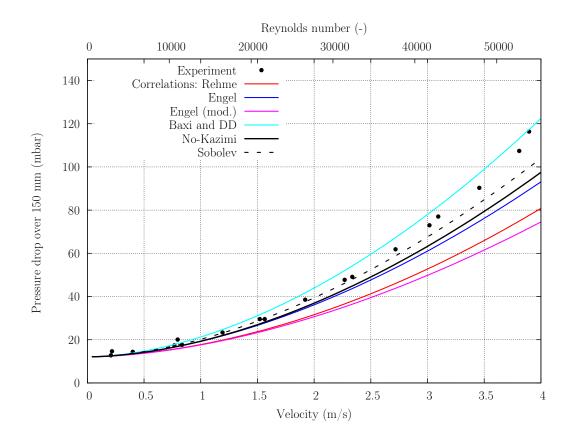


Figure 4.8. Comparison of models for computation of the single-phase pressure drop over one axial pitch of the spacers (150 mm) in the wire-wrapped bundle ($q = 95.5 \text{ W/cm}^2$, $T_{in} = 550^{\circ}\text{C}$)

This is well predicted by all correlations, and one can say that the overall trend of the pressure drop characteristics is well reproduced by all the considered single-phase models.

Then, the sensitivity study of the results to the two-phase multiplier models is shown in Fig. 4.9b. Here the results at 144 kW, obtained with the different multiplier models, presented in Eqs. 3.56 - 3.60, are shown while using the Baxi-DD model throughout for the liquid-to-wall friction factor (Eq. 3.43). The differences between the calculated results are considerably smaller than in the case of the single-phase correlations. The two-phase multiplier is seen to only slightly influence the slope with which the pressure increases when the velocity is reduced.

In order to assess the quality of the different sets of correlations $(f_{l,1\phi}, \phi_l^2)$ in a quantitative manner, the various experiments with different heat flux values (corresponding to 15, 12, 9, 6, 5, 4, 3, 2, 1 kW/pin, i.e. 117, 95, 72, 48, 40, 32, 24, 16, 8 W/cm²) have been analyzed, the measurements being compared in each case with TRACE predictions using different combinations of the physical models for $f_{l,1\phi}$ and ϕ_l^2 . The inlet temperature was held at 550°C during the different tests. Table 4.3 shows the mean absolute error $\bar{\varepsilon}$ and the absolute-error standard deviation σ (in mbar) for the different sets of models. The minimum mean error and standard deviation values for each physical model appear in bold font, the absolute minimum being marked in red. It can be seen that the Baxi-DD model gives the smallest mean absolute error, independently of the multiplication factor ϕ_l^2 . Although, overall, the standard deviations are lowest for the modified Engel model, the values are quite similar for all model combinations, and it is difficult to make a clear recommendation from this point of view.

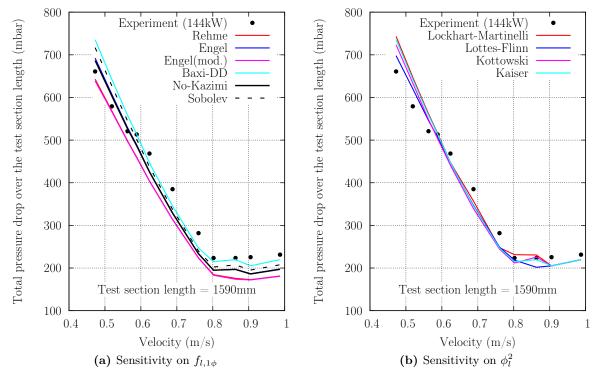


Figure 4.9. Sensitivity of the two-phase pressure drop on the different models (The Kaiser model is used throughout for ϕ_l^2 in (a), while the predictions shown in (b) are all based on the Baxi-DD model for f_l).

Table 4.3.	Quantitative estimation of the quality of the physical models for different
	$(f_{l,1\phi}, \phi_l^2)$ combinations (absolute values in mbar)

	Rel	nme	Liquid-ph Engel Engel(mod		*	e correlation Baxi-DD		No-Kazimi		Sobolev		
ϕ_l^2	$\overline{\varepsilon}$	σ	Ξ	σ	$\overline{\varepsilon}$	σ	ε	σ	Ξ	σ	Ξ	σ
LM LF Kot Kaiser	49.7 52.2 58.8 49.8	$\begin{array}{c} 49.5 \\ 44.4 \\ 51.6 \\ 50.8 \end{array}$	$34.2 \\ 45.0 \\ 44.0 \\ 34.8$	53.1 45.0 49.8 56.2	52.8 53.9 65.2 53.3	47.7 44.6 46.8 48.9	3.7 -1.3 15.0 11.4	$59.4 \\ 64.0 \\ 57.7 \\ 55.1$	$32.4 \\ 46.5 \\ 43.7 \\ 41.2$	53.4 43.6 52.3 49.9	26.8 39.4 33.1 31.2	$56.3 \\ 45.2 \\ 55.8 \\ 56.1$

Figure 4.10a presents a comparison of the experimental pressure drops and the calculated results, obtained using the Baxi-DD model in combination with the Kaiser correlation. One sees a large scatter on the single-phase results (blue points), while the prediction of the two-phase pressure drop values (red dots) is significantly better.

Grid-spaced bundle

The quality of predictions of the local loss coefficient K across grid spacers, for both singleand two-phase flow, has been assessed on the basis of the Ispra experiments using the 12-pin grid-spaced bundle (Fig. 4.3b).

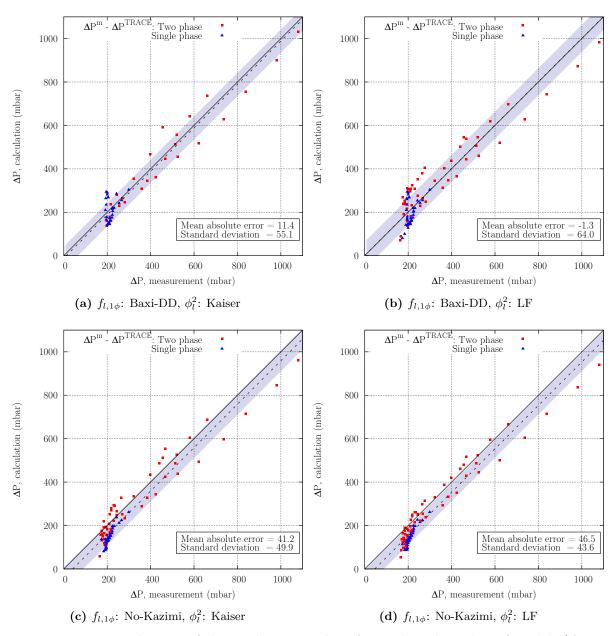


Figure 4.10. Predictions of the total pressure drop for a selected number of models $(f_{l,1\phi}, \phi_l^2)$ vs. experimental data

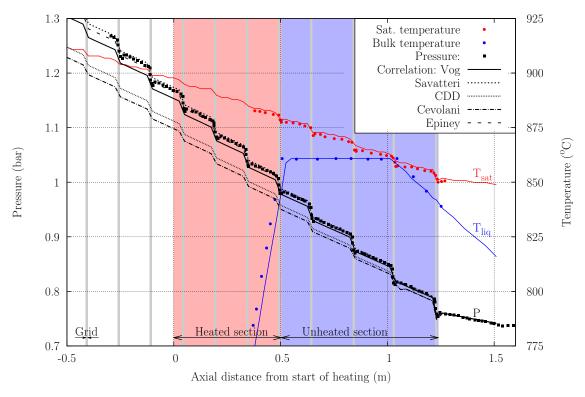


Figure 4.11. Axial variation of pressure, and bulk and saturated temperatures for single-phase flow: comparison of experimental data (points) with TRACE calculations (lines) using different models for prediction of the grid pressure loss coefficient K

Single-phase flow

In order to minimize the uncertainties due to the liquid-to-wall friction model, specific to the grid geometry, the friction losses in the bundle have been calculated using Eifler's recommendations for the Ispra experiments [Eif80]. These are based on the parallel-plate relation in the case of laminar flow:

$$f_L = \frac{96}{Re} \tag{4.5}$$

and on the following empirical relation for fully developed turbulent flow:

$$\frac{1}{\sqrt{\frac{f_T}{8}}} = 0.88 \left(\frac{1}{x}\ln(Re) + B - 4.43\right) \tag{4.6}$$

where the parameters x and B depend on the bundle characteristics (x = 0.413 and B = -0.45 for the considered geometry). Over the whole range of Re, i.e. from laminar flow to fully developed turbulent flow, the following friction factor can be used:

$$f = \left(1 + \min\left(\frac{Re}{2000}, \frac{2000}{Re}\right)\right)^{1/3} \frac{f_L \frac{2000}{Re} + f_T \frac{Re}{2000}}{\frac{2000}{Re} + \frac{Re}{2000}}$$
(4.7)

As mentioned, the use of this correlation enabled one to minimize the uncertainties due to the liquid-to-wall friction model, and thus to focus on the local pressure drop correlations. Figure 4.11 presents the axial pressure variation calculated with the different physical models, for the maximum power (32 kW/rod) with $\dot{m}_{in} = 1$ kg/sec, $T_{in} = 560^{\circ}$ C and $P_{out} = 0.74$ bar. The calculated saturated and bulk sodium temperature profiles (using the Savatteri model for K, Eq. 3.49) are also presented for comparison with the experimental data. The relative plugging value used here is $\epsilon = 0.31$, as specified by Savatteri. Using this value, one can see that the Savatteri and Epiney models give the best predictions of the pressure profile. However, in their analysis of the same experiments, Wall et al. [Wal86] reported a flow area of 551.25 mm² and 371.65 mm² in the bundle and across the grid, respectively, which gives a relative plugging value of $\epsilon = 0.326$. Using these data, the Vog and Epiney models are found to fit the experimental data exactly, whereas the Savatteri model slightly overestimates the pressure loss (+35 mbar at the test-section inlet). Then, considering that the CDD model was recommended for round and not sharp edges, an attempt has been made to adjust the grid solidity in a suitable manner. It has been found that using $\epsilon = 0.375$ yields predictions in good agreement with the experimental data.

From this analysis, it has been found that the Epiney model (Eq. 3.52) is much less sensitive to the assumed relative plugging than the other models, which is of interest since this design parameter is sometimes difficult to estimate. It can also be concluded that the recommended correlation enables one to reliably predict the pressure drop across grids in sodium flow.

Two-phase flow

Using the Savatteri model with a relative plugging value of $\epsilon = 0.31$ for the liquid-phase local friction factor, the pressure drop for two-phase flow has been calculated using the models presented in Eqs. 3.64 and 3.65. Figure 4.12 shows the measured and calculated flow characteristics for different power values in the 12-pin grid-spaced bundle (18, 15, 12, 9 W/pin, i.e. 143, 117, 95, 72 W/cm²). In each case, the local two-phase pressure drop has been calculated by multiplying the single-phase local pressure drop by the slip model multiplier (Eq. 3.65), and the Kaiser correlation has been used for the two-phase frictional pressure loss. It has been found that the results are most sensitive to the local single-phase pressure drop and that, after onset of boiling, to the rate at which the inlet velocity is decreased.

From this analysis, one can conclude that the slip multiplier gives satisfactory results for prediction of the two-phase sodium pressure loss in grid-spaced pin bundles.

4.1.3 Conclusions from this study

This section was devoted to the study of pressure drops in sodium flow. More specifically, it reports on the analysis of a selection of models for the prediction of (i) single-phase friction in wire-wrapped bundles (f_l) , (ii) the grid-spacer loss coefficient K, and two-phase multipliers for (iii) two-phase friction and (iv) two-phase grid-spacer pressure losses (ϕ_l^2 and Φ , respectively). The predictability of the selected models has been evaluated on the basis of experimental data for single- and two-phase pressure losses for sodium flow in tubes and 12-pin bundles, as a function of the inlet velocity under quasi steady-state conditions.

It appears that the Kottowski correlation (Eq. 3.59), derived on the basis of the same experimental data as used currently, does indeed appear to be the best model for predicting the pressure drop in round tubes. However, the Kaiser correlation (Eq. 3.60) – originally obtained from test data on sodium boiling in a pin bundle – yields results of comparable quality. One may thus conclude that this model is satisfactory for sodium flow in both tubular and pin-bundle geometries. From the present study, one can also recommend use of the Lockhart-Martinelli correlation (Eq. 3.56), since it predicts the experimental data quite well, even though it is based on steam-water measurements.

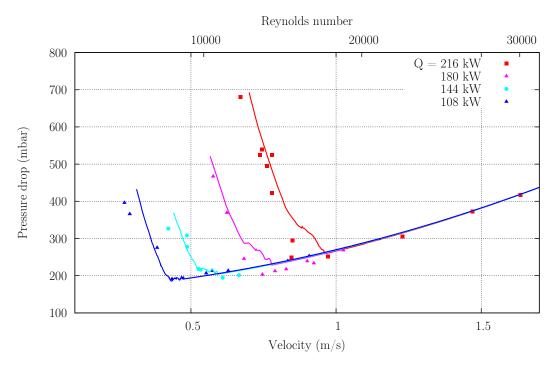


Figure 4.12. Single- and two-phase flow characteristics in the grid-spaced bundle for different power values. Comparison of experimental data (points) with TRACE calculations (lines)

For the Ispra 12-pin wire-wrapped bundle, the study of single-phase sodium flow has shown that the Baxi-DD (Eq. 3.43) and the Sobolev (Eq. 3.45) models give good predictions of the pressure drop. For the two-phase flow experimental data, it appears that the predictions are more sensitive to the single-phase friction factor than to the two-phase multiplier. Quantitative estimation of the quality of the different models has indicated that, independently of the twophase friction multiplier, the Baxi-DD model gives the lowest absolute error for the predictions. In fact, all the considered friction factor correlations (Eq. 3.40 to 3.45) fit the test data reasonably well. For the two-phase multiplier, although as mentioned there is no large sensitivity indicated, the Kaiser correlation (Eq. 3.60) is confirmed to be quite satisfactory.

The study of sodium flow in the Ispra 12-pin grid-spaced bundle has shown that the Savatteri (Eq. 3.49), Vog (Eq. 3.48) and Epiney (Eq. 3.52) models all enable one to well reproduce the test data. However, due to its lower dependency on the assumed grid solidity, the Epiney model appears to be the best for sharp-edged grid spacers. The two-phase flow study has demonstrated that, also in this case, the friction pressure drop is more sensitive to the single-phase friction factor than to the two-phase friction multiplier. Furthermore, it has been shown that use of the slip multiplier (Eq. 3.65) for the two-phase local pressure losses across grids yields satisfactory predictions.

4.2 Analysis of dryout in pin bundles

Cooling limits are reached when the liquid film on the rods of a pin bundle begins to break down. This phenomena, which represents a significant loss in the cooling efficiency, is referred to as dryout. Since dryout can lead to the melting of the structures, the conditions of cooling limits are of prime importance from the point of view of reactor safety.

Despite the technological difficulties of carrying out thermal-hydraulics experiments in rod

	SIENA (PNC)	Ispra	KfK	CEA	UKAEA
Number of pins	37	12	7&37	19	19
Spacers	Wire	Wire and grids	Grids	Wire	Grids
Heat flux distribution	Uniform and chopped cosine	Uniform	Uniform and chopped cosine	Uniform	Chopped cosine
Number of dryout tests	28 (2 test series)	13 (2 test series)	2&1	1	5

Table 4.4. Review of dryout experiments in rod-bundle geometries [Kot94]

bundles at high temperatures, there has been a number of dryout studies in liquid-metal flow performed in the 1980s. Table 4.4 gives a summary of the experiments in rod bundles for which sufficient details are available to make further analysis possible. All of them use sodium as the working fluid. Specific details relative to the SIENA and KfK experiments are given in Appendix B.

In order to assess the capability of the extended TRACE code to predict dryout and the subsequent increase in the cladding temperature, the experiments performed at the Ispra research center with the 12-pin bundles have been simulated with the new tool. Since wire spacers are used in actual SFR designs, emphasis has been placed on the wire-spaced bundles. Among the six tests performed for the investigation of dryout in each test section [Sav86, Sav88b, Sav89, Kot91], one representative test for the long wire-spaced bundle, and one for the short, have been analyzed in detail and are presented in the remainder of this section.

4.2.1 Description of the experiments and phenomenology of dryout in sodium flow

The experimental test sections used are the Ispra 12-pin wire-spaced bundles described in Subsection 4.1.1 (Fig. 4.3a), with their main characteristics given in Table 4.1. During the tests, the bundle inlet velocity was decreased stepwise, the inlet temperature, outlet pressure and added power being kept constant. Steady-state boiling was established prior to the dryout tests. With stable boiling established near to dryout, only a small flow reduction was necessary to run into dryout itself. After detection of irreversible dryout, the power was switched off and the inlet flow rate increased in order to avoid damaging the heaters.

Following the interpretation of dryout measurements in the different test-sections, Kottowski *et al.* concluded that the dryout mechanism is best exhibited by the temperature, void and pressure evolution. From the cladding wall temperature and pressure noise measurements, the authors observed three main stages [Kot91]:

- 1. formation of dry spots (hot spots) and rewetting; this pattern is very sensitive to mass flow and heat flux disturbances;
- 2. onset of non-rewetting dryout with slow growth of the dry zones;
- 3. permanent dryout with the consequence of immediate burnout (fast temperature rise, leading to clad melt).

Depending on the flow reduction from the stable boiling state, one of the following consequences was observed: rewetting of dry spots, slow growth of the dryout spots, or immediate permanent dryout. The tests showed that, especially for low heat fluxes ($< 200 \text{ W/cm}^2$), dryout starts with

rewettable hot spots in a developed two-phase environment, before this runs into permanent dryout caused by mass flow or heat flux disturbances. For high heat fluxes, the difference between dryout onset and permanent dryout is reduced significantly, or does not appear at all. Due to these different behaviors, distinction has been made between the low and high power tests (with 71.6 and 143.2 W/cm² heat flux, respectively).

4.2.2 Interpretation of the experimental results [Sav86, Sav89]

Tests with the long wire-spaced test section

Figures 4.13 to 4.15 show the evolution of the most important experimental data of the dryout test run with 71.62 W/cm² heat flux in the long wire-spaced bundle. The boundary conditions were a constant inlet temperature ($T_{in} = 550^{\circ}$ C), cover gas pressure ($P_s = 0.824$ bar) and bundle power (9 kW/pin). Before going into dryout, steady-state boiling was established for a long time. For low mass flow and low power, the pattern observed shows that the lower front of the boiling zone oscillates irregularly over the whole volume of the heated bundle and that bubbles propagate down as far as to the beginning of the heated zone. The measured axial temperatures for steady-state boiling are shown in Fig. 4.13. The mass flow was decreased stepwise to reach dryout.

Figure 4.14a shows that dryout starts in various regions of the saturated part of the bundle and then propagates. In this test, dryout was first detected at level 6. Figure 4.14b shows the simultaneous start of dryout on the different heaters at level 7. It has been experimentally observed that dryout starts from one spot and expands uniformly across the whole cross-section of the bundle.

The history of the wall and bulk temperatures, when approaching permanent dryout, is shown in Fig. 4.15. Small variations are observed in the bulk temperature, which could indicate a droplet flow, whereas the temperature measured near to the housing corresponds to the temperature of a liquid film on the wall. The void measurements indicate, with reducing mass flow, a change from slug to droplet flow and, with further flow reduction, an impoverishment of droplets in the bulk flow. This simultaneously corresponds to the appearance of rewettable dry spots, as observed from the local wall temperature at dryout onset. With small disturbances in mass flow or heat flux, these rewettable dry spots change to real, permanent dryout. This change of flow regime can also be observed from the dynamic pressure registration, viz. the local pressure oscillations (which are typical for regular boiling) attenuate and the pressure becomes stationary long before dryout.

In summary, the detailed analysis of the experiments suggests that in the case of slowly growing dry spots (observed at low power only), annular flow with droplets in the vapor stream is the predominant flow pattern. At high heat fluxes, rewettable hot spots do not appear, and permanent dryout occurs immediately. This observation is illustrated in Fig. 4.16, which shows the wall temperature history during the test with 143.2 W/cm² heat flux (18 kW/pin).

Tests with the short wire-spaced test section

Similar experiments were conducted in the short wire-spaced test section. The boundary conditions were identical to those indicated earlier ($T_{in} = 550^{\circ}$ C and $P_s = 0.824$ bar). The results for low and high power test conditions (71.6 W/cm² and 143.2 W/cm², respectively) are presented in Fig. 4.17.

Compared to the case of the long test section, large differences are observed in the experimental results. This is mainly due to the design differences, which provide a large flow area at the end of the heated section. The change in the cross-section, from pin-bundle configuration

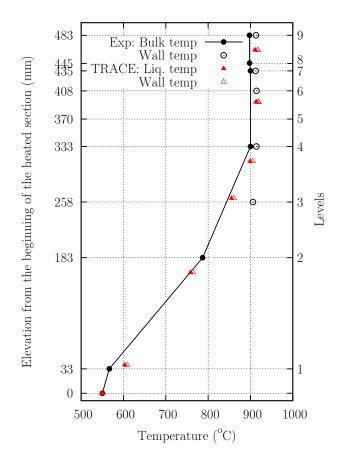


Figure 4.13. Temperature pattern for steady-state boiling

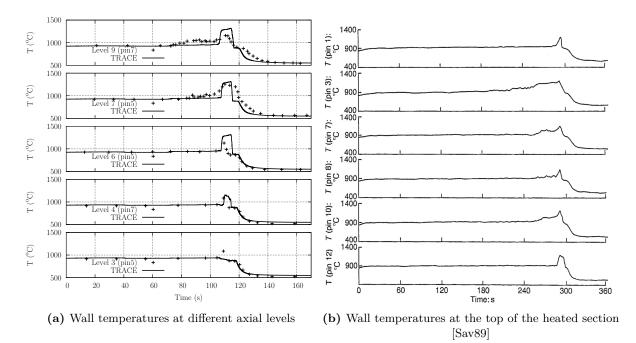


Figure 4.14. Wall temperatures at different axial level and in different heaters for illustration of the dryout propagation

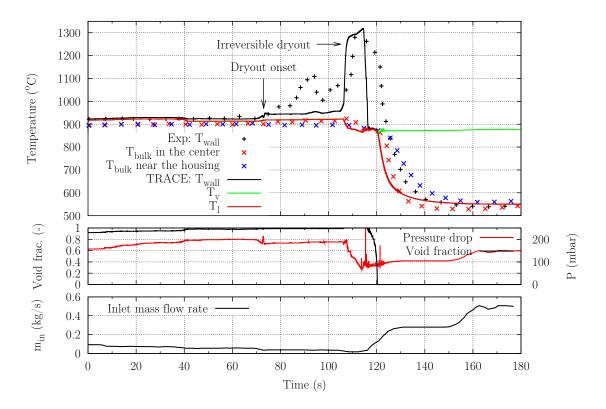


Figure 4.15. Temperature, void fraction, pressure drop and mass flow history when approaching dryout at the end of the heated section of the long-wire spaced bundle at low power (71.6 W/cm^2)

to free-flow area, is by as much as a factor of 2.3 (496.5 mm^2 to 1153.98 mm^2), which leads to a considerable pressure recovery. As direct consequence, even during steady-state boiling, vapor condenses at the top of the bundle causing cavitation, which influences the boiling and dryout pattern. Unlike in the long test section, the rewettable hot-spot pattern is observed also for high heat fluxes. In these conditions, dryout seldom occurs at the end of the heated section.

4.2.3 Analysis of the experiments with TRACE and sensitivity study

The described experiments have been simulated with the extended TRACE code to assess the validity of the implemented models for sodium two-phase flow analysis, with a particular emphasis on the wall-to-fluid heat transfer mechanisms and the dryout criterion. Results of the TRACE calculations are presented, along with the experimental measurements, in Fig. 4.13 -4.17.

In the long test-section, the calculated axial temperature profile for steady-state boiling matches very well with the experimental data (see Fig. 4.13). In particular, the results in the saturated part of the bundle (levels 4 to 9) show that the saturation temperature, and hence the pressure, is well predicted by TRACE. It should be mentioned that the presented results were obtained using the best-estimate set of implemented models for sodium boiling, viz. the SABENA models for the interfacial transfer mechanisms and the Kaiser correlation for the friction two-phase flow multiplier.

The presented experiments have been used to develop a dryout criterion that would allow an accurate prediction of the post-dryout regime for the different test conditions. As mentioned in Subsection 3.4.4, considering the previous work on sodium two-phase flow modeling, a cri-

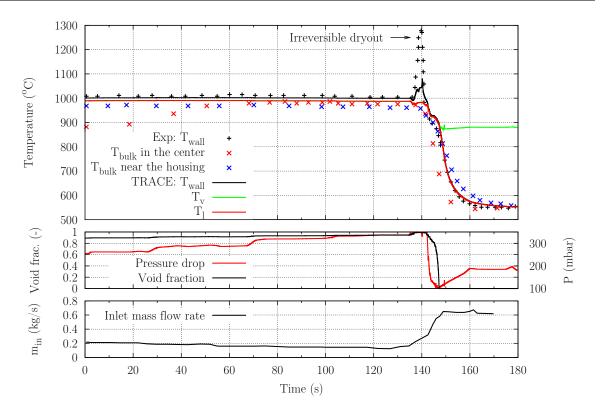
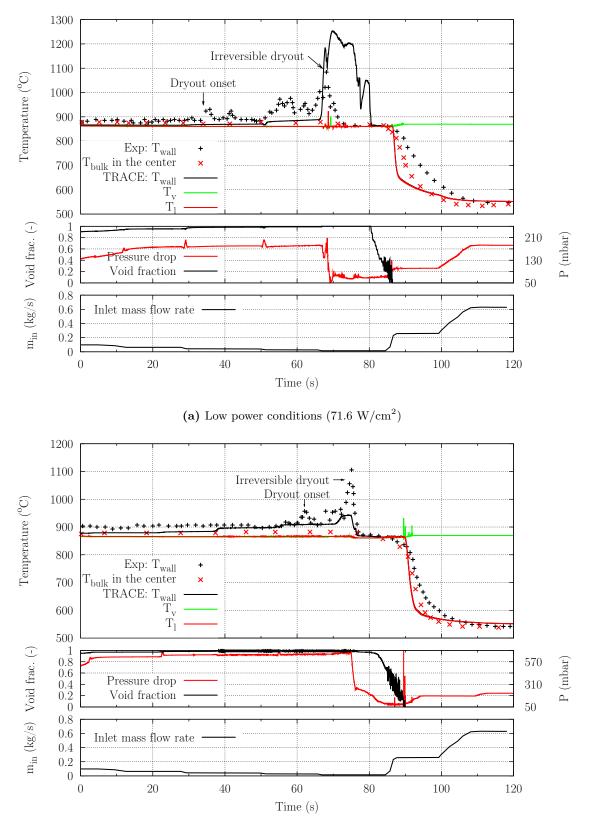


Figure 4.16. Temperature, void fraction, pressure drop and mass flow history when approaching dryout at the end of the heated section of the long-wire spaced bundle at high power (143.2 W/cm^2)

terion based on local boiling conditions (and more specifically on the void fraction and vapor quality) has been considered in TRACE. Figure 4.18 shows the sensitivity of the calculated wall temperature on the parameters a_0 and b_0 defined in Eq. 3.30, which defines the fraction of the liquid film in contact with the wall, from the annular flow to the single-phase vapor regime. The results show that the wall temperature is more sensitive to the void fraction parameter than to that based on the vapor quality. This is particularly true in the case of the short bundle. On the basis of the comparison with the experimental data, the values of $a_0 = 0.5$ and $b_0 = 1.5$ have been considered as appropriate for the proposed model.

Figure 4.14a shows that, using this correlation, TRACE can accurately predict dryout at the different bundle elevations in the long test section under the low-power test conditions. The increase in the wall temperature is predicted from levels 4 to 8 at the same time as that at which permanent dryout was observed. This is also shown in Fig. 4.15 which presents the evolution of the calculated wall and liquid temperatures, void fraction and bundle pressure drop (between levels 7 and -2). A detailed analysis suggests that TRACE predicts only a slight increase in the wall temperature (which corresponds to the experimental dryout onset), followed by an immediate increase in the wall temperature for very high void fractions ($\alpha > 0.995$). After dryout, the bundle pressure drop decreases due to the decrease in the frictional pressure drop. Considering the experimental observations, a more accurate simulation between dryout onset and permanent dryout would require taking into account the droplets in the vapor stream to allow the modeling of the rewetting of hot spots.

Similar results are presented in Fig. 4.16 for the high power test. In these conditions, TRACE can well predict the increase in the wall temperature and onset of permanent dryout.



(b) High power conditions (143.2 W/cm^2)

Figure 4.17. Temperature, void fraction, pressure drop and mass flow history when approaching dryout at the end of the heated section of the short-wire spaced bundle

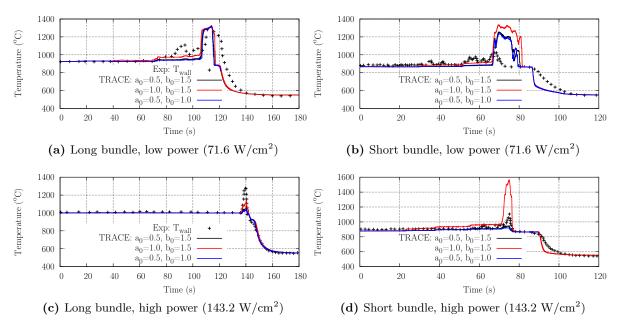


Figure 4.18. Experimental wall temperature evolution and TRACE simulation results with different a_0 and b_0 values (parameters defined in Eq. 3.30)

It should be mentioned that TRACE uses a porous-media representation of the sub-channel. In other words, the results are averaged over the cross-section area. This would explain why, in the low-power experiment, dryout is first predicted at the end of the heated section – level 7 (instead of level 6 in the measurement), where all the pin temperatures increase simultaneously (see Fig. 4.14b) – and why the predicted increase of the wall temperature is lower than in the experiment at high power. For a more detailed simulation, a sub-channel code would be needed.

Figure 4.19 presents the calculated axial profiles of void fraction, equilibrium vapor quality, pressure and wall temperature of the heaters, in the long and short bundles, for the low power conditions. It can be seen that, with imposed constant pressure at the bundle outlet, the pressure at the end of the heated section in the short test section is lower than that in the long test section, since the friction pressure losses in the open channel are lower than within the bundle. Thus, the calculated saturation temperature is lower and TRACE does not predict the condensation of vapor observed in the experiment in this zone.

The results of the calculations for the short test section, for low and high power conditions, are presented in Fig. 4.17. The low power results have been obtained for a total power of 81 kW, which corresponds to 9 working heaters (this accounts for the heaters that failed during the experimental program). A similar behavior as in the long test section can be observed, i.e. that TRACE does not allow one to model the rewetting of hot spots at dryout onset but predicts the permanent dryout and the corresponding increase in the wall temperature.

This analysis has enabled us to investigate the sensitivity of the dryout criterion presented in Eq. 3.30 and show that the considered correlation satisfactorily predicts the different tests considered here. Further verification, including the simulation of the complete set of Ispra tests and dryout experiments in different geometries, would be required for full validation of the proposed model. However, it is worth noting that this criterion has been set up on the basis of steady-state boiling near to dryout, with very small variation of the inlet flow rate. Therefore, one can assume that this criterion would be conservative for fast loss-of-flow transients since,

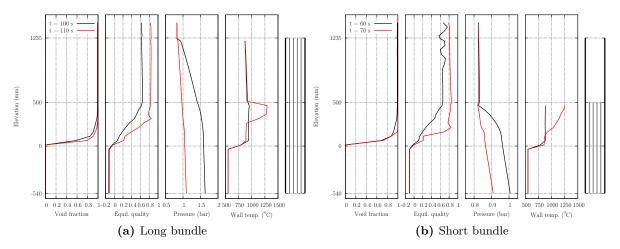


Figure 4.19. Calculated axial profiles of the void fraction, equilibrium vapor quality, pressure and wall temperature of heaters, just before and after dryout onset for low power conditions (71.6 W/cm^2)

for the same flow rate, the vapor quality would be lower under transient conditions than for steady-state conditions.

4.3 Simulation of sodium boiling under loss-of-flow conditions

In a sodium-cooled fast reactor, sodium boiling can be expected following an unprotected lossof-flow (LOF). For further validation of the new tool under transient conditions, experiments simulating a LOF under reactor conditions have been selected. The considered sodium boiling experiments were carried out in the 1980s at the Kernforschungszentrum Karlsruhe (KfK) in Germany, using out-of-pile test rigs with electrically heated pins in hexagonal wrappers simulating a fast reactor subassembly [Kai78, Bot90, Hub82b]. The experimental work simulated typical unprotected loss-of-flow accidents from the start of the flow rundown to the onset of dryout, via boiling inception. Three particular tests, representing different experimental conditions, have been analyzed currently. The reference sodium boiling test employed, i.e. Test L22, is being described here in greater detail. This test was also used in 1984 as basis for an international benchmark exercise [Hub88, Kot94], aimed at testing codes describing liquidmetal thermal-hydraulics processes in fuel rod bundles under nominal and accident single- and two-phase conditions. The representative codes qualified in this exercise were: BACCHUS-3D/SP/TP [Bot87], BACCHUS-Eb [Bas84], CAFCA-Na2 [Oli84], SABENA 3D [Nin90] and SABRE-3C [Mac84].

One- and two-dimensional analyses have been carried out with the extended TRACE code. The reference test has also been analysed with SIMMER-III to better understand the limitations of the 1D model. Both the experimental data and SIMMER results have been used as a basis for providing insights into the modeling of two-phase sodium flow with the extended TRACE code.

4.3.1 The KNS test facility and 37-pin bundle test section

The KNS loop

The Kompakter Natriumsiede-Kreislauf (KNS; German for *compact sodium-boiling loop*) facility [Hub76] is presented in Fig. 4.20a. This sodium loop was designed for boiling tests with a heated rod bundle operating under thermal-hydraulics conditions similar to those of sodium-cooled fast reactors. Different test sections (single pin, 7- and 37-pin bundles) were tested in the loop. The experiments described below [Bot90, Hub82b] simulated the flow rundown characteristics of the SNR-300 sodium-cooled fast reactor [Heu73] using a 37-pin bundle geometry.

In a typical experiment, the flow through the test section was controlled by the pump speed and by valves V1 and V3, which were also used to adjust the pressure losses and bypass flow. At the test section outlet, the "cold" bypass flow mixed with "hot" test section flow, prior to entering the sodium/sodium heat exchanger with a designed (maximum) power of 1.2 MW. The energy produced in the test section was thus transferred to the secondary circuit before the flow went to the pump tank. The latter, with its free surface, simulated a reactor upper plenum. The flow rundown characteristic being an essential feature of the experiment, it was adapted to that of SNR-300 by adding a supplementary gyrating mass to the pump motor, which varied from test to test. For every transient and, from the beginning of the transient to the onset of boiling, this characteristic could be approximated by the function:

$$\frac{\dot{m}}{\dot{m}_0} = (1+at)^{-b} \tag{4.8}$$

where \dot{m} is the mass flow rate, and a and b are the parameters given in Table 4.6. The transient was initiated by a pump trip at time t = 0.

The 37-pin bundle test section

The 37-pin bundle (Fig. 4.20b) represented the main features of an SNR-300 fuel subassembly. The pins of 6 mm o.d. were installed with a 7.9 mm pitch, and were surrounded by a hexagonal wrapper 50.6 mm wide and 2.7 mm thick. They were supported by honeycomb spacer grids of 15 mm high and were electrically heated with a sinusoidal power distribution similar to that of the SNR-300. This could be approximated by:

$$\frac{\chi}{\chi_{max}} = 0.38 + 0.62 \sin\left(\pi \frac{z + 25}{900}\right) \tag{4.9}$$

where χ is the pin linear power and z the distance (in mm) from the bottom of the heated section. The maximal allowed axial rod power, χ_{max} , was 320 W/cm. Different initial power levels were investigated experimentally to simulate the behavior of subassemblies at the center and edge of the SNR-300 core, at both nominal and partial power levels. The pin geometry, as also the heated and upper unheated lengths (the latter simulating the upper breeder zone), were identical to those of the SNR-300 fuel element. The main geometrical data of the test section are given in Table 4.5, together with those of an SNR-300 fuel assembly for comparison. Because of the experimental restrictions, the lower (unheated) part of the test bundle was shorter than that in the reactor. The corresponding, missing frictional loss was compensated by a throttle valve (V2), and the coolant inertia by an equivalent pipe length at the test section inlet.

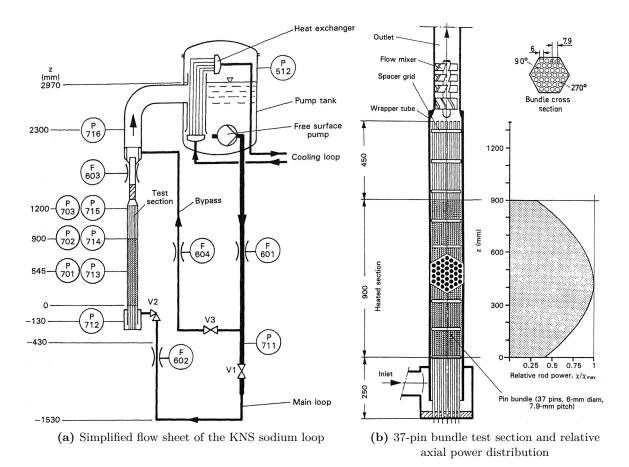


Figure 4.20. The KNS sodium boiling facility (adapted from [Bot90])

	KNS	SNR-300
Number of pins	37	169
Pin diameter (mm)	6	6
Pin pitch (mm)	7.9	7.9
Heated length (mm)	900	900
Unheated lengths (mm)		
At inlet	200	1070
At outlet	450	450
Flow area (cm^2)	11.7	47.3

Table 4.5. Geometrical parameters of the KNS pin bundle and the SNR-300 fuel assembly[Bot90]

Test No.	L22	L26	L29
Linear peak power χ_{max} ; see Eq. 4.9 (W/cm)	215.4	140.2	216.7
Initial coolant flow rate (kg/s)	3.41	2.24	3.41
Initial coolant velocity (m/s)	3.38	2.22	3.38
Inlet coolant temperature (°C)	380.0	382.2	391.2
Pump rotational speed (\min^{-1})	2706	1789	2711
Parameter <i>a</i> ; see Eq. 4.8 (s^{-1})	0.3003	0.1297	0.1943
Parameter b ; see Eq. 4.8	1.2970	2.118	1.3099

 Table 4.6.
 Specifications for the LOF experiments in the KNS loop

Test selection criteria, parameters and procedure

As mentioned earlier, three different LOF tests have currently been selected to assess the new computational tool. Since all experiments with boiling and dryout show similar results, the test L22, most completely described, has been used as the reference test for providing detailed comparisons with calculational results. Tests L26 (reduced power) and L29 (slower transient) have been used to study the influence of different test parameters on the boiling process. Table 4.6 gives the main characteristics of the experiments considered in this thesis.

The test procedure can be described in terms of two steps. The first step was to set the initial steady-state conditions, e.g. power, flow rate, inlet temperature and pressure drop. The second step started with switching-off of the pump, which was followed by flow decrease, temperature increase, boiling and dryout. The heater power was automatically switched off shortly after dryout, in order to avoid damaging the pin bundle.

4.3.2 Description of the reference test L22

The reference test L22 simulates a LOF accident in a 37-pin bundle, with thermal-hydraulics conditions similar to that of a SNR-300 fuel element at the periphery of the core at full power. The initial mass flow rate in the test section was 3.41 kg/s, the velocity 3.38 m/s, and the coolant temperature at the test section inlet/outlet was $380/539^{\circ}$ C, respectively. The average linear pin power was 215 W/cm, which corresponds to a total test section power of 0.72 MW. The normalized inlet flow rate measured in the experiment is presented in Fig. 4.21a, time t = 0 being the start of the flow rundown. The first main event is the onset of boiling at 6.11 s at a normalized mass flow rate of 25.2%. Onset of dryout was detected at 9.25 s when the mass flow rate decreased to 3.8 %. Power was automatically switched off at 9.45 s, 0.2 s after dryout onset. The characteristic signals during boiling, including pressure and wall temperature, are shown in Fig. 4.22. Figure 4.21b shows the radial and axial expansion of the boiling region, measured with either temperature or void sensors installed over the height of the test section at the bundle center, as well as at the bundle periphery (subassembly SA 1 and SA 6, respectively).

Four characteristic phases of the two-phase sodium flow (indicated in Fig. 4.22) can be distinguished from the experimental data. First, the nucleate boiling period (phase I, starts at 6.11 s) is characterized by fluctuations of the flow and static pressure signals. Boiling begins at the upper end of the heated section, in the center of the bundle, where the coolant temperature is the highest. The boiling region then radially propagates from the center to the periphery, where the coolant temperature drops near the relatively cold wall of the test section and, in the axial direction, extends predominantly downwards in the heated section. During the first phase, pressure and flow rate are not very different from those before boiling (Fig. 4.22). Once boiling has reached the relatively cold, close-to-wall coolant layer, the fluctuations of the mass flow rate

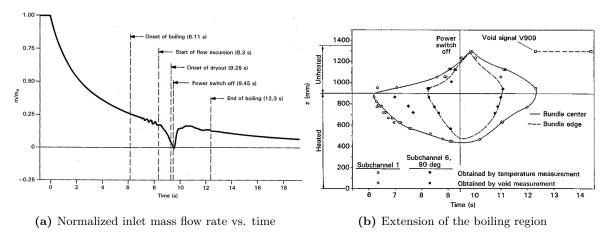


Figure 4.21. Experimental signals measured in test L22 [Bot90]

and pressure start to change into oscillations. This oscillatory boiling regime (II) starts at 6.91 s. One of the most remarkable features of the first two regimes is that the static pressure does not significantly increase with development of the two-phase flow. The increase in the hydrostatic pressure, due to axial two-phase pressure losses in the boiling region, is compensated by the pressure decrease due to buoyancy as a result of boiling, as well as by the decrease in the single-phase pressure drop due to flow reduction. During this phase, the vapor has a significant radial motion. Consequently, there is a dominating radial energy transport (with condensation of the vapor) to the surrounding close-to-wall subcooled liquid.

Once the boiling region reaches the test section wall, the direction of the vapor flow expansion changes from mainly radial to axial, since the condensation area in the radial direction is strongly reduced. The vapor-bubble "blocks" the whole test-section flow area and, as a result, the two-phase pressure drop increases rapidly and causes the inlet mass flow to sharply decrease (see Fig. 4.22). This phase (III) can be referred to as the pre-dryout period and starts with the onset of boiling in the close-to-wall region, at t = 8.31 s.

The last phase (IV) starts with dryout (at t = 9.25 s), shortly before flow reversal. Dryout is first detected in the bundle center at z = 620 mm and then spreads over the entire heated length of the boiling region. At dryout onset, the heater rod undergoes a sharp rise in temperature. During dryout, the vapor production decreases, causing the pressure rise to stop. The heater power is switched off at t = 9.45 s. Once the power is off, the vapor starts to condense and, at t = 12.3 s, the flow becomes single-phase.

4.3.3 One-dimensional calculations

Despite the strong two-dimensional character of the experiments, a one-dimensional simulation was first performed in order to evaluate the performance of a 1D simulation of the considered transients.

Computer models used for simulation

The selected experiments were simulated with the newly developed sodium two-phase flow capabilities of the TRACE code, using the optimized set of options defined from the steady-state validation study (Section 4.1). The complete loop was described in TRACE with 1D components, using a 5 mm axial mesh for the test section, and the transient flow was simulated with decreasing pump rotational speed. The heat exchanger was assumed to remove as much

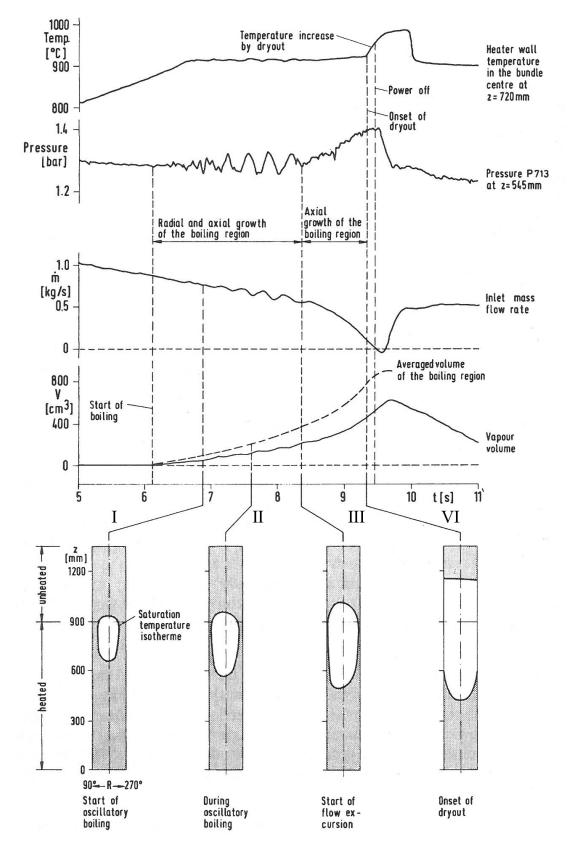


Figure 4.22. Evolution of typical signals during boiling and schematic of boiling extension in test L22 (adapted from [Kot94])

power as the heater produces in the bundle and, accordingly, the temperature in the pump tank was imposed as constant, the heat exchanger thus being simulated simply via this boundary condition. A constant coolant pressure was also imposed in the pump tank. A local hydraulic resistance was added in the downcomer pipe to simulate the throttle valve.

The same experiments were also simulated with SIMMER for enabling additional benchmarking of the extended TRACE. In this case, only the test section was simulated (with a 1D model), the flow rundown test data being used to provide the inlet boundary conditions.

A study of the influence of the geometrical parameters on the flow rundown characteristics after boiling inception has been used to estimate the parameters for the geometrical and hydraulic resistance characteristics, which are not described in the available literature (the study was done using TRACE to complete the loop representation). First, test section parameters such as the hydraulic resistance of the spacer grids, flow mixer hydraulic resistance, upflow pipe hydraulic diameter, etc., were tuned to reproduce the measured steady-state pressure at the test section inlet and outlet. The pump head was then adjusted, as per the loop flow resistance, to reproduce the test-section inlet mass flow rate.

Parameters such as the downcomer hydraulic diameter and flow resistance have been seen to influence both the single- and two-phase flow rundown characteristics. Moreover, the heat capacity of the test section wall structure, both in heated and unheated regions, has been found to strongly influence the axial temperature profile under transient conditions, as well as the temperature evolution during boiling and condensation.

Single-phase results

Results of the single-phase calculations have provided a useful check on the modeling of both the KNS loop and the test section with TRACE, as well as of the test section modeling and applied boundary conditions with SIMMER. Moreover, the correct representation of the singlephase temperature distribution, especially that prevailing just before boiling inception, is very important as it influences the dynamics of the expansion of the boiling region.

The axial temperature profiles, measured and calculated with both models at steady state and just before boiling, are shown for Test L22 in Fig. 4.23a. It is seen that the latter distribution is characterized by a steep, somewhat S-shaped, increase over the heated length, with a sharp temperature decrease in the upper unheated section. This axial temperature profile was determined essentially by the sinusoidal heat flux distribution, the flow reduction and the heat capacity of the structural material. Thus, the temperature gradient in the unheated part is due to the thermal inertia of the relatively cold structures above the test section, and is strongly dependent on the bundle wall heat capacity and thickness.

The radial temperature profile just before boiling (Fig. 4.23b) is characterized by a central temperature plateau with decreasing temperature values at the edge of the bundle, i.e. towards the wall of the test section. The profile calculated from the TRACE 2D model (described in Subsection 4.3.4) is also represented for comparison with the experimental measurements. The scatter of values on the plateau is assumed to be caused by manufacturing tolerances, and is not reproduced in the simulation. The negative temperature gradient towards the test section wall results from the lower ratio of power to mass flow in the subchannels at the edge of the bundle (the heat losses were negligible). At steady state, the calculated radial profile results in a flat distribution due to the homogenization procedure used in the TRACE porous-medium approximation.

It can be seen that the measured steady-state and transient temperature profiles are very well reproduced with both models. (Although only the 1D results are shown explicitly in Fig. 4.23a, the axial profiles obtained with the TRACE 2D model were found to be very similar).

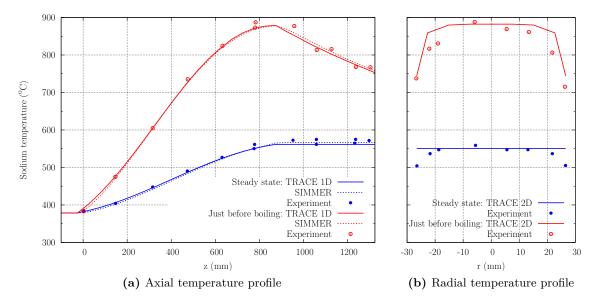


Figure 4.23. Measured and calculated coolant temperature profiles at steady-state and just before onset of boiling in Test L22

Two-phase calculations

The comparisons of experimental and TRACE-calculated results for flow, pressure and void fraction are displayed in Fig. 4.24 for Test L22. The results of the calculation for the singlephase part of the transient are seen to be quite satisfactory and in good agreement with the experimental data. Figure 4.24a shows the inlet mass flow rate, along with the main boiling events. The slight delay in predicting boiling onset in the calculation (see Fig. 4.24c) is mainly due to the averaging of the temperature over the cross-section. Once boiling starts in the calculation, the experimental and calculated results start to differ significantly. The calculated inlet mass flow rate fails more rapidly (Fig. 4.24a), and the calculated pressure rises more sharply (Fig. 4.24b), than measured. Flow reversal is predicted at 7.1 s, compared to the experimental value of 9.4 s. The differences between calculation and experiment can be largely explained by the one-dimensional approximation which has been made: while in the experiment, the vapor expanding in the radial direction condenses in the subcooled liquid zone, there is no possibility to simulate this with the one-dimensional model, in which the vapor blocks the entire crosssection as soon as boiling starts. The corresponding two-phase pressure drop increases, causing an accelerated flow decrease from the very onset of boiling. Thus, with this approximation, the first sodium boiling stage, which corresponds to a radial expansion of the boiling front, cannot be represented and the vapor flow changes directly into the axial direction.

In the simulation, the power was shut down at 7.5 s, as per the experimental criterion (0.2 s after dryout occurrence). This explains the much shorter boiling period seen in Fig. 4.24c.

Two-phase calculations with artificial friction and comparison with SIMMER

In order to enable the comparison of the TRACE computation with experimental data and SIMMER predictions, artificial friction losses have been added in the TRACE model. This allowed the delaying of the axial expansion of vapor so as to reproduce, as much as possible, the flow rundown characteristic. Addition of friction loss upstream to the test section increases the loop hydraulic resistance and makes the fluid motion in the downward direction more difficult.

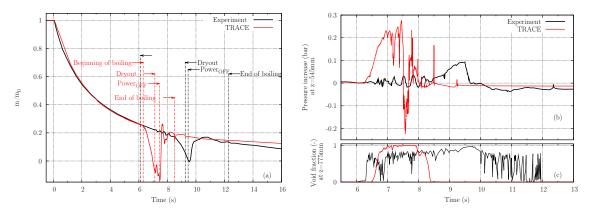


Figure 4.24. Comparison of measured (a) mass flow rate, (b) pressure and (c) void fraction with TRACE 1D results for Test L22

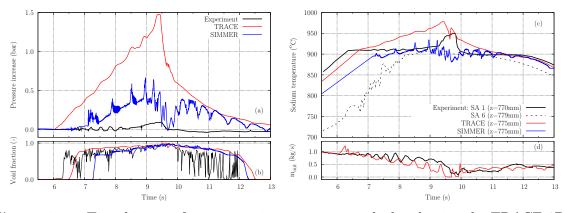


Figure 4.25. Time history of representative parameters calculated using the TRACE 1D model with artificial friction during boiling, compared to the corresponding experimental data: (a) pressure increase from beginning of boiling, (b) void fraction, (c) coolant temperature and (d) outlet mass flow rate.

Consequently, the capability of a vapor bubble to expand in the axial direction is moderated, and the sharp mass flow decrease is smoothened. This artifice, that enables one to delay the flow excursion and "fit" to the experimental inlet mass flow rate (see Fig. 4.26), does not prevent pressure from increasing at boiling onset. Such an artificial compensation has not been necessary in SIMMER, where the experimental flow rundown characteristic is provided in terms of the inlet boundary conditions. Once the flow rundown characteristic was reproduced in the above manner, TRACE results could be compared to the other data. Figure 4.25 compares the results of both TRACE and SIMMER simulations with the experimental data for the pressure, void fraction, coolant temperature and outlet mass flow rate. Characteristic features of the transient are summarized in Table 4.7.

From Fig. 4.25a, one sees that a higher increase in pressure is observed with TRACE, as compared to the SIMMER computation, and even more compared to experimental results. This is, at least in part, due to the artificial addition of extra friction losses in the TRACE model, which increases the corresponding loop hydraulic resistance. Clearly, one needs to be particularly careful in performing one-dimensional analysis, and it is necessary to be aware of the limitations induced by the approximations made.

	Experiment	TRACE	SIMMER-III
Boiling start (s)	6.11	6.17	7.30
Coolant velocity at boiling start (m/s)	0.87	0.90	0.74
Dryout onset (s)	9.25	9.30	9.00
Power swith-off (s)	9.45	9.45	9.45
Duration of two-phase flow (s)	6.2	9.8	8.2

Table 4.7. Experimental and computed data for L22 KNS LOF experiments (1D model)

 Table 4.8. Experimental and TRACE computed results for the three KNS LOF experiments (TRACE 1D model with artificial friction)

	Test L22		Test L26		Test L29	
	Exp.	Calc.	Exp.	Calc.	Exp.	Calc.
\dot{m}_{inlet}	3.41	3.41	2.24	2.24	3.41	3.41
$t_{0.5}$	2.35		3.0		3.5	
$t_{\rm Boiling \ begin}$	6.11	6.17	8.52	8.18	7.91	7.84
$t_{\rm Flow\ reversal}$	9.43	9.44	11.04	10.87	11.99	-
t_{Dryout}	9.25	9.43	12.17	10.63	11.91	11.97
$t_{\rm Power off}$	9.45		12.44		12.10	
$t_{\rm Boiling\ end}$	12.32	16.46	15.32	23.25	14.32	18.11
$\Delta t_{\rm Boiling}$	6.21	10.35	6.80	15.07	6.41	10.27

The experimental results for the coolant temperature clearly show the two-dimensional character of the flow, with the temperature gradient between the inner and outer subchannels. Taking into account the fact that the calculated fluid temperature is averaged over the crosssection, it can be seen from Fig. 4.25c that the SIMMER results reproduce the experiment very well. The temperature increase in the TRACE computation is linked to the pressure evolution explained above. Nevertheless, the general trend is well reproduced, especially at the beginning and end of boiling. Results for the void fraction show the capability of the new model to predict boiling onset (Fig. 4.25b). Compared to experimental data, the delay in both models is due to the averaging of the temperature over the cross-section: while in the experiment, boiling begins at the center of the bundle, the overall temperature has to be higher in the 1D model in order to predict void formation.

Comparisons for others tests

As mentioned, two other sets of experimental conditions have been simulated, in addition to the reference test L22. These corresponded to reduced power (Test L26) and a slower transient (Test L29). The artificial friction coefficient was kept constant, as the experiments were performed without altering the throttling conditions of the valves. A comparison of the most representative transient parameters, between experiment and TRACE results, is presented for all the three selected tests in Table 4.8. The flow rundown characteristic, being highly dependent on the boiling process, has been considered as a representative criterion for evaluating the quality of the two-phase flow regime modeling.

Figure 4.26 displays both experimental and TRACE calculated inlet mass flow rates for the three cases. The physical modeling has been identical for all of them. The beginning of

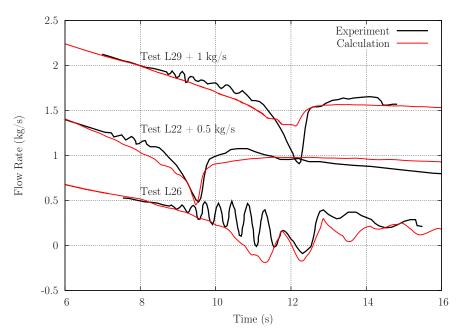


Figure 4.26. Experimental and TRACE calculated inlet mass flow for the different tests using 1D representation with artificial friction.

the transients is not shown here, but it has been seen that the calculated single-phase flow corresponds well to the experimental results. Test L22 is very well reproduced, as detailed in the preceding subsection.

From a general point of view, the variation of the test conditions from those of L22 does not cause significant changes in the course of events during LOF. As mentioned, Test L26 corresponds to a reduced power without altering the valves' throttling conditions. The pump speed was also reduced so as to maintain the same power-to-flow ratio as in Test L22. The comparison of the two experiments reveals a slower flow transient, with much higher-amplitude oscillations during the boiling period and short inlet flow reversals before the onset of dryout. These differences are also reproduced by the simulation, apart from the large oscillations. Test L29 is equivalent to Test L22 but has a slower flow rundown. There is no noticeable qualitative difference in the experimental results compared with those for Test L22. The corresponding computed inlet mass flow rate compares well with the experimental plot, apart from the slight flow reversal, which was not reproduced.

4.3.4 Two-dimensional calculations

In order to benchmark the new, two-phase sodium flow modeling more accurately, as also to study the influence of the closure relations used in the extended TRACE code, the KNS test section has been modeled in greater detail with a two-dimensional representation. The aim thereby has been to enable reproduction of the multi-dimensional aspects of the sodium boiling, the most important being the radial expansion of the boiling front in the early stages.

TRACE representation

The 2D (r-z) vessel component available in TRACE (with porous medium approximation) has been used for the 2D simulation of the test section. The hexagonal assembly has been approximated by a circular channel, with preservation of the total and flow cross-section areas of the test section. The axial meshing was chosen to be the same as in the 1D model. The test section cross-section is represented as a porous medium divided into 4 radial cells for the assembly flow with, respectively, 3, 9, 15 and 10 pins.

Sensitivity study for the interfacial closure relations

Calculations with the different sets of interfacial constitutive relations for area, momentum and heat transfer (as presented in Section 3.4) were first performed to characterize their influence on the TRACE results.

The model using No-Kazimi correlations [No87], as described by Eqs. 3.12, 3.16 and 3.22, was found to lead to a much longer boiling period, i.e. about 20 s compared to 12 s in the experiment.

The Schor model [Sch84] (Eqs. 3.13, 3.17, 3.23), with its simplified representation of interfacial heat transfer, did not give satisfactory results. However, to be consistent with Schor's recommendations, the interfacial mass transfer should have been calculated from gas theory [Sch84] and not from the thermal energy jump relation.

Calculations with the SABENA model [Nin90] have been found to give the best agreement with the experimental data. This model uses a very simple flow pattern, assuming that annular flow is the dominant regime. Then, the interfacial area per unit volume is calculated from Eq. 3.14 and the interfacial friction coefficient from the Wallis correlation (Eq. 3.18). The vapor temperature is assumed to be at the interface temperature (at saturation), with a high vaporto-interface heat transfer coefficient ($a_i h_{ig} = 10^8 \text{ W/m}^3 \cdot \text{K}$). The HTC from liquid-to-interface is given by Eq. 3.24. TRACE results, obtained using this particular set of correlations, have been chosen to be presented in the following. The dryout criterion used here is that based on the thermodynamic quality, as recommended by Bottoni [Bot90].

Comparison of TRACE results with L22 test data

The calculation once again produced good agreement with the experiment for the single-phase part of the transient (see Fig. 4.23). Results during boiling are detailed in Fig. 4.27. Figure 4.27a presents the inlet and outlet mass flow rates for the two-phase flow period, together with the most characteristic times into the transient. Comparison with the experimental data shows the capability of the model to reproduce the flow rundown characteristic quite well. Although the calculated outlet mass flow predicts higher oscillations, compared with the experimental data, the 2D TRACE modeling does reproduce the general trend. Further studies of the physical models should enable improvement of the accuracy.

Boiling onset is predicted at 6.5 s, compared to 6.1 s in the experiment. Immediately after boiling inception, the boiling region expands radially and pressure oscillates around a constant average value (Fig. 4.27b). Figure 4.27c compares the calculated void fraction in the central and peripheral regions of the bundle with the experimental results for the central subchannel. It is seen that boiling inception in the outer subchannel is predicted at t=8 s, i.e. 1.5 s after boiling onset at the center of the bundle. These results show the capability of TRACE to predict and reproduce the radial expansion of vapor during the first stage of boiling. As soon as the boiling front reaches the test section wall, the pressure rises abruptly and the flow decrease is accelerated. In contrast to the 1D model, artificial friction losses were not used in the 2D model and, as a consequence, the predicted pressure evolution is in much better agreement with experiment (Fig. 4.27b), and the start of flow coastdown does not occur earlier (Fig. 4.27a).

Figure 4.28 shows the experimental and calculated axial expansion of the boiling region over time. The TRACE calculation of the two-phase flow region very well reproduces the tendency of void to expand more deeply into the heated (radial direction) than into the unheated (axial

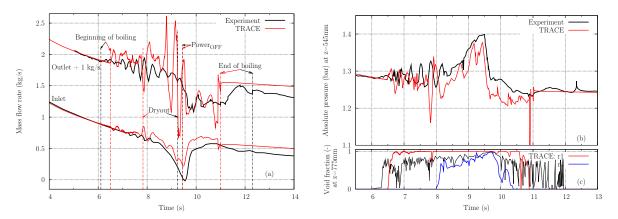


Figure 4.27. Comparison between test data and TRACE results using the 2D model: (a) inlet and outlet mass flow rates, (b) absolute pressure and (c) void evolution

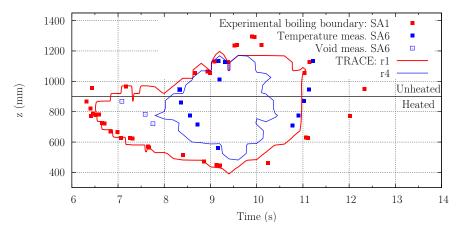


Figure 4.28. Extension of the boiling region in the L22 test: comparison of the test data with TRACE results using the 2D model

direction) part of the bundle during the first boiling stage. In the radial direction, boiling reaches the outer subchannel at ~ 7.8 s, which compares well with the experimental value of 8.3 s and gives nearly the same time for the two-dimensional expansion of the boiling zone as in the experiment. The downward expansion of vapor also compares very well with experiment. The calculated duration of 4.5 s for the boiling is ~ 2 s shorter than the experimental value, and the results show a numerical instability at the time of bubble collapse. The sensitivity study for the different interfacial closure relations, described briefly in the previous section, has shown that the prediction of boiling collapse is very sensitive to the correlations used in the model.

It should be mentioned that, in these calculations, regions with x > 0.8 have been assumed to be dryout regions for the evaluation of the wall-to-coolant HTC. This value is much higher than that recommended by Bottoni (x > 0.3) [Bot90] and has been chosen, somewhat arbitrarily, on the basis of the calculated results for the clad temperature.

Comparisons for others tests

Also for the other two KNS tests, i.e. L26 and L29, the SABENA set of interfacial correlations was found to yield the best results for the two-dimensional TRACE simulations. With the inlet mass flow rate and the pressure evolution being highly dependent on the boiling process,

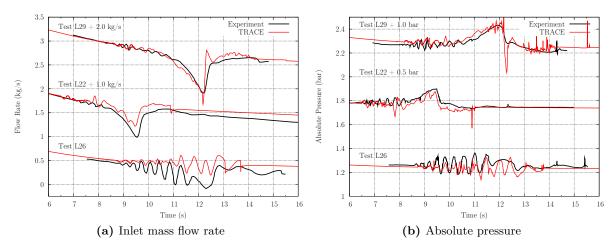


Figure 4.29. Experimental and TRACE results during boiling, using the 2D model for the different tests

these parameters have been considered as representative criteria for evaluating the quality of the two-phase flow modeling. The corresponding comparisons of the calculated results with experimental data during boiling are depicted, for all three tests, in Fig. 4.29. The beginning of the transients is not shown here, the single-phase calculations corresponding well to experiment in each case.

It is seen that, for each of the three sets of experimental conditions, the general features of the transient are reproduced quite well with the extended TRACE code, the prediction of the pressure variation being somewhat more accurate than that of the inlet mass flow rate. The two-dimensional model enables one to reproduce the different phases characteristic of sodium boiling: the increase in pressure is only predicted once the boiling region reaches the wall of the test section and not just after boiling inception, as is the case with the one-dimensional model. It has been found that the numerical instability at the time of bubble collapse is very sensitive to the physical models used.

4.3.5 Conclusions from this study

The simulations have shown the limitations of the one-dimensional approximation, where there is no possibility to model condensation of the vapor expanding radially into the outer subcooled region of the bundle cross-section. In a first approach, addition of artificial friction losses enabled one to limit the axial expansion of the boiling region, thus making possible the comparison of the results with the experimental data. In this situation, the TRACE computed void fraction was found to compare well with both the test data and 1D SIMMER calculations. Both 1D models predicted the increase in pressure and the flow excursion immediately after boiling inception, somewhat overestimating the test data in each case.

Considering the multi-dimensional character of boiling in these experiments, a 2D model of the test section (with porous medium approximation) was developed. Using different models for the interfacial closure relations, we could confirm the conclusions drawn from the steady-state boiling experiments presented in Section 4.1. The sensitivity on the different interfacial closure relations showed that parameters such as mass flow rate, pressure and boiling duration are indeed quite dependent on the physical models used. The calculated results have been found to compare very well with experiment when assuming, as approximation, a simplified flow regime map (with dominant annular flow), together with the correlations used in the SABENA code for representing the interfacial exchange mechanisms during the two-phase flow. The 2D simulations have thus demonstrated the ability of the extended TRACE code to predict, with reasonable accuracy, boiling inception, void fraction, radial and axial expansion of the boiling region, pressure evolution, coolant and clad temperature, etc.

In future, the KNS experiments should be used to further validate the dryout criterion developed on the basis of quasi steady-state experiments as presented in Section 4.2. Also, this study has highlighted the need to further study the physical models applied for the condensation phase.

4.4 Conclusions

This chapter has presented the validation of the extended TRACE code, for the simulation of sodium single- and two-phase flow, through the comparison of TRACE results with test data in different geometries and flow conditions.

The two-phase flow characteristics of the Ispra tubular test section have enabled one to study the influence of the interfacial and wall-to-fluid closure relations. It has been shown that the calculated results are very dependent on the physical models. A sensitivity analysis, using the different models presented in Chapter 3, has permitted definition of the most appropriate set of correlations. The calculated results have been found to compare very well with experiment when assuming a simplified flow regime map with dominant annular flow, together with the correlations used in the SABENA code for representing the interfacial exchange mechanisms and the Kaiser correlation for the computation of the wall-to-fluid friction factor during the two-phase flow.

These models have also enabled one to satisfactorily predict the pressure drop in bundle geometry when selecting appropriate models for the simulation of the different spacer types (wire-wrapper or grid). The study revealed that, in the two-phase regime, the calculated results are more sensitive to the models representing the spacers for computation of the single-phase friction than to correlations used for the two-phase friction multiplier. Both the single- and twophase flow pressure drops have been accurately predicted in the different considered geometries, demonstrating the capability of TRACE to accurately simulate sodium boiling under quasi steady-state conditions.

For validation beyond dryout, a set of experiments used to investigate dryout in sodium flow was selected and successfully simulated with the extended tool, demonstrating the code's capability to predict dryout onset. Also, the increase of wall temperature beyond dryout was satisfactorily predicted by TRACE. This study highlighted the high sensitivity of the results to the post-dryout models used and the resulting need for an accurate modeling. Further validation work for a wider range of conditions is recommended in this context.

Finally, sodium boiling under reactor conditions during a loss-of-flow transient has been successfully simulated using the models defined previously. Comparisons of TRACE results with a selected set of experiments have demonstrated the applicability of the physical models to accurately predict sodium boiling in similar-to-reactor conditions during LOF.

In summary, the presented simulations have demonstrated the ability of the extended TRACE code to predict, with satisfactory accuracy, boiling inception, void fraction, radial and axial expansion of the boiling region, pressure evolution, coolant and clad temperature, etc. Further validation of the two-phase sodium modeling in TRACE is still needed in the post-dryout regime and during condensation. This can be achieved through the simulation of complementary experiments, using different test sections and experimental conditions, e.g. some of the experiments described in Appendix B.

CHAPTER **C**

Validation of TRACE and PARCS using Phenix reactor test data

S IMULATION of the Phenix reactor's primary circuit, as described in the present chapter, represents a considerable increase in the complexity of the investigated system. This has effectively enabled a validation of the FAST code system under reactor conditions. Thereby, different aspects have been considered. The first one integrates simulation of the core neutronics, the objective being an in-depth understanding of the core response to external perturbations. The second one, purely thermal-hydraulics, focuses on the simulation of the sodium single-phase flow in the primary circuit.

Details about the Phenix reactor, complementary to the information given in Chapter 2, are provided in Section 5.1. Experimental data acquired during the Phenix end-of-life tests have been used for the current validation. In particular, data from the Natural Convection (NC) test have been applied. This test, described in greater detail in Section 5.2, essentially consisted of two parts, viz. (i) a relatively short unprotected phase, with the core responding to a loss of cooling in the tertiary circuit, and (ii) a longer phase, following manual reactor shutdown and tripping of the primary and secondary pumps, in which natural convection was established in the primary pool. The latter part – involving purely thermal-hydraulics phenomena, as mentioned above – has been analyzed using TRACE, and the results are presented in Appendix C. The focus in the present chapter is on analysis of the first, unprotected part of the NC test.

In order to study the core behavior during the unprotected part of the transient, different models of the Phenix core, viz. a simplified point-kinetics model and a coupled thermalhydraulics/3D-kinetics model, have been developed in TRACE and with TRACE/PARCS, respectively. Section 5.3 presents the analysis with the point-kinetics model developed in TRACE. This has enabled one to understand the different phenomena taking place during the transient. In particular, the decomposition of the reactivity feedbacks and a sensitivity analysis have revealed the pertinent effects contributing to the core response and their relative importance. The phenomena that need to be accurately modeled have been identified.

The 3D model has been developed, first, for a more detailed analysis of the transient and, more importantly, for the explicit validation of TRACE/PARCS coupled thermal-hydraulics/ neutronics analysis using reactor experimental data. Though the coolant remained in the liquid phase throughout the transient, the test data are very valuable for benchmarking the coupled calculational tool, which will later be used for analysis of the SFR core response in accidental situations (in Chapter 6). Section 5.4 describes (1) the different steps followed for the preparation of the inputs, (2) the validation of the TRACE/PARCS model for steady-state conditions, using ERANOS static calculations and Phenix experimental data, and (3) the TRACE/PARCS validation for the transient using the NC test data.

The conclusions from the various analyses are presented in Section 5.5.

5.1 Description of the Phenix reactor

A brief history of the development of the Phenix reactor was given in Chapter 2. The present section describes the Phenix primary circuit and core characteristics, in terms of information complementary to that provided in Section 2.2.

5.1.1 Phenix reactor circuits

The Phenix reactor is an integrated pool-type reactor – the core, primary coolant pumps and intermediate heat exchangers (IHXs) being located in the same vessel. Figure 5.1 presents an axial cross-section of the reactor block. The main vessel is 10 m high and 12 m in diameter, and holds \sim 800 tones of sodium, which provides the system with a high inertia. The core is suspended at the slab forming the upper part of the reactor block. The hot sodium (560°C) flowing out of the core at \sim 2800 kg/s is contained in an inner vessel. It flows through the IHXs to be pumped from the cold pool (400°C) by the primary pumps that drive it into the diagrid. The diagrid supports all the core SAs and allows an adequate distribution of the flow to the different core regions in relation to the thermal power to be removed from each SA, thanks to different openings at each SA inlet. The diagrid is connected to the main vessel via a conical shell.

Three independent secondary circuits, each composed of two IHXs, provide the transfer of heat from the IHXs to the steam generators (SGs) via an intermediate sodium loop (Fig. 5.2). This sodium is not radioactive, thanks to the neutron shielding surrounding the core. Each circuit contains \sim 140 tones of sodium, flowing at \sim 800 kg/s from the IHXs (where it is heated from 350°C to 550°C under normal operating conditions) to the SGs. The latter are composed of three parts: evaporator, superheater and reheater. The first part provides slightly overheated steam at 375°C, which then exits the superheater and reheater at 512°C. The thermal energy is thus transported as steam from the SG and transformed into electrical power (250 MWe), using a turbo-generator set connected to the electrical grid.

5.1.2 Phenix core

A cross-section of the Phenix core is presented in Fig. 5.3. It consists of 110 fissile sub-assemblies (SAs) surrounded by 86 breeder blanket SAs and a number of steel reflector and neutron shielding SAs, the latter being especially designed to limit the activation of the secondary-coolant sodium in the IHXs. Depleted uranium oxide acts as axial blanket in the lower and upper parts of the fuel pins. The fuel in the active core is composed of (U-Pu)O₂ mixed oxide, with 23% and 28% Pu content at the center and the periphery of the core, respectively. The inner zone is composed of 54 SAs which contain less Pu than the 56 SAs in the outer zone, in order to flatten the power profile within the core. A fuel SA contains ~10 kg of Pu for a total mass of 226 kg. The full core contains a total of ~1 ton of plutonium and generates ~600 MWth, with a neutron flux of ~ 7×10^{15} n/cm²·s at the core center.

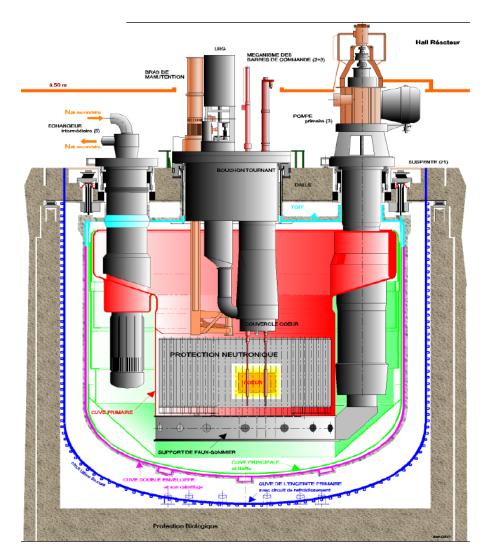


Figure 5.1. Phenix primary circuit [Sau09]

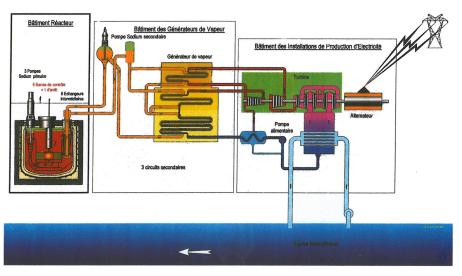


Figure 5.2. Phenix plant: details of the loops [Sau09]

		Fuel	Axial upper	Axial lower	Radial
			blanket	blanket	blanket
Number of pins	-	217	37	217	61
Lattice pitch	cm	12.72	12.72	12.72	12.72
Ext. pitch wrapper tube	cm	12.37	12.37	12.37	12.37
Pellet external diameter	cm	0.542	1.295	0.55	1.215
Clad external diameter	cm	0.655	1.425	0.655	1.34
Spacer wire diameter	cm	0.115	0.386	0.115	0.108
Pins pitch	cm	0.777	1.820	0.777	1.457
Height	cm	85.0	26.2	33.7	164.9
Total height	cm		26	64.9	

 Table 5.1. Characteristics of the Phenix core sub-assemblies [Var09]

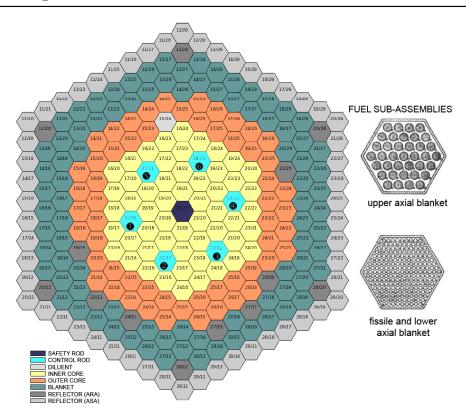
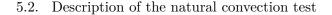


Figure 5.3. Axial cross-section of the Phenix core [Gau10] and details of the fuel SAs [Var09]

Figure 5.4 shows the axial cross-section of the different SAs, and Table 5.1 provides their main design characteristics. Each core sub-assembly is enclosed in a hexagonal steel tube (wrapper), fixed at the bottom to the diagrid.

The core reactivity is controlled by six absorber rods (containing boron carbide pellets), arranged in the inner core. A specific absorber SA, acting as complementary shutdown system, was added at the core center in 1996. The absorber rods are held from the top by control-rod (CR) drives fixed to the slab of the reactor block (see Fig. 5.1).



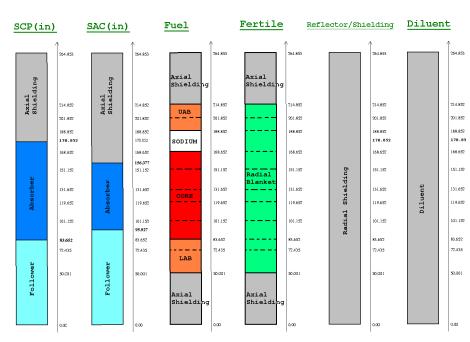


Figure 5.4. Axial composition of the different SAs [Var09]

5.2 Description of the natural convection test

As mentioned in Section 2.2, a series of end-of-life (EOL) tests have been performed in Phenix in order to better understand the core behavior under special operating conditions and acquire test data for the qualification of calculational tools. This section describes the Natural Convection (NC) test [Pia11], which originally aims at studying the establishment of natural convection in the core and further the validation of thermal-hydraulics codes. The acquired data have been used for setting up an international benchmark exercise and studied at PSI in the frame of a Coordinated Research Project (CRP), initiated by the IAEA Technical Working Group on Fast Reactors (TWG-FR). The TRACE analysis (and comparison with experimental results) of the purely thermal-hydraulics part of the test, i.e. the establishment of natural convection, is presented in Appendix C. The analyses presented in the following sections focus on the simulation of the core neutronics during the first 8 minutes of the transient, prior to the reactor SCRAM and pump trips.

From a reduced power state (120 MWth), the NC test was initiated by the dryout of two of the three steam generators in the tertiary circuit, with constant speed of the primary and secondary pumps (see Fig. 5.2 for illustration of the Phenix loops). The deficiency in cooling led to an increase of 40°C of the core inlet temperature. The different reactivity feedbacks induced a decrease of the power down to 40% of the initial value. The reactor was manually shutdown after 458 s, when the difference between the primary and secondary temperatures in the IHXs decreased to 15°C. The three primary pumps were simultaneously tripped (t = 466 s). The main experimental data of interest during this first, unprotected phase of the transient – viz. the inlet core temperature, power and reactivity evolution – are presented in Fig. 5.5.

After the manual trip of the three primary pumps, their rotating speed decreased to zero on mechanical inertia in about 3 minutes. The secondary pumps were tripped simultaneously with the primary pumps, and their rotating speed decreased to 110 rpm. Figure 5.6a shows the average secondary mass flow rate in the IHXs during the complete transient. After the SCRAM,

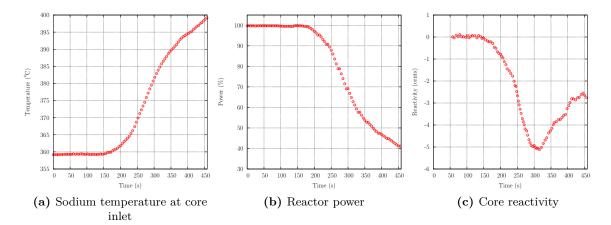


Figure 5.5. Relevant experimental data characterizing the unprotected part of the NC test

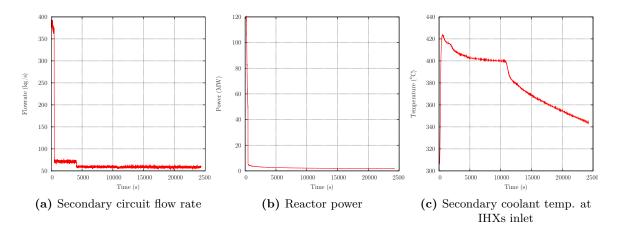


Figure 5.6. Relevant experimental data characterizing the complete Phenix NC test

 Table 5.2.
 Summary of the main events characterizing the Natural Convection test in the Phenix reactor

Tir	ne	Action
	0 s 458 s 466 s 10320 s 24300 s	Dryout of the steam generators SCRAM Primary and secondary pump trips Opening of the two SG containments End of the test

the core power decreased to the decay heat level (see Fig. 5.6b). During the following 2 hours, no action was taken and natural convection established in the core. After 10320 s (1h52min), the containments of two SGs were opened. This allowed air natural circulation to occur in the SG containments and improved the cooling of the intermediate circuit. The evolution of the secondary coolant temperature at the IHX inlet is shown in Fig. 5.6c. Table 5.2 summarizes the main events of the NC test.

5.3 TRACE point kinetics analysis of the Phenix core response to an increase of the inlet sodium temperature

The experimental data obtained from the NC test are of prime interest for the validation of code systems used to analyze sodium-cooled fast reactors such as the TRACE code and, to a larger extent, coupled calculations incorporating detailed 3D kinetics analysis (e.g. TRACE/PARCS). In order to gain a more in-depth understanding of the transient behavior of SFR cores in general, and of the Phenix core in particular, the unprotected phase of the NC test has first been simulated with a TRACE point-kinetics model.

First, the TRACE thermal-hydraulics model representing the Phenix core is described (Subsection 5.3.1). Then, the point-kinetics model developed for the current analysis is presented. Optimization of the kinetics parameters is discussed in Subsection 5.3.2, while Subsection 5.3.3 presents the reactivity feedbacks specific to fast-neutron systems – mainly relative to the various expansion mechanisms – that have been implemented in TRACE to allow a realistic modeling of the core behavior. Following the comparison of the TRACE results with the experimental data (Subsection 5.3.4), a study of sensitivity of the core power and reactivity to the different feedbacks, in order to define their relative importance, is presented in Subsection 5.3.5.

5.3.1 TRACE model of the Phenix core

In the scope of the present analysis, the modeling of Phenix has been limited to the core region. A schematic of the developed TRACE model is shown in Fig. 5.7a. The model consists of four parallel channels representing the different core regions, i.e. inner core, outer core, fertile blanket, and reflector region plus all bypasses. The correct flow distribution was achieved thanks to singular friction losses in the diagrid. A single-node heat structure (HTSTR) was linked to the pipe representing the diagrid to compute the radial expansion. A high exchange area was used in order to ensure that its temperature evolution follows that of the inlet core during transient.

The heated channels were coupled to heat structures. According to the CEA recommendations, 90% of the fuel pins were modeled as linked fuel (with closed gap), the remaining 10% being considered as free fuel with open gap. This corresponds to different gas-gap conductance values, viz. 5000 and 1500 W/m²·K for fuel with closed and open gap, respectively (as recommended by the CEA). A gap conductance of 2500 W/m²·K was used for the blanket pins. The axial power distribution was computed from a 3D static neutronics ERANOS model of the core developed in the frame of a previous study [Ada10], and is shown in Fig. 5.7b. The radial power distribution is indicated in Table 5.3.

Appropriate boundary conditions were defined at the core inlet and outlet in order to reproduce the correct core state. The mass flow rate and temperature evolution were specified at the core inlet with the FILL component. The nominal core outlet pressure was fixed via the BREAK component (1.6 bar at the bottom of the hot pool).

Local friction losses have been used to reproduce the correct core gagging and obtain a realistic flow rate distribution in the different regions of the core. The core pressure drop specified in the CRP -1.955 bar - was successfully reproduced at nominal state (which corresponds to a power of 360 MWth with an inlet flow rate of 1200 kg/s). Table 5.3 shows that the flow rates and temperatures calculated by TRACE at reduced power (120 MWth) satisfactorily reproduce the experimental data. This state corresponds to the reactor operating conditions prior to the NC test.

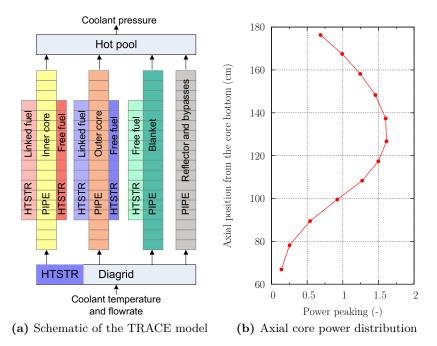


Figure 5.7. Schematic of the TRACE core model and axial power distribution for 0D analysis

	Power	Mass flow (kg/s)		Temperature (°C)	
	(MW)	Exp.	Calc.	Exp.	Calc.
Inner core	61.7	1055	554	447	446
Outer core	48.8	1055	503	-	438
Blanket	8.2	149	148	-	399
Reflector	1.1	80	79	-	359

Table 5.3. Comparison of TRACE calculated results (Calc.) with the experimental data(Exp.) at 120 MWth

5.3.2 Optimization of the kinetics parameters

The kinetics parameters, viz. the delayed neutron fractions β_i and the corresponding decay constants λ_i for each precursor group *i*, were first calculated from an ERANOS model of the Phenix core developed in the frame of the earlier mentioned study [Ada10]. The computed data have then been optimized such that, when specifying the experimental reactivity, the calculated power accurately reproduces the experimental values. Figure 5.8 shows the optimized kinetics parameters, together with CEA specifications and the values calculated from the ERANOS model. It can be seen that the adjusted set of parameters corresponds to the CEA specifications within 10% (-10% for β_i and +10% for λ_i) and gives an effective fraction of delayed neutron β_{eff} of 292 pcm, compared to 325 pcm as specified by the CEA. In order to minimize the uncertainties due to the kinetics parameters, the optimized set has been used for the sensitivity study on the different feedback coefficients presented hereafter. A prompt neutron life time of 0.38 μ s was used throughout the analysis.

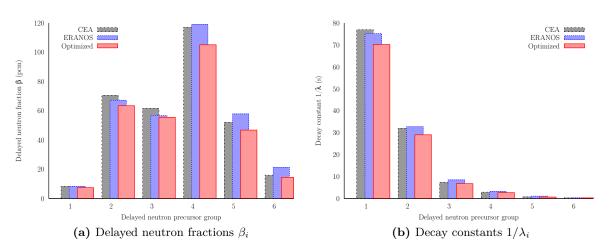


Figure 5.8. Comparison of different sets of kinetics parameters for the Phenix core

5.3.3 Implemented reactivity feedbacks

Since the TRACE code has been originally developed for the safety analysis of water-cooled reactors with thermal neutron spectra, further models have been added at PSI to allow the accurate simulation of fast-neutron spectrum systems. A decomposition of the reactivity as currently computed in TRACE for the present analysis is given by Eqs. 5.1 to 5.5:

$$\Delta \rho(t) = \Delta \rho_{Doppler}(t) + \Delta \rho_{fuel}(t) + \Delta \rho_{diagrid}(t) + \Delta \rho_{vessel}(t)$$
(5.1)

$$\Delta \rho_{Doppler}(t) = \sum_{i} K_{D_i} \ln \frac{T_{f_i}(t)}{T_{f_i}(0)} \text{ with } i \in \{\text{inner core, outer core, blanket}\}$$
(5.2)

$$\Delta \rho_{diagrid}(t) = K_{rad} \left[T_{in}(t) - T_{in}(0) \right]$$
(5.3)

$$\Delta \rho_{fuel}(t) = K_{axi} \left[\sum_{i} n_i \left(\overline{T_{c_i}}(t) - T_{c_i}(0) \right) + \sum_{j} n_j \left(\overline{T_{f_j}}(t) - T_{f_j}(0) \right) \right] \times \frac{1}{n_{\text{rod}}}$$
with $i \in \text{alogad gap fuel (inper sore outer sore)}$

with
$$i \in \text{closed-gap}$$
 fuel {inner core, outer core}

and
$$j \in \text{open-gap}$$
 fuel {inner core, outer core, blanket} (5.4)
= $K_{\text{rel}}[T_{\text{in}}(t-\delta) - T_{\text{in}}(0)]$ (5.5)

$$\Delta \rho_{vessel}(t) = K_v \left[T_{in}(t-\delta) - T_{in}(0) \right]$$
(5.5)

where ρ is the reactivity and the different K's are the feedback coefficients for the Doppler effect (D), as well as for diagrid (rad), fuel (axi) and vessel (v) expansion. \overline{T} is the volume-averaged temperature over the fuel length, and the sub-scripts f and c refer to fuel and clad, respectively. $n_{\rm rod}$ represents the number of rods, and corresponds to 10546 (10937) pins with closed gap and 1172 (1215) with open gap in the inner (outer) core. δ is the time delay characterizing the vessel temperature response to the core inlet temperature perturbation.

The sodium density effect has been neglected, since its contribution in the Phenix core is very small (-0.018 pcm/°C). An analysis including this effect showed its very small contribution. Moreover, it is compensated by a positive effect of comparable magnitude, viz. the axial expansion of the hexagonal wrappers (0.013 pcm/°C), which was also neglected.

It can be seen from Eq. 5.2 that the Doppler effect has a logarithmic dependency on the fuel temperature, corresponding to the fast-neutron spectrum. For a more accurate modeling, a zone-wise Doppler constant has been computed (see values in Table 5.4). In particular, the distinction between the fissile and fertile core regions is of prime importance since the

corresponding average fuel temperatures have opposite evolutions in the considered transient. Figure 5.9a shows the time dependency of the fuel temperatures in the different core zones. The temperatures in the fissile region decrease due to the reducing power, whereas in the fertile core the fuel is heated by the increasing sodium inlet temperature. An increase in the fuel temperature corresponds to a broadening of absorption cross-section resonances, a change which results in an increase in the 238 U capture rate and leads to an insertion of negative reactivity. Figure 5.9b shows the zone-wise contributions of the Doppler effect to the reactivity feedback. It is seen that the inner and outer fissile core regions provide a positive effect, whereas the contribution of the fertile core is negative.

The other effects of interest here result from different expansion mechanisms. The most important feedback in the considered transient is the radial expansion of the diagrid, which causes a negative reactivity feedback when there is an increase of the sodium inlet temperature. The expansion of the diagrid, which supports the core, moves the fuel SAs away from each other, increasing the inter-SA gap and therefore the coolant volume fraction. The introduction of a higher coolant-to-fuel ratio increases the probability of neutron down-scattering around the sodium resonance at 2.85 keV. This results in an increased ²³⁸U capture rate and a reduction of the reactivity [Sun11].

Equation 5.4 details the computation of the reactivity feedback due to the fuel axial expansion. Distinction has been made between the linked and free fuel with closed and open gas-gap, respectively. In the first case, the fuel pellets are considered to be sufficiently irradiated such that the fuel-clad gap has been closed by fuel swelling, and that they have become mechanically linked to the cladding. In this case, the axial expansion is assumed to be driven by the average cladding temperature whereas, for fuel with open gap, it is assumed to be driven by the average fuel temperature. Figure 5.10b shows the axial expansion feedback contributions of the different core regions and fuel types during the considered transient. The average cladding temperatures in the different core regions (cf. Fig. 5.10a) follow the evolution of the increasing inlet temperature, producing a negative reactivity feedback. In the free fuel regions, the reduction of power leads to a decrease of the fuel temperatures (cf. Fig. 5.9a), associated with a positive reactivity feedback. Consequently, it can be noticed that, in the fuel regions, the different fuel types (linked and free fuel) bring opposite contributions to the reactivity, which significantly reduces the overall effect of the fuel expansion in both the inner and outer core. From this point of view, the blanket region contributes the most to the reactivity feedback when considering the fuel expansions. Expansion of the cladding has negligible effect (less than 0.01 pcm/ $^{\circ}$ C) and has not been modeled here.

The last effect taken into account in this study is the vessel expansion. Following the evolution of the core inlet temperature, the vessel is slowly heated up by the increasing temperature in the cold pool. The vessel temperature is assumed to follow the core inlet temperature with a time delay δ [Ber90]. Since the vessel is fixed to the slab at the top of the reactor, and since it indirectly holds the core, an expansion of the vessel will move the core slightly downward. This results in a relative extraction of the control assemblies, which are held by drives fixed to the same slab at the top of the reactor. The relative expansion of the core, vessel and control rods should thus be taken into account accurately in pool-type reactors. In the considered transient, the core outlet temperature remains almost constant (less than 10°C variation). Therefore, in a first approximation, the expansion of the CR drives has been neglected. Taking into account the vessel expansion reactivity feedback enables one to qualitatively reproduce the shape of the reactivity evolution as measured during the test. To illustrate the importance of this phenomenon, Fig. 5.11b shows a comparison between the measured and the calculated reactivity, with and without vessel expansion feedbacks. The time delay δ and feedback coefficient K_v have been determined on the basis of the experimental reactivity ($\delta = 130$ s and $K_v = 0.5$ pcm/°C).

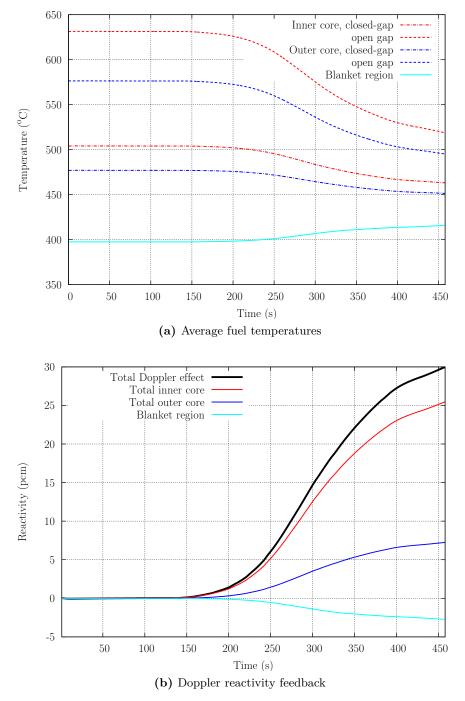


Figure 5.9. Average fuel temperatures and decomposition of the Doppler reactivity feedback among the different core regions

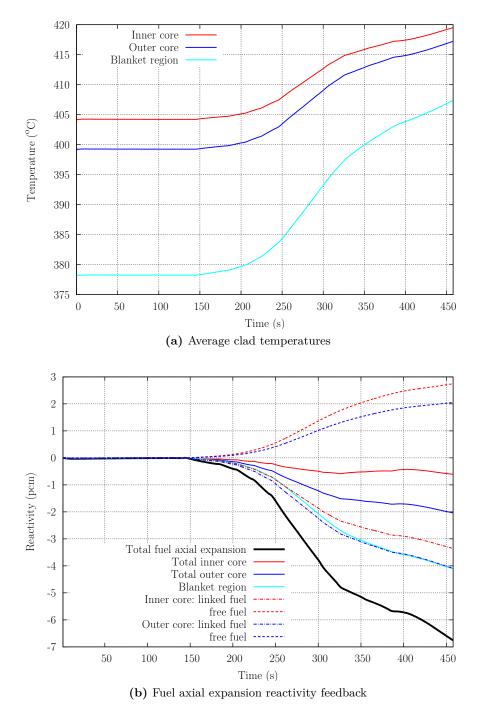


Figure 5.10. Average clad temperatures and decomposition of the fuel axial expansion reactivity feedback in the different core regions

 Table 5.4. Reactivity feedback coefficients of the Phenix core, calculated from ERANOS and used in the TRACE point-kinetics model

Doppler constant K_D : inner core	$-404.7~\mathrm{pcm}$	Diagrid radial expansion	-1.11 pcm/°C
outer core	$-173.7~\mathrm{pcm}$	Fuel axial expansion	-0.72 pcm/°C
blanket region	$-101.0~\mathrm{pcm}$		

The reference values of the feedback coefficients have been calculated from the ERANOS 3D static neutronics model, simulating different core states at 293 and 1000 K. The computed results are given in Table 5.4.

5.3.4 Comparison of the TRACE results with the experimental data

Figure 5.11 shows the power and reactivity evolutions during the transient, as computed from various TRACE calculations, along with the experimental data. The reference calculation (with vessel expansion) corresponds to the solution of the point-kinetics model as described in the former subsection, using the feedback coefficients presented in Table 5.4. The solution without accounting for the vessel expansion is shown in order to illustrate the importance of this reactivity feedback, as discussed previously.

Comparing the TRACE reference solution with the experimental data, it is seen that the power evolution is very well predicted at the beginning of the transient (t<250 s). Then, the calculated reactivity decreases at a lower rate than during the experiment, which results in a slight over-estimation of the power. After t=300 s, the shape of the reactivity evolution is well reproduced, mainly thanks to the vessel expansion modeling.

A third TRACE calculation, called 'best-estimate' results, is also presented in Fig. 5.11. This solution has been obtained considering all the fuel pellets to be with closed gas-gap (instead of the 90% specified by the CEA). As discussed in the following subsection, the calculated reactivity has been found to be very sensitive to the modeling of the fuel. This solution is presented here to illustrate that the TRACE results can very well match with the experimental data while using the defined specifications within a range of $\pm 10\%$. A more complete analysis of the calculated results has been possible thanks to the sensitivity study presented in the following.

5.3.5 Sensitivity analysis with respect to the different reactivity feedbacks

In order to better understand the core response to the increasing core inlet temperature, a sensitivity analysis has been performed with respect to the different reactivity feedbacks. This was carried out assuming 10% variation on each reactivity coefficient, viz. on K_D , K_{rad} , K_{axi} and K_v , as well as on the ratio of linked to free fuel. The reference case was calculated with the values given in the former section. Then, calculations were performed while perturbing each coefficient separately, assuming a variation of +10 or -10%. It should be emphasized that the effects were studied separately. Though this analysis is not as complete as, for example, a sampling technique for the propagation of uncertainties, it has allowed one to identify the most important feedback effects occurring in this transient.

Figure 5.12 presents the power and reactivity evolution obtained for a selection of effects. The 'Doppler' case corresponds to a change of 10% of the Doppler constants K_{D_i} , the 'Diagrid' case to that of the same change of radial expansion coefficient K_{rad} . The sensitivity on the fuel burn-up has also been studied assuming different proportions of linked and free fuel. This is referred to as the 'Gas-gap' case (open or closed), which has been calculated using two

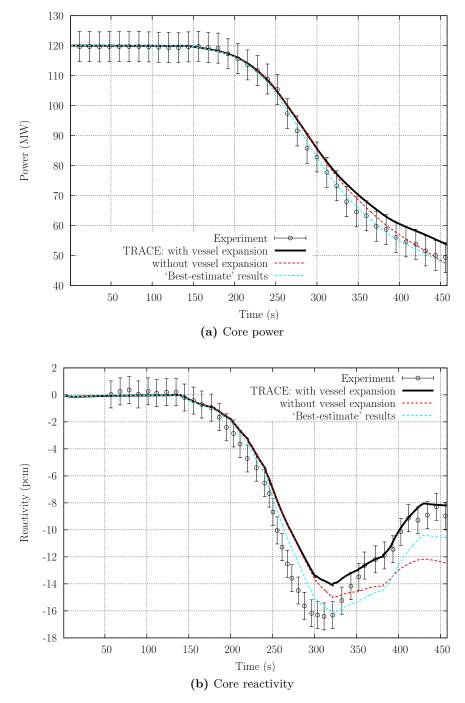


Figure 5.11. Comparison of the calculated and experimental reactivity considering or not the vessel expansion feedback together with the 'best-estimate' TRACE results

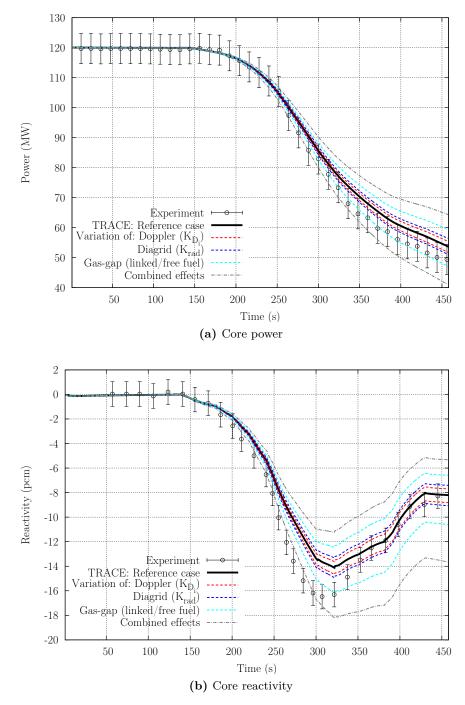


Figure 5.12. Sensitivity of the calculated power and reactivity evolution to variation of different feedback coefficients and comparison with the experimental data

different ratios of linked to free fuel: 100/0% and 80/20%, instead of the specified 90/10%. These changes mostly impact the fuel temperature and the corresponding axial expansions, as well as the Doppler effect. The study has enabled an evaluation of the reactivity changes for different fuel modeling assumptions (as mentioned, the different gas-gap conductance values, corresponding to an open or closed gap, result in different fuel temperatures). The last case presented in Fig. 5.12 corresponds to 'Combined effects' and serves to provide an estimate of the extreme boundaries of power and reactivity variation when combining the variations of the different coefficients. The lowest boundary has been calculated using $K_D - 10\%$, $K_{rad} + 10\%$, $K_{axi} + 10\%$, $K_v - 10\%$ and 100% of linked fuel. The opposite variations have been used for obtaining the upper boundary, with 80% of linked fuel.

Figure 5.13 shows the decomposition of the different reactivity feedbacks. The solid lines correspond to the reference calculation. The dashed lines illustrate the variation range of each effect when perturbing the corresponding coefficient, without showing the impact on the other feedbacks. The combined variation of effects, resulting from the variation of all effects together as specified above, is shown on the total reactivity to illustrate the range of variation due to changes of $\pm 10\%$ of the different feedback coefficients. From this figure, it can be seen that the diagrid expansion is the first effect produced in this transient. It is also the most important feedback. It can be noticed that the time dependency of its contribution to the reactivity almost exactly follows that of the core inlet temperature (cf. Fig. 5.5a). This highlights the importance of an accurate prediction of the core inlet temperature during the transient. The second most important feedback is the Doppler effect, and this is mainly an inner core contribution (see Fig. 5.9b). The fuel axial expansion provides a negative feedback, thanks to the linked fuel – driven by the increasing clad temperature – and the blanket expansion, as detailed in Fig. 5.10b. The decomposition of the fuel axial expansion into the different core regions and its sensitivity to the burn-up (through the variation of the linked/free fuel ratio) has demonstrated the importance of accurately modeling the gas-gap conductance and fuel expansion mechanisms, since, in the considered transient, the linked fuel (expansion of which is assumed to be driven by the clad temperature) brings an opposite contribution to that of the free fuel (assumed to be driven by the fuel temperature). The sensitivity on the fuel thermal conductivity, also influenced by the fuel burn-up, has been studied but is not presented here since this effect has been found to have only a small influence on the calculated value of the reactivity. Finally, the vessel expansion brings a delayed positive contribution opposite to that of the diagrid expansion, due to the relative movement of the core, vessel and control assemblies as discussed in Subsection 5.3.3.

5.3.6 Conclusions from the point kinetics analysis

The increase of 40° C of the sodium core inlet temperature at the beginning of the Natural Convection test leads to a reduction by 60% of the power in the Phenix reactor. The presented point-kinetics model for the prototype fast reactor, developed in TRACE within the FAST project, has enabled us to better understand the core behavior during the considered transient. It has been shown that the diagrid radial expansion provides the first and most important feedback effect in this transient. The increase of the diagrid temperature moves the core SAs away from one another, thus producing a negative reactivity feedback. The resulting power decrease causes a decrease of the fuel temperature, which yields a positive Doppler reactivity feedback. The opposite evolutions of the fuel (decreasing) and clad (increasing) temperatures have shown the need for an accurate simulation of the fuel axial expansion, since burned fuel could bring an opposite contribution to that of fresh fuel – due to closed or open gas-gap, respectively.

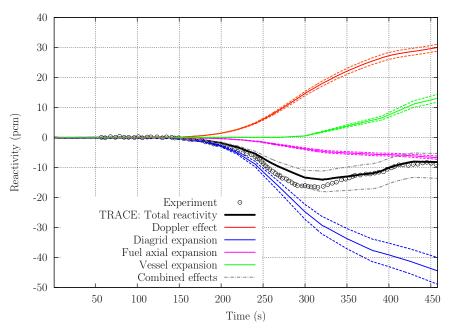


Figure 5.13. Decomposition of the reactivity and illustration of the sensitivity of the different feedback mechanisms to a variation of $\pm 10\%$ on the feedback coefficients

The sensitivity study conducted has enabled identification of the most important effects in the considered transient, namely the diagrid expansion, the Doppler effect and the fuel axial expansion. These have highlighted the need to accurately predict the core inlet temperature, gap conductance and fuel expansion mechanisms.

Finally, the experimental power and reactivity evolution could be satisfactorily reproduced, and the core behavior better understood. As such, the present analysis represents a step towards the in-depth understanding of sodium-cooled fast reactor (SFR) behavior under transient conditions.

5.4 Coupled TRACE/PARCS 3D-kinetics analysis of the Phenix NC test

The unprotected part of the Natural Convection test has also been used for supplementary validation of the FAST code system, viz. of coupled TRACE/PARCS calculations. This coupled model enables a more detailed 3D analysis of the transient. The various experimental data have allowed an in-depth testing of the TRACE/PARCS simulations under both steady-state and transient conditions.

Subsection 5.4.1 presents the successive steps for the development of the 3D coupled thermalhydraulics/kinetics model. Validation of the model, first against ERANOS static calculations, and then against Phenix experimental data at steady state, is discussed in Subsection 5.4.2. The comparison of the results of the transient simulation with the test data is presented in the last subsection.

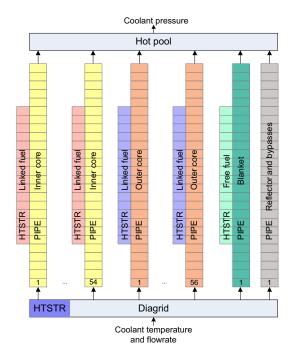


Figure 5.14. Schematic of the TRACE full core model

5.4.1 Development of the TRACE/PARCS model

TRACE full core model

For a detailed 3D analysis of the Phenix core behavior, a full core model has been developed with TRACE. The model is similar to that used for the 0D analysis (Fig. 5.7a), but with a greater degree of detail concerning the modeling of the fuel sub-assemblies. Every single fuel SA has been represented by a dedicated pipe and its associated HTSTR. Consequently, the model now consists of 110 parallel channels and HTSTRs for representation of the 54 inner core SAs and the 56 outer core SAs. This allows one to compute a detailed, assembly-wise power and temperature distribution. The full core model is presented in Fig. 5.14. The SAs in the blanket and reflector region have each been grouped into one single channel, since less detail is needed in these regions. All fuel pins have been modeled as linked fuel with closed gap, using a gas-gap conductance of 5000 W/m²·K. A gap conductance of 2500 W/m²·K was used in the blanket pins. The flow rate was assumed to be the same in every SA from a given core region, so that the gagging was identical for each pipe in the region. The same boundary conditions as those used in the point kinetics analysis have been applied, i.e. imposed inlet temperature, inlet flow rate and outlet pressure.

Table 5.5 shows that the experimental flow rate distribution at reduced power (120 MWth, 1284 kg/s) was well reproduced considering the different core regions. Unfortunately, the experimental assembly-wise flow rate is not available for comparison.

PARCS and ERANOS 3D model of the Phenix core

The Phenix core has been modeled in PARCS [Dow06] in terms of sets of homogeneous computational nodes in hexagonal geometry. The core presented in Fig. 5.3 has been fully described

	Mass flow (kg/s)		Difference	
	Exp.	Calc.	(kg/s)	(%)
Inner core Outer core	1055	$\begin{array}{c} 552 \\ 503 \end{array}$	-0.24	-0.02
Blanket	149	148	-1	-0.67
Reflector	80	81	1	1.25

Table 5.5. Comparison of TRACE calculated results (Calc.) for mass flow with theexperimental data (Exp.) at 120 MWth

with 110 fuel SAs, 86 blanket SAs, 6 CR SAs, 1 safety rod and 3 additional rows of reflector SAs. The nodal scheme is identical to that used in TRACE, the axial mesh size being about 10 cm. Radially, the node size is of the order of the fuel assembly flat-to-flat distance, i.e. 12.7 cm. The core geometry was set up for room temperature conditions. The mesh and dimensions were also chosen to be identical to those defined in ERANOS – or, more specifically, in the 3D nodal code VARIANT [Pal05] – in order to allow a consistent comparison of results for validation purposes (see next subsection).

As presented in Chapter 2, PARCS uses macroscopic cross-sections for a reference state and accounts for the reactivity feedbacks, corresponding to any other given state, by using derivatives of the macroscopic cross-section with respect to state variables (see Eq. 2.7). Currently, five main state variables are taken into account: the fuel temperature, coolant density, thermal radial expansion of the core, thermal axial expansion of the core, and relative position of the control rods.

The reference values for the self-shielded macroscopic cross-sections Σ_0 and the different derivatives for use in PARCS have been produced using the cell code ECCO [Rim02] (part of ERANOS), in conjunction with its fine (1968) energy group neutron data library ERALIB1, based on JEF-2.2 nuclear data and evaluated with NJOY. For each core region, a heterogeneous cell calculation was carried out using 33 collapsed energy groups.

Different core states were simulated to compute each of the cross-section derivatives (see Eq. 2.7). The reference state 'REF', defined for calculation of the macroscopic cross-sections Σ_0 , was chosen to be that at room temperature (293 K). To account for the Doppler effect, i.e. to calculate the derivatives with respect to the fuel temperature, the core simulation was repeated with the fuel temperature changed to 1000 K, all other input values being kept the same (this core calculation will be referred to as 'DOP' in the following). The coolant density reactivity feedback (effectively, the sodium void effect) was computed from a core calculation 'NAD', similar to 'REF', except that the coolant density was set to 777 kg/m³, instead of the reference-case value of 950 kg/m³. As regards the axial expansion effect, this was obtained from a core calculation for room temperature but with axially expanded fuel regions (core state 'AXI'). Finally, the radial expansion effect was obtained through a computation at room temperature but with a dilated, fuel assembly flat-to-flat distance (core state 'RAD'). The total core fuel mass was preserved in all the considered states.

Table 5.6 summarizes the different core states for which macroscopic cross-sections were obtained in order to compute the derivatives with respect to each state variable. The reference macroscopic cross-sections and the corresponding derivatives were then processed from ERANOS into PARCS format using ERANOSTOPARCS.

The six control rods and the safety rod (see Fig. 5.3) have been simulated explicitly in order to allow individual positioning of each CR. Each control assembly (CA) is described with the

 Table 5.6. Description of the core states considered for computing the derivatives of the macroscopic cross-sections with respect to the different state variables

Case	REF	DOP	NAD	AXI	RAD
T_F (K)	293	1000	293	293	293
$ ho_C ~({ m kg/m^3})$	950	950	777	950	950
$\Delta h \ ({ m cm})$	0	0	0	2.197	0
$\Delta p \ ({\rm cm})$	0	0	0	0	0.170

corresponding follower region, the change of cross-sections due to the presence of the absorber being effectively simulated through derivatives. These have been validated against "static" modeling, in which the CA lower region was defined with the follower cross-sections and the upper region with the absorber cross-sections.

Mapping scheme

PARCS has been coupled directly to TRACE, with the latter providing the temperature and density field information to PARCS during the steady-state and transient calculations. This is achieved using an appropriate mapping scheme, linking both the pipe component nodes and the heat-structure nodes to the corresponding neutronics nodes. In order to facilitate the mapping, the nodalization schemes in the PARCS and TRACE models were chosen to be identical. The mapping scheme is specified in an external input deck file and is read by the code during the initialization process. Various tests have been performed to check the adequacy of the mapping scheme, e.g. the positions of individual pipes and control rods have been tracked to control their correct linkage with the neutronics nodes.

5.4.2 Validation of the coupled TRACE/PARCS model

After the verification of the TRACE and PARCS models in stand-alone mode, the coupled TRACE/PARCS (FAST) model has been validated through the comparison of the computational results with, first, reference static ERANOS-2.1 calculations, and then with experimental data from the Phenix reactor.

Validation using ERANOS

Static ERANOS-2.1 calculations have been used to systematically verify the PARCS macroscopic cross-sections and derivatives, as well as the assembly-wise power distribution. The 3D HEX-Z ERANOS core model used for the benchmarking was basically the same one as used earlier for the production of the reference cross-sections and derivatives (Subsection 5.4.1) and developed in a previous study [Ada10]. Effectively, for comparison purposes, the core states listed in Table 5.6 were calculated with both the TRACE/PARCS coupled model and with ERANOS.

It should be noted that the sodium density of 777 kg/m³ chosen for the 'NAD' core state of Table 5.6 corresponds to a sodium temperature of 1000 K. Similarly, the axial and radial expansions considered for the 'AXI' and 'RAD' states simulated in ERANOS correspond to an average fuel temperature and an inlet temperature of 1000 K, respectively. Correspondingly, the TRACE/PARCS model was used in a zero-power mode, using TRACE, to set each temperature to 1000 K.

Case	REF	DOP	NAD	AXI	RAD
$\partial \Sigma / \partial \ln T_f$	Ø	Ξ	Ø	Ø	Ø
$\partial \Sigma / \partial ho_c$	Ø	Ø	Ξ	Ø	Ø
$\partial \Sigma / \ \partial R$	Ø	Ø	Ø	Ξ	Ø
$\partial \Sigma / \ \partial H$	Ø	Ø	Ø	Ø	Ξ
Axial coef.	0	0	0	$c_{\rm axi}$	0
Radial coef.	0	0	0	0	$c_{\rm rad}$

Table 5.7. Description of the input files used for simulation of the different core states with TRACE/PARCS (\emptyset : derivative not present; \exists : derivative included in the input)

 Table 5.8. Comparisons of the effective multiplication factors, obtained with ERANOS and with TRACE/PARCS, for the different core states

	ERA	NOS	TRACI	TRACE/PARCS		
	$k_{ m eff}$	$\Delta \rho ~({\rm pcm})$	$k_{\rm eff}$	$\Delta \rho ~({\rm pcm})$		
REF	1.01674		1.01081			
DOP	1.00821	-853	1.00229	-852		
NAD	1.01680	6	1.01000	-81		
AXI	1.01151	-523	1.00644	-437		
RAD	1.00871	-803	1.00268	-813		
All effe	cts summed			-2184		
All effe	cts together		0.98875	-2206		

In order to carry out the desired comparisons with ERANOS in a systematic manner, different states have been considered. First, the reference macroscopic cross-sections were tested, by removing all the derivatives. With the geometry having been kept constant (by setting the thermal expansion coefficients equal to zero), the effective multiplication factor then obtained essentially corresponded to room temperature, i.e. 'REF' was the calculated core state. Then, each of the derivatives was validated in turn. This was done, case by case, by removing all derivatives from the PARCS input, except the one being tested. Table 5.7 illustrates a summary of the TRACE and PARCS inputs used to simulate the different states.

The results of the code-to-code comparisons carried out in the above manner are given in Table 5.8, together with the comparison of the different reactivity feedbacks. The axial expansion case is only presented for a qualitative comparison, since the two models treat axial expansion differently with respect to control assembly position. Large discrepancies are seen in the coolant effect. Its small contribution in the Phenix core makes it difficult to assess accurately. Apart from these two effects, the reactivity feedbacks are in good agreement between ERANOS and TRACE/PARCS. Is is also noteworthy that, calculating the four feedbacks separately in PARCS, and then summing them, yields nearly the same result as a single calculation with all feedbacks present simultaneously (with all temperatures at 1000 K, $k_{\rm eff} = 0.98875$). This indicates that the linear parametrization of the cross-sections, which assumes independence of the different derivatives, is a good approximation.

It can be noticed in Table 5.8 that the k_{eff} values obtained with TRACE/PARCS, i.e. with the FAST code system, are about 600 pcm lower than the corresponding values from ERANOS, even though both sets of neutronics calculations are based on diffusion theory. The

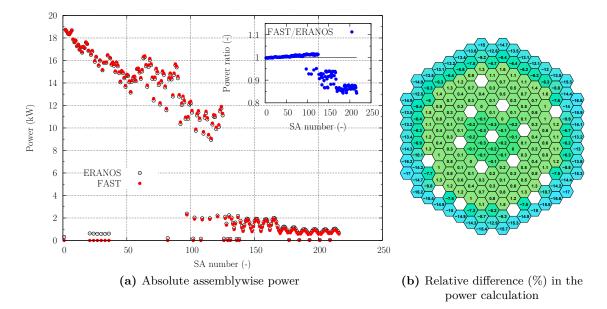


Figure 5.15. Comparison of FAST and ERANOS computed power distributions at 1000K

differences may be attributed, at least in part, to different nodal schemes. VARIANT uses a variational nodal method based on the even-parity form of the transport equation [Pal05] whereas PARCS uses the Triangle-based Polynomial Expansion Nodal (TPEN) method. For an accurate solution, the later method requires discontinuity factors to permit flux discontinuities at the node boundaries [Pou07]. Therefore, the radial heterogeneity of Phenix core (between the fissile and the fertile core) would need to be modeled using assembly discontinuity factors (ADFs), which would enable one to reproduce the discontinuity of the homogeneous flux at the border of two different zones (typically between the outer core and the blanket region) [Smi86]. A brief study using the ADFs in PARCS has shown the sensitivity of $k_{\rm eff}$ on the latter, and further work should be done in this direction for improvement of the code-to-code comparison.

The significant discrepancy between PARCS and ERANOS in the blanket region is clearly seen in the assembly-wise power distribution, presented in Fig. 5.15. The comparison of the computed power distributions shows that PARCS is in very good agreement with ERANOS in the fissile core (SA number lower than 125), with less than 2% differences, but that it underpredicts the power in the blanket SAs by almost 15%. Using a PARCS model with ADFs in the blanket region only, we were able to reproduce an accurate power distribution in the blanket SAs. However, this also resulted in a deformation of the power in the fissile core such that the discrepancies with respect to ERANOS were, overall, larger. Considering that the power generated in the blanket region corresponds to less than 7% of the total power, and that the power distribution in the fissile core is in very good agreement with ERANOS, the present model has been considered accurate enough for application to the transient analysis. A complete model, describing the flux discontinuities in the different radial zones (inner core, outer core and blanket region), would be clearly needed for a more accurate modeling of the Phenix core with PARCS.

Validation using experimental data at steady state

For validation against measurements, results of the TRACE/PARCS computation have been compared with experimental data from the control rod shift (CRS) test [Vas11], which was

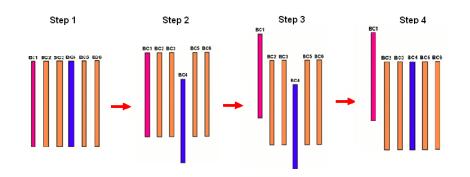


Figure 5.16. Schematic of the control assembly configuration for each of the four test steps

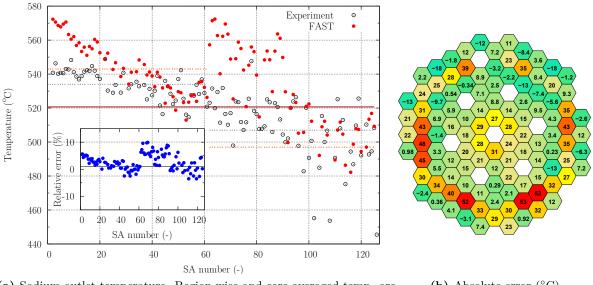
also part of the Phenix end-of-life tests performed in 2009. During this test, the CRs were positioned at different elevations in order to study different CR configurations for the same core power. The main goal thereby was to quantify the impact of a rod insertion and/or extraction on the radial power distribution. The experimental data from the CEA have been shared in the framework of another IAEA CRP. These include the assembly-wise outlet temperature, measured by thermocouples located 75 mm above each fuel SA.

The initial state for the test was a slightly reduced power, viz. 335 MWth, with inlet and outlet temperatures of 375.5°C and 522.7°C, respectively. Four control rod configurations were studied (see also Fig. 5.16):

- 1. All six control rods in a bank;
- 2. Five rods in a bank and one rod inserted by 266 mm in relation to the bank;
- 3. Four rods in a bank, one rod inserted by 229 mm and one extracted by 278 mm, in relation to the bank;
- 4. Five rods in a bank and one rod extracted by 324 mm in relation to the bank.

The test has been previously analyzed in detail with the ERANOS code [Ada10], and the discussion here is mainly on the TRACE/PARCS simulation. For the present purpose, we have used the experimental data for the reference state (all control rods in a bank, 139.4 mm above the bottom of the fissile core), and mainly the assembly-wise outlet temperature.

Figure 5.17a shows the experimental SA outlet temperatures in the fissile core, as compared with the TRACE/PARCS predictions. The assembly-wise absolute error is displayed in Fig. 5.17b. The largest discrepancies are seen in the outer core SAs (last two rows in the figure), with up to 53°C over- and 18°C under-estimation of the measurements. High discrepancies are also seen in the central row of the inner core, where the temperatures are, on average, overpredicted by 25°C. Considering the good agreement of the radial power distribution between TRACE/PARCS and ERANOS in the fissile core (Fig. 5.15), it is clear that the discrepancies on the outlet temperature distribution are mainly due to an inaccurate modeling of the flow rate distribution. It is noteworthy to recall that the experimental gagging of the Phenix core has not been specified, and that, in the TRACE model, the flow rate has been assumed to be equal in SAs from the same core region. The region-wise flow rate was shown to be in good agreement with the test data (Table 5.5), but no data were available for comparison of the assembly-wise flow rate distribution. Comparing the calculated and measured temperatures averaged over the different zones, one can see that the predicted average temperature is 10°C



(a) Sodium outlet temperature. Region-wise and core averaged temp. are represented as dashed and solid lines, respectively
 (b) Absolute error (°C)

Figure 5.17. Sodium outlet temperature in the inner core calculated with FAST, compared to the measured data, for the reference state of the Control Rod Shift test

higher in the inner core and 10°C lower in the outer core. This indicates that the flow rate distribution is slightly under-estimated in the inner core. When averaging over the entire fissile core, the heat balance is very well reproduced, with both the experimental and calculated temperatures at 521°C. For a more accurate model and in order to be able to reproduce the experimental temperature distribution more accurately, consideration of the detailed gagging of the core would be necessary.

5.4.3 Transient calculation

The Natural Convection test, as presented in Section 5.2, has been simulated with the coupled TRACE/PARCS model. The experimental data could thus be used for validation of the coupled calculation of the transient. Also, the 3D model provided complementary results to those obtained from the point kinetics analysis.

The boundary conditions applied to the coupled model were identical to those used in the 0D study: the experimental sodium inlet temperature (Fig. 5.5a) has been specified, together with constant values for the inlet mass flow rate and outlet pressure.

The results for the sodium outlet temperature are shown in Fig. 5.18, along with the available measurements. The comparison with the test data shows better agreement than the results obtained at a higher power (at 335 MW, presented in Fig.5.17), although only a less detailed analysis can be made. The hottest temperature, in SA 21/20, is over-predicted only by 6°C. The inner core outlet temperature matches very well with the test data at steady state. Towards the middle of the transient, discrepancies appear between the 3D model and both the 0D model and the measurements. The differences between the two sets of computed results are mainly due to the limitations of the coupled code system, as explained in the following.

Figure 5.19 presents the evolution of power, as computed with the 3D and 0D models. Due to the current modeling of the fuel in the 3D case (where all fuel pins are represented as linked fuel with closed gap), only results from a 0D model assuming 100% of the fuel linked can be

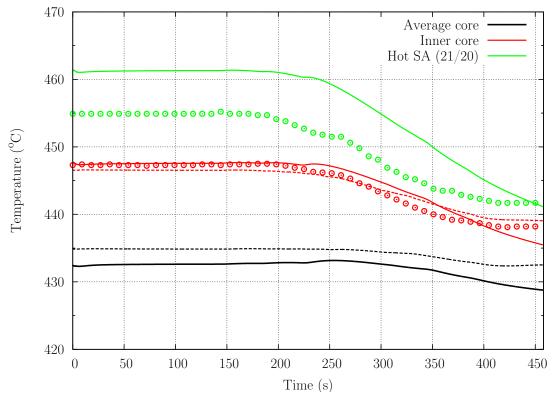


Figure 5.18. Comparison of experimental and calculated outlet sodium temperatures – Exp.: dots, 0D (ref. calc.): dashed lines, 3D: solid lines

used for comparison. Also, the coupled TRACE/PARCS calculation does not as yet allow one to simulate the reactivity feedback due to the vessel expansion and resultant movement of the core. Therefore, an additional set of 0D results, that does not account for the vessel expansion, has been included in order to provide a basis for direct comparison of the 0D and 3D results. Effectively, the current 3D results need to be compared to the 0D results not accounting for the vessel expansion, along with the assumption of closed-gap in all fuel pins. These considerations allow one to explain the differences noted in the computed outlet sodium temperatures (Fig. 5.18), by considering the different trends of the two 0D models, with and without vessel expansion. The simulation of this reactivity feedback in the coupled model would enable us to improve the results and better match with the test data.

Figure 5.19 shows that, under identical assumptions, the power evolution predicted by the 0D model has a comparable trend to that provided by the coupled TRACE/PARCS model. This indicates that the main restriction of the point-kinetics model, viz. a constant power distribution over time, is justified for the considered transient – where the external perturbation (increase of the inlet coolant temperature) does not create any local perturbation (such as boiling, for example). The assumption of a time-independent power distribution is verified in Fig. 5.20, which illustrates the radial and axial flux distributions at the beginning and at the end of the transient. The similarities between the two states clearly show that the point-kinetics model is a good approximation to provide the integral parameters in the considered transient.

Figure 5.21 presents the decomposition of the reactivity feedbacks as computed with the 3D and 0D models, without vessel expansion and with linked fuel in the latter for direct comparison with the former. Discrepancies appear around the time t=250 s, after which the total reactivity from the 0D model becomes more negative than that calculated from the 3D models. After

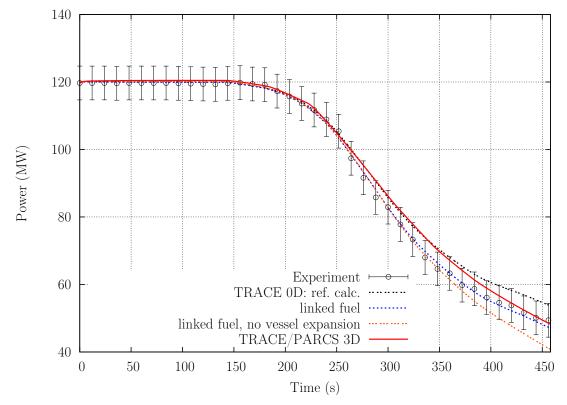


Figure 5.19. Experimental and computed power evolution using different models

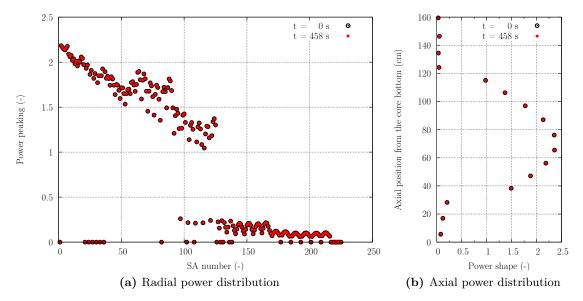


Figure 5.20. Power distribution in the core computed with the coupled TRACE/PARCS model at the beginning (t=0 s) and end of the NC transient (t=458 s)

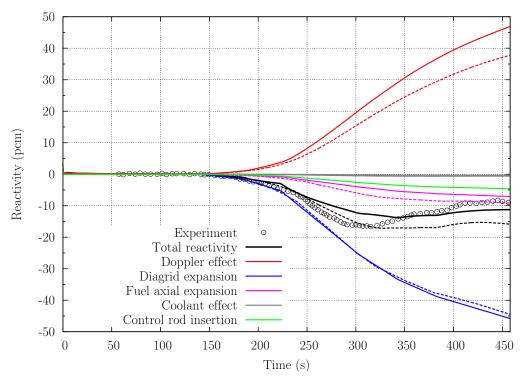


Figure 5.21. Reactivity decomposition – Exp.: dots, 0D: dashed lines, 3D: solid lines

 $t\sim300$ s, similar, parallel evolutions are predicted. The major discrepancies appear on the Doppler component, as also on the fuel axial expansion. Moreover, the 3D model predicts a small feedback from the relative insertion of the control rod in the core (CR component) due to the axial expansion of fuel. This feedback had been considered negligible in the 0D analysis of the present transient (due to the almost constant outlet sodium temperature) but, in the light of these results, it should be integrated into the 0D model for a more accurate simulation.

In order to understand the discrepancies on the Doppler and fuel expansion reactivity components, the comparison is shown in Fig. 5.22 of the computed fuel and clad average temperatures in the different core regions (in the 3D model, the inner core temperature represents the average, over the 54 inner core SAs, of the individual SA average temperatures, and similarly for the outer core temperature). It is seen that the two different models predict the average temperatures within $\sim 15^{\circ}$ C. The detailed 3D model predicts, on the whole, lower fuel temperatures and higher clad temperatures than the 0D model. Though the decrease of the fuel temperature is smaller in the 3D calculations than in the 0D results, the Doppler brings a higher positive feedback to the reactivity. This suggests that the values for the Doppler constants used in the 0D model yield a smaller effect than that computed through the derivatives in the 3D model. A similar comment can be made for the axial fuel expansion (driven by the cladding temperature), where larger changes in the temperatures are seen in the 0D model, which nevertheless presents a smaller reactivity feedback.

Finally, it should be noted that, even using a detailed 3D model, the shape of the total reactivity does not exactly reproduce the experimental data, especially around 250 s. The discrepancies can come from the 3D modeling, in the light of the comparison between the 0D and 3D results. Also, the accurate modeling of the fuel, through coupled thermal-mechanical calculations, could lead to an improvement of the results.

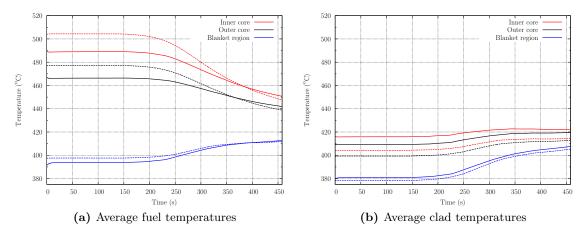


Figure 5.22. Comparison of the computed average temperatures in the different core regions - 0D: dashed lines, 3D: solid lines

5.5 Conclusions

The experimental data available from the natural convection test in the Phenix reactor have enabled an in-depth understanding of the transient behavior of a sodium-cooled fast reactor core and provided, for the very first time, an experimental validation of the coupled TRACE/PARCS calculational tool. The models developed for the analysis of the core neutronics have helped identify the different reactivity feedbacks contributing to the power decrease in response to an increase of the core inlet temperature.

The point-kinetics model developed in TRACE integrated the following feedbacks: Doppler effect, diagrid radial expansion, fuel axial expansion and vessel expansion, the coolant density effect and control rod insertion having been considered negligible for the present study. The coupled TRACE/PARCS model enabled one to model the Doppler effect, diagrid radial expansion, fuel axial expansion, coolant density effect and control rod insertion. Contrary to the 0D model, which assumes a constant value for each feedback coefficient in the defined core regions, the 3D model provides a detailed analysis of the power evolution through the computation of the macroscopic cross-section and neutron flux, taking into account the changes in the state variables in every fuel node.

Thanks to the coupled model, it has been shown that, during the considered transient, the core power shape remains constant, so that the 0D model is a good approximation for the representation of the core neutronics. The decomposition of the different reactivity feedbacks has shown that the diagrid radial expansion and the Doppler effects are the two main feedbacks in this transient, with opposing contributions to the reactivity. The considered transient requires a particularly detailed modeling of the core structures, since the fuel and clad temperatures can have opposite evolutions in different regions – typically between the fissile and fertile zones. The sensitivity study on the reactivity components has revealed the need to accurately simulate the fuel behavior, i.e. the fuel-clad interaction and gas-gap conductance, for the accurate computation of the Doppler and fuel axial expansion effects. This could be achieved using the FRED code, which forms part of the FAST code system for modeling of the fuel thermal-mechanics. Considering the uncertainties on the fuel burn-up, it has been possible to reproduce the experimental power and reactivity evolution within the range of the experimental uncertainties with the 0D model. It would have been interesting to have had a non-negligible coolant density effect in order to benchmark the modeling of this reactivity feedback.

The coupled TRACE/PARCS model, developed for a detailed 3D analysis, should be improved to allow an accurate modeling of the flow and temperature fields. With regards to the simulation of the blanket region, the use of assembly discontinuity factors should improve the calculated radial power distribution (currently under-estimated by $\sim 20\%$ in comparison with ERANOS static calculation). More detailed design specifications, such as the core gagging scheme, would be needed to allow an accurate prediction of the sodium outlet temperatures, and more generally, of the temperature fields. Lastly, the vessel expansion needs to be integrated into the computation of the macroscopic cross-sections in PARCS for a complete modeling of the reactivity evolution.

In brief, the limitations of the present TRACE/PARCS model have been identified. Further work and more detailed design specifications are clearly needed for an accurate 3D modeling of the Phenix core. However, when considering integral parameters such as average temperatures and power evolution, the coupled model gives promising results. The various analyses have shown that the point-kinetics model is a good approximation and gives satisfactory results for the considered transient. A detailed model of the fuel behavior would be needed for a more accurate solution.

CHAPTER (

Coupled TRACE/PARCS transient analysis of the ESFR

THE FINAL STEP of the present research has been to demonstrate the capabilities of the new calculational tool by applying it to the analysis of a Gen-IV SFR core under accident conditions. The aim thereby is to investigate in detail the transient behavior of the core during an event involving boiling onset, e.g. the early phase of a hypothetical severe accident prior to the melting of materials.

The core design selected for this first-of-a-kind analysis is one of the ESFR core concepts developed in the frame of the EURATOM 7th Framework Program (FP). Section 6.1 gives the background and main objectives of the project, along with the ESFR main characteristics. The development of the associated TRACE and PARCS models is presented in Section 6.2. A methodology similar to that developed for the analysis of the Phenix core has been used for verification of the coupled TRACE/PARCS model (Section 6.3).

The transient of interest analyzed here is a hypothetical loss-of-flow accident without SCRAM, i.e. an unprotected loss-of-flow (ULOF). Such an event is of prime importance for the safety demonstration of an SFR, since boiling may occur and lead to a core disruptive accident (CDA). Section 6.4 first describes the simulated transient and then presents the TRACE/PARCS results in terms of the overall core behavior, along with a detailed analysis of the coupled thermal-hydraulics/kinetics phenomena occurring after boiling onset. Additionally, a detailed description and analysis of the two-phase flow in a boiling sub-assembly are provided.

A summary and conclusions from the various analyses are given in Section 6.5.

6.1 The ESFR project and core concepts

6.1.1 The project [Fio11]

The basic core design employed for the present study has been developed in the framework of the Collaborative Project on the European Sodium-cooled Fast Reactor (CP ESFR). Following the 6th Framework Program (FP) Specific Support Action called "Roadmap for a European Innovative SOdium-cooled FAst Reactor – EISOFAR" [Com08], the CP ESFR is part of the 7th FP, created to address the EURATOM Work Program 2008 [EU08] for *Innovative Reactor Systems – Advanced Nuclear Systems*. The project merges the contributions of 24 European

partners and aims to provide solution to the technical requirements identified by the EISOFAR exercise.

The key research goals for European Gen-IV sodium-cooled fast reactors can be summarized as follows:

- Enhanced safety compared to former SFR concepts. In particular, improvement of safety through the achievement of a robust architecture toward abnormal situations and a robust safety demonstration.
- The guarantee of a financial risk similar to that of other means of energy production, through the improvement of economic competitiveness and the reliability and availability of the system.
- A flexible and robust management of nuclear materials, especially waste reduction through minor actinide burning.

Through a 4-year program, the CP ESFR aims at supporting the development of a European SFR, mainly contributing to viability and performance issues. The project potentially represents the European contribution to Gen-IV SFR R&D.

The CP ESFR is structured into five main technical sub-projects (SPs). As the only Swiss participant, PSI also contributes to SP3, which investigates the options for the safety concept and for physical protection & proliferation resistance. Based on the "working horses" provided by SP1 and SP4, the main goal of SP3 is safety demonstration. Among the generic objectives, this includes the capability to prevent accidents and the demonstration that, under all circumstances, their consequences do not violate safety criteria.

In particular, regarding the core design, two concepts are currently proposed for the 3600 MWth core: one based on oxide fuel and one on carbide fuel. Improvement of the basic working-horse designs should consider the following goals:

- Enhancement of the core safety by means of reduction of the sodium void effect and/or optimization leading to gain significant margins on the behavior of these cores in the frame of general unprotected transients (ULOF and UTOP¹)
- Enhancement of the nominal core performances (average discharged burn-up, core plutonium inventory, cycle length, etc.).

6.1.2 Considered ESFR core

The basis for the present study is the preliminary oxide-fuel ESFR core. The core design has been proposed by the CEA, which provided the geometrical data and material definitions. The study has been performed for the core at beginning of life (BOL), i.e. with fresh fuel. Table 6.1 gives the steady-state nominal conditions.

The 3600 MWth core is composed of inner and outer fuel regions with different plutonium mass contents (14.5% and 17%, respectively), in order to flatten the core power shape during the cycle. The fissile regions contain 225 and 228 fuel sub-assemblies (SAs), respectively. The targeted minimal fuel residence time is 2050 equivalent full power days. The average and maximum core burn-up values are 105 GWd/tHM and 155 GWd/tHM, respectively, for an average power density of 206 W/cm³.

The control rod system consists of 12 DSDs (Diverse Shutdown Devices) and 24 CSDs (Contol and Shutdown Devices). The CSD absorber rods contain natural boron carbide ($\sim 19.9\%$

¹Unprotected Transient Over Power

Reactor power	MWth	3600
Core inlet temperature	$^{\circ}\mathrm{C}$	395
Core outlet temperature	$^{\circ}\mathrm{C}$	545
Average core structure temperature	$^{\circ}\mathrm{C}$	470
Average fuel temperature	$^{\circ}\mathrm{C}$	1227

Table 6.1. Oxide-fuel ESFR core (working horse): nominal conditions

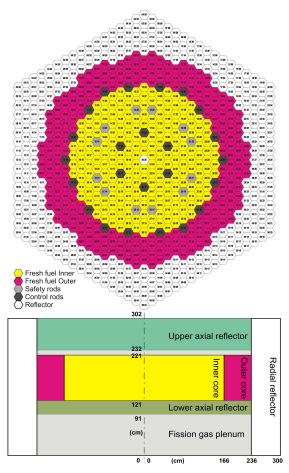


Figure 6.1. Horizontal and axial cross-sections of the ESFR core as modeled in TRACE/PARCS (adapted from [Fio11]).

of ${}^{10}\text{B}$) whereas the DSD absorber rods contain enriched boron carbide (90% of ${}^{10}\text{B}$). The core region is surrounded by three rings of reflector assemblies and additional rows of SAs as radial shielding.

The original CEA concept has been slightly modified in the context of the present study in order to enable 60° (for PARCS) and 30° (for TRACE) symmetries. This has allowed a highly decreased computational time, without changing either the basic analysis methodology being applied or the overall behavior of the reactor. Figure 6.1 presents horizontal and vertical cross-sections of the modeled core, with the different zones clearly indicated.

6.2 Development of the TRACE/PARCS model

6.2.1 PARCS model

The ESFR core has been modeled in PARCS in terms of sets of homogeneous computational nodes in hexagonal geometry. Thereby, considering a 60° symmetry, one sixth of the core has been described with 85 fuel sub-assemblies, 60 reflector channels and 7 control and safety sub-assemblies (to represent the total of 817 assemblies). Axially, the mesh size is about 10 cm, while radially the size of the node is of the order of the fuel assembly flat-to-flat distance (21 cm).

The methodology presented for the development of the Phenix core model in PARCS (see Chapter 5, Subsection 5.4.1) has also been applied for the ESFR core. The self-shielded macroscopic reference cross-sections Σ_0 and the different derivatives for use in PARCS (see Chapter 2, Eq. 2.7) have been produced using the cell code ECCO in conjunction with its adjusted, 1968 energy group, neutron data library ECCOLIB_JEFF_31. For each core region, a heterogeneous cell calculation was carried out to produce cross-sections in 33 collapsed energy groups.

The core states defined in Table 5.6 have been computed to simulate each of the reactivity feedback components, the reference macroscopic cross-sections and the corresponding derivatives being then obtained using the ERANOSTOPARCS procedure.

The two control rod banks and the safety rod bank (see Fig. 6.1) have been simulated explicitly in order to allow separate movement of each bank. Each control assembly (CA) is described with the corresponding follower region, the change of cross-sections due to the presence of the absorber being effectively simulated through derivatives. These have been verified against "static" modeling, in which the CA lower region was explicitly defined with the follower cross-sections and the upper region with the absorber cross-sections.

6.2.2 TRACE model

A 1/12 thermal-hydraulics representation of the ESFR core has been performed in TRACE for the coupled calculation with PARCS. This model thus consists of 51 parallel channels: 45 fuel assemblies (FAs), 5 control and safety assemblies (CAs) and 1 pipe to represent all bypasses, including inter-assembly gaps and reflector assemblies. Each pipe has a different flow area such that, corresponding to its position, the full core can be reproduced from the symmetric model. Each pipe representing a fuel assembly is linked to a heat structure (HTSTR), the power distribution for which is calculated by PARCS during the coupled simulation.

Details of the complete reactor system layout were not directly available for this study. Therefore, as first application of the coupled TRACE/PARCS model to a two-phase flow scenario accident, it was decided to explicitly describe only the core. Consequently, appropriate boundary conditions have been applied at the inlet for coolant temperature and mass flow rate, using a FILL component, and at the outlet for pressure via a BREAK component. Figure 6.2 shows a schematic of the ESFR 1/12 TRACE model currently used, along with the SAs considered in the model.

The final step of the TRACE model development was the estimation of radial and axial thermal expansion coefficients, as used by PARCS, to calculate the changes of the macroscopic cross-sections with respect to the axial and radial core thermal expansion. In practical terms, this allows converting a change in the temperature δT into changes in the axial and radial core sizes $(\delta z, \delta r)$ for applying the corresponding thermal expansion feedbacks using the cross-section derivatives $\frac{\partial \Sigma}{\partial z}$ and $\frac{\partial \Sigma}{\partial r}$.

The radial expansion is driven by the diagrid temperature, since a dilatation of the diagrid would spread the fuel assemblies and insert negative reactivity. Considering that, at the begin-

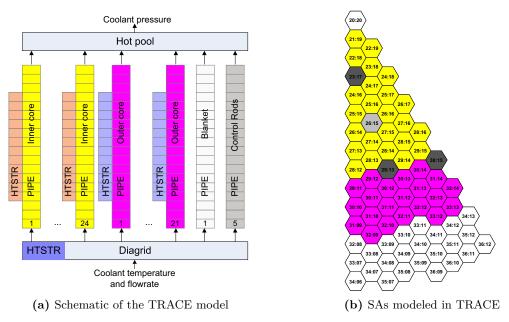


Figure 6.2. The TRACE core model

Table 6.2. Axial and radial thermal expansion coefficients used in PARCS

Thermal Coeffici	ents (10^{-5} K^{-1})
Axial c_{axi}	1.2
Radial $c_{\rm rad}$	1.8

ning of life, there is no mechanical interaction between the fuel pellets and the cladding, it may be assumed that the axial core expansion is driven by the fuel thermal expansion.

As compared to ERANOS, in which the thermal expansions are applied using a temperaturedependent expansion coefficient, the coefficients used in PARCS have been averaged over temperature. The corresponding thermal expansions are calculated for the diagrid material (SS316) using the inlet temperature evolution to provide the radial core thermal expansion, and for MOX fuel using the core-average fuel temperature for the axial expansion. Table 6.2 gives the thermal expansion coefficients used in the present model.

The developed TRACE model was coupled to the PARCS model via an appropriate mapping scheme, linking both the pipe component nodes and the heat-structure nodes to the corresponding neutronics nodes.

6.3 Verification of the TRACE/PARCS model

After the verification of the TRACE and PARCS models in stand-alone mode, the final step has been the verification of the coupled TRACE/PARCS model. This was achieved following the systematic methodology developed for the verification of the Phenix core model (detailed in Subsection 5.4.2). First, the validation of the macroscopic cross-sections and their derivatives was performed through the comparison of the effective multiplication factors, as calculated using ERANOS and TRACE/PARCS. Table 6.3 presents the results of this code-to-code comparison. It is seen that the $k_{\rm eff}$ values obtained with TRACE/PARCS, i.e. with the FAST code system,

Table 6.3.	Comparisons	of the effectiv	e multiplication	factors, o	btained with
TRACE/PARCS	and with ER	ANOS, for the	e different ESFF	core stat	es (see Table 5.6)

$k_{\rm eff}$	REF	DOP	NAD	AXI	RAD	HOT	INI
ERANOS TRACE/PARCS					$\frac{1.02834}{1.02499}$		
$\Delta k \; ({ m pcm})$	-282	-276	-295	-212	-335	-473	-403

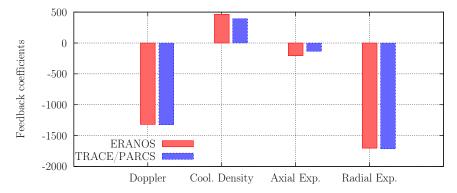


Figure 6.3. Comparison of TRACE/PARCS and ERANOS calculated feedback coefficients for the Doppler effect (pcm), coolant density (pcm/(g/cm3)), as also axial and radial expansions (pcm/cm)

are systematically about 280 pcm lower than the corresponding values from ERANOS, even though both sets of neutronics calculations are based on diffusion theory. The differences may be attributed to the different nodal schemes used in ERANOS (i.e. VARIANT) and PARCS, with a better agreement compared to that obtained for the Phenix core due to the absence of fertile SAs in the ESFR design – and thus less heterogeneous radial flux.

Additionally, particular attention has been given to verification of the reactivity feedbacks for the different effects, as obtained from the following equation:

$$\Delta \rho_i = \frac{1}{k_{\text{eff}_{\text{REF}}}} - \frac{1}{k_{\text{eff}_i}} \tag{6.1}$$

where i represents the parameter varied in the perturbed case (DOP, NAD, AXI, RAD). Figure 6.3 shows the values of the Doppler constant and of the feedback coefficients for the coolant density, and the axial and radial expansion effects, as obtained from the TRACE/PARCS and ERANOS calculations for the reference and perturbed core states. It can be seen that the TRACE/PARCS results are in very good agreement with the ERANOS calculations, the discrepancies not being larger than 5% for the considered feedbacks, except for the axial expansion case, where the absolute value is quite small.

Two additional core states have been calculated to validate the complete model. Each of these takes all the reactivity feedbacks into account in a single calculation and are (i) a 'HOT' case, with all temperatures set to 727°C (i.e. with the coolant density corresponding to this temperature, $\rho_C = 777 \text{ g/m}^3$), and (ii) an 'INI' case, corresponding to zero-power reactor operation, with all temperatures set to 395°C ($\rho_C = 857.6 \text{ kg/m}^3$, corresponding to this temperature). The results are included in Table 6.3. Consistency was obtained with ERANOS results for these simulations, thus demonstrating adequacy for the simultaneous consideration

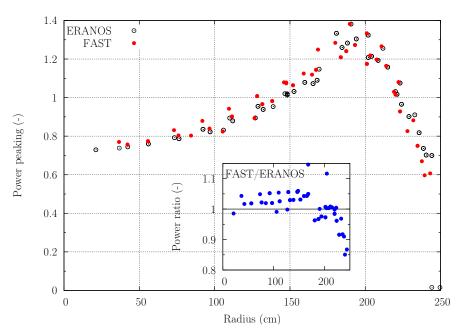


Figure 6.4. Comparison of the radial power distributions calculated with TRACE/PARCS and ERANOS, for the 'INI' core state (all temperatures at 395°C)

of the different feedback effects.

Finally, results for the steady-state power distributions across the core have been compared between TRACE/PARCS and ERANOS. Figure 6.4 shows the comparison of the normalized radial power distributions for the INI case, i.e. at zero-power hot conditions, with all temperatures set to 395°C. The code-to-code comparison shows satisfactory results, even though the power calculated using the FAST code slightly over-estimates ERANOS results in the inner core and under-estimates them in the outer core.

One may also note that, at beginning of life, the highest power density in the core occurs at the interface between the inner and outer fissile fuel zones (SA 30:10 in Fig. 6.2b, at r=190 cm).

6.4 Analysis of the ESFR core response to a ULOF

The behavior of an SFR core following a loss-of-flow without reactor shutdown characterizes, at least in part, the core's inherent safety characteristics. As such, an unprotected loss-of-flow (ULOF) event is one of the major transients of interest for demonstrating the passive safety of the core. Also, as mentioned earlier, such an event could potentially initiate a core disruptive accident, and is thus of prime importance in the safety analysis of an SFR.

This section presents the analysis of the ESFR core behavior during a typical ULOF. The main objective here is to demonstrate the new tool's capability for simulating a wide range of transient conditions, including boiling onset. Little attempt has been made thereby to consider possible changes to the reference core design and/or to take certain negative reactivity effects into account that could mitigate the transient. As such, with the current core concept and with the considered modeling, this hypothetical event leads to a severe accident since the boiling onset is shortly followed by the melting of the fuel and clad. Nevertheless, the results provide the basis for an improved understanding of the core behavior after boiling onset and should thus be useful for guiding future design improvements.

This section is divided into three parts. Subsection 6.4.1 describes the considered accident scenario. Results of the TRACE/PARCS analysis are presented in detail in Subsection 6.4.2. Finally, Subsection 6.4.3 focuses on a detailed description of sodium two-phase flow in a boiling sub-assembly.

6.4.1 Description of the accident scenario

For the present study, a typical flow run-down has been simulated. The inlet mass flow rate can be described, from the beginning of the transient to the onset of boiling, by the function:

$$\frac{\dot{m}(t)}{\dot{m}_0} = \left(1 - \frac{\dot{m}_\infty}{\dot{m}_0}\right) \exp(-at) + \frac{\dot{m}_\infty}{\dot{m}_0} \tag{6.2}$$

where \dot{m} is the inlet mass flow rate, and \dot{m}_0 and \dot{m}_∞ represent the values of the mass flow rate at steady state and after establishment of natural convection, respectively. a is a parameter that can be calculated as function of the half-time $t_{1/2}$:

$$a = \frac{1}{t_{1/2}} \ln \left(\frac{1 - \dot{m}_{\infty} / \dot{m}_0}{\frac{1}{2} - \dot{m}_{\infty} / \dot{m}_0} \right)$$
(6.3)

where $t_{1/2}$ represents the time after which the flow has been reduced by 50%. The parameters characterizing the transient are mainly defined by the primary pump characteristics and primary circuit layout. The exact characteristics of the ESFR primary system are not known yet, and a half-time of $t_{1/2}=10$ s, with a natural convection flow rate of 20% of the initial value $(\dot{m}_{\infty}=0.2\dot{m}_0)$, have been used here.

It should be emphasized that this analysis is restricted to the simulation of the core only. Consequently, the present model does not allow us to take into account the response of the secondary circuit during the transient. In the present study, the core inlet temperature has been assumed to be constant. Thus, the radial expansion reactivity feedback, which is induced by changes of the diagrid temperature, is not taken into account; nor are the vessel expansion mechanisms, first because of the model assumptions, and second due to the code system limitations. It is important to recall that the diagrid expansion was the largest negative reactivity feedback in the Phenix NC test (see Chapter 5). The consequences of these limitations will be addressed in detail in the discussion of the transient analysis.

6.4.2 Results of the TRACE/PARCS analysis and their discussion

In the following presentation of the analysis results, the time of boiling onset, at 26.5 s, is indicated with a vertical dashed-line in the various figures to emphasize the consequences of boiling on the core behavior and thus enhance comprehension.

Figure 6.5 presents the evolution of the core power during the simulated ULOF. It can be seen that the core power very slightly decreases at the beginning of the transient. Directly after boiling onset, it quickly rises with a rate of increase of \sim 720 MW/s, reaching more than 8000 MW at the end of the transient. The power escalation leads to fuel melting onset \sim 37 s after the pump trip. The core behavior has been simulated up to the clad melting (assumed at 1350°C).

The decomposition of the reactivity changes during the transient enables one to understand the phenomena taking place in terms of the different individual feedback effects. The results are presented in Fig. 6.6. After the loss-of-flow, the efficiency of the core cooling is decreased due to the reduction of the coolant velocity at the core inlet. The fuel thus becomes hotter, which generates a negative reactivity feedback through the Doppler effect (the broadening of

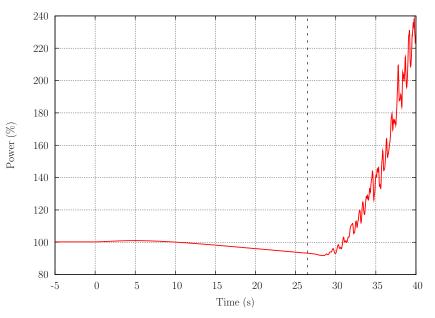


Figure 6.5. Evolution of the ESFR core power during the ULOF

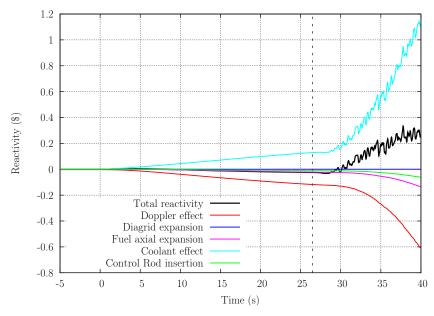


Figure 6.6. Evolution of the core reactivity and decomposition into the different feedbacks during the ULOF

the cross-section resonances increases the 238 U capture rate). At the same time, the coolant is heated. The decreasing coolant density in the active core induces a spectrum hardening, mainly due to reduction of the probability of neutron down-scattering around the sodium resonance at 2.85 keV. This results in a decrease of the 238 U capture rate in the resonance region and inserts a positive reactivity feedback [Sun11].

Figure 6.7 shows the evolution of the main core hydraulic parameters, viz. the inlet and outlet mass flow rates, temperatures and pressures. With an almost constant power and a decreasing coolant velocity, the coolant and fuel temperatures keep increasing at a constant

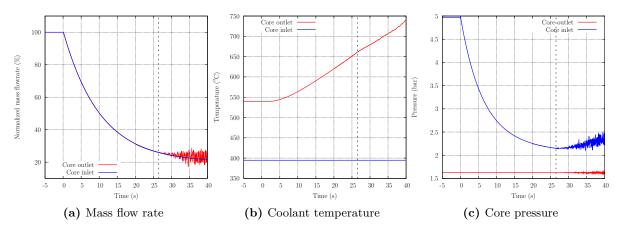


Figure 6.7. Evolution of the main variables at the core inlet and outlet during the ULOF

rate (up to $\sim 12^{\circ}$ C/s). When the coolant temperature reaches the saturation point ($\sim 950^{\circ}$ C), vapor is generated in the corresponding fuel sub-assemblies. In the present core configuration, the hottest channel, as mentioned earlier, is located in the SAs of the outer core (SA 30:10 in Fig. 6.2b), where the power peaking factor is the highest at beginning of life. The impact of boiling on the core integral parameters is clearly seen by the calculated outlet core mass flow rate and pressure.

Figure 6.8 shows the development of the boiling region in time. Boiling onset is first predicted at the top of the active core (see Fig. 6.8a), in the hottest channels (SA 30:10 and symmetric SAs). The boiling region first expands up and down within the same SA (Fig. 6.8b), before propagating to the neighboring channels (Figs. 6.8b-6.8c). The sodium boiling induces a local blockage of the SA and the void fraction rises further, going up to dryout (indicated in the figures by the regions with a void fraction higher than 0.957 – used as one of the dryout criteria). A detailed analysis of the boiling behavior in an SA is given in the following subsection.

In this unprotected transient, the power excursion causes the local boiling rate to be much higher than the condensation rate. Therefore, after boiling onset, the vapor state goes up very rapidly to dryout, leading to the melting of the fuel and cladding. Figure 6.9 shows the void and velocity maps at the end point of the transient simulation. It is seen that, at this stage, the void has propagated from the middle of the outer core, at the top of the active zone, to a generalized boiling region which includes all the outer core SAs and reaches into the inner core SAs. Axially, nearly the entire active length and upper reflector region are voided. Figure 6.9b shows that the voided SAs are blocked by the two-phase flow, resulting in zero or even negative velocities downward of the boiling region.

A core map presenting the spatial variation of void importance along a central cut of the core is given in Fig. 6.10 [Sun11]. A juxtaposition of the boiling map with the void importance map shows that boiling first occurs in a region with a positive value of the void reactivity feedback. Thus, the appearance of boiling at the top of the outer core leads to an increase in the reactivity, and hence in the power. The growth of the voided region occurs both radially and axially into parts of the core where the void importance is either even more positive than at the initial location (towards the inner core) or less positive and/or negative (towards the reflector regions). The absolute value of the void coefficient being higher in the active core than in the reflector region, the result is clearly a significant positive reactivity insertion. Overall, the reactivity inserted by the void effect rises at an increasing rate with the development of boiling in the core (see Fig. 6.6).

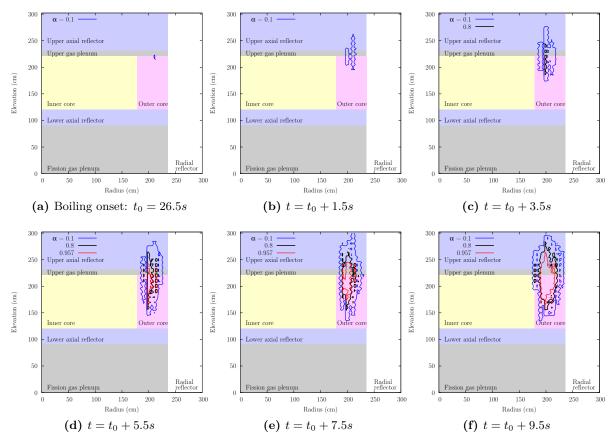


Figure 6.8. Evolution of the void region in the core after onset of boiling at $t_0 = 26.5s$.

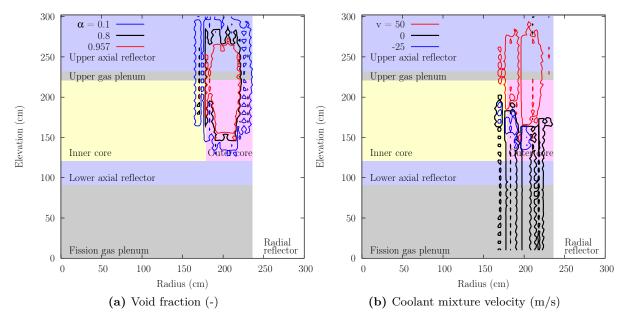


Figure 6.9. Maps of the void fraction and coolant velocity at the end point of the transient simulation $(t = t_0 + 12.5s)$

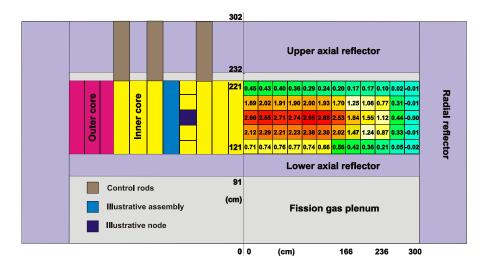


Figure 6.10. Void reactivity importance map (pcm) for a central vertical cut of the core (right). The left-hand side of the figure shows a schematic of the modeling used for obtaining the results. [Sun11]

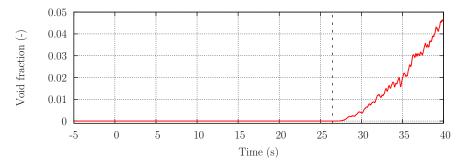


Figure 6.11. Evolution of the core integral void fraction during the ULOF

The oscillations in the void reactivity feedback seen in Fig 6.6 can be explained by the evolution of the core integral void fraction, presented in Fig. 6.11, where similar oscillations can be observed. It is seen that the development of boiling in the core, though non-monotone, is rising at an increasing rate. Figure 6.6 shows that, after boiling onset, the rate of the reactivity inserted by the void effect (>0.06/s) is much higher than that resulting from the coolant density changes in the liquid phase (0.006/s) at the beginning of the transient. The slope continues to increase due to the development of void in regions with, overall, higher void importance, reaching a rate greater than 0.1/s at the end point of the transient simulation.

In the present study, the Doppler effect and other effects providing a negative reactivity feedback, viz. the axial fuel expansion and relative insertion of the CRs in the core (due to axial fuel expansion), are not sufficient to compensate for the positive void effect, and the ULOF results in a strong power excursion. In a more comprehensive analysis, additional negative reactivity feedbacks would be taken into account, viz. the radial expansion, the vessel expansion and the CR drive expansion. These effects have not been simulated here due to limitations of

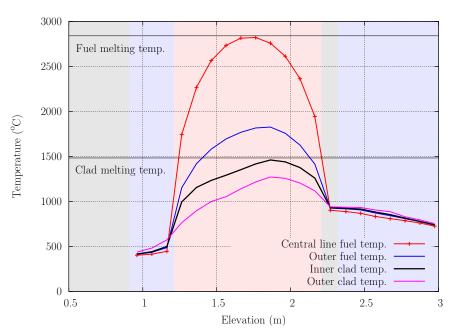


Figure 6.12. Axial profiles of the material temperatures in the hottest channel

the TRACE/PARCS modeling and/or restrictions on the degree of detail available for the ESFR design.

The radial expansion is driven by changes of the diagrid temperature. Therefore, it is only effective once the coolant has traveled through the primary circuit, from the core outlet to the core inlet. The increase in inlet coolant temperature would mitigate the power excursion with a delayed insertion of negative reactivity, but this requires simulation of the entire primary circuit and could, therefore, not be considered here. It is important to note that, in the case of a ULOF, and contrary to the transient studied in the Phenix reactor (more similar to a ULOHS²), this feedback would be much slower acting than the Doppler effect, which comes from the increase in fuel temperature.

The vessel expansion mechanism is further delayed by the thermal inertia of the structures and would occur only after the coolant effect.

The major simplification here is the omission of the feedback resulting from the insertion of the control rods into the core due to the dilatation of the CR drive mechanisms by heating up of the sodium in the hot collector. This feedback can be a very important effect in pool-type SFR concepts [Sei10], and some studies have been done in which the CR drive expansion feedback is included. Since this effect is highly dependent on the design, only brief studies using simplified models could be made. In the present case, it appears that the insertion of the CRs due to the dilatation of the drives would delay the onset of boiling but would not change the overall core behavior once boiling was reached. Therefore, as first approximation, it has been decided to present the more conservative study with the effect neglected.

The axial profiles of the material temperatures in the hottest channel just before clad melting are shown in Fig. 6.12. It has been seen that the fuel melting occurs 37 s after the ULOF, very shortly followed (within less than 1 s) by the clad melting.

Figure 6.13 shows the radial and axial power profiles at the beginning and at the end point of the transient simulation. It is seen that power is shifted from the inner core to the outer core

²Unprotected Loss of Heat Sink

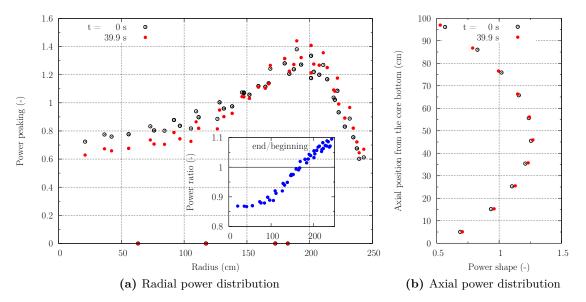


Figure 6.13. Power distribution in the core computed with the coupled TRACE/PARCS model at the beginning (t=0 s) and end point of the transient simulation (t=39.9 s)

SAs, where the two-phase flow developed. The deformation corresponds radially to about 15% and axially to up to 6% of the nominal power shape.

For a more complete analysis of the behavior of boiling SAs, detailed results characterizing the hottest channel state during the transient are presented in the remainder of this section.

6.4.3 Detailed analysis of a two-phase flow instability

This analysis focuses on the thermal-hydraulics parameters calculated for the hottest channel. The mass flow rate, pressure, void fraction and temperatures are presented in Figs. 6.14-6.16. One of the main objectives here, along with the detailed analysis, is to understand the two-phase flow instabilities shown by the disturbances in the thermal-hydraulics parameters.

For the purpose of flow static stability analysis, the knowledge of the following pressure drops is required [Sei84]:

- The internal characteristic (IC), which represents the variation of pressure drop induced by the single or two-phase flow when the inlet mass flow rate is varied under constant power, constant outlet pressure and constant inlet temperature;
- The external characteristic (EC). As the channel is part of a circuit, the hydraulic boundary conditions are dependent on the external loop. The EC corresponds to the variation of the pressure drop over the channel extremities (inlet and outlet) induced by the external circuit when the inlet mass flow rate of the subassembly is varied. (For example, the EC for natural convection in a loop may be a constant driving pressure provided by the liquid column height.)

From the physical properties of sodium at low pressure, the IC can be expected to have an "S" shape. Examples of ICs for sodium two-phase flow up to dryout were presented in Chapter 4 (e.g. Figs. 4.5 and 4.6). Figure 6.17 presents typical internal and external characteristic curves at high and low power. The intersection point between the internal and external characteristics corresponds to a *working point*. The stability of this working point depends on the shape of the

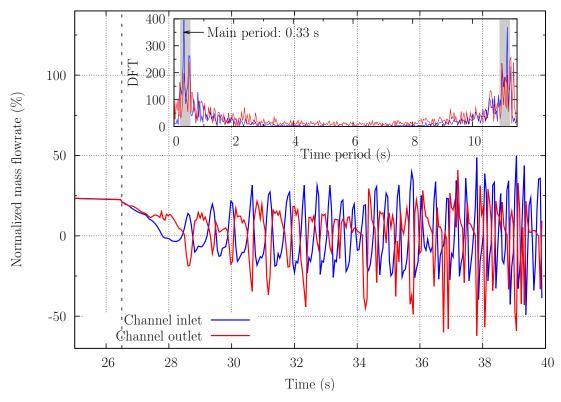


Figure 6.14. Mass flow rate and associated frequency spectrum obtained with a discrete Fourier transform (DFT)

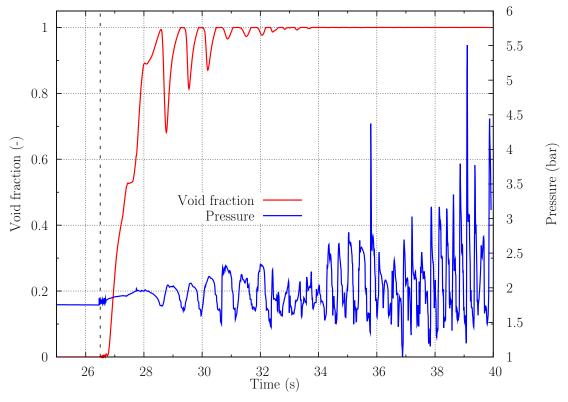
two curves [Bou73]. According to the Ledinegg criterion [Led38], a stable working point can be found on the S curve (at the flow rate Q_0) when, at the intersection between the IC and the EC, one has:

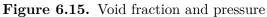
$$\left(\frac{\partial \Delta P_{EC}}{\partial Q}\right)_{Q_0} < \left(\frac{\partial \Delta P_{IC}}{\partial Q}\right)_{Q_0} \tag{6.4}$$

where Q is the inlet flow rate of the channel and ΔP_{EC} , ΔP_{IC} represent the external and internal characteristics, respectively. This criterion is only valid for steady-state and slow transient conditions, and knowledge of the pressure drop at different powers is absolutely necessary for prediction of the two-phase flow stability.

If the Ledinegg criterion is not satisfied, a flow excursion will develop: the flow will decrease progressively from point B to point C in Fig. 6.17a, and vapor will start to fill the heated zone. A new stable working point, at high quality, may theoretically be reached (point C in Fig. 6.17a, where Eq. 6.4 is satisfied). In the considered transient, dryout occurs during the flow excursion and stable high-quality boiling cannot be reached due to the power escalation.

It can be seen from Fig. 6.17b – which presents typical internal characteristics for sodium flow at low power – that, contrary to the shape at elevated power, the pressure drop at boiling onset decreases significantly with decreasing mass flow rate. This is qualitatively due to the fact that the two-phase frictional pressure drop is not sufficient to compensate for the decreasing gravitational pressure drop at low mass flow rates. This principally occurs when boiling first develops at the sub-assembly outlet, where the hydraulic diameter is large in comparison with that within the pin bundle, thus limiting the increase of the frictional pressure drop. When the mass flow rate is further decreased, the boiling zone penetrates into the bundle (with low





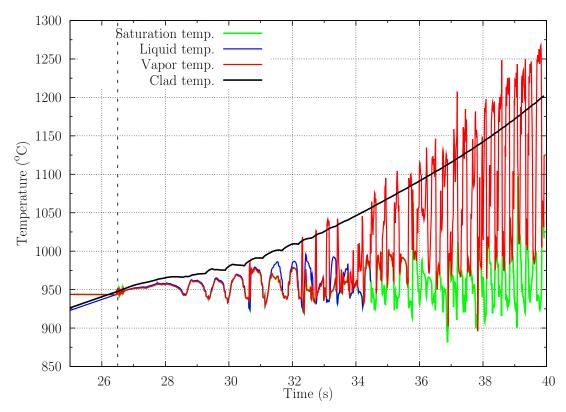


Figure 6.16. Coolant temperature at the top of the heated region

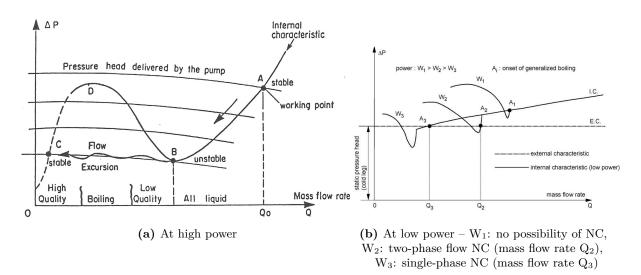


Figure 6.17. Typical shapes, at (a) high and (b) low power, of the internal characteristic $\Delta P_{IC}(Q)$ and of the pressure-head curves (external characteristic) for a sodium boiling channel [Sei84]

hydraulic diameter), which results in an increase of the frictional component that becomes sufficient to increase the total pressure drop. According to Fig. 6.17b and to the Ledinegg criterion, it appears possible to reach a stable two-phase flow of sodium in a low-quality boiling regime (Point A_2 in Fig. 6.17b). A correct prediction of the shape of the internal characteristic for different power levels is clearly required to predict the stable low-quality boiling state. In this case, low quality boiling would start at the end of the heated length and stabilize without reaching dryout.

In the considered transient, instabilities can be seen from the calculated mass flow rate at the inlet and outlet of the hottest channel, as presented in Fig. 6.14. The observed oscillations result from dynamic instabilities and can be attributed to interactions with the neighboring channels in the core, as explained in the following.

The boiling onset at t=26.5 s is followed by a significant reduction of the channel flow rate. When the void fraction is high enough (typically $\alpha > 0.6$), the frictional losses due to the two-phase flow are sufficient to reverse the flow in the boiling SA. In the considered channel, the flow excursion occurs 1.3 s after boiling onset. The local blockage induced by the boiling further decreases the cooling efficiency and the void fraction continues to increase (Fig. 6.15). After dryout (point D in Fig. 6.17a), the frictional pressure drop for the single-phase vapor flow, in this case, is not able to overcome the decrease in the gravitational pressure drop, and the total pressure drop across the SA decreases (see Chapter 4, Subsection 4.1.2 for detailed discussion of the SA pressure drop). When the pressure drop from the two-phase flow in the SA falls below the pressure head imposed by the external loop, sodium can re-enter the SA (at t=28.4 s). The entering liquid sodium slightly decreases the void fraction. For illustration, the calculated void fraction and pressure at the top of the active core in the hottest channel is presented in Fig. 6.15. It is seen that, after re-wetting, the void fraction drops from almost 1 to ~ 0.7 . This return to the annular flow regime causes the friction pressure drop to increase again, thus limiting the liquid coolant re-entry. The second flow reversal occurs no longer than 0.35 s after the flow re-entrance. This process is repeated at different axial levels of the SA over several time intervals.

It is seen from Fig. 6.14 that the inlet and outlet flow oscillations are $\sim 180^{\circ}$ out-of-phase.

Similar oscillations were observed between the inlet flow rates of two parallel channels in an experiment reproducing boiling of sodium-potassium alloy in parallel channels [Sor06]. The experimental results indicated that the interaction between the channels led to large-scale, 180° out-of-phase oscillations of the coolant parameters (flow rate, temperature, pressure) inside the loops, with a period of about 3 s. Additionally, the interaction produced a strong increase of the flow rate fluctuations, up to 600% larger than the fluctuations in the case of a single assembly. The authors explained that these large-scale oscillations were the consequence of pressure wave propagation, resulting from the hydraulic interaction between the parallel channels and creating periodic reductions of the flow rate.

In his review of two-phase flow instability, Bouré [Bou73] considers that the dynamic instabilities are transported by two kinds of waves: pressure or acoustic waves, and void or density waves. In any real system, both kinds of waves are present and interact with velocities that differ in general by one or two orders of magnitude. The analysis of the mass flow rate predicted by TRACE with the direct Fourier transform (DFT) method shows that there is a characteristic oscillation frequency in the range of 2-5 Hz, which corresponds to a period of 0.21-0.55 s. The frequency spectrum of the mass flow rate in presented in Fig. 6.14, where the characteristic period is highlighted with darkened zones. The relatively high frequency of the oscillations indicates that the simulated instability is characterized by pressure waves and seems to be comparable to the phenomena observed in the experiment presented in [Sor06]. It can be seen from the mass flow rate and pressure evolution (Fig. 6.14 and 6.15) that the amplitude of the oscillations increases in time with increasing frequency. Towards the end point of the transient simulation, the oscillations reach up to 50% of the nominal flow rate and almost 100% of the pressure level.

The evolutions of the coolant and clad temperatures at the top of the active core are shown in Fig. 6.16. It is seen that boiling onset is predicted when the liquid temperature reaches the saturation temperature, at t=26.5 s. The liquid temperature follows the saturation point, which is fixed by the oscillating pressure. After establishment of the single-phase vapor regime in the node of interest (at t>34 s, see Fig. 6.15), the heat from the cladding is directly transferred to the vapor which becomes superheated. Cooling limits are reached shortly after the onset of boiling, and the clad temperature rises at an increasing rate. The results clearly show that, at this height of the core, clad melting is about to occur in the next few seconds.

6.5 Conclusions

The use of the FAST code system, which now allows sodium two-phase flow simulation with the extended TRACE code, has enabled, for the very first time, the performance of a detailed analysis of an SFR core under transient conditions with boiling onset. The coupling between thermal-hydraulics and 3D kinetics allowed an accurate accounting of the space-dependent reactivity feedbacks, such as the void and Doppler effects.

The analysis has been carried out while considering, as basis, the oxide-fuel ESFR core design at the beginning of life. The developed TRACE/PARCS model has been verified using ERANOS static calculations, according to the methodology presented in Chapter 5.

Focus has been on studying the core behavior during a hypothetical loss-of-flow without reactor shutdown (ULOF). The TRACE/PARCS simulation provided results for the core thermalhydraulics and neutronics parameters up to clad melting, predicted to occur ~ 10 s after the boiling onset. The decomposition of the reactivity into the different feedback components showed that the power excursion is due to the positive void reactivity feedback. In the present study, boiling has been predicted to occur at the top of the active core in the outer core subassemblies, where the void coefficient is positive. The vapor then propagates to regions with, on average, higher void importance (towards the core center), thus leading to a strong power excursion. The severe fuel damage is first caused by fuel melting, very shortly followed by clad melting.

It has been seen that the newly coupled tool is able to predict the expansion of the boiling region and calculate the corresponding feedbacks, thanks to the detailed 3D-kinetics modeling. The results obtained thus provide a strong basis for an in-depth understanding of the SFR core response to external perturbations and its behavior during accidental situations which include coolant boiling.

Detailed analysis of the thermal-hydraulics parameters in a boiling sub-assembly has shown that strong instabilities occur due to interactions between neighboring parallel channels. The inlet and outlet mass flow rates have been found to oscillate $\sim 180^{\circ}$ out-of-phase, with a major period around 0.33 s in the studied case. This phenomenon is characteristic of pressure waves and is similar to that observed in a two-channel sodium boiling experiment [Sor06]. It has been seen that stable boiling can only be reached under given geometrical and thermal conditions. Thereby, the Ledinegg criterion (Eq. 6.4) is of fundamental importance for the prediction of stability. The possibility of achieving stable boiling without dryout is one of the topics which should be addressed in considering possible design changes for improving SFR safety (see Section 7.3).

CHAPTER

Conclusions and recommendations for future work

THE PRESENT DOCTORAL RESEARCH has, in the context of advanced Generation-IV Sodiumcooled Fast Reactors (SFRs), focused on the development and application of a new calculational tool for transient single- and two-phase coolant flow modeling, coupled to a spatial neutron kinetics treatment of the core. The development mainly relates to the thermal-hydraulics of two-phase sodium flow, modeled through appropriate extension of the TRACE code, which was previously limited to single-phase modeling of sodium.

A positive value for coolant density reactivity feedback coefficient in actual SFR designs makes safety demonstration a key issue for the sodium-cooled Gen-IV concept. On the one hand, the void effect strongly depends upon the two-phase flow phenomena and, on the other hand, the power change caused by this reactivity effect has strong impact on the two-phase flow. Moreover, since the value of the coolant void effect is spatially dependent to a considerable degree, a detailed thermal-hydraulics model coupled to 3D neutron kinetics is necessary for an accurate modeling of the core response to external perturbations.

The newly developed calculational tool allows adequate coupled modeling for such analysis, thanks to its implementation within the frame of the FAST code system, which includes models for spatial neutron kinetics as integrated in the PARCS code. As a first step, two-phase models and equations-of-state for sodium have been implemented in TRACE. Then, validation of these models has been carried out using data from out-of-pile sodium boiling experiments conducted under different test conditions. Additional validation of the coupled calculation for single-phase sodium flow has been made possible via analysis of a recent end-of-life test performed in the Phenix reactor. As final step, the new calculational tool has been applied to the simulation of an unprotected loss-of-flow (ULOF) event in a specific Gen-IV SFR, viz. the ESFR. The results obtained have provided the basis for an improved understanding of the core behavior during a transient which involves boiling of the coolant. This should be helpful for the consideration of possible design changes which would improve SFR safety.

This concluding chapter first provides a chapter-wise summary of the thesis (Section 7.1). The main achievements of the conducted research are presented in Section 7.2, while Section 7.3 provides certain concluding remarks.

7.1 Chapter-wise thesis summary

The general context of nuclear energy today and the main issues related to Gen-IV systems have been presented in the first chapter, in order to introduce the reader to the general framework of the current research. An overview of sodium-cooled fast reactor technology worldwide and of the state-of-the-art concerning calculational tools for sodium systems has been provided in Chapter 2. Also described in this chapter is the description of the code system used as basis for the present study, viz. the FAST code system, containing the thermal-hydraulics code TRACE and the spatial neutron kinetics code PARCS.

Chapter 3 has focused on the extension of the TRACE code, previously limited to liquid sodium coolant, to the modeling of sodium two-phase flow. The two-fluid, 6-equation model available for steam-water flow has been used as basis. A review of closure relations suitable for sodium flow modeling has been carried out, and the different models have been introduced into the extended TRACE code.

The quality of the models, as implemented in TRACE, have been assessed in Chapter 4. The different steps have been presented for the validation of the sodium two-phase flow modeling using out-of-pile experimental data. These correspond to the analysis of experiments dedicated to the study of (i) pressure drop and (ii) dryout in quasi steady-state boiling, and (iii) sodium boiling during loss-of-flow transients. It has thus been possible to validate the extended code under different conditions and to assess the influence of the interfacial and wall-to-fluid transfer mechanisms. The ability of the code to satisfactorily predict the main boiling phenomena – such as boiling onset, void fraction, pressure evolution, coolant and clad temperature – has been demonstrated.

Validation of the coupled TRACE/PARCS calculational scheme has been performed on the basis of the unprotected part of the natural convection test performed at the Phenix sodium-cooled fast reactor. This is presented in Chapter 5. First, a point kinetic analysis has been carried out, in order to provide an in-depth understanding of the core behavior during the considered transient. Then, a TRACE/PARCS model of the Phenix core has been developed. Its application to the above mentioned transient has enabled one, for the first time, to compare results from the FAST code system with experimental data from a sodium-cooled fast reactor. Although certain limitations of the TRACE/PARCS modeling, i.e. the FAST code system, have been identified, the comparison of core-integral parameters, such as evolution of the power and average coolant temperatures, have been found to give promising results.

Finally, application of the new calculational tool to an advanced SFR under hypothetical accident conditions, including coolant boiling, has been presented in Chapter 6. The design considered for this study is the ESFR 'working-horse' concept. The analysis of the core behavior during an unprotected loss-of-flow event has demonstrated the ability of the FAST code system, with the extended TRACE code, to predict boiling onset and to describe the following development of the boiling phenomena. The corresponding core response has been adequately simulated through the consideration of 3D neutron kinetics. The overall core behavior has been presented, along with an analysis of the instabilities which develop in the boiling sub-assemblies, thus providing a basis for the consideration of possible design improvements.

7.2 Main achievements

As sketched above, the principal results achieved during the present doctoral research effectively correspond to four principal stages of the work, viz.:

- Extension of the TRACE code for sodium single- and two-phase flow modeling.
- Validation of sodium flow modeling in general, and of the implemented models in particular, using out-of-pile sodium boiling experiments in different geometries and test conditions.
- Validation of TRACE standalone and coupled TRACE/PARCS results, using experimental data from the Phenix natural convection test before reactor shutdown.
- Application of the extended TRACE code, in conjunction with 3D neutron kinetics modeling, for analysis of the ESFR core behavior during an unprotected transient (ULOF) with boiling onset.

Extension of the TRACE code for sodium two-phase flow modeling

The two-fluid, six-equation model available in TRACE for the representation of steam-water flow has appeared to be quite suitable for being adapted to the simulation of sodium two-phase flow, without restrictions on either the velocity or the temperature field. As indicated earlier, the underlying advantage of using TRACE for modeling sodium thermal-hydraulics is that it can easily be coupled to the 3D neutron kinetics code PARCS, which forms part of the FAST code system. This flexible platform has been extensively verified for a range of fast reactor applications and allows further coupling with static neutronics (via ERANOS) and fuel rod behavior (via FRED).

The extension of the TRACE code, previously limited to the simulation of single-phase sodium coolant, has been carried out through the implementation of equations-of-state and closure relations specific to sodium. A review has first been performed of the models available in the open literature for the representation of the interfacial and wall-to-fluid transfer mechanisms. The different correlations have then been implemented as options in the extended TRACE code. From the validation study carried out, it has been possible to recommend a set of models which provide satisfactory results, while considering annular flow as the dominant regime up to dryout and a smooth breakdown of the liquid film after dryout onset. The main closure relations recommended for sodium two-phase flow modeling are summarized in Table 7.1, where the various terms are defined in the list of abbreviations and symbols (p.224).

Validation of TRACE sodium single- and two-phase flow modeling

The sodium two-phase models, as implemented in the TRACE code, have been validated on the basis of sodium boiling experiments. A review of the relevant experiments, mainly performed in the 1980s, is provided in Appendix B. The experimental facilities with sufficient design specifications are presented, in order to provide a reliable database for the benchmarking of sodium two-phase flow thermal-hydraulics codes.

In the scope of this doctoral research, complementary experiments have been selected for validation of the extended TRACE code. The quasi steady-state sodium boiling experiments from the Ispra research center have provided a practical means for indirectly checking the applicability of the current sodium models through the use of appropriate two-phase flow characteristics. Thus, the pressure drop is an easily measurable parameter characterizing the two-phase flow.

Single-phase $\alpha = 0$	Pre-dryout regime $0 < \alpha < 0.957$	Post-dryout regime $\alpha \ge 0.957$
x = 0	0 < x < 0.3	$x \ge 0.3$
0	$A_i = 4 rac{{igvee lpha}}{D_h}$	$A_i = 4 \frac{\nabla \alpha}{D_h}$
0	$c_{i,1} = A_i rac{ ho_g}{2} f_i, ext{ with } f_i = 0.005 \left[1 + 150(1 - \sqrt{lpha}) ight]$	$c_{i,2} = c_{i,1} / \left(\frac{1 - \alpha}{1 - 0.99} \right)$
0 0	$h_{il,1} = \frac{2\sigma}{2-\sigma} \sqrt{\frac{M}{2\pi R}} \frac{h_{fg}^2 M P_s(T_l)}{RT_s^{2.5}}$ $h_{ig,1} = 10^8$	$h_{il,2} = h_{il,1} \times \left(\frac{1-\alpha}{1-0.99}\right)$ $h_{ig,2} = 10^{8}$
$= 8 \left[\left(\frac{8}{Re} \right)^{12} + \frac{1}{(a+b)^{3/2}} \right]^{1/12}$	$f_{wl,1} = \phi_l^2 f_{l,1\phi}$ $\ln \phi = 1.48 - 1.05 \ln \sqrt{X_{LM}} \dots$ $\dots + 0.09 \left(\ln \sqrt{X_{LM}} \right)^2$	$f_{wl,2} = C f_{wl} f_{wl,1}^{\rm a}$
0	0	$f_{wg,2} = (1 - C f_{wl}) f_{wg,1}{}^{\mathrm{a,b}}$
$0.047 \left(1 - e^{-3.8(P/D-1)} \right) \dots \\ \dots \times \left(Pe^{0.77} + 250 \right)$	$h_{wl,1} = N u_1 _{\phi} rac{k_l}{D_h}$	$h_{wl,2}=C\!f_{wl}h_{wl,1}{}^{\mathrm{a}}$
0	0	$h_{wg,2} = (1 - Cf_{wl}) h_{wg,1}^{a,c}$
	$\frac{1}{(P/D-(P/D-50)^{3/2})}$	

7. Conclusions and recommendations for future work

A sensitivity study, using the different physical models, has enabled one to define the most appropriate set of correlations. Effectively, sodium two-phase flow has been satisfactorily modeled over a wide range of heat fluxes. Sodium boiling in different geometries (tubular section and pin bundles), with different spacer types for pin bundles (wire-wrapper or grid), have been simulated. The study has revealed that, for two-phase flow in tube bundles, the calculated results are more sensitive to the models for the single-phase friction losses at spacers than to correlations used for the two-phase friction multiplier. The capability of TRACE to accurately predict wall and coolant temperatures has demonstrated the validity of the heat exchange model. Both single- and two-phase flow pressure drops have been accurately predicted in the different considered geometries, demonstrating the capability of TRACE to accurately simulate sodium boiling under quasi steady-state conditions.

A complementary set of experiments investigating dryout in sodium flow was selected for validation of the models beyond the annular flow regime. These experiments have been successfully simulated with TRACE, and the analysis has permitted one to recommend the dryout criterion presented in Table 7.1. The considered correlations have been found to satisfactorily predict the wall temperature evolution beyond dryout in the different tests considered. The study has highlighted the high sensitivity of results to the post-dryout models used and the resulting need for an accurate modeling.

The two-phase flow model has then been applied to the simulation of a loss-of-flow from an integral experiment with conditions similar to reactor conditions. The calculated results showed good agreement with the experimental data.

In summary, the various experiments selected for the present research have permitted validation of the extended TRACE code, starting from the two-phase pressure drop at quasi steadystate to the simulation of a loss-of-flow transient, including the study of dryout onset and the post-dryout regime. Effectively, the presented simulations have demonstrated the ability of TRACE to predict, with satisfactory accuracy, the main two-phase flow characteristics: boiling inception, void fraction evolution, radial and axial expansion of the boiling region, pressure evolution, as well as coolant and clad temperatures.

Validation of the FAST code system on the basis of reactor tests

The simulation of the Phenix reactor and analysis of the end-of-life Natural Convection (NC) test has, on an experimental basis, enabled an in-depth understanding of the transient behavior of a sodium-cooled fast reactor core and provided, for the very first time, an experimental validation of the FAST code system on the basis of actual reactor tests. The study has been twofold, viz.:

- Validation of the TRACE sodium single-phase flow model through the modeling of the complete primary circuit and simulation of the establishment of natural convection in the Phenix reactor, as presented in Appendix C. The largest discrepancies, in this context, have been observed for the beginning of the transient, demonstrating the importance of accurate simulation of the reactor-structure thermal inertia. The "blind" results provided very good prediction of the experimental data acquired towards the end of the transient.
- Development of (i) a point kinetics TRACE model and (ii) a coupled TRACE/PARCS model of the Phenix core, for integration of the core neutronics into the simulation and understanding of the transient core behavior through the study of the NC test before reactor shutdown, characterized by an increase of sodium temperature at the core inlet under nominal flow-rate conditions. The 3D neutron kinetics model revealed that the core power shape remained constant during the transient, thus indicating that the point-kinetics model is a good approximation for the considered perturbation.

7. Conclusions and recommendations for future work

The reactivity decomposition into the different reactivity feedbacks has shown that the diagrid radial expansion and the Doppler effects are the two main feedbacks during the analyzed Phenix transient, with opposing contributions to the reactivity. The considered transient requires a particularly detailed modeling of the core structures, since the fuel and clad temperatures can have opposite evolutions in different regions – typically the fissile and fertile zones. The sensitivity study on the reactivity components has revealed the need to accurately simulate the fuel behavior, i.e. the fuel-clad interaction and gas-gap conductance, for the accurate computation of the Doppler and fuel axial expansion effects. Considering the uncertainties on the fuel burn-up, it has been possible, with the point-kinetics model, to reproduce the experimental power and reactivity evolution within the range of the experimental uncertainties.

The application of the TRACE/PARCS model to the NC test has enabled one to identify the code and model limitations, viz. (i) the difficulty to accurately reproduce the power distribution in a heterogeneous core, (ii) the need to integrate the vessel expansion mechanism into the PARCS computation of the macroscopic cross-sections and (iii) the need of more detailed specifications for the accurate modeling of the flow and temperature fields.

Thanks to the presented study, it has already been possible to reproduce, with the TRACE/ PARCS model, the power evolution within the measurement uncertainties. The reasons for the observed discrepancies, e.g. on the assembly-wise outlet temperatures, have been identified, and the comparison of integral parameters, such as the zone-average temperature, has given very promising results.

Application of the FAST code system to the transient analysis of an advanced SFR core with boiling onset

After validation of (i) the TRACE sodium two-phase model and (ii) the TRACE/PARCS calculational tool, the FAST code system has been used to provide an assessment of the transient behavior of an advanced SFR core. The study of an unprotected loss-of-flow event for a reference ESFR core concept has demonstrated the new calculational tool's capability to adequately simulate the core response through the modeling of single- and two-phase flow, coupled to 3D neutron kinetics. Thereby, the space-dependent reactivity feedbacks, such as the void and Doppler effects, have been modeled accurately.

This study provided results for the thermal-hydraulics and neutronics parameters during the pre-severe phase of the accident, i.e. up to the clad melting, which occurred ~ 10 s after boiling onset. It is important to note that a number of reactivity feedbacks, such as the diagrid expansion, the vessel expansion and the control rod drive expansion, that could have mitigated the transient, have not been taken into account. The main objective of the study has been demonstration of the new calculational tool's capability to simulate a wide range of conditions, including boiling onset and clad dryout.

The analysis has shown the ability of the TRACE/PARCS modeling to predict the expansion of the boiling region and calculate the resulting feedbacks. Since boiling onset appears at the top of the active zone, in regions with a positive void worth, it leads to an increase of power through the void reactivity feedback. The vapor then propagates to regions with higher void importance (towards the core center), which results in a strong power excursion. Globally, the power evolution has been seen to follow that of the core-integral void fraction.

The detailed analysis of a boiling sub-assembly has permitted to bring to the fore the instabilities which develop in such channels. This has revealed the capability of the code to predict the interactions between parallel boiling channels, as observed experimentally in certain dedicated facilities.

The in-depth assessment of the behavior of an SFR core during boiling, as rendered possible by the new calculational tool, should enable studies on possible design improvements. Thus, for example, one might foresee modification of the channels and pump hydraulic characteristics, to ensure that boiling can stabilize, according to the Ledinegg criterion, at low vapor quality, without clad dryout. Another possibility could be to aim at "directing" the expansion of the boiling region towards zones with negative void reactivity effect, e.g. the reflector. This might be achieved through appropriate modification of the sub-assembly wrapper design.

7.3 Recommendations for future work

Following the present doctoral research, a number of improvements and further investigations can be carried out. This section summarizes the work that should be done for further development and validation of the sodium two-phase modeling in TRACE, along with possible improvements of the coupled TRACE/PARCS treatment of transients. Additionally, recommendations related to a broader application of the developed calculational tool are proposed.

Further validation and improvement of the TRACE sodium two-phase flow model

In the frame of this doctoral research, only a restricted number of sodium boiling experiments could be studied to provide a basis for validation of the implemented TRACE modeling of sodium two-phase flow. The need to further validate the models has clearly been indicated. In particular, considering the large sensitivity of the wall temperature on the dryout model, further investigations need to be carried out in order to provide an accurate simulation of the dryout and its consequences over a wider range of conditions. This can be achieved through the analysis of some of the experiments presented in Appendix B.

Although the use of annular flow as dominant pre-dryout regime has been recommended currently, the study has revealed certain limitations of this assumption. Thus, the analysis of the Ispra experiments has shown that one needs to model droplet entrainment, in order to obtain more accurate results of the wall temperature between dryout onset and permanent dryout. Should, in the future, appropriate experimental data be available, one could consider the use of a three-field model and implementation of one-dimensional interfacial area transport equation, similar to the TRACE development work currently in progress for steam-water flow [Tal11]. This would replace the conventional, flow-regime dependent correlations and the regime transition criteria for computation of the interfacial flow area, thus allowing dynamic tracking of this parameter. Furthermore, it would eliminate potential numerical oscillations which can result from the use of conventional static correlations.

It should be noted that the original TRACE models for vapor condensation have been used throughout the present study. Consequently, a more detailed investigation of the condensation mechanisms in sodium flow is needed to confirm accurate modeling of the underlying physics.

Finally, due to the intrinsic characteristics of the liquid metal, it has been seen that boiling instabilities can develop in sodium two-phase flow. The reasons behind this are twofold:

- Steady-state instabilities occur when the Ledinegg criterion (see Eq. 6.4) is not fulfilled.
- Dynamic instabilities can develop due to interactions between parallel boiling channels.

This experimentally observed feature of sodium boiling can easily accentuate numerical instabilities in the two-phase-flow simulation, due to difficulties in simulating the sharp variations of the thermal-hydraulics variables (such as void fraction, pressure, mass flow, etc.), both in space (between nodes) and in time. Though a strong effort has been made currently to develop a robust model, the inherent characteristics of sodium boiling and the associated instabilities do make the simulation very challenging and code failure can still be expected to occur due to convergence deficiency. In this context, the development of a more robust calculational scheme is to be recommended. Furthermore, as mentioned above, the use of a three-field model and one-dimensional interfacial area transport equation could help to eliminate potential numerical oscillations stemming from the use of conventional static correlations [Tal11].

Additional detailed studies of sodium boiling instabilities with TRACE would enable one to gain a better understanding of the phenomena and help ensure an accurate modeling. In particular, steady-state instability could be easily studied using a single-channel model integrated into a loop. The variation of the channel's hydraulic parameters (defining the internal characteristic) and that of the loop (defining the external characteristic) would enable a parametric study to be carried out for verifying the Ledinegg criterion. Such a study could be inspired by the recent analysis reported by Seiler et al. [Sei10]. Additionally, the instabilities resulting from interactions between parallel channels could be investigated through simulation of the dedicated experiments performed at IPPE in Russia [Sor06].

Improvement of the PARCS code for SFR transient analysis

A certain extension of the PARCS code – as part of the FAST code system – is needed for optimal application to SFR transient analysis. The major limitation currently identified is the code's inability to generate macroscopic cross-sections for characterizing certain expansion mechanisms inherent to the SFR pool concept, e.g. vessel expansion. Control rod (CR) relative movement has been given some consideration currently, but additional work is needed for an accurate modeling. It needs to be borne in mind that these effects are highly dependent on the reactor design.

Improvement of the developed Phenix core models

The analysis of the Phenix core behavior during the natural convection test has revealed the mechanisms that need to be accurately simulated. In particular, the detailed modeling of the fuel characteristics (i.e. fuel-clad interaction and gas-gap conductance) has been found to be of major importance for adequate representation of both the Doppler effect and fuel/cladding expansion. A complementary study, incorporating a detailed modeling of the fuel pins through coupling with the FRED code – which forms part of the FAST code system – is certainly to be recommended.

The computation of the kinetics parameters (i.e. β_i and λ_i) should be further investigated, in order to provide more accurate results and thus avoid any need for adjustments.

Finally, improvements specific to the coupled TRACE/PARCS model could be achieved through consideration of:

- a detailed gagging scheme, should more design specifications be provided by the CEA. This would largely improve prediction of the assembly-wise, outlet sodium temperature distribution.
- assembly discontinuity factors to account for the large flux discontinuity between the outer core and blanket regions. Though this improvement would enhance the modeling of the blanket region, it is not very important in the context of the present study.

Application of the new calculational tool for broadened analysis of SFR transient behavior

The calculational tool developed during this doctoral research offers a number of new applications rendered possible by the adequate simulation of single- and two-phase sodium thermalhydraulics coupled to 3D neutron kinetics. Thus, the implemented TRACE/PARCS modeling provides the basis for a comprehensive analysis of SFR core behavior during transients including boiling. In particular, the study presented in Chapter 6 has underlined the capabilities of the developed calculational tool to analyze SFR safety in transient situations involving the possible insertion of positive reactivity due to the void effect.

Significant work can now be done for optimization of the SFR core concept from the viewpoint of enhanced safety. For example, based on the presented analysis, one could consider possible design modifications such as that of the sub-assembly hydraulic characteristics, in order to stabilize boiling in the low-quality regime without clad dryout [Sei10], or modification of the sub-assembly wrappers, to "direct" the spread of boiling to regions with negative void effect.

For enhancing the new calculational tool's capabilities for SFR design optimization even further, the developed core model should be integrated into the primary circuit, in order to account for all the possible reactivity feedbacks, including the response of the secondary loop. This would enable an extensive study of optimized core behavior during unprotected transients (mainly ULOF and UTOP). Such an analysis should be performed considering the different SFR core states during the fuel cycle.

Additionally, it would be of generic interest to identify the conditions in which coupled spatial neutron kinetics/two-phase thermal-hydraulics plays an important role. This could be achieved through the development of a point-kinetics model for the ESFR concept, followed by the comparative analysis of selected transients using both 0D and 3D models.

7.4 Concluding remarks

The present work has contributed to the development of a calculational tool that allows comprehensive analysis of advanced SFR core behavior during transients, especially those accompanied by sodium boiling and subsequent possible insertion of positive reactivity due to the void effect. To the author's knowledge, such a calculational tool has not been available previously.

A sodium two-phase flow model has been implemented into TRACE. The capability of the extended code to accurately model sodium single- and two-phase flow has been demonstrated on the basis of comparisons with out-of-pile experiments. For the first time, the single-phase sodium flow model in TRACE, as also the developed TRACE/PARCS calculational tool, have been validated using experimental data from a fast power reactor. The detailed analysis of the transient behavior of the Phenix core has enabled identification of the most important reactivity feedbacks and the mechanisms which need particularly accurate modeling. Finally, the application of the developed calculational tool to analysis of the ESFR during an unprotected loss-of-flow event has provided a comprehensive understanding of the core behavior during the transient, including propagation of the boiling region.

In conclusion, the presented research has led to the development of a key calculational tool for SFR safety analysis through the adequate consideration of two-phase flow thermal-hydraulics, coupled to 3D neutron kinetics. A first application has already provided important results, demonstrating the tool's potential for usage in SFR design optimization aimed at enhanced safety. Recommendations have been made for further developments and improvements.

Appendices

Appendix A

Equations-of-state

Additional models have been implemented in TRACE for calculating sodium liquid and vapor thermal properties. The corresponding adaptation and benchmarking have been based on the SIMMER-III code [Tob02], the SAS4A code [Cah00] as well as on the Fink and Leibowitz publication [Fin96]. The properties analysed include temperature dependencies for:

- liquid density;
- sonic velocity in liquid;
- vapor pressure at saturation;
- vapor density at saturation;
- liquid specific heat;
- vapor specific heat;
- liquid thermal conductivity;
- vapor thermal conductivity;
- liquid viscosity;
- vapor viscosity;
- enthalpy of vaporization;
- surface tension.

Comparisons have been done for the temperature range 100 - 1500°C, limited from below by the sodium melting point and from above by the stainless steel melting point

Liquid density

TRACE calculates the liquid density according to the following equation:

$$\rho_l = 1011.8 - 0.22054 T_l - 1.9226 \times 10^{-5} T_l^2 + 5.6371 \times 10^{-9} T_l^3$$
(A.1)

It can be seen from Fig. A.1 that the temperature dependency for the liquid density is almost linear and very close to that used in SIMMER.

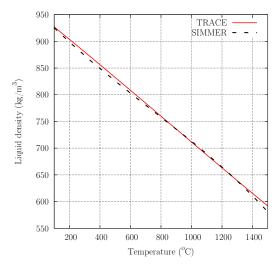


Figure A.1. Liquid density of sodium

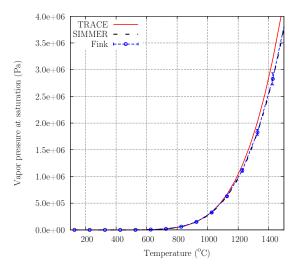


Figure A.3. Sodium vapor pressure at saturation

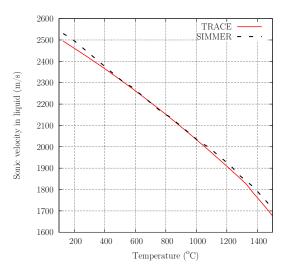


Figure A.2. Velocity of sound in liquid sodium

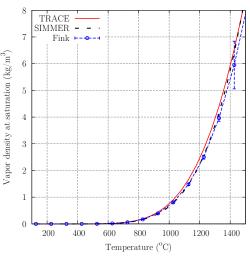


Figure A.4. Sodium vapor density at saturation

Sonic velocity in liquid

TRACE's sonic velocity in liquid sodium is seen to be in good agreement with the SIMMER model (Fig. A.2).

Saturation pressure and vapor density at saturation

The vapor density is calculated in TRACE by the ideal gas law. Therefore, for the two-phase flow, the vapor density linearly depends on the vapor pressure at saturation. Comparison of the vapor pressure at saturation with SIMMER shows that TRACE overestimates this parameter, e.g. at ~1500°C by ~15% (Fig. A.3). However, the vapor density calculated by TRACE by the ideal law is in good agreement with the SIMMER prediction based on the non-ideal gas formulation for calculating the gas density at saturation (Fig. A.4).

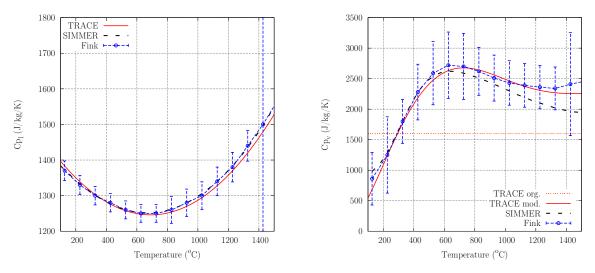


Figure A.5. Sodium liquid specific heat

Figure A.6. Sodium vapor specific heat

Liquid specific heat

TRACE computes the liquid specific heat according to the following equation:

$$c_{p,l} = 1646.97 - 0.831587 T_l + 4.31182 \times 10^{-4} T_l^2$$
(A.2)

This model is very close (within 1%) to both the SIMMER and Fink data (see Fig. A.6), and well within the uncertainties recommended by Fink.

Vapor specific heat

Originally, a constant value of $\sim 1600 \text{ J/kg/K}$ was used in TRACE for the sodium vapor specific heat, which significantly differs from the function used in other codes. A new correlation, based on the SAS4A approach, has been implemented such that:

$$c_{p,v} = 2.1409 \times 10^{3} - 2.2401 \times 10^{1} T_{v} + 7.9787 \times 10^{-2} T_{v}^{2} - 1.0618 \times 10^{-4} T_{v}^{3}$$
(A.3)
+6.7874 × 10⁻⁸ $T_{v}^{4} - 2.1127 \times 10^{-11} T_{v}^{5} + 2.5834 \times 10^{-15} T_{v}^{6}$

This model is in a good agreement with the Fink data and compares relatively well with the SIMMER model (see Fig. A.6).

Liquid thermal conductivity

The sodium liquid thermal conductivity is calculated in TRACE according to:

$$k_l = 1.1641922 \times 10^2 \exp\left(-7.0184779 \times 10^{-4} T_l\right)$$
 (A.4)

The temperature dependence is almost linear and is in a good agreement with both the SIMMER results and Fink data (see Fig. A.7).

Vapor thermal conductivity

The constant value of 1.0, used in the original TRACE code for the sodium vapor thermal conductivity, has been replaced by a tabulated function taken from the SIMMER code (see

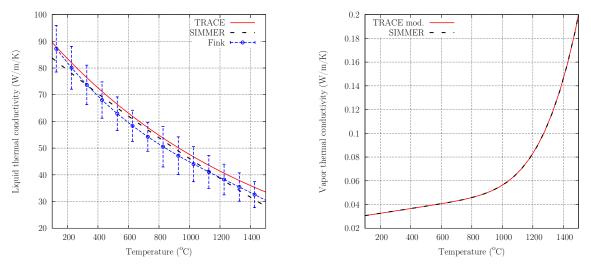


Figure A.7. Liquid thermal conductivity

Figure A.8. Vapor thermal conductivity

Fig. A.8).

Liquid viscosity

The sodium liquid viscosity is calculated in TRACE according to the following equation:

$$\mu_l = 0.11259 \times 10^{-3} \frac{\exp\left(\frac{0.74908\,\rho_l}{T_l}\right)}{(1000/\rho_l)^{\frac{1}{3}}} \tag{A.5}$$

This model is in a good agreement with that in SIMMER and with Fink data (see Fig. A.9).

Vapor viscosity

The constant value of 0.0002 in the original TRACE code for the sodium vapor viscosity has been replaced by the following model [Gra80]:

$$\mu_v = 1.261 \times 10^{-5} + 6.085 \times 10^{-9} \left(T_v - 273.15 \right) \tag{A.6}$$

This model is, once again, in good agreement with that used in SIMMER (see Fig. A.10).

Enthalpy of vaporization

TRACE was originally using the water enthalpy of vaporization for sodium coolant. The model recommended by Fink has been implemented in the modified TRACE version:

$$H_{fg} = \left[393.37 \left(1 - \frac{T}{T_c}\right) + 4398.6 \left(1 - \frac{T}{T_c}\right)^{0.29302}\right] \times 10^3 \text{ with } T_c = 2509.46$$
(A.7)

This is in a good agreement with the SIMMER model (see Fig. A.11).

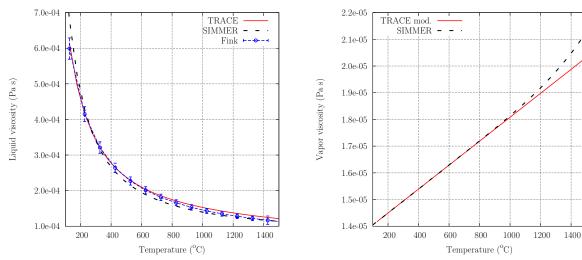


Figure A.9. Liquid viscosity

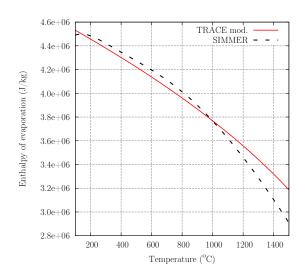


Figure A.11. Enthalpy of vaporization

Figure A.10. Vapor viscosity

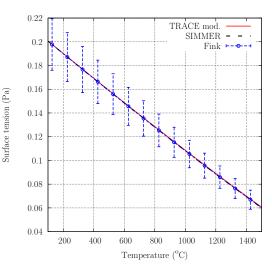


Figure A.12. Surface tension of liquid sodium

Surface tension

The liquid sodium surface tension was originally also calculated from water properties. The model recommended by Fink has been implemented in TRACE:

$$\sigma = 0.2405 \left(1 - \frac{T_{sat}}{T_c} \right)^{1.123} \text{ with } T_c = 2509.46$$
 (A.8)

This is in very good agreement with SIMMER (see Fig. A.12).

Overall, it can be concluded that the modified TRACE equations of state correlate well with the corresponding SIMMER equations and the data recommended by Fink. The main thermodynamic properties for liquid and vapor sodium currently used in the modified TRACE code are summarized in Table A.1.

T K	$c_{p,l} \ kJ/kg/K$	$ ho_l \ kg/m^3$	$k_l \ W/(m.K)$	$\mu_l \\ 10^5 Pa.s$	$\sigma mN/m$	$H_{fg} \ kJ/kg/K$	$c_{p,v} \ J/kg/K$	$rac{ ho_v}{kg/m^3}$	$k_v W/(m.K)$	$\mu_v \ 10^5 Pa.s$
400	1.383	920.9	87.9	61.45	197.8	4 511.1	1.1	1.24E-09	0.0312	1.417
500	1.339	897.4	82.0	41.66	187.3	$4 \ 436.3$	2.5	5.03E-07	0.0331	1.462
600	1.303	873.8	76.4	32.04	176.8	4 359.5	4.9	2.63E-05	0.0351	1.506
700	1.276	850.0	71.2	26.48	166.4	$4\ 280.3$	9.0	0.000431	0.0371	1.551
800	1.258	826.0	66.4	22.89	156.1	4 198.6	15.6	0.00343	0.0392	1.596
000	1.248	801.9	61.9	20.39	145.9	4 114.1	26.2	0.0170	0.0413	1.641
1000	1.247	777.7	57.7	18.54	135.7	$4 \ 026.5$	42.3	0.0603	0.0437	1.686
1100	1.254	753.5	53.8	17.11	125.6	$3 \ 935.5$	66.1	0.168	0.0468	1.731
1200	1.270	729.2	50.1	15.98	115.6	3 840.6	100.0	0.394	0.0513	1.775
1300	1.295	705.0	46.7	15.04	105.7	3741.2	146.9	0.805	0.0585	1.820
1400	1.328	680.9	43.6	14.26	95.9	$3 \ 636.9$	210.2	1.48	0.0702	1.865
1500	1.370	656.8	40.6	13.59	86.3	3 526.7	293.7	2.50	0.0887	1.910
1600	1.420	632.8	37.9	13.00	76.7	$3\ 409.6$	402.0	3.96	0.1169	1.955
1700	1.479	608.9	35.3	12.48	67.3	$3\ 284.3$	539.8	5.95	0.1584	2.000
1800	1.547	585.2	32.9	12.01	58.0	$3\ 148.9$	712.8	8.54	0.2178	2.044
1900	1.624	561.1	30.7	11.59	48.9	3 001.0	927.0	11.9	0.3011	2.089
2000	1.709	536.4	28.6	11.18	39.9	2 836.7	$1 \ 189.1$	16.0	0.4181	2.134
2100	1.802	510.4	26.7	10.79	31.2	$2\ 650.0$	1 506.5	21.2	0.5856	2.179
2200	1.904	481.8	24.9	10.40	22.8	$2 \ 430.6$	1 887.2	27.7	0.8365	2.224
2300	2.015	448.2	23.2	9.97	14.7	$2\ 157.5$	$2 \ 340.0$	36.3	1.2450	2.269
9/00	2.135	403.4	21.6	9.43	7.1	$1\ 773.9$	2874.3	49.3	2.0190	2.313

Appendix B

Review of sodium boiling experiments available for code benchmarking

Many experiments have been performed in the past to investigate sodium boiling phenomena. A textbook, reporting the 26 years' activity of the Liquid Metal Boiling Working Group (LMBWG) and edited by Kottowski [Kot94], gives an overview of various experiments and the associated analysis performed within the group.

This appendix aims at giving an overview of the test data available for the benchmarking of sodium thermal-hydraulics codes. In particular, the focus has been brought on those out-ofpile experiments, which are described in sufficient detail in the open literature to allow one to perform the associated modeling and analysis in a reliable manner.

Table B.1 gives a summary of selected sodium boiling experiments. Though this list is not exhaustive, it should provide a good overview of relevant experiments performed in the past. When possible, the test conditions and area of investigations are mentionned. Table B.2 presents the main characteristics of the test sections used for these experiments.

Some references for pool boiling experiments are briefly listed in Section B.1. Section B.2 summarizes the experiments performed at PNC, Japan, in the SIENA facility, and presents some relevant test data. Further experiments from the KNS loop are presented in Section B.3, thus completing the description presented in Section 4.3. Most of the tests performed at the JRC-Ispra have been described in Chapter 4 and are therefore not further detailed here. Section B.4 briefly describes other relevant sodium boiling experiments.

Lab. and facility	Tubular test section	Annular test section	Pin bundle
PNC SIENA		Incipient boiling [Kik74] Steady-state [Kik75] LOF [Kik78c]	 7 pin: Local flow blockage [Kik77] Incipient boiling [Kik78b] Transient LOF, TOP [Kik78a, Kik79] 19 pin: LOF [Kik81] 37 pin: LOF [Hag84], flow blockage [Uot84], dryout at decay power levels [Yam87]
KfK KNS [Hub76]	Heat transfer [Sch70] Boiling dynamics [Pep70] Pressure drop, dryout: [Kai74, Bot78]	Steady-state [Kai77b] LOF [Kai77b]	 7 pin: steady-state [Kai75, Kai77a, Kai79] LOF [Abe76] 37 pin: steady-state [Hub87, Kai88] Low power under NC [Kai82, Kai84, Kai87] LOF [Hub82b, Hub82a, Hub87, Hub88, Bot90] Dryout behind local blockage [Hub78, Hub84]
JRC-Ispra [Kot84]	Steady-state [Kot84]	Steady-state [Kot84]	12 pin : steady-state [Eif80] pressure drop [Kot84, Sav88b, Wal86, Sav86] dryout [Sav89, Kot91, Sav88a, Sav86]
ORNL THORS [Gna84]			19 pin [Gna84] 61 pin [Gna84]
CEA-Grenoble [Sei90] CFNa and CESAR		Slow transient [Sch82]	19 pin : general aspects [Sei84] steady-state, slow and fast transients [Sei84]
IPPE (fluid=Na-K) AR-1 [Sor05]			Two parallel 19-pin bundles [Sor05] heat transfer during NC [Efa07] instabilities during NC [Sor06]
Others	Heat transfer: [Lur65, Noy66, Sin70, Xia06] Expulsion dynamic [Sin70]	Pressure drop [Zei80]	

 Table B.1.
 Summary of relevant sodium boiling experiments

ts
men'
periı
g exp
boiling
ium
sodiu
ted
selec
for
nsed
ions
secti
test
various
of the v
s of
cteritics
ති
ı char
Main
B.2.
ດ
Table

		Pipe ch	Pipe characteristics		Heater characteristics	racteristi	S	
	A^{a}	$D_{h^{\mathrm{a}}}$	$D_{ m in}/D_{ m out}$ or flat-to-flat distance	$D_{ m rod}/{ m p}$	$D_{ m wire}/h_{ m pitch}$	Inlet leneth	Heated length	Outlet length
	(mm^2)	(mm)	(mm)	(mm)	$(\mathrm{mm})/(\mathrm{mm})$	(mm)	(mm)	(mm)
PNC, SIENA:								
Annular	164.87	6.4	$6.6 \ / \ 9.8$	6.6		80	009	860
7-pin bundle			24.0	$6.5 \; / \; 7.9$	$1.3 \ / \ 264.8$	350	450	715
19-pin bundle			36.7	$6.5 \ / \ 7.9$		350	465	200
37-pin bundle	924	3.43	50.4	$6.5 \ / \ 7.9$		148	450	715
KfK, KNS:								
Tubular		6	I	I	I		212	150
7-pin bundle			22.0	$6.0 \ / \ 7.9$	grid	200	009	445
37-pin bundle	1170		50.6	$6.0 \ / \ 7.9$	grid	200	006	450
JRC-Ispra:								
Tubular		6.6	I	ı	ı	380	1000	380
Annular			6.6/8.6	6.6	ı	009	009	009
2-pin (wire, long)	496.5	3.8	. 1	$8.0 \ / \ 10.4$	$2.4 \; / \; 150$	540	500	735
2-pin (wire, short)	496.5	3.8	ı	$8.0 \ / \ 10.4$	$2.4\ /\ 150$	540	500	ı
12-pin (grid, long)	550.8	4.93	ı	$8.0 \;/\; 10.4$	grid	540	500	735
l2-pin (grid, short)	550.8	4.93	I	$8.0 \ / \ 10.4$	grid	540	500	I
CEA-Grenoble:								
Annular			6.6	6.6	I	ı	400	009
19-pin bundle	728.5	3.88	45.85	$8.65 \ / \ 9.95$	$1.28 \; / \; 180$	100	600	494
IPPE:								
19-pin bundle	1264	12.57	ı	8 / 9.48	I	30	830	1270

B.1 Pool boiling experiments

A number of sodium pool-boiling experiments have been performed to study general aspects of sodium two-phase flow. In particular, studies of the sodium heat-transfer properties under free-convection conditions have been reported by Noyes and Lurie [Noy63, Lur64, Noy66, Lur65]. Other pool-boiling experiments have been performed to investigate general boiling phenomena such as sodium ejection and superheat [Smi68], sodium incipient and nucleate boiling [Sch74], and the sodium boiling curve [Sch75]. These experiments are not detailed here since the focus is brought on reactor conditions, i.e. mainly forced and natural convection conditions in pipes and bundles.

B.2 The SIENA experiments

In Japan, sodium boiling experiments have been carried out in the frame of safety considerations for LMFBRs. These were conducted by the Power reactor and Nuclear fuel development Corporation (PNC) at the O-arai Engineering Center in the 1970s. Different test sections were built and used in the sodium boiling and fuel failure propagation test loops constituting the SIENA facility [Kik77]. Figure B.1 illustrates a schematic diagram of the facility. The SIENA loops were divided into the Sodium Boiling test Loop (SBL), containing the test section T-1 for single-pin experiments, and the Fuel failure Propagation test Loop (FLP), which contained the test sections T-2 for 7-pin experiments and T-3 for 19-pin or 37-pin experiments. Figure B.2 shows the different test sections used for the investigations, except for the second 37-pin bundle (test section 37G) which is not described here. The loops provided sodium flows up to 3×10^{-3} m³/sec with inlet sodium temperatures up to 750° C and system pressures up to 6 bar. A maximum power of 650 kW could be supplied to the electrically heated pins.

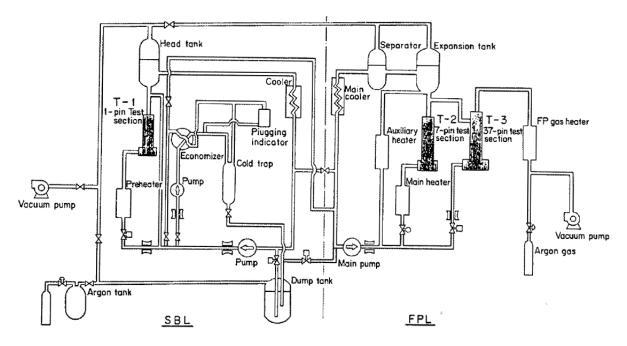


Figure B.1. Schematic diagram of the Sodium Boiling and Fuel Failure Propagation Test Facility, SIENA

Expansion tank

-12

-11

-10

-9 -8 -7

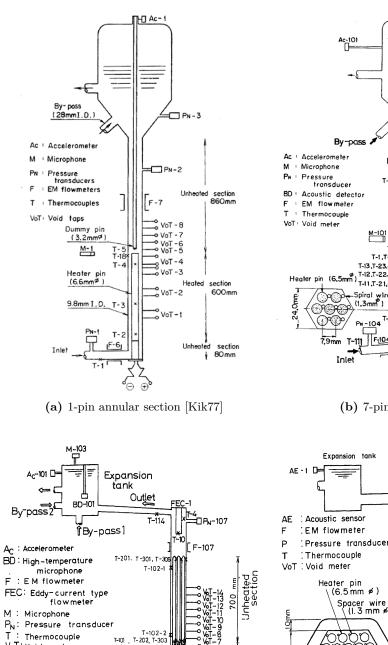
- 4

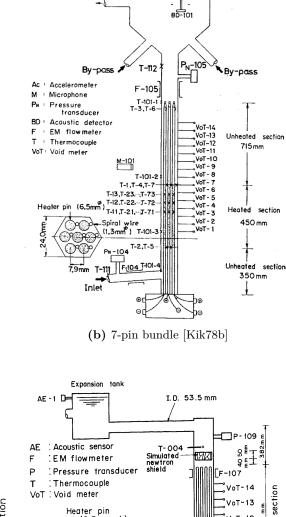
Unheated

Heated section

-148mm Unheated section

Ac-102





VoT Spacer wire ∖(1.3 mm ≠) / nT 1.5 T-102-2 202, T-303 --- T-3124 --- T-3123 t-101 t-1014 t-1013 VoT: Void meter .4 mm Heater pin ¹⁻¹⁰¹³ (6.5 mm¢) H eated section T-312 3 Spacer wire 、(1.3 m m^p) ß ŝ V6T--2 VoT-2 T-102-3 165 VoT-1 T-1011, T-302,T-310 /oT-36.7 ___P-108 Р_N-106 BD-102 <u>C</u> 7.9 mm Inheated T-203 T-206 T-305 e E Sodium inlet T-113 r⊷ 7.9 350 T-003 F-103 0 AE-2 -102-Inlet F-106 €D⊕D I.D. 53.5mm Ð €

(c) 19-pin bundle [Kik81]

(d) 37-pin bundle 37F [Hag84]

Figure B.2. Schematic diagram of the test sections used in the SIENA facility

B.2.1 The annular test section and associated tests

Description of the annular test section

The annular test section, presented in Fig. B.2a, simulated a single channel of a fast reactor core. This consisted of a vertical, type-316 stainless-steel tube of 9.8 mm inside diameter containing an electrically heated pin 6.6 mm in diameter and 780 mm long. The heater pin had an effective heated length of 600 mm. A power flux of up to 300 W/cm² was available. The outer wall was maintained under adiabatic conditions, thanks to a compensating heater and a thermal insulator installed on the wall to compensate for the dissipated heat.

The by-pass of the test section simulated subchannels adjacent to the boiling subchannel, so that, even under boiling conditions, the experiment could be performed with a constant pressure difference between the test-section inlet and outlet.

Instrumentation

The positions of the different detectors are indicated in Fig.B.2a. The sodium inlet and outlet temperatures were measured with the use of the chromel-alumel thermocouples T-1 and T-5, respectively. Three thermocouples (T-2, T-3 and T-4) were embedded in the inner surface of the tantalum sheath (a 0.6 mm thick cladding) of the heater pin to monitor the pin-surface temperature. Eight potential-tap-type void-meters (VoT-1 to VoT-8) were used to indicate the onset of coolant boiling and to define further propagation of the vapor bubbles. The sodium inlet and outlet velocities were measured with the electromagnetic flowmeters F-6 and F-7, respectively. Three pressure gauges (P_N-1 to P_N-3) were used to record the change in pressure during boiling. A piezoelectric type accelerometer (Ac-1) and a condenser type microphone (M-1) were also installed to measure the acoustic boiling noise.

Steady-state experiments

First, steady-state experiments were performed to investigate incipient sodium boiling and superheat [Kik74, Kik75]. The inlet temperature and flow rate were held constant, and the heat flux was gradually increased up to boiling inception. The initiation of boiling was anticipated from the sodium outlet temperature, and actual onset of boiling was detected from the output signals of the void-meters, flowmeters and pressure gauges. After boiling onset, the heat flux was further increased step-by-step until the heater surface temperature began to rise sharply, thus reaching dryout conditions.

Figure B.3 shows the experimental results from a typical run. The experimental conditions were: 561° C inlet temperature, 2.38 l/min inlet flow rate (corresponding to a velocity of 0.96 m/sec), and close to atmospheric pressure (0.01 kg/cm²·G pressure gauge, corresponding to an absolute pressure of 1.01 bar). The typical patterns of inlet and outlet flow velocities, inlet and outlet temperatures, pin-surface temperatures and void fraction during the different stages of boiling (incipient boiling, bubbly, slug and annular flows) are represented:

- At boiling onset, the outlet flowmeter F-7 registered an abrupt change of the flow, followed by oscillations that indicate a repetition of bubble formation. From the sodium outlet temperature (T-5), it is clear that the liquid around the vapor bubbles was highly subcooled.
- Following an increase of the power flux, the outlet temperature still remained below saturation, and boiling continued in a subcooled environment. The void fraction increased up to an almost constant value of 0.3 in the bubbly flow regime.

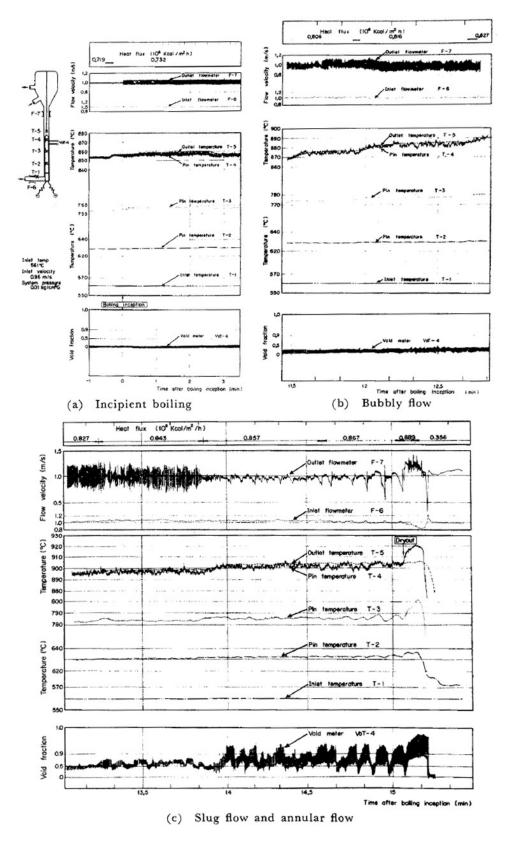


Figure B.3. Experimental records from flowmeters, thermocouples and void-meter during steady-state boiling (run B-102) in the SIENA annular test-section [Kik75]

B. REVIEW OF SODIUM BOILING EXPERIMENTS AVAILABLE FOR CODE BENCHMARKING

- Further increase of the heat flux gradually raised the void fraction up to about 0.7. This stage was considered to be representative of the slug flow regime.
- An increase of the heat flux up to $0.857 \times 10^6 \text{ kcal/m}^2 \cdot \text{h} (99.6 \text{ W/cm}^2)$ changed the outlet flow signal F-7, now in the region of the bubbles. The sodium outlet temperature T-5 reached saturation. This was considered to be the annular flow regime, with a liquid film thickness estimated to be approximately 0.13 mm.
- Upon further increase of the heat flux to 0.889×10^6 kcal/m²·h (103 W/cm²), the pinsurface temperature T-4 registered a sharp rise, indicating the dryout of the residual liquid film. This resulted in a large generation of vapor bubbles which blocked the channel, as indicated by the decreasing inlet flow rate (F-6). The outlet flow rate, on the other hand, was increased by the ejection of liquid. In order to preserve the heater integrity, the heat flux was quickly decreased to 0.356×10^6 kcal/m²·h (41.4 W/cm²).

Additionally, the steady-state boiling experiments under forced-convection conditions revealed that the incipient boiling wall superheat (between 9 and 69°C) decreased exponentially with increasing flow velocity [Kik74] and that the two-phase flow pattern changed, with increasing heat flux, from bubbly flow to slug and annular flow [Kik75].

Loss-of-flow experiments

Since the voiding rates in fast reactor coolant channels during an accident can differ significantly from the steady-state boiling situation, experiments under loss-of-flow conditions were performed in the single-pin annular channel. The experimental results have been reported by Kikuchi [Kik78c]. The tests were conducted with a constant heat flux, and the inlet flow rate was reduced or stopped according to the following methods:

- pump coast-down, to simulate a pump coast-down accident;
- sudden pump stop, which simulated the flow coast-down caused by a pipe rupture accident;
- valve closure, simulating inlet channel flow blockage.

The experiments were operated with heat fluxes ranging from 32 to 129 W/cm^2 , flow velocity at boiling inception between 0 and 0.65 m/sec, inlet temperature between 352 and 424°C, and cover gas pressure between 1.09 and 1.16 bar.

Figure B.4 shows typical records of temperatures, flowates, void meters, accelerometer and pressure transducers during an experiment (run FC-104), conducted by the sudden pump stop method. The experimental conditions were a heat flux of 32 W/cm^2 , inlet temperature of 391°C and cover gas pressure of 1.12 bar.

The initial bubble formed at the end of the heated section, 53 s after the beginning of the LOF. It expanded rapidly, expelling the upper and lower liquid columns. Boiling onset caused abrupt changes in readings of the outlet flowmeter, accelerometer and pressure transducers, which were followed by oscillations. The bubble repeated its expansion and contraction three times. Even though the power was switched off at 54.27 s, the boiling continued for a while. A large bubble collapsed at 54.54 s, which caused the upper liquid column to re-enter and collapse with the lower column, generating small bubbles. These small bubbles disappeared at 55 s.

In the described experiment, the single-bubble slug expulsion pattern was dominant. The thickness of the residual liquid film was evaluated as between 0.05 and 0.29 mm. Observations indicated that this became thinner with higher incipient-boiling wall superheat [Kik78c].

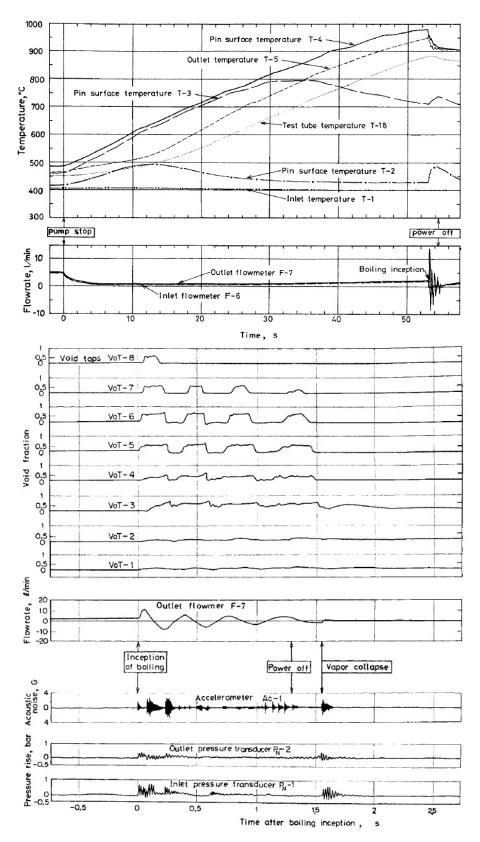


Figure B.4. Experimental records from flowmeters, thermocouples, void meters, accelerometer and pressure transducers during transient LOF boiling (run FC-104) in the SIENA annular test-section (adapted from [Kik78c])

B.2.2 The 7-pin bundle test section and associated tests

Since the boiling phenomenon in a reactor fuel assembly can be quite different from that in single-pin geometry, further experiments were conducted by PNC using a 7-pin bundle. Different test conditions were used to investigate forced-convection incipient boiling: quasi steady-state [Kik78b], local boiling downstream with a local flow blockage [Kik77], and transient boiling under loss-of-flow [Kik78a] and overpower conditions [Kik79].

Description of the 7-pin bundle test section

The 7-pin bundle test section is shown in Fig. B.2b. It consisted of an electrically heated 7-pin bundle centered in a hexagonal tube of 24 mm inside flat-to-flat distance. The heater pins were 6.5 mm in diameter and 1515 mm long, which is approximately the half-length of the fuel pins of the Japanese LMFBR prototype MONJU. The pitch-to-diameter ratio was 1.22. The heater pins were wrapped in a 1.3 mm diameter wire with 264.8 mm helical pitch. They could be operated at a maximum heat flux of 300 W/cm². The outer wall was kept under adiabatic condition, thanks to a compensating heater and a thermal insulator. The by-passes of the test section enabled to simulate other subassembly channels adjacent to the boiling channel.

In order to investigate local boiling, a grid spacer, which covered 42% of the total flow area, was mounted in a dedicated experiment at the distance of 350 mm from the start of the heated section. The grid spacer consisted of seven stainless steel tubes of 7.9 mm outer diameter and 5 mm height. A 0.5 mm thick stainless steel plate was welded upstream of the grid spacer and blocked the six central subchannels. This locally blocked bundle has been described by Kikuchi et al. [Kik77].

Instrumentation

The pin-surface temperatures were measured by many chromel-alumel thermocouples (T-11 through T-65) of 0.3 mm diameter, which were embedded in the outer surface of each pin. The wire-wrap thermocouples T-1 \sim T-7 indicated the local coolant temperatures. The thermocouples T-101-1 \sim T-101-4 were welded on the outside surface of the hexagonal tube to measure the local tube temperatures. The inlet and outlet sodium temperatures were measured by the thermocouples T-111 and T-112, respectively.

The sodium velocities at the inlet and outlet were measured by the electromagnetic flowmeters F-104 and F-105, respectively.

Potential-tap type void meters (VoT-1~VoT-4) were used for the detection of vapor bubbles at the inception of boiling and for recording their subsequent behavior.

Strain-gauge type pressure transducers (P_N -104 and P_N -105) were used to record the changes in pressure during boiling at the bundle inlet and outlet.

Three types of acoustic transducers were used to measure the acoustic noise associated with boiling, viz. a high-temperature lithium niobate microphone (BD-101), quartz accelerometers (Ac-101 and Ac-102) and a condenser-type microphone (M-101).

Incipient boiling under forced-convection conditions

A first series of experiments was conducted to measure the temperature distributions in the bundle under non-boiling conditions. Then, with constant flow rate, inlet temperature and cover gas pressure, the heat flux was gradually increased up to the inception of boiling. Particular emphasis has been brought on the incipient boiling (IB) superheat and voiding patterns.

A study on the effect of flow velocity on the degree of IB superheat revealed that, similarly to the results obtained in single-channel geometry, the IB wall superheat decreases with increasing flow velocity.

Figure B.5 shows typical records of the void meters, thermocouples, pressure transducer and flowmeters in the case of single-bubble slug expulsion (experiment 7B-167). This rapid coolant voiding was observed in the case of high superheat. The experimental conditions were: 445° C inlet temperature, 0.43 m/s inlet velocity with a cover gas pressure of 1.04 bar and a heat flux of 91.8 kW/cm². Void was first detected at VoT-6, at the end of the heated section. It then expanded rapidly, expelling the upper and lower columns of liquid. The signals from the flowmeters (F-104 and F-105) and pressure transducer (P_N-104) showed abrupt changes upon boiling inception, followed by oscillations. The central pin-surface temperature (T-13) decreased nearly to saturation and remained more or less constant after boiling inception. The outlet temperature T-6 and outer pin-surface temperature T-33, however, remained below saturation.

The first bubble collapsed 0.64 s after boiling onset, downstream of the heated section, according to the associated pressure pulse registered by the pressure transducers. Even though power was decreased at 2.26 s, boiling continued for a while.

Local sodium boiling behind local flow blockage

Local boiling phenomena were investigated in the locally blocked 7-pin bundle. The inlet temperature, flow rate and outlet pressure were held constant, and the heat flux was gradually increased up to boiling inception. After boiling onset, the heat flux was further increased step-by-step until dryout occurred.

Experimental results for incipient boiling, and for the bubbly and slug flow regimes, have been reported by Kikuchi et al. [Kik77]. Figure B.6 shows the change in the heat flux, flow velocities, temperatures, void fractions and pressure rises under annular flow and dryout conditions. The large oscillations observed in the outlet mass flow rate (F-105) at the beginning of the period covered indicate a wavy pattern of fairly long period, quite different from the slug flow. This change was due to the slowing down of the bubble collapse, since the outlet temperature (T-112) approached the saturation temperature. The bulk boiling indicated an annular flow regime. A further increase of the heat flux up to 180.2 W/cm² produced an alternate mode in the outlet flow signal (F-105). This change was due to the ejection of liquid films and/or liquid droplets, followed by the generation of a large amount of vapor bubbles. This reduced the inlet flow rate, as revealed by the sharp decrease in the F-104 record. A rapid increase of the void fractions indicated the rapid voiding of the upstream region. Then, the pin-surface temperatures (T-12 and T-13) registered a sharp rise, indicating the occurrence of dryout of the residual liquid film. The power was quickly shut down to preserve the heaters' integrity.

Transient loss-of-flow conditions

In order to study sodium boiling under loss-of-flow conditions, the flow was reduced or stopped during the tests, while maintaining a constant inlet temperature, cover gas pressure and heat flux. The methods used were similar to those applied in the single-channel test section, i.e. pump coast-down, sudden pump stop and valve closure.

Figure B.7 shows typical signals from thermocouples and flowmeters during a sudden pump stop experiment (run 7FC-105). The experimental conditions were a heat flux of 49 W/cm², inlet temperature of 476°C and cover gas pressure of 1.07 bar. The flow rate decreased after the pump power was switched off at 0 s. The coolant remained in single phase during the first 11.6 s. The outlet flowmeter (F-105) registered an abrupt change upon boiling onset. Because of the

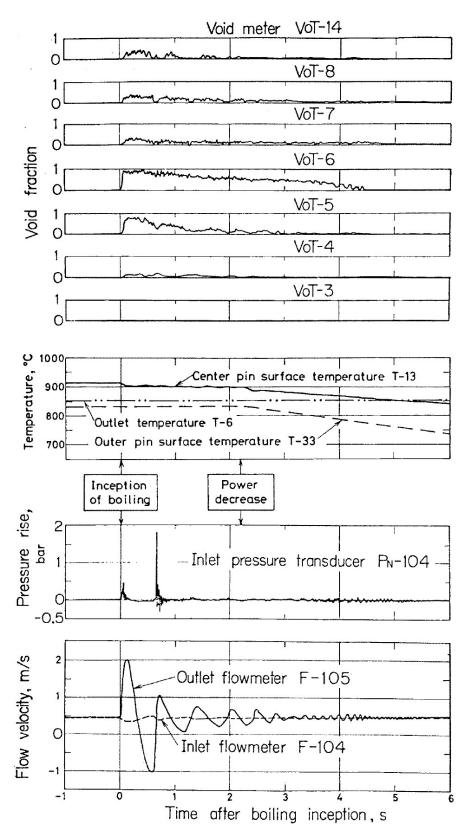


Figure B.5. Experimental records from void-meters, thermocouples, pressure transducer and flowmeters during single-bubble slug expulsion (run 7B-167) in the SIENA 7-pin bundle [Kik78b]

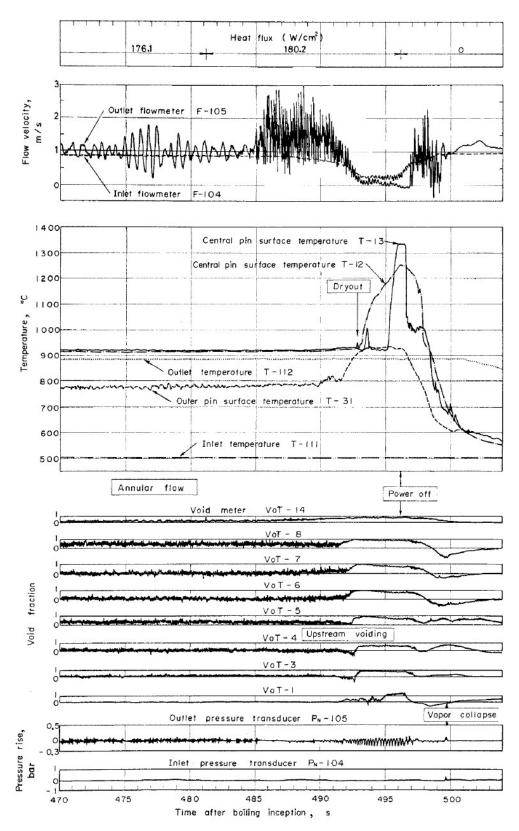


Figure B.6. Experimental records from flowmeters, thermocouples, void-meters and pressure transducers during steady-state boiling (run LB-214) in the SIENA locally blocked 7-pin bundle [Kik77]

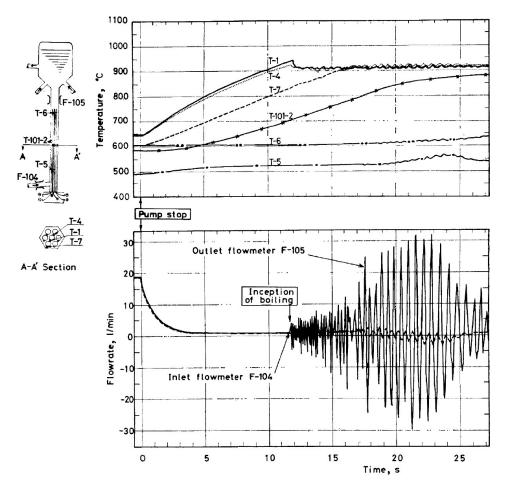


Figure B.7. Experimental records from thermocouples and flowmeters during a loss-of-flow transient (run 7FC-105) in the SIENA 7-pin bundle [Kik78a]

large radial temperature gradient between the central subchannel (T-1 and T-4) and the outer subchannel (T-7), the boiling was initially limited to the central subchannel. While the vapor bubble repeated its formation and collapse, the outer subchannel temperature (T-7) increased to the saturation temperature and the boiling region slowly spread to the outer subchannel. Signals from the void-meters, flowmeter, pressure transducer and noise detector are provided in [Kik78a]. Boiling was first detected at the end of the heated section (VoT-6). When the bubble entered the outer subchannel, its growth was sharply delayed and it immediately condensed since the coolant was highly subcooled in the outer subchannel. The bubble then repeated its formation and collapse. The pressure transducer $P_N - 104$ recorded larger amplitudes at the bubble collapse than at its formation. The boiling region then spread slowly and the vapor reached the void-meters VoT-4 and VoT-9 14.0 s after boiling onset. The quieter signal from the pressure transducer indicated that the bubble did not collapse completely during the expansion of the void region. Even though the heater power was switched off 15.5 s after boiling onset, boiling continued for a while. Following the vapor collapse, registered 17.1 s after boiling onset, the upper liquid column collided with the lower column. The pressure pulse associated with this sodium hammer phenomenon was measured to be 3.38 bar by the inlet pressure transducer $(P_N - 104).$

Results from experiments with a high superheat showed a rapid coolant voiding and have been described in detail by Kikuchi [Kik78a].

In general, two-dimensional voiding patterns were found to be dominant in 7-pin geometry. No strong effects were observed of the temperature ramp rate on the incipient-boiling wall superheat, and the data were scattered over a range as large as $\sim 190^{\circ}$ C. The thickness of the residual liquid film (0.05 to 0.29 mm) was observed to become thinner with higher IB wall superheat.

Transient overpower conditions

Further experiments were undertaken to evaluate the sodium boiling phenomena under overpower conditions in the 7-pin bundle. Experimental results obtained on the pressure rise taking place upon vaporization and vapor collapse, and voiding patterns observed under transient overpower conditions, were reported by Kikuchi [Kik79].

Figure B.8 presents test data recorded during a typical overpower transient (run 7B-185). The experimental conditions were: inlet temperature 448°C, inlet flow velocity 0.92 m/s and cover gas pressure 1.025 bar. The heat flux was first held at an initial value, and then linearly increased until boiling inception. Upon boiling inception at 5.48 s, the outlet flow velocity (F-105) registered abrupt changes followed by large oscillations – indicating bubble formation and collapse, while the inlet flow velocity (F-104) remained constant. The outer subchannel temperature (T-7) is seen to increase at a slower rate than the central subchannel temperature (T-1), indicating the formation of a large gradient in the radial temperature distribution. After the power switch-off at 7.13 s, the outlet temperature (T-6) continued to rise for some time, due to the heat capacity of the unheated parts and the heat transport delay.

Records from the void-meters reveal that the initial bubble was formed at the level of VoT-7, i.e. at the end of the heated section. Upon reaching the subcooled region, the bubble growth was inhibited and the bubble finally collapsed. The bubble formation and collapse was then successively repeated, as indicated by the pulsation of pressure transducers $P_N - 104$ and $P_N - 105$, larger oscillations being recorded upon bubble collapse than upon bubble formation. The boiling region then slowly spread downstream, as indicated by the void-meters, and the rise of the peripheral temperature (following that of the central subchannel) suggests that the boiling also spread in the radial direction. Boiling was still recorded for a while beyond the power switch-off, i.e. 1.65 s after boiling inception. The sharp peak registered by the pressure transducers at 1.97 s represents the collapse of a fairly large bubble, following which the upper liquid column collided with the lower column and then rebounded, generating a number of small bubbles, which, in turn, disappeared at 2.61 s.

B.2.3 The 19-pin bundle test section and associated tests

Larger-scale experiments using an electrically heated 19-pin bundle were performed to obtain a better understanding of the boiling phenomenon in a full-size LMFBR subassembly. Results of incipient-boiling wall superheat, pressure rises at vaporization and vapor collapse, and coolant dynamics have been published by Kikuchi and Haga [Kik81].

Description of the 19-pin bundle test section

A sketch of the 19-pin bundle test section is presented in Fig. B.2c. It consisted of an electrically heated 19-pin bundle centered in a hexagonal channel of 36.7 mm flat-to-flat inside distance. The heaters were similar to those used in the 7-pin bundle, i.e. 6.5 mm in diameter and 1515 mm long. The bundle pitch was 7.9 mm, which corresponds to a pitch-to-diameter ratio of 1.22. Each pin was wound with a 1.3 mm diameter wire in clockwise direction at a 264.8 mm helical pitch. The heater pins had a heating length of 465 mm and could be operated at a

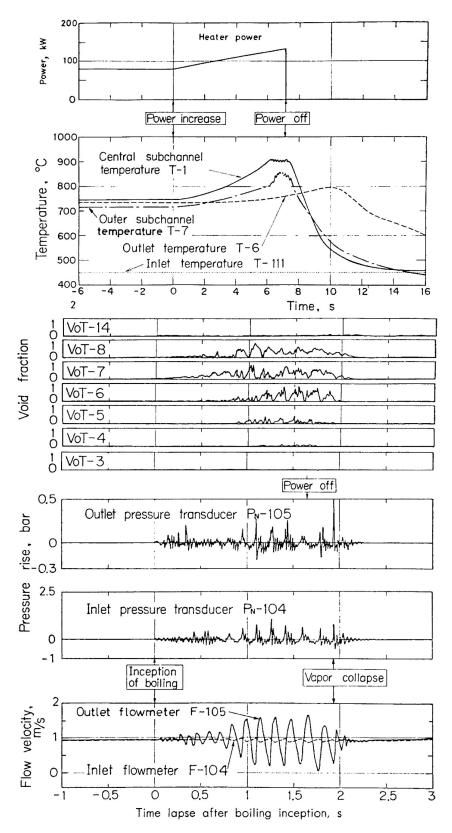


Figure B.8. Experimental records of heater power, temperatures, void fraction, pressure and flow velocity during an overpower transient (run 7B-185) in the SIENA 7-pin bundle [Kik79]

maximum heat flux of 300 W/cm^2 . The outer wall was kept under adiabatic conditions, thanks to a compensating heater and a thermal insulator. The by-passes of the test section enabled one to simulate other subassembly channels adjacent to the boiling channel.

Instrumentation

Numerous chromel-alumel thermocouples were installed at various points along the test section. The thermocouples T-1011 through T-3124 (0.3 mm diameter) were embedded in the outer surface of the pins to measure the pin-surface temperature. The coolant temperature was measured by thermocouples T-101 through T-306, wounded on the wire-wrapper. The coolant inlet and outlet temperatures were measured by the thermocouples T-113 and T-114, respectively. Thermocouples T-4 and T-10 provided local coolant temperatures at the outlet. Thermocouples T-102-1 \sim T-102-4 were welded on the outside surface of the hexagonal channel wall.

Void was detected and measured with the potential-tap void-meters VoT-1 through VoT-14.

The sodium velocities at the inlet and outlet were measured with electromagnetic flow meters F-106 and F-107, respectively.

The strain-gauge type pressure transducers P_N -106 and P_N -107, installed at the inlet and outlet, respectively, measured the change of pressure during sodium boiling.

Acoustic noise associated with boiling was detected by three acoustic transducers of different types, viz. quartz accelerometers (Ac-101 and Ac-102), lead-zirconate-titanate microphones (M-103 and M-104) and high-temperature lithium niobate microphones (BD-101~BD-103).

Loss-of-flow experiments

The operating procedures were similar to those followed using the 7-pin bundle, with a first series of experiments conducted under steady-state non-boiling conditions and a second series dedicated to the investigation of transient boiling phenomena under loss-of-flow conditions. The inlet temperature, outlet cover gas pressure and heat flux were held constant. The flow was reduced or stopped using similar methods as applied with the annular and 7-pin bundle test-sections: pump coast-down, sudden pump stop and valve closure.

Figure B.9 shows typical measurements of the pin-surface temperature distribution 440 mm downstream from the starting point of the heated section, under different steady-state non-boiling conditions, viz.

- at flow velocity (0.95 m/s), with a heat flux of 11.2 W/cm² and inlet temperature of $286.1^{\circ}C$;
- at higher flow velocity (4.66 m/s), with a heat flux of 55.3 W/cm² and inlet temperature of 245.4° C.

Results from a pump coast-down experiment (run 19FC-111) are presented in Figs. B.10a and B.10b. The experimental conditions were: heat flux 150 W/cm², initial steady-state flow velocity 2.44 m/s, inlet temperature 366° C and cover gas pressure 1.04 bar. Boiling onset was detected 15.4 s after the pump coast-down and resulted in an abrupt change of the outlet flow rate (F-107), followed by violent oscillations which indicate the successive formation and collapse of bubbles. No high superheat was observed at boiling inception. Similarly to the described LOF experiment in the 7-pin bundle, the surrounding subchannel temperatures at the top of the heated section (represented by T-202 and T-303) are seen to have a delayed increase compared to that of the central subchannel temperature (T-101). This indicates the formation

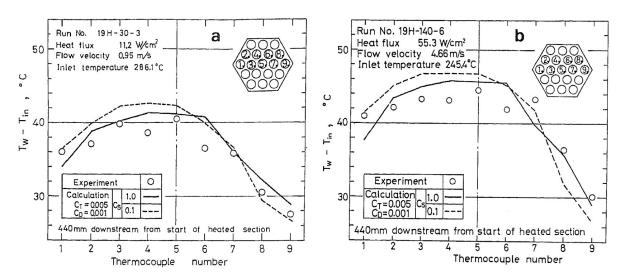


Figure B.9. Measured pin-surface temperature distributions under steady-state non-boiling conditions in the SIENA 19-pin bundle [Kik81]

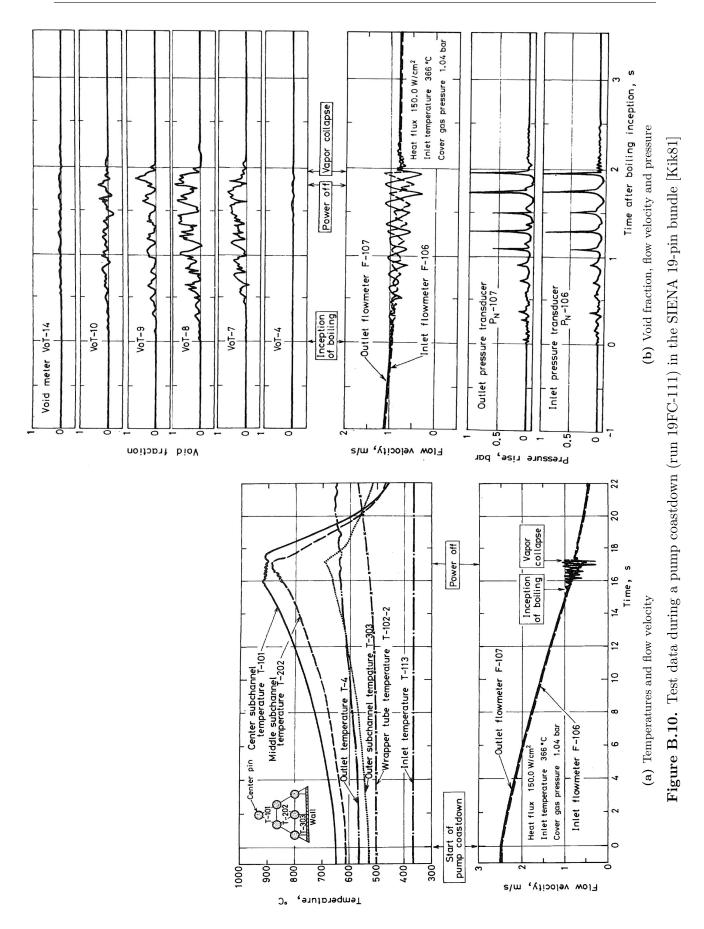
of a temperature gradient in the bundle steeper than that at initial steady state. The expansion of the boiling region is also very similar to that observed in the 7-pin bundle LOF experiment. The initial bubble was detected at the top end of the heated section (VoT-8). When reaching the outer, subcooled subchannel, its growth rate decreased and the bubble collapsed. Generation and collapse of bubbles was then repeated, as indicated by the pulsations registered by the pressure transducers P_N -106 and P_N -107, with larger oscillations upon collapse of the bubble than at its formation. The void region then spread axially, as indicated by the void-meters, and also radially, as suggested from the temperature rise of the surrounding subchannels. Power was switched off 1.8 s after boiling inception. The collapse of a large bubble was recorded 1.95 s after boiling onset, as per the sharp peak registered by the pressure transducers, upon which the upper liquid column collided with the lower column and then rebounded, generating a number of small bubbles, which, in turn, disappeared 2.6 s after boiling inception.

Figure B.11, which represents the evolution of the boiling region, highlights the fact that boiling was initiated in a highly subcooled liquid of the surrounding subchannel, as evidenced by the temperatures in Fig. B.10a. In this evaluation, a slug bubble was assumed to occupy the total cross-sectional flow area and expand both up- and down-stream like a piston. The singledotted line, which represents the interface between liquid and vapor regions and was evaluated from flowmeter signals, indicates that the axial vapor expansion was extremely limited compared with the two-phase region (solid line representing the interface between liquid single-phase and liquid-vapor two-phase regions, drawn from void-meter signals). This means that the bubbles, which were generated in the hottest central subchannel, had their growth markedly inhibited because of the highly subcooled liquid in the surrounding channels. The boiling region is seen to spread slowly in both the axial and radial directions.

Other experiments, conducted by sudden pump stop and valve closure methods, showed similar effects of the steep temperature gradient on the transient boiling phenomena.

B.2.4 The 37-pin bundle test section and associated tests

Further experiments were performed by PNC in 37-pin bundles to study (i) boiling regime transition and dryout conditions during a loss-of-flow transient [Hag84], as well as (ii) sodium



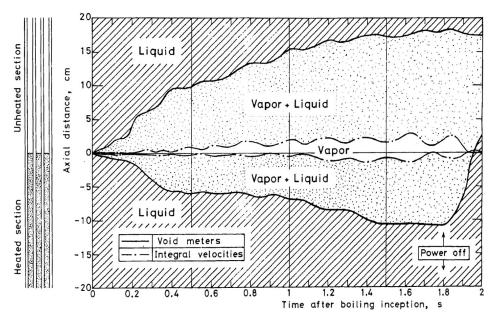


Figure B.11. Experimental results of the axial-channel voiding pump coastdown (run 19FC-111) in the SIENA 19-pin bundle [Kik81]

boiling and dryout in partially blocked fuel subassemblies [Uot84], and (iii) flow patterns and dryout under sodium boiling conditions at quasi steady-state low-heat-flux levels [Yam87]. Two 37-pin bundles (37F and 37G) were built for the purpose.

Description of the 37-pin bundle test section

The test section 37F is presented in Fig. B.2d. It consisted of 37 electrically heated pins, with tantalum as heating element. The electrical resistance of tantalum is changed by temperature, such that the maximum heat flux during boiling was higher than the mean axial heat flux by 10-20%. Because one pin had failed in a preliminary experiment, every boiling run was conducted with 36 pins heated (the position of the defective pin is illustrated in Fig. B.13d). The heat flux distribution was uniform. The diameter of each pin was 6.5 mm and the pin pitch was 7.9 mm. The cladding consisted of 0.55 mm thick SUS-316. A spacer wire of 1.3 mm diameter was wrapped around each pin with a helical pitch of 265 mm. The bundle had a 450 mm heated length and a 715 mm simulated fission-gas plenum at its downstream position. The total length of the pins was 1515 mm. The bundle was centered in an hexagonal Inconel 600 tube of 50.4 mm flat-to-flat inside diameter and 10 mm thickness. The gap between the peripheral pins and the inner duct wall was 1.45 mm. A thermal insulator on the outer wall of the hexagonal tube minimized heat losses through the duct wall.

Instrumentation

Chromel-alumel thermocouples of 0.3 mm diameter were located at 10 positions, labeled alphabetically from A to J, to measure pin-surface and subchannel temperatures. They were embedded in the outer surface of the pin clad, and the probes for the subchannel temperatures were projected from the pin surface. Subchannel thermocouples were located in several spacer wires. The test-section inlet and outlet temperatures and outer duct wall temperatures were monitored by additional thermocouples. Two types of void-meters were used, viz. 14 resistive void-meters, attached within the test section, and 10 Chen-type void-meters, located in the spacer wires. The sodium velocities at the inlet and outlet of the test section were measured by electromagnetic flow-meters. Pressure transducers were also installed at the inlet and outlet of the test section to measure the pressure changes during boiling.

Loss-of-flow experiments

Loss-of-flow experiments were performed to investigate the transition of boiling regime and dryout conditions in sodium flow during such a transient. Similar operating procedures were followed as for the other test sections, with a first series of experiments under steady-state non-boiling conditions and a second series under loss-of-flow conditions. A total of 34 runs were conducted.

Figure B.12 shows typical measurements of the coolant temperature profiles for different runs across two sections at X = -198 mm and -11.3 mm, where X denotes the distance from the downstream end of the heated zone (a negative value indicates a section located upstream from the end of the heated zone). Results for high flow (run 37H-260-2) and low flow (run 37H-30-2) are presented in Fig. B.12a. It appears that at section C (X = -198 mm) the temperature profile at low flow was steeper than that at high flow. This may be due to insufficient mixing between the subchannels. However, at section G (186.7 mm downstream from section C), the temperature profiles in the two runs were almost identical.

In the series of boiling experiments, the pin power was shut-down at the inception of flow reversal to maintain the integrity of the bundles, except for Run 37FC-34, which was the only case terminated by the occurrence of dryout. A summary of the results recorded during this test is presented here. More detailed results as well as test data from other tests have been reported by Haga [Hag84].

The experimental conditions of Test 37FC-34 were: inlet temperature 530° C, initial steadystate flow velocity 5.24 m/s, system pressure at the end of the heated zone 1.46 bar, steady-state heat flux 89.4 W/cm², average heat flux during boiling 74.4 W/cm², and maximum heat flux during boiling 80.3 W/cm².

The flow coast-down started at 0 s. Boiling was initiated at 14 s, when the inlet velocity had decreased to 0.67 m/s. The radial temperature distributions before the flow coast-down and at boiling inception are shown in Fig. B.12b. Figure B.13 shows the evolution of selected experimental records during the transient. The central pin temperatures (T-101G and T-203G in Fig. B.13a) quickly reached the saturation temperature, followed later by the temperature in the third subchannel ring (T-306G). The temperature ramp rate in the outermost subchannel ring was so low that T-408G only reached saturation at 26 s. Since the saturated-temperature regions were seen to coincide with the voided zones [Hag84], it can be assumed that the voided region covered the entire cross-section area at that time. Figure B.13d shows how the saturated temperature regions expanded radially at cross-sections G and F (X=-11.3 and -33.4 mm, respectively).

The inlet flow velocity showed an increase of the period and amplitude at 26 s (see Fig. B.12b), followed by a further acceleration of its decreasing rate. These changes in the inlet flow would be due to the multiplied pressure loss caused by the voided zone, which would have grown enough to occupy the entire cross-section. The first inlet flow reversal is observed at 30 s, and then repeated several times. The negative peak values of flow reversal increased gradually until the coolability crisis (i.e. dryout) was reached. The pin power was automatically shut-down when the temperatures exceeded 1000° C.

Figure B.13b shows the evolution of the pin-surface temperatures at section D, upstream of the heated zone (X=-143.8 mm). The central subchannel temperature reached saturation at 26 s, after what the outer subchannel thermocouples recorded an accelerated ramp rate.

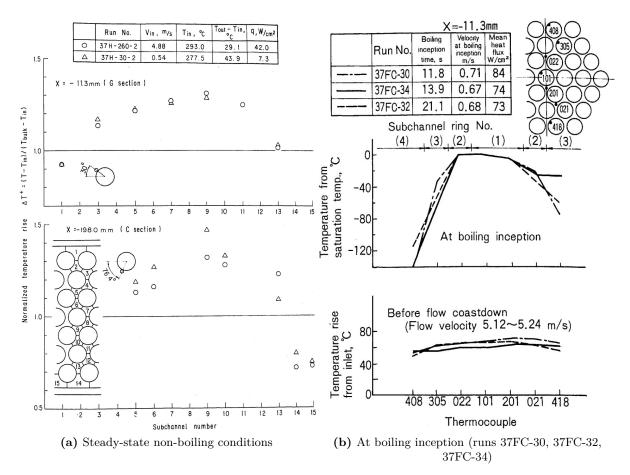
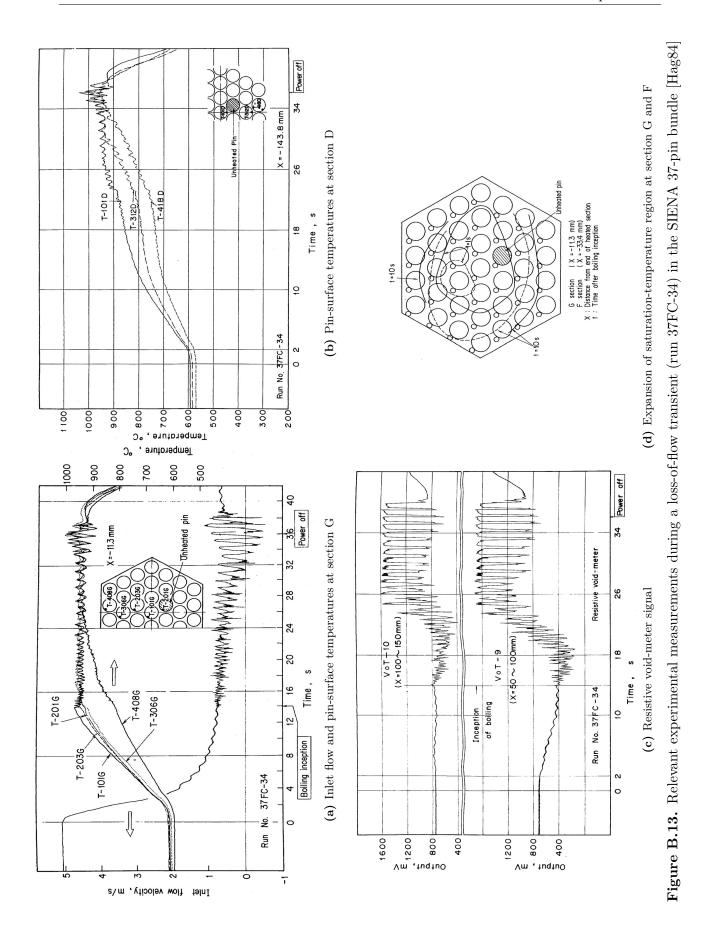


Figure B.12. Measured pin-surface temperature distributions in the SIENA 37-pin bundle [Hag84]

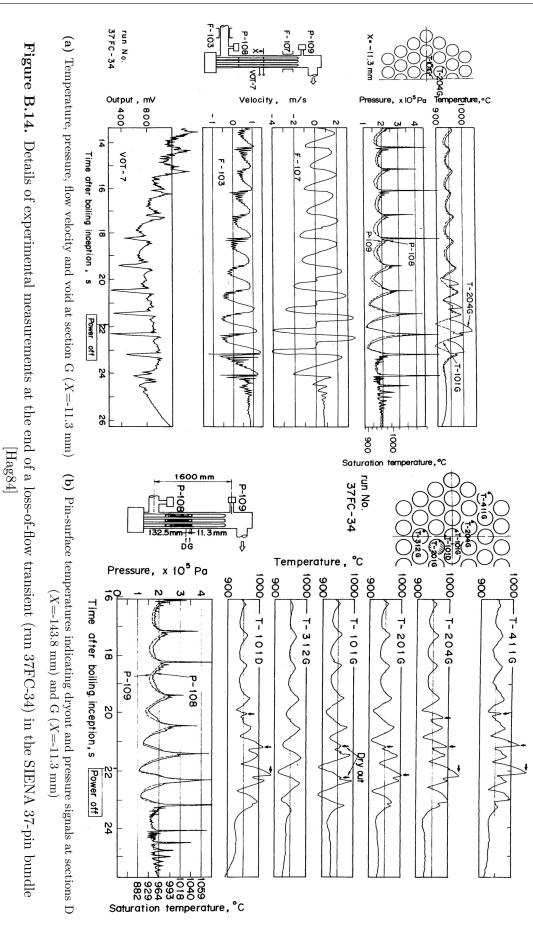
Figure B.13c shows records of the resistive void-meters VoT-9 and VoT-10, which give ouputs corresponding to the averaged void fraction over an axial length of 50 mm. The chain of trapezoidal signals after 20 s suggets that slugs of void and liquid passed alternately.

Figure B.14 shows details of the test data toward the end of the transient. The pressure spikes periodically observed are due to the bubble collapse. Initially, it was observed from the temperature records that the temperature saturation corresponded to the changing pressure. Signal T-204G (Fig. B.14a) shows an excursion departing from the saturation temperature (thus indicating the onset of dryout) at around 20 s after boiling inception. Then, the void-meter indicates that the dried pin experienced rewetting at 19.3 s, after having been covered by vapor for about 1 s. It is seen that the inlet flow reversal first occurred at 19.4 s. Meanwhile, liquid could be supplied in the bundle, thus enabling rewetting to occur. Also, it can be noticed that dryout was not detected by T-101G, thus demonstrating the importance of local phenomena in dryout. The records of thermocouples at different radial and axial locations (Fig. B.14b) indicate that dryout may occur over the wide region covered by void.

Summarizing the different results, boiling onset was first observed at the end of the heated zone, and then expanded mainly to the central upstream subchannels and to the unheated downstream subchannel according to the expansion of the saturation-temperature region. When the bubble covered the whole flow cross-section, the inlet flow reduction was accelerated. The inlet



191



and outlet flow velocities oscillated violently upon the piston-like bubble growth and collapse, and an inlet flow reversal was observed. Dryout of pin surfaces occurred after the inception of flow reversal. Dryout was temporarily stopped by rewetting, but took place again in the next flow reversal. This sequence was repeated several times. Gradually, the dryout region expanded over the entire voided region.

B.3 The KNS experiments

As presented in Chapter 4, a series of experiments investigating sodium boiling was carried out in the 1980s at the Kernforschungszentrum Karlsruhe (KfK) in Germany. A dedicated facility, the KNS loop¹, was designed for this purpose. General sodium boiling phenonema were investigated in single-pin, 7-pin and 37-pin bundle geometries. The KNS loop and the various test sections used for the experiments are presented in Fig. B.15.

B.3.1 The tubular test section and associated tests

Basic research on sodium two-phase flow was performed using a tubular test section. The test section, presented in Fig. B.15b, consisted of an HF-induction heated Ni-tube of 9 mm inner diameter and 168 mm heated length. Experiments performed by Peppler et al. [Pep70] focused on the understanding of the vapor bubble dynamics in sodium flow, including bubble nucleation, growth and shrinkage. Investigations of the heat transfer in sodium two-phase flow were reported by Schleisiek [Sch70]. A test series, comprising more than 60 single tests, was aimed at measuring the two-phase pressure loss and film thickness up to dryout under quasi steady-state boiling conditions. Results of the two-phase friction pressure drop measurements have been reported by Kaiser et al. [Kai74].

B.3.2 The 7-pin bundle test section and associated tests

Further experiments were performed in an electrically heated 7-pin bundle to investigate the characteristics of sodium boiling up to the coolability limits in multi-pin bundles. The important aspects of these investigations, reported by Kaiser and Peppler [Kai77a], were the flow patterns and two-phase pressure drops. In particular, the results provided a source of data against which the two-phase pressure drop correlations used in sodium boiling codes can be validated [Kai77a, Kai79]. These data have also been presented in Fig. 3.7.

Quasi steady-state was achieved by reducing the mass flow rate stepwise by means of the throttling valve at the inlet of the bundle, maintaining the heat flux and cover gas pressure at constant values. Experiments at both low $(30-42 \text{ W/cm}^2)$ and high $(132-173 \text{ W/cm}^2)$ power were conducted. Comparison of the results obtained in pin geometry with the single-channel experiments showed remarkable differences in the dryout behavior. In the first case, dryout occurred with vapor quality as low as about 34%, whereas this limit was measured to be in the range 85-98% in the tubular section. Also, the adiabatic two-phase pressure drops were seen to be lower in the bundle geometry than in the tubular test section.

Sodium boiling experiments under loss-of-flow conditions were also conducted. The main results have been reported by Aberle et al. [Abe76].

¹Kompakter Natriumsiede-Kreislauf (KNS); German for *compact sodium-boiling loop*

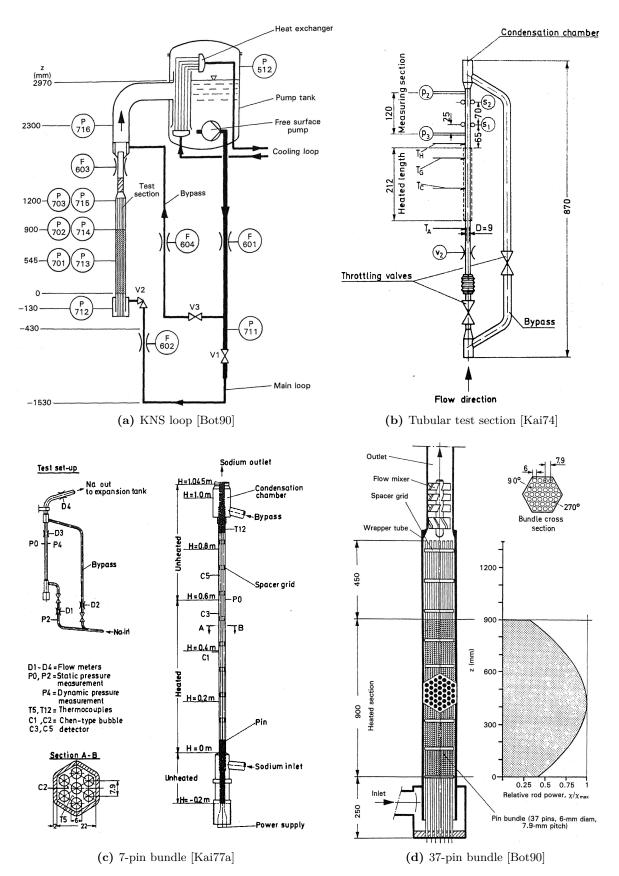


Figure B.15. Schematic diagrams of the KNS loop and associated test sections

B.3.3 The 37-pin bundle test section and associated tests

In the context of fast breeder reactor safety analysis, steady-state and transient sodium boiling tests were performed in an electrically heated 37-pin bundle. The 37-pin bundle was described in Section 4.3 and is illustrated in Fig. B.15d. The steady-state boiling experiments served the investigation of general two-phase flow phenomena. A series of experiments was carried out under natural convection conditions, at decay heat level [Kai84, Kai87]. Another group of tests was conducted under conditions of local blockage, simulating a fuel subassembly with 49% central and 21% corner blockages [Hub84]. Furthermore, extensive work was carried out to study transient sodium boiling simulating a ULOF², from the start of the flow rundown via boiling inception to the onset of dryout.

Results from the steady-state experiments

A series of steady-state boiling experiments under forced-convection conditions was performed in the 37-pin bundle. The test data [Hub87, Kai88] supplied information about the axial and radial void distribution in the bundle, the two-phase pressure drop and boiling heat transfer. The tests were performed at constant heat flux and cover gas pressure (0.8 bar), and the flow was decreased stepwise. The average length of a step was about 2 min. The coolant inlet temperature was in the range of 380-410°C. Figures B.16 and B.17 show the axial and radial temperature and void distributions, respectively, in the steady-state test S33. The test was performed in six steps, with an average heat flux of 77 W/cm² and an inlet flow velocity between 0.76 and 0.34 m/s. The inlet flow velocity was 0.58 and 0.338 m/s for the second and sixth step, respectively.

Figure B.16 shows that the radial temperature profile across the flow cross-section is flatter for the lower flow rate. The coolant axial temperature measurements provide valuable data for the evaluation of the two-phase pressure drop. The large impact of the spacer grids and of the change in the flow cross section at the upper end of the bundle are readily seen on the pressure profile (see Fig. B.16). The measurements of void fraction show very steep gradients at the lower boiling boundary (see Fig. B.17), mainly due to the large vapor/liquid density ratio, typical of alkali metals.

Test data for sodium boiling under natural convection conditions

Further experiments were performed in the 37-pin bundle test section under natural convection conditions, with pin power in the range of the decay power of an LMFBR. The main objectives of the tests were [Kai87]:

- 1. Investigation of cooling of a pin bundle under boiling conditions at decay heat level up to the limits of cooling. These limits were approached in the tests by decreasing the coolant flow rate under the assumption of highly increased flow resistances in the cold leg of the reactor circuit in the case of emergency cooling;
- 2. Determination of the power in excess of the decay power which can be removed from a pin bundle without loss of cooling;
- 3. Investigation of the limit of the pin power which can be removed continuously, with totally blocked bundle inlet.

²Unprotected Loss-Of-Flow

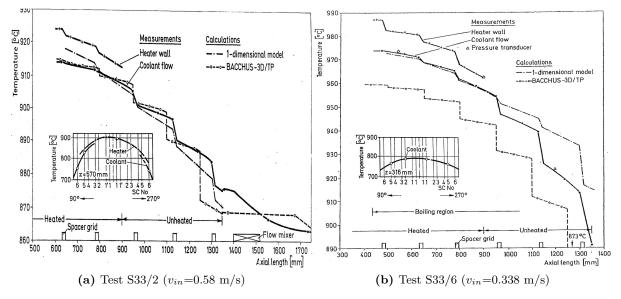


Figure B.16. Axial and radial temperature profiles for steady-state boiling in the KNS 37-pin bundle (Test S33) [Kai88]

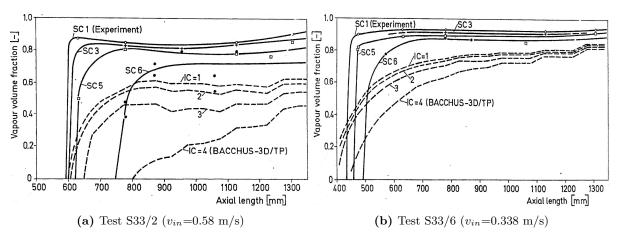


Figure B.17. Axial distributions of void for steady-state boiling in the KNS 37-pin bundle (Test S33) [Kai88]

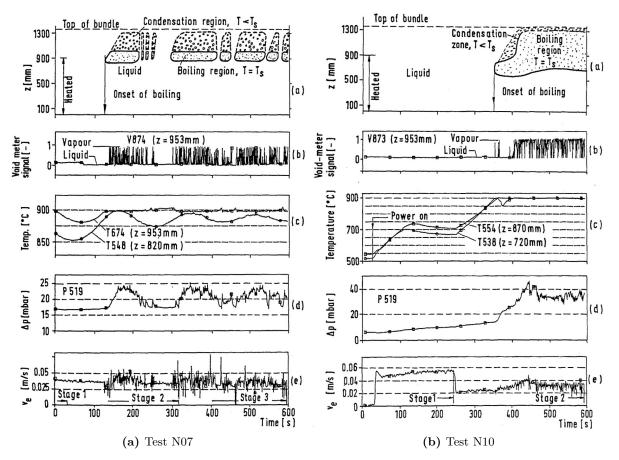


Figure B.18. Characteristic signals and development of boiling under natural convection conditions in the KNS 37-pin bundle [Kai87]

During the tests, the pump and the heat exchanger were out of operation, the low heat input being fully compensated by the heat losses from the loop. The throttle valves V1 and V2 (see Fig. B.15a) were used to set increased flow resistances in the cold leg of the natural convection loop. Except for the very first tests, the bypass valve V3 was closed.

Results of a first series, where only low void quality was obtained, were reported by Kaiser et al. [Kai82]. Investigations of the effects of higher vapor quality were reported later [Kai84]. Eventually, the relevant experimental results were summarized by Kaiser and Huber [Kai87].

Figure B.18 illustrates results from two significant tests with boiling, N07 and N10, conducted with an even power distribution over the cross-section. The pin power was set to 8 W/cm. It shows the temporal axial void distribution, the void meter signal at z=953 mm, two coolant temperature signals, the pressure drop P519 across the throttle valves, and the coolant inlet velocity. The experimental conditions, as well as the course of the boiling tests, are detailed in [Kai87].

Loss-of-flow experiments

As mentioned in Chapter 4, loss-of-flow experiments performed in the 37-pin bundle in the KNS sodium loop were used as basis for a benchmark exercise organized by the LMWBG in 1984. The main results of the reference test, Test L22, were published by Huber et al. [Hub82b]. This test has already been presented and successfully used for the validation of the extended

TRACE code (see Section 4.3).

Experimental data from tests performed at reduced power (Test L26) or slower flow rundown (Test L29) have also been presented in Chapter 4. More detailed results are available in [Hub82b]. Bottoni et al. [Bot90] reported test data from Test L60, characterized by a strong power tilt ($\pm 25\%$) across the bundle cross-section, as also from Test L58, which simulated a slow pump rundown for a power level reduced to around one-third of the nominal value and with increased coolant inlet temperature.

B.4 Other experiments

In addition to the above mentioned experiments, a 19-pin bundle mockup was used in the CFNa and CESAR loops at CEA-Grenoble to investigate steady-state boiling. The results have been applied to perform analysis of slow transient-boiling instability [Sei84, Sei90]. The test section consisted of a bundle with 60 cm heated length and 50 cm prolongation, and an outlet tube of 2 cm internal diameter and 100 cm length. Experiments were performed for various power levels (1, 2, 3, 5, 8, 10, 12 and 16 kW/pin).

A number of experiments were performed using 19 and 61-pin bundles in the THORS facility [Gna84] at the Oak Ridge National Laboratory (ORNL). Sodium temperatures as high as 1010°C were reached, and cladding temperatures went beyond the melting point of stainless steel (1400°C).

A large program of in-pile investigations of various accident types involving sodium boiling phenomena was carried out at the CABRI and SCARABEE facilities at CEA-Cadarache [Nis86, Bai80, Woo80]. Selected experiments from the CABRI loop have been successfully simulated with the extended TRACE code coupled to the thermal-mechanics code FRED [Pon10].

APPENDIX C

TRACE analysis of the latter part of the Phenix Natural Convection test

As mentioned in Chapter 5, data from the latter part of the Phenix Natural Convection (NC) test have been used to validate TRACE single-phase sodium flow modeling. The experimental data have been shared by the CEA in the frame of a Coordinated Research Project (CRP), initiated by the IAEA Technical Working Group on Fast Reactors (TWG-FR).

The Phenix reactor's main characteristics and details of the NC test have been described in Sections 5.1 and 5.2, respectively. This appendix first presents, in Section C.1, the TRACE model of the Phenix primary circuit developed for the analysis. Steady-state calculations at nominal (350 MWth) and reduced (120 MWth) power are compared to the experimental data in Section C.2 for the validation of the model. Section C.3 presents the 'blind' comparison, i.e. the comparison of the test results with those computed prior to the communication of the experimental data, so-called 'pre-test' results. A summary of the analysis is given in Section C.4.

C.1 TRACE model of the Phenix primary circuit

For the analysis of the Natural Convection test, the entire primary circuit was modeled in TRACE. The modeling of the intermediate circuit was limited to the heat exchangers (IHXs) with appropriate boundary conditions on the inlet temperature, flow rate and outlet pressure. The experimental power evolution was used as boundary condition.

Figure C.1 presents the nodalization scheme developed in TRACE to model the Phenix reactor. Special attention has been focused on the accurate simulation of the component elevation, the pool free surfaces and the heat-structure description. Various heat structures have been used to represent:

- the wall between the hot and cold pool;
- the power evacuated through the roof;
- the power evacuated by the emergency cooling circuit (heat structure connected to the vessel cooling system);
- the steel in the pump and diagrid.

Described below are the geometry and nodalization scheme for the core, the pools, the IHXs, the pumps and the diagrid.

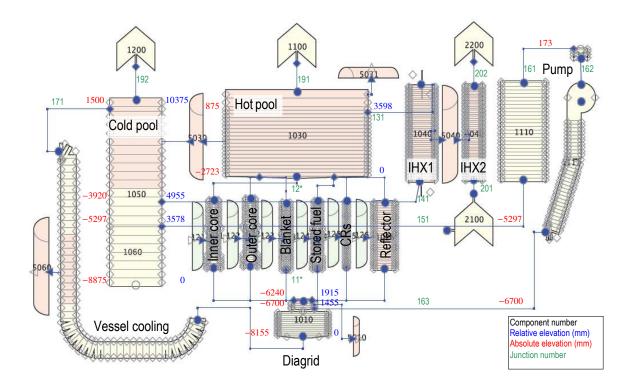


Figure C.1. TRACE nodalization scheme of the Phenix reactor

C.1.1 The core

The Phenix core is composed of inner and outer fissile core regions surrounded by blanket sub-assemblies (SAs) and a number of steel assemblies for reflection and shielding purposes. Figure C.2 presents a scheme of the flow distribution in the different zones. A fraction of the total flow ($\sim 10\%$) is deviated to the lower part of the diagrid and used to cool the main vessel.

The TRACE model considers the following six regions: inner core (54 SAs), outer core (56 SAs), blanket (86 SAs), fuel stored in the core, control rods and steel reflector. The main design characteristics have been presented in Chapter 5.

In order to reproduce the correct pressure drop in the core, a simplified model of the inner vessel (diagrid, core and hot pool) was developed. The latter allowed one to adjust the gagging of each core region in an independent way. For this purpose, each region was simulated with the corresponding nominal conditions, the inlet temperature and flow rate being imposed by a FILL. The hot pool was simulated with a free surface. A BREAK was used to simulate the IHX flow discharge. Having the appropriate core outlet pressure imposed, together with the corresponding flow rate and power, the friction coefficient could easily be adjusted to reproduce the core pressure drop as specified by the CEA. This procedure was repeated for each core region, taken separately, and thus enabled one to reproduce the correct core friction losses in the complete model.

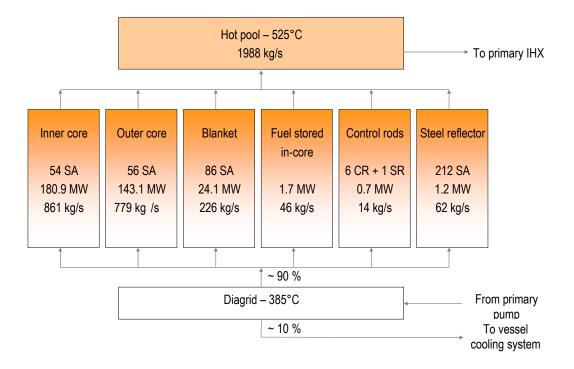


Figure C.2. Distribution of the flow in the Phenix primary circuit

C.1.2 Hot and cold pools

The hot and cold pools are represented with a pipe connected to a BREAK component. The use of side junctions allowed one to connect the different components at the correct elevation. The outlet plenum has been simulated with side junctions (instead of the PLENUM component), as recommended in the TRACE user manual. The hot pool is connected to the IHX in the middle of cell 19, the elevation of which is +875 mm as per the pool nodalization and IHX first-cell orientation (the connecting cell has to be horizontal to ensure that the perpendicular junction is located in the middle of the source cell). The IHX outlet is connected in the middle of cell 11 of the cold pool (-3920 mm). The orientation of the pump and cold pool being identical (i.e. vertical), the pump is connected via a side junction linked at the top of cell 20 of the cold pool (-5297 mm). Furthermore, the vessel cooling component is linked at the top of cell 22 of the cold pool (+1500 mm). The free surface in the latter has not been considered in the modelisation and the component was directly linked to the cold pool.

In order to reproduce the correct levels, the free surfaces of both pools have been initialized at 1783 mm, which corresponds to the specified level at 400°C. The volume of the bottom cells have been adjusted to obtain the sodium mass of 265 t and 536 t in the hot and cold pool, respectively, the specification being assumed to be at 400°C.

C.1.3 IHX and secondary circuit

The four intermediate heat exchangers (IHXs) have been simulated with two counter-current pipes, a downflow pipe in the primary side and an upflow pipe in the intermediate circuit. In order to represent the correct elevation, the primary side pipe was connected to the pools via perpendicular junctions and horizontal cells. This ensured that the IHXs were effectively

connected to the middle of the corresponding pool cells, as mentioned above. The hydraulic diameter, which could not be calculated from the specified design characteristics, was adjusted such as to allow one to reproduce the correct pressure losses between the hot and cold pools. This could be done knowing the pool levels under nominal conditions.

Since the modeling of the intermediate circuit has been limited to the IHXs, appropriate boundary conditions specified by the CEA have been used, viz. the inlet temperature and mass flow rate evolutions presented in Chapter 5, Fig. 5.6.

C.1.4 Pump and diagrid

The three pumps have been simulated together, using a three-fold rated flow and keeping the other rated characteristics at their nominal values. The built-in TRACE pump has been used, yielding satisfactory results. The specified steel mass of 82.5 tonnes was accurately modeled, but an assumption was made on the heat-exchange area since the latter has not been provided by the CEA.

In the diagrid component, the total pump flow divides between the core (~90%) and the vessel cooling system (~10%), as indicated in Fig. C.2. Since the geometry of the diagrid is complex and not detailed in the CRP specifications, the area and friction losses have been adjusted to reproduce the correct flow distribution. This was done using the specifications at nominal power presented in the following section. The specified steel mass of 74.6 tonnes was correctly modelled. The heat-exchange area was assumed to be ~250 m².

C.2 Steady-state results

Prior to the NC test, pre-test 'blind' calculations were performed. The different members participating in the CRP agreed to perform the necessary model adjustments (due to limited design specifications) on the basis of the nominal Phenix operating conditions, viz. corresponding to 350 MWth. The model has been used as such to simulate the Natural Convection test, starting from the reduced power at 120 MWth.

This section presents the different adjustments, performed for 400°C and 350 MWth, together with the comparison of TRACE steady-state results with the test data at both nominal and reduced power.

C.2.1 Cold conditions: 400° C

In order to ensure that the circuit elevations were accurately modeled, a simulation at zeropower, zero-flow was performed at 400°C (initialization temperature for all components). The results showed that no flow was generated, and that the pool levels remained at the initial value of 1783 mm. This demonstrated that the relative elevations of the different components were correctly represented.

C.2.2 Nominal power: 350 MWth

The next step in the validation of the model has been performed for nominal operating conditions, viz. at 350 MW, the pump rotational speed being set at 56.55 rad/s and the intermediate inlet temperature and flow rate at 320°C and 1380 kg/s, respectively.

At this stage, the losses in the diagrid were adjusted to reproduce the core and vessel cooling flow rates. It has been seen that the area of the diagrid mainly influenced the total pump flow, while the hydraulic diameter and friction factor in the lower part of the diagrid affected the flow distribution between the core and the vessel cooling system. The latter was adjusted to

			М	ass flow (k	(g/s)			Elevati	ion (mm)
	Core	Inner core	Outer core	Blanket	Stored fuel	CRs	Reflector	Hot pool	Cold pool
Phenix	1988	861	779	226	46	14	62	2061	1325
TRACE	1988.1	849.1	779.8	236.3	46.7	14.0	62.3	2175	1460
Δ	0.1	-11.9	0.8	10.3	0.7	0.0	0.3	114	135
$\epsilon(\%)$	0.0	1.4	0.1	4.4	1.5	0.0	0.5	5.2	9.2

Table C.1. Comparison of TRACE-calculated results with the experimental data at 350MWth

			Tempe	erature (°C)		
	Inlet core	Outlet core	Inlet IHX1	Outlet IHX1	Inlet IHX2	Outlet IHX2
Phenix	385	525	525	385	320	525
TRACE	384	523	522	383	320	518
Δ	-0.9	-1.7	-2.8	-1.6	0.	-6.8
$\epsilon(\%)$	0.1	0.2	0.4	0.2	0.	0.9

correspond to about 10% of the core flow rate. Due to a lack of detail in the design specifications, the diagrid area was adjusted to simulate the specified total flow with the specified pump head and rated values.

The inlet plenum friction losses were adjusted in order to reproduce the correct hot pool elevation, which is determined by the diagrid and core friction losses. Then, the IHX geometry (mainly hydraulic diameter) was adjusted to reproduce the correct cold pool elevation. Table C.1 presents the comparison of the calculated flow distributions, pool elevations and temperatures with the test data. It can be seen that the computed results agree very well with the experiment, with less than 5% differences on the mass flow rates and 1% on the temperatures. The highest discrepancies are seen on the values of the pool elevations, predicted with up to 13.5 cm absolute error. Overall, the computed results satisfactorily reproduce the Phenix measurements.

C.2.3 Reduced power: 120 MWth

As mentioned previously, the NC test was initiated from a reactor steady-state corresponding to the reduced power of 120 MWth. The model described formerly was used as such, changing only the following boundary conditions: power of 120 MW, pump rotational speed of 36.6 rad/s, secondary-side IHX inlet temperature of 308°C and flow rate of 760 kg/s. Table C.2 gives the main results corresponding to this steady-state. The comparison of TRACE-computed results with the test data shows good agreement, thus demonstrating the validity of the model at an operating point different from that used for the model adjustments.

			М	ass flow (k	m (g/s)			Elevation (mm	
	Core	Inner core	Outer core	Blanket	Stored fuel	CRs	Reflector	Hot pool	Cold pool
Phenix	1284	10)55	149	30	9	41	1876	1569
TRACE	1283.5	546.1	501.7	154.8	30.7	9.2	40.9	1922	1579
Δ	-0.5	-7	.0	5.8	0.7	0.2	-0.1	46	10
$\epsilon(\%)$	0.04	0	.7	3.9	2.3	2.2	0.2	2.4	0.6

 Table C.2. Comparison of TRACE-calculated results with the experimental data at 120 MWth

			Tempe	rature (°C)		
	Inlet core	Outlet core	Inlet IHX1	Outlet IHX1	Inlet IHX2	Outlet IHX2
Phenix	358	432	432	360	308	432
TRACE	358	430	430	357	308	430
Δ	-0.1	-1.4	-2.1	-2.8	0.	-2.2
$\epsilon(\%)$	0.02	0.2	0.3	0.4	0.	0.3

C.3 Results of the NC test

The Natural Convection test was initiated by the dryout of two of the three steam generators in the tertiary circuit, with constant speed of the primary and secondary pumps. The reactor was manually shutdown after 458 s, when the difference between the primary and secondary temperatures in the IHXs decreased to 15°C. The three primary pumps were manually tripped at 466 s, and their rotating speed decreased with mechanical inertia. The speed of the secondary pumps was automatically reduced 60 s after the SCRAM and stabilized at 110 rpm. After about 1 hour (4080 s), back-up motors were used and the secondary pump speed reduced to 100 rpm. About 3 hours after the beginning of the transient, the containments of the two operating SGs were opened to allow air natural convection to occur. The test was terminated after 6h45min.

Table C.3 summarizes the main events characterizing the NC test. Three different steps can be defined, delimited by (1) the reactor and pump trips and (2) the opening of the steam generator (SG) containments.

The comparison of the TRACE pre-test results with the experimental data is presented through Figs. C.3 to C.6.

TimeAction0 s0 sDryout of the steam generators7min46s458 sSCRAM7min54s466 sPrimary and secondary pump trips2h52min10320 sOpening of the two SG containments			
7min46s458 sSCRAM7min54s466 sPrimary and secondary pump trips	Tin	ne	Action
6h45min 24300 s End of the test	7min46s 7min54s 2h52min	458 s 466 s 10320 s	SCRAM Primary and secondary pump trips Opening of the two SG containments

 Table C.3. Summary of the main events characterizing the Natural Convection test in the

 Phenix reactor

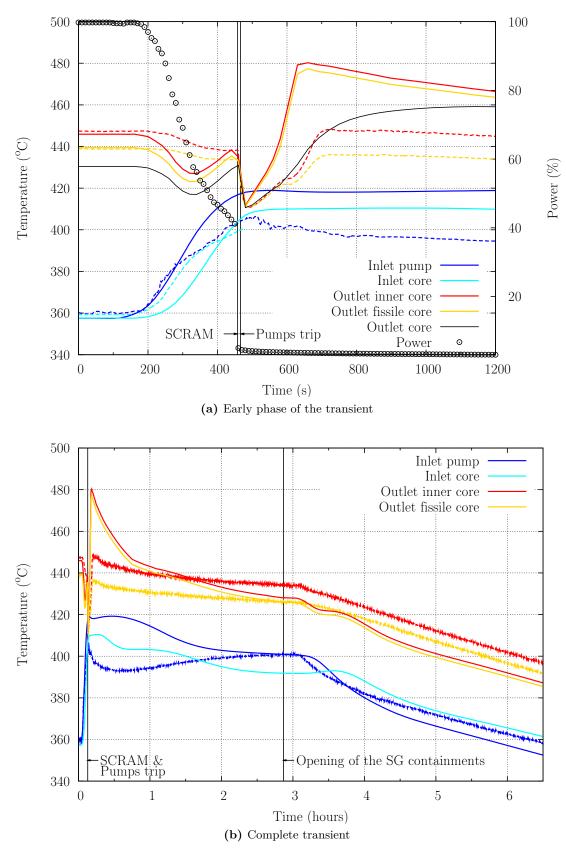


Figure C.3. Evolution of the core power and temperatures during the NC transient. Exp.: dashed lines, TRACE: solid lines.

C. TRACE ANALYSIS OF THE LATTER PART OF THE PHENIX NATURAL CONVECTION TEST

The cooling deficiency created by the dryout of the steam generators (SGs) increased the coolant inlet temperature by 40°C and led to a reduction by 60% of the power in the Phenix reactor (see Fig. C.3a). The various reactivity feedbacks in place have been studied using point kinetics and coupled TRACE/PARCS models, as presented in Chapter 5.

Figure C.3 shows the evolution of the core temperatures calculated by TRACE and compared to the experimental data. The experimental inlet core temperature is only displayed up to the pump trip since this measurement is only relevant in forced convection (due to the position of the sensor).

As seen in Table C.2, TRACE predictions at steady-state are very satisfactory.

At the beginning of the transient, the inlet pump and core temperatures increase. Figure C.3a shows that TRACE predicts a constant rise rate, which results in an overestimation of the pump inlet temperature after ~ 300 s since the experimental increase rate starts to slow down at that time. This may be attributed to the formation of a convective flow in the lower part of the cold pool, which would be initiated by the increasing temperature difference and which would mix the cold sodium from the pool bottom with the hotter fluid coming from the IHX. This is not represented with the TRACE 1D model but might be improved using a 3D representation of the cold pool.

The predicted core inlet temperature follows the evolution of the pump inlet temperature with a time delay due to the thermal inertia of the diagrid structure. The comparison with the experiments, where the two temperatures stay very close (within $\sim 10^{\circ}$ C), indicates that the pump and diagrid heat-transfer areas have been over-estimated in the present model and should be reduced in a post-test analysis.

The experimental inner-core and average fissile-core outlet temperatures are available for comparison with the calculated results. The sharp decrease in the reactor power only results in a small decrease ($\sim 10^{\circ}$ C) of the experimental core outlet temperature due to the increase of the core inlet temperature and constant flow rate. It can be seen that TRACE predicts a sharper drop – due to an under-estimation of the inlet core temperature caused by the diagrid thermal inertia – succeeded by a slight increase, the rate of which is comparable to that of the inlet core temperature. Thus, the predicted trends in the outlet core temperature can be understood from the evolution of the core inlet temperature, and a better prediction of the core inlet temperature should enable one to improve the calculated outlet temperature. It should be recalled that the simplified core model presented in Chapter 5 showed that TRACE satisfactorily predicted the outlet temperature when the experimental inlet core temperature was used as boundary condition (see Fig. 5.18).

After the reactor and pump trips, TRACE satisfactorily predicts the sharp drop measured in the core outlet temperature but largely over-predicts the following increase in temperature caused by the reduction of the flow rate. A later study has shown that the simulation of the core structures (mainly the SA wrappers) delayed the increase by 50 s, thus better reproducing the shape of the experimental data. However, the amplitude predicted by TRACE remains $\sim 40^{\circ}$ C too high, and the accounting of the over-predicted inlet core temperature would only explain $\sim 20^{\circ}$ C of the difference. The rest might be due to a change in either the flow rate or power distribution between the fissile core and the other core regions that are not reproduced in the model. Also, it should be mentioned that the temperature sensors are located 10 cm above the top of the SAs. Previous Phenix tests have shown that the SA outlet core temperatures are under-estimated by up to 30°C during the first minutes of natural convection, due to a chimney effect forming at the core outlet and the low coolant flow rate, especially during the establishment of natural convection, when the sodium in the hot pool is colder than at the core outlet. Therefore, one should be careful when comparing the test data with 1D-results, and a 3D representation of the hot pool could help to improve the computed results.

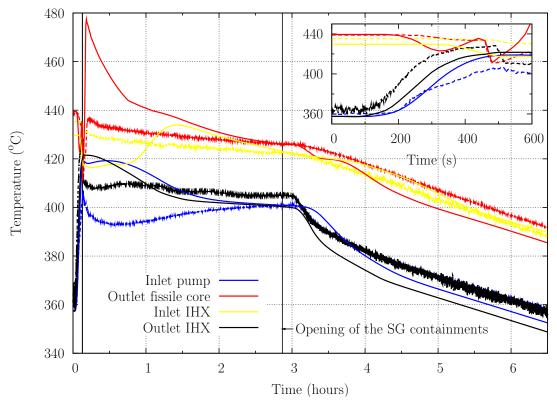
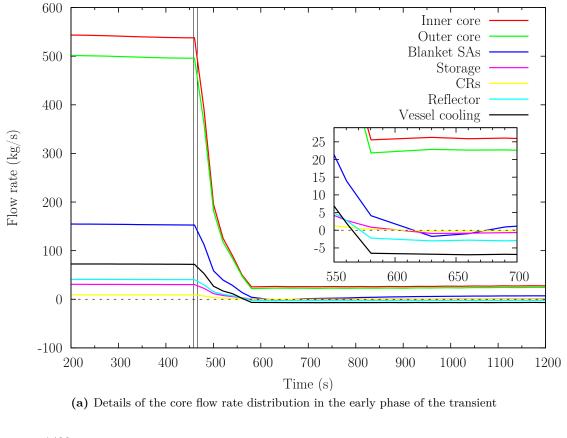


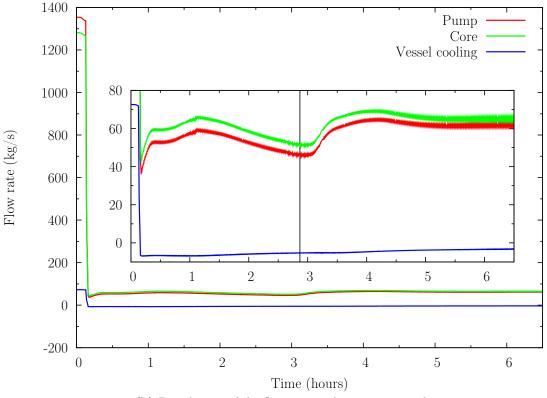
Figure C.4. Evolution of the primary pool temperature during the NC transient. Exp.: dashed lines, TRACE: solid lines.

The long-term results for the core temperature evolutions are presented in Fig. C.3b. It appears that the pump inlet temperature is over-estimated during the first two hours of the transient. The differences between the computed pump and core inlet temperatures are related to the pump and diagrid thermal inertia. The error on the pump inlet temperature seems to pass on to the core outlet temperature, which is first largely over-estimated during the first hour and then under-estimated by $\sim 15^{\circ}$ C after 3 hours and towards the end of the transient.

Additionally, Figure C.4 shows the evolution of the primary temperatures at the IHX inlet and outlet, along with the experimental data. At the beginning of the transient, the computed IHX outlet temperature is too low by 10 to 20°C, but the prediction is still satisfactory when one considers the high stratification of temperatures at the IHX outlet window – as much as 80° C variation at nominal power. However, TRACE does not predict the temperature drop measured at about 500 s, which coincides with the secondary flow rate reduction. After the secondary pump trips, the primary outlet IHX sodium temperature drops down to that of the secondary-side at the IHX inlet. This might come from the surrounding sodium in the cold pool, which would cool down the sodium in the IHX by conduction after the loss of flow. In the TRACE results, the primary outlet IHX temperature follows the evolution of the secondary inlet IHX, which is used as boundary condition. An additional heat structure representing the IHX outer shell and its immersion in the cold pool could enable one to better reproduce the experimental results. However, the actual model gives quite satisfactory results beyond the first hour after which, despite an under-estimation of the IHX outlet and core outlet temperatures by ~ 10°C, the evolutionary trend of the primary temperatures is well reproduced.

The analysis of the core flow rate distribution, presented in Fig. C.5a shows that, after the pump trip, a reverse flow is predicted in the coldest channels. This illustrates the earlier





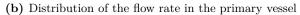


Figure C.5. Evolution of the flow rates during the NC transient

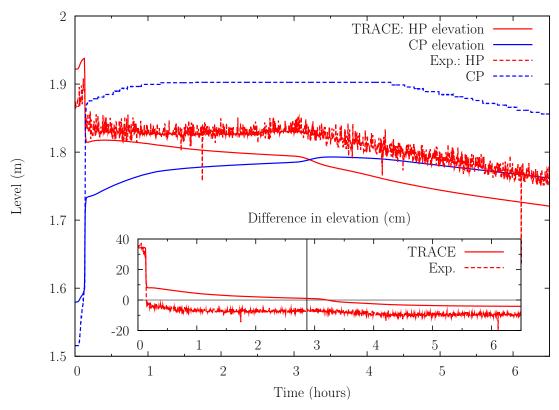


Figure C.6. Evolution of the pool levels during the NC transient

mentioned modification of the hydraulic path at the core outlet, through the formation of a chimney effect in the hottest channels of the fissile core and a reverse flow in the lateral, cold part of the core. A more detailed analysis revealed that the lower and colder part of the cold pool slowly heats up. The resulting homogenization of the temperatures decreases the natural convection flow rate after about the first hour, as can be seen in Fig. C.5b. The opening of the steam generator containments (after ~ 3 hours) enhances the cooling efficiency through air circulation. This improves the cooling of the reactor vessel and results in further stratification of the cold pool. The NC mass flow rate is thereby increased (see Fig. C.5b), and stabilizes at about 5% of the initial flow rate.

Figure C.6 presents the calculated and measured pool levels. The prediction of the steadystate is quite satisfactory, though over-estimated by almost 50 mm. After the pump trips, the elevation difference between the hot and cold pools decreases sharply and even reverses. It is seen that TRACE is able to predict the sharp drop, although this is of smaller amplitude, and is not able to reproduce the corresponding inversion in pool elevation. The TRACE error on the cold pool level is almost 20 cm. Still, the evolutionary trend of the difference in elevation is quite well reproduced. The discrepancies with respect to the measurements might be due to differences in the computed temperatures as function of pool height, which result in errors in the sodium density. The pool levels thus represent a good practical measure for checking the average pool temperatures in a post-test calculation.

Table C.4 summarizes the transient phenomenology during the different phases of the test.

$\frac{\text{Third phase}}{t > 10320 \text{ s}}$ Op. of SG cont.	Second phase 458 s <t<10320 s<br="">Reactor SCRAM Prim. and sec. pumps trip</t<10320>	$\frac{\text{First phase}}{\text{s} < \text{t} < 458 \text{ s}}$ SG dryout		
Direct flow in all the chan- nels (see Fig. C.5a). Decay heat power.	Reverse flow in the cold- est core channels (see Fig. C.5a). Decay heat power.	Due to the core inlet tem- perature increase, drastic decrease of the core power down to 40% of the nomi- nal value (see Fig. C.3a).	Core	Table (
More efficient cooling, which results in a core mass flow rate increase (see Fig. C.5b) and in a nearly homogeneous cooling of the hot pool (stratification of 10° C).	Modification of the hy- draulic paths: chimney ef- fect for the hotter fluid and reverse flow in the lateral, cold part of the core.	The flow goes mainly from the core outlet to the IHX inlet window.	Hot pool	Table C.4. Summary of the NC test phenomenology
More efficient cooling fol- lowed by a decrease of the temperatures and a strat- ification between the lower and upper parts (stratifica- tion of 50°C).	Slow heating of the lower, coldest part, which reduces the stratification.	High stratification at the IHX outlet window (nearly 60°C).	Cold pool	t phenomenology
More efficient cooling through the IHX, which results in the cooling of the whole reactor vessel and stratification in the cold pool.	Stabilization and homog- enization of the tempera- tures, which decrease the natural convection flow rate (see Fig. C.5b).	Fast heating of the lower part of the cold pool.	Global behavior within the primary vessel	

C.4 Summary of the analysis

A complete model of the Phenix primary circuit has been developed in TRACE and validated initially on the basis of steady-state results at nominal and reduced power. From the comparison of the blind TRACE calculation with the experimental data obtained during the NC test, it appears that the biggest discrepancies in the temperature evolutions are seen at the beginning of the transient. TRACE predictions are very satisfactory after the first two hours of the transient, with less than 10°C under-prediction of the primary pool temperatures.

The major sources of error during the early transient seem to be related to the simulation of the reactor structures. A finer modeling, including the core SA wrappers and the description of the IHX as integrated into the reactor pools, has been performed in a post-test analysis. The results, a selection of which is briefly presented in Fig. C.7, show the following improvements on:

- the core inlet temperature, through the reduction of the pump and diagrid heat-tranfer area, thus decreasing the corresponding thermal inertia;
- the core outlet temperature, due to the improved core inlet temperature and the better representation of the core structures (mainly SA wrappers), which enabled one to improve the results during the 200 s following the SCRAM;
- the IHX outlet temperature, through the representation of the IHX outer shell and its integration into the cold pool, which results in a global improvement of the temperatures;
- the evolutions of the pool levels which, despite the remaining error on the predicted absolute levels, are now very well reproduced (see Fig.C.7b).

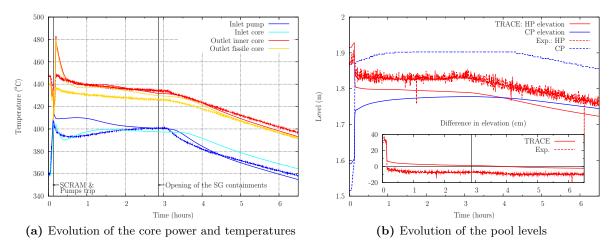


Figure C.7. Results of the NC test post-test analysis

In summary, the analysis has demonstrated the need to accurately simulate the reactor structures, since these define the thermal inertia of the system during the first phase of the transient. Furthermore, it has been found difficult to compare the computed 1D-results with the test data due to the high-temperature stratification occurring in the pools. Nevertheless, the simulated reactor behavior and temperatures match very well with the experimental data after the first two hours and, in general, the TRACE blind predictions may be considered as having been quite satisfactory.

C. TRACE ANALYSIS OF THE LATTER PART OF THE PHENIX NATURAL CONVECTION TEST

This first-of-its-kind benchmark, which has enabled one to compare results from the TRACE code with experimental data from a sodium-cooled fast reactor, constitutes an important step towards further validation of the sodium single-phase flow modeling in TRACE.

Bibliography

- [Abe76] J. Aberle et al. Sodium boiling experiments in a 7-pin bundle under flow rundown conditions. Tech. Rep. KfK 2378, Kernforschungszentrum Karlsruhe, 1976.
- [Ada10] R. Adams. Coupled neutronic/thermal-hydraulic simulation of selected Phenix End-of-Life tests. Master's thesis, ETHZ-EPFL, 2010.
- [Aut79] M. I. Autruffe, G. Wilson, B. Stewart, and M. Kazimi. A proposed momentum exchange coefficient for two-phase modeling of sodium boiling. In Int. Mtg. on Fast Reactor Safety Tech. 4, pp. 2515 – 2521. Seattle, WA, 1979.
- [Bai80] J. Bailly, A. Tattegrain, and J. Saroul. The SCARABEE facility its main characteristics and the experimental program. *Nucl. Eng. Des.*, vol. 59(2):pp. 237 – 255, 1980.
- [Bas84] G. Basque, L. Delapierre, D. Grand, and P. Mercier. BACCHUS; a numerical approach to two-phase flow in a rod bundle. *Nucl. Eng. Des.*, vol. 82(2-3):pp. 191 – 204, 1984.
- [Ber90] P. Bergeonneau, M. Vanier, M. Favet, J. D. Antoni, K. Essig, and J. Adam. An analysis of the dynamic behavior of the core. *Nucl. Sci. Eng.*, vol. 106:pp. 69 – 74, 1990.
- [Boh90] W. Bohl and L. Luck. SIMMER-II: a computer program for LMFBR disrupted core analysis. Tech. Rep. LA-11415-MS, Los Alamos National Laboratory, 1990.
- [Bot78] M. Bottoni and A. Kaiser. Two-phase pressure drop of boiling sodium: evaluation of results obtained from tubular experiments and analysis of liquid-vapor friction coefficients for viscous and turbulent flows. In 8th Liquid Metal Boiling Working Group (LMBWG). 1978.
- [Bot84] M. Bottoni et al. Development of the three-dimensional two phase flow COMMIX2-SM computer program. In 11th Liquid Metal Boiling Working Group (LMBWG), pp. 8 – 23. 1984.
- [Bot87] M. Bottoni, B. Dorr, C. Homann, and D. Struwe. State of development of the computer programme BACCHUS-3D/TP for the description of transient two-phase flow conditions in LMFBR fuel pin bundles. *Nucl. Eng. Des.*, vol. 100:pp. 321 – 349, 1987.
- [Bot90] M. Bottoni, B. Dorr, C. Homann, G. Huber, K. Mattes, F. Peppler, and D. Struwe. Experimental and numerical investigations of sodium boiling experiments in pin bundle geometry. *Nucl. Tech.*, vol. 89:pp. 56 – 82, 1990.

- [Bou73] J. A. Bouré, A. E. Bergles, and L. S. Tong. Review of two-phase flow instability. Nucl. Eng. Des., vol. 25:pp. 165 – 192, 1973.
- [Bub08] E. Bubelis and M. Schikorr. Review and proposal for best fit of wire-wrapped fuel bundle friction factor and pressure drop predictions using various existing correlations. *Nucl. Eng. Des.*, vol. 238:pp. 3299 – 3320, 2008.
- [Cah00] J. Cahalan, T. Ama, G. Palmiotti, T. Taiwo, and W. S. Yang. Development of a coupled dynamics code with transport theory capability and application to accelerator-driven systems transients. In *Int. Conf. on the Physics of Reactors (PHYSOR)*, Paper 197. May 7-12 2000.
- [Cam82] F. Camous. THEBES: a thermohydraulic code for the calculation of transient two phase flow in bundle geometry. In 10th Liquid Metal Boiling Working Group (LMBWG). 1982.
- [Car92] C. Carrico, E. Lewis, and G. Palmiotti. Three dimensional variational nodal transport methods for cartesian, triangular, and hexagonal criticality calculations. *Nucl. Sci. Eng.*, vol. 111:pp. 168 – 179, 1992.
- [Cev95] S. Cevolani. ENEA themohydraulic data base for the advanced water cooled reactor analysis. Tech. rep., 1st Research Co-ordination Mtg. of IAEA CRP on Thermohydraulic Relationships for Advanced Water Cooled Reactors, 1995.
- [Che66] J. Chen. Correlation for boiling heat transfer to saturated fluids in convective flow. *I&EC process design and development*, vol. 5(3):pp. 322 – 329, July 1966.
- [Che70] J. C. Chen and S. Kalish. An experimental investigation of two-phase pressure drop for potassium with and without net vaporization. In 4th Int. Heat transfer Conf., Chapter B8.3, vol. 6. 1970.
- [Cig88] M. Cigarini and M. Dalle Donne. Thermohydraulic optimization of homogeneous and heterogeneous advanced pressurized water reactors. Nucl. Tech., vol. 80:pp. 107 – 132, 1988.
- [Com55] U. A. E. Commission. Liquid-Metals Handbook: Sodium-NaK Supplement. July 1955. US Navyand US Government Printing Office.
- [Com08] E. Commission. Roadmap for a European Innovative SOdium cooled FAst Ractor EISOFAR. March 2008.
- [Dev86] J. Devos and D. Struwe. Sensitivity study with the BLOW boiling model of the European accident code in the context of whole core LOF calculations. In 12th Liquid Metal Boiling Working Group (LMBWG). 1986.
- [Dow06] T. Downar, Y. Xu, and T. Kozlowski. PARCS v2.7 U.S. NRC Core Neutronics Simulator USER MANUAL. Purdue University, August 2006.
- [Efa07] A. D. Efanov, A. Sorokin, E. Ivanov, G. Bogoslovskaya, et al. Heat transfer under natural convection of liquid metal during its boiling in a system of channels. *Thermal Eng.*, vol. 54:pp. 214 – 222, 2007.
- [Eif80] W. Eifler and R. Nijsing. Experimental and analytical studies on the single phase flow characteristics of the 12-rod sodium boiling test section. *European Appl. Res. Rept.-Nucl. Sci. Tech.*, vol. 2:pp. 1071 – 1121, 1980.

- [Eng79] F. Engel, R. Markley, and A. Bishop. Laminar, transition, and turbulent parallel flow pressure drop across wire-wrap-spaced rod bundles. *Nucl. Sci. Eng.*, vol. 69:pp. 290 – 296, 1979.
- [Epi10] A. Epiney, K. Mikityuk, and R. Chawla. TRACE qualification via analysis of the EIR gas-loop experiments with smooth rods. Ann. Nucl. Energy, vol. 37:pp. 875 – 887, 2010.
- [EU08] EU. Work programme 2008: Euratom for nuclear research and training activities. FP7 Euratom Work Programme, November 2008. ftp://ftp.cordis.europa.eu/pub/fp7/docs/euratom_wp_2008_en.pdf.
- [Fen81] H. Fenech. Heat transfer and fluid flow in nuclear systems. Pergamon Press, 1981.
- [Fin96] J. Fink and L. Leibowitz. A consistent assessment of the thermophysical properties of sodium. *High Temp. and Mat. Science*, vol. 35:pp. 65 – 103, 1996.
- [Fio11] G. Fiorini and A. Vasile. European Commission 7th Framework Programme: The Collaborative Project on European Sodium Fast Reactor (CP ESFR). Nucl. Eng. Des., vol. 241:pp. 3461 – 3469, 2011.
- [Gau10] P. Gauthé. IAEA CRP on natural convection test in Phenix. Tech. Rep. CEA/DEN/CAD/DER/SESI/LSMR/NT DO 4, CEA, 2010.
- [GIF02] GIF. A Technology Roadmap for Generation IV Nuclear Energy Systems. GIF-002-00. U.S. DOE, 2002.
- [Gna84] P. Gnadt, J. Carbajo, J. Dearing, A. Levin, R. MacPherson, B. Montgomery, S. Rose, R. Thornton, and J. Wantland. Sodium boiling experiments in the THORS facility. *Nucl. Eng. Des.*, vol. 82(2-3):pp. 241 – 280, 1984.
- [Gra80] M. R. Granziera and M. S. Kazimi. A two dimensional, two fluid model for sodium boiling in LMFBR fuel assemblies. Tech. Rep. MIT-EL-80-011-06984544, MIT, May 1980.
- [Hag84] K. Haga. Loss-of-flow experiment in a 37-pin bundle LMFBR fuel assembly simulator. Nucl. Eng. Des., vol. 82(2-3):pp. 305 – 318, 1984.
- [Heu73] G. Heusener, G. Kessler, and H. Lauber. Analysis of hypothetical accidents for SNR-300. Tech. Rep. KfK 1834, Kernforschungszentrum Karlsruhe, 1973.
- [Hub76] F. Huber, K. Mattes, and W. Till. KNS der kompakte Natriumsiedekreislauf für sicherheitstechnische Untersuchungen im Rahmen des schnellen Brüter-Programms. *KfK-Nachrichten*, pp. 24 – 28, 1976.
- [Hub78] F. Huber, E. Jenes, and K. Mattes. Beschreibung der Teststrecken zum lokalen Sieden im kompatken Natriumsiedekreislauf. Tech. Rep. KfK 2475, Kernforschungszentrum Karlsruhe, 1978.
- [Hub82a] F. Huber, K. Mattes, W. Peppler, W. Till, and D. Wall. Loss of flow experiments in sodium in an electrically heated 37 pin bundle with sinusoidal axial heat flux distribution. In Int. Top. Mtg. on Liquid Metal Fast Breeder Reactor Safety and Related Design and Operational Aspects. 1982.

- [Hub82b] F. Huber, K. Mattes, W. Peppler, W. Till, and D. Wall. Loss of flow simulation experiments with the KNS 37 pin bundle. In 10th Liquid Metal Boiling Working Group (LMBWG). 1982.
- [Hub84] F. Huber and W. Peppler. Boiling and dryout behind local blockages in sodium cooled rod bundles. Nucl. Eng. Des., vol. 82(2-3):pp. 341 – 363, 1984.
- [Hub87] F. Huber, A. Kaiser, K. Mattes, and W. Peppler. Steady state and transient sodium boiling experiments in a 37-pin bundle. Nucl. Eng. Des., vol. 100:pp. 377 – 386, 1987.
- [Hub88] F. Huber, K. Schleisiek, G. Basque, M. Bottoni, P. M. Riboud, H. Ninokata, D. N. Wall, and J. D. Macdougall. Comparative study of thermohydraulic computer code simulations of sodium boiling under loss of flow conditions. In 13th Liquid Metal Boiling Working Group (LMBWG), pp. 727 – 812. 1988.
- [IAE06] IAEA. Fast reactor database. IAEA-TECDOC-1531 ISBN 92-0-114206-4. IAEA, Vienna, Austria, 2006.
- [IAE10] IAEA. Nuclear power reactors in the world. ISBN 978-92-0-105610-9. 2010.
- [Ich07] M. Ichimiya, T. Mizuno, and S. Kotake. A next generation sodium-cooled fast reactor concept and its R&D program. Nucl. Eng. Tech., vol. 39:pp. 171 – 186, 2007.
- [Ish80] M. Ishii and K. Mishima. Study of two-fluid model and interfacial area. Tech. Rep. ANL-80-111 (NUREG/CR-1873), Argonne National Laboratory, 1980.
- [Kai74] A. Kaiser, W. Peppler, and L. Vöröss. Type of flow, pressure drop, and critical heat flux of a two-phase sodium flow. *Nucl. Eng. Des.*, vol. 30:pp. 305 315, 1974.
- [Kai75] A. Kaiser and W. Peppler. Steady state boiling experiments in a 7-pin bundle. In 6th Liquid Metal Boiling Working Group (LMBWG). 1975.
- [Kai77a] A. Kaiser and W. Peppler. Sodium boiling experiments in a seven-pin bundle: Flow patterns and two-phase pressure drop. *Nucl. Eng. Des.*, vol. 43(2):pp. 285 293, 1977.
- [Kai77b] A. Kaiser and W. Peppler. Sodium boiling experiments in an annular test section and flow rundown conditions. Tech. Rep. KfK 2389, Kernforschungszentrum Karlsruhe, 1977.
- [Kai78] A. Kaiser, W. Peppler, and L. Vöröss. Untersuchungen des Strömungsform, des Druckabfalls und des kritischen Wärmeflusses einer Zweiphasenströmung mit Natrium. Tech. Rep. KfK 2845, Kernforschungszentrum Karlsruhe, 1978.
- [Kai79] A. Kaiser. Two-phase pressure drop of boiling sodium in rod-bundle geometries: comparison of experimental results with Lockhart-Martinelli correlation. Two-phase momentum, heat and mass transfer in chemical, Process. and Energy Eng. Systems, vol. 2:pp. 583 – 596, 1979.
- [Kai82] A. Kaiser, F. Huber, W. Peppler, and W. Till. Natural convection decay heat removal experiments including boiling in a 37-pin bundle. In 10th Liquid Metal Boiling Working Group (LMBWG), pp. 71 – 98. 1982.
- [Kai84] A. Kaiser, F. Huber, W. Peppler, and W. Till. Natural convection experiments with sodium including boiling in a 37-pin bundle. AIChE Journal, vol. 80(236):pp. 134 – 139, 1984.

- [Kai87] A. Kaiser and F. Huber. Sodium boiling experiments at low power under natural convection conditions. Nucl. Eng. Des., vol. 100(3):pp. 367 – 376, 1987.
- [Kai88] A. Kaiser, F. Huber, M. Bottoni, and B. Dorr. Contribution to sodium boiling heat transfer, pressure drop, and void distribution in multi-pin geometry. In 13th Liquid Metal Boiling Working Group (LMBWG), pp. 71 – 98. 1988.
- [Kat58] T. Katsuhara. Influence of wall roughness on two-phase flow frictional pressure drops (in Japanese). Trans. JSME, vol. 24:pp. 1050 – 1056, 1958.
- [Kik74] Y. Kikuchi, T. Takahashi, K. Haga, and D. Okouchi. Incipient boiling of sodium flowing in a single-pin annular channel. *Nucl. Sci. Tech.*, vol. 11:pp. 172 186, 1974.
- [Kik75] Y. Kikuchi, K. Haga, and T. Takahashi. Experimental study of steady-state boiling of sodium flowing in a single-pin annular channel. Nucl. Sci. Tech., vol. 12:pp. 83 – 91, 1975.
- [Kik77] Y. Kikuchi, Y. Daigo, and A. Ohtsubo. Local sodium boiling behind local flow blockage in simulated LMFBR fuel subassembly. *Nucl. Sci. Tech.*, vol. 14:pp. 774 – 790, 1977.
- [Kik78a] Y. Kikuchi. Transient boiling of sodium in a seven-pin bundle under loss-of-flow conditions. *Nucl. Sci. Tech.*, vol. 15:pp. 658 667, 1978.
- [Kik78b] Y. Kikuchi and K. Haga. Incipient boiling of sodium in seven-pin bundle under forced convection conditions. Nucl. Sci. Tech., vol. 15:pp. 533 – 542, 1978.
- [Kik78c] Y. Kikuchi and K. Haga. Transient boiling of sodium in a single-pin geometry under loss-of-flow conditions. Nucl. Sci. Tech., vol. 15:pp. 100 – 108, 1978.
- [Kik79] Y. Kikuchi. Transient boiling of sodium in seven-pin bundle under transient overpower conditions. Nucl. Sci. Tech., vol. 16:pp. 287 – 294, 1979.
- [Kik81] Y. Kikuchi and K. Haga. Sodium boiling experiments in a 19-pin bundle under lossof-flow conditions. Nucl. Eng. Des., vol. 66(3):pp. 357 – 366, 1981.
- [Kot84] H. Kottowski and C. Savatteri. Fundamentals of liquid metal boiling thermohydraulics. Nucl. Eng. Des., vol. 82(2-3):pp. 281 – 304, 1984.
- [Kot91] H. Kottowski, C. Savatteri, and W. Hufschmidt. A new critical heat flux correlation for boiling liquid metals. Nucl. Sci. Eng., vol. 108:pp. 396 – 413, 1991.
- [Kot94] H. Kottowski, editor. Liquid Metal Thermal-hydraulics. ISBN 3-926956-22-4. INFO-RUM Verlags- und Verwaltungs Gmbh, 1994.
- [Lah93] R. Lahey and F. Moody. The thermal-hydraulics of a boiling water nuclear reactor, chap. 5, p. 285. ISBN 0-89448-037-5. American Nuclear Society, 1993.
- [Led38] M. Ledinegg. Unstabilität der Strömung bei natürlichem und Zwangumlauf. Die Wärme, vol. 48:pp. 891 – 898, 1938.
- [Loc49] R. Lockhart and R. Martinelli. Proposed correlation of data for isothermal two-phase, two-component flow in pipes. *Chem. Eng. Progress*, vol. 45:pp. 39 – 48, 1949.
- [Lot56] P. Lottes and W. Flinn. A method of analysis of natural circulation boiling systems. Nucl. Sci. Eng., vol. 1:p. 420, 1956.

- [Lur64] H. Lurie and R. Noyes. Boiling studies for sodium reactor safety. Part II: Pool boiling and initial forced convection tests and analyses. Tech. Rep. NAA-SR-9477, Atomics International. Div. of North American Aviation, Inc., Canoga Park, Calif., 1964.
- [Lur65] H. Lurie. Sodium boiling heat transfer and hydrodynamics. In Application of High Temp. Instr. to Liq. Metal Ap., pp. 549 – 571. 1965.
- [Mac84] J. Macdougall and J. Lillington. The SABRE code for fuel rod cluster thermohydraulics. Nucl. Eng. Des., vol. 82(2-3):pp. 171 – 190, 1984.
- [Mar76] R. Markley and F. Engel. LMFBR blanket assembly heat transfer and hydraulic test data evaluation. Tech. Rep. EY-76-C-02-3045-004, Westinghouse Electric corporation, 1976.
- [Mik05] K. Mikityuk, S. Pelloni, P. Coddington, E. Bubelis, and R. Chawla. FAST: An advanced code system for fast reactor transient analysis. Ann. Nucl. Energy, vol. 32(15):pp. 1613 – 1631, 2005.
- [Mik09] K. Mikityuk. Heat transfer to liquid metal: review of data and correlations for tube bundles. Nucl. Eng. Des., vol. 239:pp. 680 – 687, 2009.
- [Mik10] K. Mikityuk, J. Krepel, S. Pelloni, A. Chenu, P. Petkevich, and R. Chawla. FAST code system: Review of recent developments and near-future plans. J. Eng. for Gas Turbines and Power, vol. 132:p. 102915, 2010.
- [Mik11] K. Mikityuk and A. Shestopalov. FRED fuel behaviour code: Main models and analysis of Halden IFA-503.2 tests. *Nucl. Eng. Des.*, vol. 241(7):pp. 2455 2461, 2011.
- [Moo44] L. Moody and N. Princeton. Friction factors for pipe flow. *Trans. ASME*, vol. 671-684, 1944.
- [NEA08] NEA. Nuclear Energy Outlook. Org. Eco. Co-op. and Dev., 2008.
- [NEA10] NEA. Uranium 2009: Resources, Production and Demand. Org. Eco. Co-op. and Dev., 2010.
- [Ngu85] H. Nguyen. A finite element method for one-dimensional sodium boiling simulation. In Third Int. Top. Meet. on Reactor Thermal-hydraulics, p. 17.C. Oct. 15-18 1985.
- [Nin86] H. Ninokata. Analysis of low-heat-flux sodium boiling test in a 37-pin bundle by the two-fluid model computer code SABENA. Nucl. Eng. Des., vol. 97:pp. 233 – 246, 1986.
- [Nin88] H. Ninokata. Interpretations of sodium boiling and two-phase flow experiments in pin bundles by the use of the basic two-fluid model. In *Third Int. Top. Mtg. on Nuclear Power Pant Thermal Hydraulics and Operations (NUPTHO-3).* 1988.
- [Nin89] H. Ninokata and A. Deguchi. Assessment of the physical models in a two-fluid model code and interpretation of experiments. *Nucl. Energy*, vol. 28:pp. 161 – 170, 1989.
- [Nin90] H. Ninokata and T. Okano. SABENA: Subassembly boiling evolution numerical analysis. Nucl. Eng. Des., vol. 120:pp. 349 – 367, 1990.
- [Nis86] K. Nissen et al. Interpretation of selected CABRI loss-of-flow experiments. In Int. Conf. Fast Reactor Safety, vol. 1, pp. 115 – 120. 1986.

- [No82] H. No and M. Kazimi. Wall heat transfer coefficient for condensation and boiling in forced convection of sodium. Nucl. Sci. Eng., vol. 81:pp. 319 – 324, 1982.
- [No87] H. No and M. Kazimi. An investigation of the physical foundations of two-fluid representation of sodium boiling in the liquid-metal fast breeder reactor. Nucl. Eng. Des., vol. 97:pp. 327 - 343, 1987.
- [Nov72] E. H. Novendstern. Turbulent flow pressure drop model for fuel rod assemblies utilizing a helical wire-wrap spacer system. *Nucl. Eng. Des.*, vol. 22:pp. 19 – 27, 1972.
- [Noy63] R. Noyes. Boiling studies for sodium reactor safety. Part I. Experimental apparature and results of initial tests and analysis. Tech. Rep. NAA-SR-7909, Atomics International. Div. of North American Aviation, Inc., Canoga Park, Calif., 1963.
- [Noy66] R. Noyes and H. Lurie. Boiling sodium heat transfer. *AIChE Journal*, pp. 92 100, 1966.
- [Nuk10] Nuklearforum Schweiz. Kernkraftwerke der Welt, August 2010. http://www.nuklearforum.ch/.
- [Oli84] J. Olive, P. Jolas, and S. Aubry. Description of the multidimensional thermohydraulic code CAFCA-NA for the analysis of LMFBR fuel assemblies under forced convection in case of partial or total blockages. In 11th Liquid Metal Boiling Working Group (LMBWG). 1984.
- [Pal87] G. Palmiotti, J. Rieunier, C. Gho, and M. Salvatores. BISTRO: Optimized twodimensional S_n transport code. In *Top. Mtg. on Advances in Reactor Physics, Mathematics and Computation.* Paris, France, 1987.
- [Pal93] G. Palmiotti, C. Carrico, and E. Lewis. Variational nodal methods with anisotropic scattering. Nucl. Sci. Eng., vol. 115:pp. 233 – 243, 1993.
- [Pal05] G. Palmiotti et al. VARIANT: Variational Anisotropic Nodal Transport for multidimensional cartesian and hexagonal geometry calculation. Tech. Rep. ANL-95/40, Argonne National Laboratory, 2005.
- [Pap84] J. Papin, P. Obry, and H. Fierz. Interpretation of the SCARABEE APL1 and APL2 experiments with the MULTICANA code. In 11th Liquid Metal Boiling Working Group (LMBWG), pp. 223 – 246. 1984.
- [Pel11] S. Pelloni and K. Mikityuk. A new cross-section generation model in the FAST code system and its application to gas- and sodium-cooled Generation IV fast reactors. Ann. Nucl. Energy, vol. 38(1):pp. 1 – 13, 2011.
- [Pep70] W. Peppler, E. Schlechtendahl, and G. Schultheiss. Investigation on dynamic boiling in sodium cooled fast reactors. *Nucl. Eng. Des.*, vol. 14:pp. 23 – 42, 1970.
- [Pia11] D. Pialla, D. Tenchine, P. Gauthé, and A. Vasile. Natural convection test in Phenix reactor and associated CATHARE calculation. In Int. Top. Mtg. on Nucl. Reactor. Thermalhydraulics (NURETH-14), 14-99. 2011.
- [Pla73] T. Playle. Simulation of sodium boiling using a water model: voiding and re-entry processes. Chem. Eng. Sci., vol. 28:pp. 1199 – 1211, 1973.

- [Pon10] A. Pont Ribas. Simulation of CABRI loss-of-flow experiments with the TRACE/FRED codes. Master's thesis, ETHZ, 2010.
- [Pou07] J. Pounders, B. Bandini, Y. Xu, and T. Downar. Calculation of accurate hexagonal discontinuity factors for PARCS. Tech. Rep. B-T-3711, International RELAP5 Users' seminar, 2007.
- [Reh73] K. Rehme. Pressure drop correlations for fuel element spacers. Nucl. Tech., vol. 17:pp. 15 23, 1973.
- [Ric58] B. Richardson. Some problems in horizontal two-phase two-component flow. Tech. rep., ANL-5949, 1958.
- [Rim97] G. Rimpault. Physics documentation of ERANOS: the ECCO cell code. Tech. rep., CEA, 1997.
- [Rim02] G. Rimpault, D. Plisson, J. Tommasi, R. Jacqmin, et al. The ERANOS code and data system for fast reactor neutronic analyses. In Int. Conf. on the Physics of Reactors (PHYSOR). October 1-10 2002.
- [Rin97] A. Rineiski and J.-Y. Doriath. Time-dependent neutron transport with variational nodal method. In M&C '97 Int. Conf. Saratoga Springs, NY, USA, 1997.
- [Rou09] J. Rouault, J. Sepantie, and D. Verwaerde. French R&D program on SFR and the ASTRID prototype. In Int. Conf. on Fast Reactors and Related Fuel Cycles: Challenges and Opportunities (FR09), no. IAEA-CN-176 in FRP-02. 7-11 December 2009.
- [Sau09] J. F. Sauvage. *Phénix, 35 years of history: the heart of a reactor.* CEA, EDF, http://www.iaea.org/inisnkm/nkm/aws/fnss/phenix/book/ 2009.
- [Sav86] C. Savatteri, R. Warnsing, J. Loens, and H. Kottowski. Results and comparison of dry-out in grid and wire spaced bundles at single- and two-phase flow. In 12th Liquid Metal Boiling Working Group (LMBWG), pp. 164 – 190. 1986.
- [Sav88a] C. Savatteri, R. Warnsing, F. Gillino, and H. Kottowski. Comparison and interpretation of dry-out measurements in grid and wire spaced bundles. In 13th Liquid Metal Boiling Working Group (LMBWG), pp. 121 – 157. 1988.
- [Sav88b] C. Savatteri, R. Warnsing, and H. Kottowski. Two-phase flow pressure drop of boiling sodium in grid and wire-spaced bundles. In 13th Liquid Metal Boiling Working Group (LMBWG), pp. 99 – 120. 1988.
- [Sav89] C. Savatteri, R. Warnsing, F. Gillino, and H. Kottowski. Comparison and interpretation of dry-out measurements in grid and wire spaced bundles. *Nucl. Energy*, vol. 28:pp. 145 – 154, 1989.
- [Sch70] K. Schleisiek. Heat transfer and boiling during forced convection of sodium in an induction-heated tube. Nucl. Eng. Des., vol. 14(1):pp. 60 – 68, 1970.
- [Sch74] H. Schins. Incipient and nucleate boiling of sodium. Atomkernergie, vol. 24:pp. 243 246, 1974.
- [Sch75] H. Schins. Contribution to the boiling curve of sodium. Atomkernergie, vol. 26:pp. 48 - 52, 1975.

- [Sch82] K. Schleisiek and J. Siebertz. Summary of benchmark calculations. In 10th Liquid Metal Boiling Working Group (LMBWG), pp. 71 – 98. 1982.
- [Sch84] A. L. Schor, M. S. Kazimi, and N. E. Todreas. Advances in two-phase flow modeling for LMFBR application. Nucl. Eng. Des., vol. 82:pp. 127 – 155, 1984.
- [Sei84] J. Seiler. Studies on sodium-boiling phenomena in out-of-pile rod bundles for various accidental situations in LMFBR: Experiments and interpretations. Nucl. Eng. Des., vol. 82(2-3):pp. 227 - 239, 1984.
- [Sei90] J. Seiler, G. Cognet, E. Leborgne, J. Moreau, J. Pages, J. Papin, B. Rameau, J. Lahaye, and J. Olive. French LMFBR core thermo-hydraulic studies for nominal and accident conditions. *Nucl. Eng. Des.*, vol. 124(3):pp. 403 – 415, 1990.
- [Sei10] J. Seiler, D. Juhel, and P. Dufour. Sodium boiling stabilisation in a fast breeder subassembly during an unprotected loss of flow accident. *Nucl. Eng. Des.*, vol. 240(10):pp. 3329 – 3335, 2010. 4th Int. Top. Mtg. on High Temperature Reactor Technology (HTR 2008), with Regular Papers.
- [Sin70] R. Singer and R. Holtz. Expulsion dynamics of sodium and non-metallic fluids. Atomkernenergie, pp. 211 – 215, 1970.
- [Smi68] D. Smidt, P. Fette, W. Peppler, E. Schlechtendahl, and G. Schultheiss. Problems of sodium boiling in fast reactors. Tech. Rep. KfK 790, KfK, 1968.
- [Smi86] K. S. Smith. Assembly homogenization techniques for light water reactor analysis. Prog. in Nucl. Energy, vol. 17(3):pp. 303 – 335, 1986.
- [Sob06] V. Sobolev. Fuel rod and assembly proposal for XT-ADS pre-design. In Coordination mtg. of WP1 & WP2 IP EUROTRANS. Bologna, Feb. 8-9 2006.
- [Sor05] G. Sorokin and A. Sorokin. Experimental and numerical investigation of liquid metal boiling in fuel subassemblies under natural circulation conditions. *Prog. in Nucl. Energy*, vol. 47(1-4):pp. 656 – 663, 2005. Innovative Nuclear Energy Systems for Sustainable Development of the World.
- [Sor06] G. Sorokin, H. Ninokata, A. Sorokin, H. Endo, and E. Ivanov. Experimental and numerical study of liquid metal boiling in a system of parallel bundles under natural circulation conditions. *Nucl. Sci. Tech.*, vol. 43:pp. 623 – 634, 2006.
- [Spo00] J. W. Spore et al. TRAC-M/FORTRAN 90 (version 3.0) Theory Manual. Los Alamos Nat. Lab., Los Alamos, NM 87545, July 2000. LA-UR-00-910.
- [Sun11] K. Sun, J. Krepel, K. Mikityuk, S. Pelloni, and R. Chawla. Void reactivity decomposition for the Sodium-cooled Fast Reactor in equilibrium fuel cycle. Ann. Nucl. Energy, vol. 38:pp. 1645 – 1657, 2011.
- [Tal11] J. D. Talley, S. Kim, J. Mahaffy, S. M. Bajorek, and K. Tien. Implementation and evaluation of one-group interfacial area transport equation in TRACE. *Nucl. Eng. Des.*, vol. 241(3):pp. 865 – 873, 2011. International Conference on Structural Mechanics in Reactor Technology (SMiRT19), Special Section.

- [Tob02] Y. Tobita, S. Kondo, H. Yamano, S. Fujita, K. Morita, W. Machek, P. Coste, S. Pigny, J. Louvet, and T. Cadiou. The development of SIMMER-III, an advanced computer program for LMFR safety analysis. In *Joint IAEA/NEA Tech. Mtg. on the Use of Computational Fluid Dynamics Codes for Safety Analysis of Reactor Systems (including Containment)*. 2002.
- [Tod84] N. Todreas. Coolant mixing in LMFBR rod bundles and outlet plenum mixing transients. Tech. Rep. DOE/ET/37240–109-PR, MIT, 1984.
- [Tod90] N. Todreas and M. Kazimi. Nuclear Systems I: Thermal Hydraulic Fundamentals. ISBN 1-56032-051-6. Taylor & Francis Group, 1990.
- [Uot84] M. Uotani and K. Haga. Experimental investigation of sodium boiling in partially blocked fuel subassemblies. *Nucl. Eng. Des.*, vol. 82(2-3):pp. 319 328, 1984.
- [Var09] F. Varaine et al. IAEA CRP on Phenix end of life tests: Control rod withdrawal. Tech. Rep. CEA/DEN/CAD/DER/SPRC/LEDC, to be published in IAEA CRP report, 2009.
- [Vas11] A. Vasile et al. The Phenix final tests. In Int. Cong. on the Adv. in Nucl. Power Plants (ICAPP-11), Paper 11298. 2011.
- [Vog71] P. Vog, D. Markfort, and E. Ruppert. A thermal-hydraulic analysis for fuel elements with liquid metal cooling. Int. Conf. on Heat and Mass Transfer, 1971.
- [Wal81] A. Waltar and A. Reynolds. Fast Breeder Reactors. ISBN 0-08-025983-9. New York a.o., Pergamon Press, 1981.
- [Wal86] D. N. Wall and A. A. Cooper. An analysis of the pressure drop and dryout results from the second ISPRA 12-pin gridded cluster. In 12th Liquid Metal Boiling Working Group (LMBWG), pp. 191 – 220. 1986.
- [Wey84] B. Wey, R. Overton, and G. Hughes. Improved inter-assembly heat transfer modelling under low flow conditions for the super system core (SSC). In 11th Liquid Metal Boiling Working Group (LMBWG), pp. 556 – 593. 1984.
- [Wik07] Wikipedia, the free encyclopedia. LMFBR schematics, 2007. http://en.wikipedia.org/wiki/Image:LMFBR_schematics.png.
- [Wil69] S. J. Wilcox and W. Rohsenow. Film condensation of liquid metal precision of measurements. Tech. Rep. D.S.R 71475-62, MIT, 1969.
- [Woo80] W. Woods, C. Girard, D. Struwe, A. Cooper, A. Davies, R. Herbert, D. Moxon, M. Hugla, S. Kaldi, M. Bottoni, and H. Jacobs. Thermohydraulic aspects of the interpretation of the SCARABEE fuel failure experiments. *Nucl. Eng. Des.*, vol. 59(2):pp. 257 – 273, 1980.
- [Xia06] Z.-J. Xiao, G.-Q. Zhang, J.-Q. Shan, X.-S. Bai, and D.-N. Jia. Experimental research on heat transfer to liquid sodium and its incipient boiling wall superheat in an annulus. *Nucl. Sci. Tech.*, vol. 17(3):pp. 177 – 184, 2006.
- [Yam87] K. Yamaguchi. Flow pattern and dryout under sodium boiling conditions at decay power levels. Nucl. Eng. Des., vol. 99:pp. 247 – 263, 1987.

- [Yam03] H. Yamano, S. Fujita, Y. Tobita, and al. SIMMER-III: a computer program for LMFR core disruptive accident analysis, version 3.1: model summary and program description. Tech. Rep. JNC TN9400 2003-071, Japan Nuclear Cycle Development Institute, 2003.
- [Yam08] H. Yamano, S. Fujita, Y. Tobita, I. Sato, and H. Niwa. Development of a threedimensional CDA analysis-code: SIMMER-IV and its first application to reactor case. *Nucl. Eng. Des.*, vol. 238:pp. 66 – 73, 2008.
- [Zei80] Y. Zeigarnick and V. Litvinov. Heat transfer and pressure drop in sodium boiling in tubes. Nucl. Sci. Eng., vol. 73:pp. 19 – 28, 1980.

List of abbreviations and symbols

	ABBREVIATIONS
ADF	Assembly Discontinuity Factor
ADS	Accelerator Driven System
ANL	Argonne National Laboratory (USA)
ATWS	Anticipated Transient Without Scram
BOL	Beginning Of Life
BWR	Boiling Water Reactor
$\mathbf{C}\mathbf{A}$	Control Assembly
CDA	Core Disruptive Accident
CEA	Comissiariat à l'énergie atomique (France)
CEFR	China Experimental Fast Reactor
CMFD	Coarse Mesh Finite Difference
CP	Collaborative Project
CRP	Coordinated Research Project
CRS	Control Rod Shift (part of the Phenix EOL tests)
\mathbf{CR}	Control Rod
CSD	Control and Shutdown Device
\mathbf{DFT}	Direct Fourier Transform
DOE	Department of Energy (USA)
DSD	Diverse Shutdown Device
EC	External Characteristic
EDF	Electricité de France

LIST OF ABBREVIATIONS AND SYMBOLS

EFR	European Fast Reactor
EISOFAR	European Innovative SOdium cooled FAst Reactor
EOL	End-Of-Life
EOS	Equation-Of-State
ERANOS	European Reactor ANalysis Optimized calculation System
ESFR	European Sodium-cooled Fast Reactor
EURATOM	EURopean ATOMic energy community
FAST	Fast-spectrum Advanced Systems for power production and resource managemenT
FBR	Fast Breeder Reactor
FZK	ForschungsZentrum Karlsruhe (Germany)
GFR	Gas-cooled Fast Reactor
GIF	Generation-IV International Forum
GNEP	Global Nuclear Energy Partnership
HEM	Homogeneous Equilibrium Model
HTC	Heat Transfer Coefficient
HTSTR	HeaT STRucture
IAEA	International Atomic Energy Agency
IB	Incipient Boiling
IC	Internal Characteristic
IFR	Integral Fast Reactor
IHX	Intermediate Heat eXchanger
INPRO	INternational PROject on innovative nuclear reactors and fuel cycles
IPPE	Institute of Physics and Power Engineering (Russia)
IRSN	Institut de Radioprotection et de Sûreté Nucléaire (France)
JAEA	Japan Atomic Energy Agency (Japan)
JRC	Joint Research Center
KfK	Kernforschungszentrum Karlsruhe (Germany)
KNS	Kompakter Natriumsiede-Kreislauf (German for $compact \ sodium-boiling \ loop)$
LBE	Lead-Bismuth Eutectic
\mathbf{LFR}	Lead-cooled Fast Reactor

LMFBR	Liquid-Metal Fast Breeder Reactor
LOCA	Loss-Of-Coolantd Accident
LOF	Loss-Of-Flow
LWGR	Light-Water-cooled Graphite-moderated Reactor
LWR	Light Water Reactor
$\mathbf{M}\mathbf{A}$	Minor Actinide
METI	Ministry of Economy, Trade and Industry (Japan)
MEXT	Ministry of Education, Culture, Sports, Science and Technology (Japan)
MOX	Mixed OXide
MSR	Molten Salt Reactor
NC	Natural Convection (part of the Phenix EOL tests)
NPP	Nuclear Power Plant
ODS	Oxide Dispersion-Strengthened
OEC	O-arai Engineering Center (Japan)
PARCS	Purdue Advanced Reactor Core Simulator
PHWR	Pressurised Heavy Water Reactors
PSI	Paul Scherrer Institute (Switzerland)
SA	Sub-Assembly
SCWR	Supercritical-Water-Cooled Reactor
SFR	Sodium-cooled Fast Reactor
\mathbf{SG}	Steam Generator
SPV	Single-Phase Vapor
\mathbf{SP}	Sub-Project
TRACE	TRAC/RELAP Advanced Computation Engine
TWG-FR	Technical Working Group on Fast Reactors
UK	United Kingdom
ULOF	Unprotected Loss-Of-Flow
ULOHS	Unprotected Loss-Of-Heat-Sink
UNGG	Uranium Naturel Graphite Gaz (French for Natural uranium graphite gas)
US NRC	US Nuclear Regulatory Commission (USA)

LIST OF ABBREVIATIONS AND SYMBOLS

USA	United States of America
USSR	Union of Soviet Socialist Republics
UTOP	Unprotected Transient Over Power
VHTR	Very-High-Temperature Reactor

GENERAL SYMBOLS

A	flow area	m^2
A_s	undisturbed flow area	m^2
A_v	projected grid area	m^2
B_{cell}	cell volume	m^3
Cf_{wl}	fraction of liquid in contact with the wall	-
С	drag coefficient	-
С	thermal expansion coefficient	K^{-1}
c_p	specificic heat	$J/kg\cdot K$
C_v	modified loss coefficient $\left(\frac{K}{\epsilon^2}\right)$	-
D	diameter	m
D_h	hydraulic diameter	m
e	internal energy	J
F	intermittency factor	
f	friction factor	-
G	mass flux	$kg/s \cdot m^2$
g	gravitational acceleration	m/s^2
Н	wire-wrap pitch length	m
h	convection heat-transfer coefficient	$W/m^2 \cdot K$
H_{fg}	latent heat of vaporization	$J/kg\cdot K$
Κ	Feedback coefficient	-
Κ	form loss coefficient	-
k	thermal conductivity	$W/m \cdot K$
$k_{\rm eff}$	effective criticality factor	-
L	length	m

ṁ	mass flow rate	$\rm kg/s$
N	number of neutrons available after breeding	-
N	number of test points	-
Nu	Nusselt number	-
Р	perimeter	m
Р	pressure	Pa
P_t	rod pitch for wire-wrap configuration $(D_r + 1.0444D_w)$	m
P_w	wetted perimeter	m
Pe	Peclet number	-
Pr	Prandtl number	-
Q	volumetric flow rate	m^3/s
q	heat flux	W/m^2
r	root-mean-square error	-
Re	Reynolds number	-
S	neutron source term	$n/cm^3 \cdot s$
S	slip ratio $\left(\frac{v_g}{v_l}\right)$	-
\overline{T}	average temperature	Κ
t	time	S
T_B	coolant bulk temperature	К
T_w	wall temperature	К
v	velocity	m/s
x	flow quality	-
X_{LM}	Lockhart-Matinelli parameter	-
z	elevation	m
	GREEK SYMBOLS	

α	void fraction	-
$\alpha(E)$	capture-to-fission ratio $\left(\frac{\sigma_c}{\sigma_f}\right)$	-
eta	delayed neutron fraction	-
δ	time delay	\mathbf{s}

LIST OF ABBREVIATIONS AND SYMBOLS

ϵ	relative plugging or grid solidity $\left(\frac{A_v}{A_s}\right)$	-
ε	absolute error	bar
$\overline{arepsilon}$	mean absolute error	bar
Г	interfacial mass-transfer rate	$ m kg/s{\cdot}m^3$
λ	delayed neutron decay constant	s^{-1}
μ	dynamic viscosity	Pa·s
ν	kinematic viscosity	m^2/s
ν	number of neutrons released per fission	-
Φ	two-phase multiplication factor for local pressure loss	-
ϕ	neutron flux	$n/cm^2 \cdot s$
ϕ_l	two-phase friction multiplication factor	-
ρ	density	kg/m^3
ρ	reactivity	pcm (10^{-5})
Σ	macroscopic cross-section	${\rm cm}^{-1}$
σ	microscopic cross-section	cm^2
σ	standard deviation of the absolute error	bar
heta	angle of the flow direction with the vertical	rad
χ	pin linear power	W/cm
ψ	intermittency factor	

Subscripts

_

1ϕ	single-phase
2ϕ	two-phase
axi	axial
В	bulk
С	coolant
с	capture
с	clad
CHF	critical heat flux
D	Doppler

230

EC	external characteristic
eff	effective
f	fuel
f	fission
g	gas
g	group
i	interfacial
IC	internal characteristic
in	inlet
L	laminar flow
l	liquid
m	medium
out	outlet
r	rod
rad	radial
S	saturation
SPV	single-phase vapor
T	turbulent flow
Tt	transition flow
v	vapor
v	vessel
w	wall
	Superscripts
c	calculated
m	measured

Acknowledgments

The present research has been carried out in the framework of the FAST project, in the Laboratory for Reactor Physics and Systems Behavior (LRS) of the Paul Scherrer Institute (PSI), and of the Doctoral School in Energy of the École Polytechnique Fédérale de Lausanne (EPFL). The work, mainly conducted at PSI, has been partly supported by the CP-ESFR project within the 7th EURATOM-FP, and the results of the current study constitute an important part of the Swiss contribution.

This work could not have been performed without the support and contributions of a number of persons to whom I am particularly grateful:

- Prof. Rakesh Chawla, the director of my thesis, for his friendly and helpful guidance, advice and numerous corrections which have brought highly added value to this work and the different documents published under his wing.
- Dr. Konstantin Mikityuk, leader of the FAST group, for his great supervision. His knowledge and advice have considerably contributed to this work. I benefited from numerous productive discussions and ideas to overcome the scientific difficulties of this thesis. His kindness, remarkable availability, support and working rigor created an excellent studious atmosphere. I really appreciated sharing his office and learnt a lot from this experience in his group.
- The whole FAST team, including the permanent staff and visiting students. I would like to especially thank Sandro Pelloni for his kind availability and great help with ERANOS, Jiri Krepel for the good atmosphere and various technical discussions, and Aaron Epiney and Kaichao Sun, with whom I shared an office, for the pleasant working atmosphere.
- Philippe Jacquemoud, for the computing support and for his personal help, as also for his good mood and the nice atmosphere he helps create within LRS.
- The whole LRS team, with special thanks to my colleagues and friends, Younsuk Yun for her kindness and enthusiasm, Hanna Kröhnert, Davide Bertolotto and Stefano Capena for the nice time we had together, and Jordi Freixa and Arto Ylönen from LTH for the numerous nice biking trips.
- The various students that I have seen passing through the FAST group during my PhD and had an opportunity to help with in the supervision of their work, particularly Robert Adams, Arnau Pont Ribas, Bruno Colin, Florian Reiterer and Claudia Codau.
- Gaëtan Girardin, in charge of the experimental facilities of LRS at EPFL, for all the nice time spent with students during the teaching experiments with the CROCUS reactor.
- Alexander Stanculescu for the kind atmosphere created during the Phenix CRP, and all the other members of the CRP for their active contributions. Special thanks to Justin

Acknowledgments

Thomas for his valuable collaborative work, and to Tanju Sofu and Thomas Fanning for their support at ANL.

This list could be extended to the numerous other colleagues and friends I met at PSI and during business trips. In particular, I would like to thank Anka for the nice time we spent together. Furthermore, I should not forget to thank swiss *nuclear* for the financial support which enabled me, as young researcher, to participate in a number of very interesting conferences and meetings around the world and thus make new contacts within the international nuclear community.

I would also like to thank Fabian Jatuff and Elsa Merle-Lucotte who, in special ways, helped me to carry out this Ph.D within the FAST group.

Last but not least, I would like to thank my family for always being there, without account for the distance, and Stevan for his wide-based personal support, ranging from technical help with Latex and Linux scripts, via scientific discussions, to the philosophical discussions we had during coffee breaks.

Finally, I sincerely thank Prof. Minh Quang Tran, Prof. Kostadin Ivanov and Dr. Alain Zaetta, who kindly accepted to form the jury for this thesis.

Aurélia Chenu

Date of birth: 18.02.1985 Nationality: French

☑ 148 c. du Montmiandon, 07100 Annonay, France
☑ aurelia.chenu@epfl.ch
☎ +33 (0)4 75 32 18 79
ⓐ +41 (0)76 535 02 18

PROFESSIONAL EXPERIENCE

2007 - 11	PhD Thesis , Paul Scherrer Institute (PSI), Switzerland, Single- and Two-phase Sodium Flow Modeling for Coupled Neutronics/Thermal-hydraulics Transient Analy- sis of Advanced Sodium-cooled Fast Reactors. Supervisors: R. Chawla, K. Mikityuk.
2007 – 10	Assistant for reactor practicals at EPFL, Switzerland, for students in 3rd year of the Physics Bachelor and in 1st year of the Nuclear Engineering Master.
2008 - 10	Supervisor of two Master theses and three undergraduate students.
2009 - 10	Chief Scientific Investigator from Switzerland (PSI) and Coordinator of the benchmark activities based on the Phenix End-Of-Life natural convection test within a Coordinated Research Project (CRP) organized by the IAEA Technical Working Group on Fast Reactors (TWG-FR).
2009	License "Chef d'exploitation du réacteur CROCUS de l'EPFL", Laboratory for Reactor Physics and Systems Behavior (LRS), EPFL.
2007	Master Thesis , Comissariat à l'énergie atomique (CEA Cadarache), France, <i>Study</i> of the Possibility of Development of the CATHARE code for transient analysis of the Molten Salt Reactor MSBR. Supervisor: M. S. Chenaud.
2006	2-month Internship , Centro Atómico Bariloche, Laboratory of "Neutrones y Reactores", Argentina, <i>Determination of In- and Au-slab thicknesses with different neutronics techniques</i> . Supervisor: R. Granada.

Education

2007 – 11	École Polytechnique Fédérale de Lausanne (EPFL) , Switzerland, PhD student in Energy. Professor: Rakesh Chawla.
2009	Expert in radioprotection for B- and C-domains, Strahlenschutzschule, CH – 5232 Villigen PSI.
2004 – 07	École Nationale Supérieure de Physique de Grenoble (ENSPG) , the French Higher Institute of Physics, part of the INPG (Technical University of Grenoble). Master in Energy and Nuclear Engineering with high honors.
2006	Instituto Balseiro , Bariloche, Argentina, the top Institute in Physics and Engineering in South America. Exchange student.
2002 - 04	Cycle Préparatoire Polytechnique (CPP): a two-year university level course as preparation to enter French INP engineering schools.

Skills

Reactor Physics	Reactor thermal-hydraulics and neutronics. Sodium two-phase flow modeling.
Computing Sciences	
	Windows and Linux systems. Programming languages: C++, Fortan 77, Fortran 90.
	Nuclear engineering code systems: TRACE (U.S. NRC), PARCS (U.S. NRC), FAST (PSI), ERANOS (CEA), CATHARE (CEA), SIMMER (JAEA/KIT/CEA).
Languages	Fluent in French (native language), English and Spanish. Good command of German.

PUBLICATIONS

Journal Articles

- [3] A. Chenu, K. Mikityuk, R. Chawla, 2011. Pressure drop modeling and comparisons with experiments for single- and two-phase sodium flow, *Nucl. Eng. Des.*, In Press.
- [2] K. Mikityuk, J. Krepel, S. Pelloni, A. Chenu, P. Petkevich and R. Chawla, 2010. FAST code system: review and recent developments and near-future plans, *Journal of Engineering for Gas Turbines and Power*, vol. 132/ 102915.
- [1] A. Chenu, K. Mikityuk, R. Chawla, 2009. TRACE simulation of sodium boiling in pin bundle experiments under loss-of-flow conditions, *Nucl. Eng. Des.* 239, 2417 2429.

Proceedings

- [6] A. Chenu, K. Mikityuk, R. Chawla, 2011. TRACE analysis of selected ISPRA experiments on dryout in sodium two-phase flow, 11th Int. Congress on Advances in Nuclear Power Plants (ICAPP-11), Paper 11289, Nice, France, May 2 - 5.
- [5] A. Chenu, K. Mikityuk, R. Chawla, 2010. Modelling of sodium boiling for coupled neutronic / thermal-hydraulic transient analysis of the Gen-IV SFR, European Nuclear Conference (ENC), Nominated best paper of the ENEN PhD Event, Barcelona, Spain, May 30 - June 2.
- [4] A. Chenu, K. Mikityuk, R. Chawla, 2010. A Coupled 3D Neutron Kinetics / Thermal-Hydraulics Model of the Generation IV Sodium-Cooled Fast Reactor, 10th Int. Congress on Advances in Nuclear Power Plants (ICAPP-10), Paper 10281, San Diego, California, USA, June 13 - 17.
- [3] A. Chenu, K. Mikityuk, R. Chawla, 2010. Modeling of Friction Pressure Drop for Sodium Two-Phase Flow in Round Tubes, 10th Int. Congress on Advances in Nuclear Power Plants (ICAPP-10), Paper 10282, San Diego, California, USA, June 13 - 17.
- [2] A. Chenu, K. Mikityuk, R. Chawla, 2009. One- and Two- dimensional Simulations of Sodium Boiling under Loss-of-flow Conditions in a Pin Bundle with the TRACE Code, 13th Int. Topical Meeting on Nuclear Reactor Thermal Hydraulics (NURETH-13), N13P1108, Kanazawa, Japan, Sept. 27 - Oct. 2.
- A. Chenu, K. Mikityuk, R. Chawla, 2009. Modeling of Sodium Two-phase Flow with the TRACE Code, 17th Int. Conf. on Nuclear Engineering (ICONE-17), Paper 75131, Brussels, Belgium, July 12 - 16.

Others

- [5] A. Chenu, R. Adams, K. Mikityuk, R. Chawla, 2010. Computational analysis of selected Phenix End-of-Life Tests with the FAST code system, NES Scientific Report (PSI publication).
- [4] A. Chenu, K. Mikityuk, R. Chawla, 2008. Modelling of sodium two-phase flow with the TRACE code, NES Scientific Report (PSI publication).
- [3] A. Tartaglione, J. J. Blostein, A. Villanueva, A. Chenu, J. Dawidowski, R.E. Mayer, 2006. Detección de gammas prompt empleando una fuente pulsada de neutrones, XXXIII Reunión Anual de la Asociación Argentina de Tecnología Nuclear, Buenos Aires, Argentina, November 20-23.
- [2] A. Tartaglione, J. J. Blostein, A. Villanueva, A. Chenu, R.E. Mayer, 2006. Detección de sustancias mediante espectroscopía de gammas prompt empleando una fuente pulsada de neutrones, 91 Reunión Anual de Física, AFA 2006, Merlo, San Luis, Argentina, September 25-29.
- [1] J. J. Blostein, A. Tartaglione, A. Villanueva, A. Chenu, J. Dawidowski, 2006. Estudio de resonancias nucleares de absorción neutrónica mediante la detección de gammas prompt, 91 Reunión Anual de Física, AFA 2006, Merlo, San Luis, Argentina, September 25-29.

Awards

Best paper and best presentation prize at the ENEN (European Nuclear Education Network) PhD Event 2010 in Barcelona, Spain.